

1998

# INVESTIGATION INTO THE MATERIALS AND MANUFACTURING OF A NEW THIN FILM MAGNETORESISTIVE SENSOR

MA, YONG QING

<http://hdl.handle.net/10026.1/2834>

---

<http://dx.doi.org/10.24382/3896>

University of Plymouth

---

*All content in PEARL is protected by copyright law. Author manuscripts are made available in accordance with publisher policies. Please cite only the published version using the details provided on the item record or document. In the absence of an open licence (e.g. Creative Commons), permissions for further reuse of content should be sought from the publisher or author.*

**INVESTIGATION INTO THE MATERIALS  
AND MANUFACTURING OF A NEW THIN FILM  
MAGNETORESISTIVE SENSOR**

by

**YONG QING MA**

A thesis submitted to the University of Plymouth  
in partial fulfilment for the degree of

**DOCTOR OF PHILOSOPHY**

School of Electronic, Communication and Electrical Engineering  
Faculty of Technology

**December 1998**

REFERENCE ONLY

UNIVERSITY OF SOUTHWEST ENGLAND	
Item No.	9003856041
Date	25 FEB 1999 T
Class No.	T681.2 MA
Contl. No.	X703831339
LIBRARY SERVICES	

90 0385604 1



LIBRARY STORE

This copy of thesis has been supplied on condition that anyone who consults it recognises that its copyright rests with its author and that no quotation from the thesis and no information derived from it may be published without the author's prior written consent.

Copyright © 1998 by Yong Qing Ma



## **ABSTRACT**

### **INVESTIGATION INTO THE MATERIALS AND MANUFACTURING OF A NEW THIN FILM MAGNETORESISTIVE SENSOR**

**YONG QING MA**

There is increasing interest in utilising very thin anisotropic magnetoresistive films (typically in the range of a few nano-metres) to make magnetic sensors which can be made very small and with a high signal-to-noise ratio. In this thesis, a new type of sensor is investigated which has a pair of thin film MR stripes whose magnetisation is switched alternately in opposite directions using bias fields from currents in overlay conductor films. The investigation considers in particular the Barkhausen noise in these sensors and its relationship with factors such as sensor film thickness.

The effect of thickness and grain size on the coercivity of  $\text{Ni}_{81}\text{Fe}_{19}$  permalloy thin films deposited by r.f. sputtering with negative substrate bias is systematically investigated as a function of under-layer materials, thickness, and substrate temperature. The results show that there is a minimum in coercivity at a thickness of about 7.5 nm with a grain size of 4 nm. This may be attributed to the grain size via its relationship with magnetic domain wall thickness. A tantalum under-layer favours a (111) (low anisotropy) surface plane in permalloy sensor films. Elevated deposition temperature may reduce defects in the films.

A comparison of the magnetic domain wall structure and the state of magnetisation in the very thin (5 ~ 30 nm) permalloy films with and without Ta underlayer is made by using Lorentz TEM observation. The result shows that it is different in both cases. With Ta underlayer, the wider, straighter and more regular domain walls together with less rippling in magnetisation in adjacent domains may lead to a reduction in the Barkhausen noise.

Barkhausen noise studies of films are carried out by sweeping an ac field of 77 Hz onto the permalloy films and recording the induced output voltage due to the flux change as a function of time on a digital storage oscilloscope. Barkhausen noise and corresponding hysteresis of the sensor is studied by analysis of the MR response of various sensors together with their magnetoresistive hysteresis, which may be reduced or improved by using a suitable external high frequency field (5 kHz to 20 kHz). Variation in the sensitivity of the sensor to the magnitude of a switched-biasing field was measured by applying a very small alternating field (from about tens to a few hundreds of nano-Tesla) at frequency above about 250 Hz and varying a transverse dc field component ( $\delta H_x$ ). The effect of biasing field frequency and external linearising field on the sensitivities of these MR sensors is studied using an in-house built measurement system.

Highly sensitive magnetoresistive sensors (120 different types have been available within 30 substrates) have been designed and then fabricated by photolithography in a temperature and humidity controlled clean room. Sensor thicknesses are typically in the range from 5 nm to 40 nm and other dimensions typically (10  $\mu\text{m}$  ~ 80  $\mu\text{m}$  wide) and 6.4 mm long. The sensor is linear in the range from zero to 14 400 nT. It produces an almost noise-free output of 20 to 30 millivolts for a field change of about 160 nano-Tesla.

### **AUTHOR'S DECLARATION**

At no time during the registration for the degree of Doctor of Philosophy has the author been registered for any other University award.

This study was financed with the aid of a studentship from the University of Plymouth.

A programme of advanced study was undertaken, which included a list of guided reading and an advanced course in the principles of electro-magnetics, supervised training for micro-fabrication in a class-100 clean room at the CRIST facility, and in transmission electron microscopy. Instruction in Lorentz TEM for magnetic domain observation and thin film microstructure analysis was going at the Department of Materials in the Oxford University. Relevant scientific seminars were attended.

The work contained in this thesis was partially presented at several international conferences, three papers have been published in research journals. Copies of publications are enclosed in the appendix of this thesis.

#### **Publications:**

- D J Mapps, Y Q Ma and M A Akhter, Optimisation of Material and Structure for a Switched-bias Magnetoresistive Sensor, in the press at *J. Sensors and Actuators*.
- M A Akhter, D J Mapps, Y Q Ma, A K Petford-Long and R Doole; Domain Walls and Magnetic Properties of Very Thin Permalloy Films for Magnetoresistance Sensors, *J. of IEEE Trans. Magnetics*. Vol. 34, No 4, p1147~1149, July., 1998.
- M A Akhter, D J Mapps, Y Q Ma, A K Petford-Long and R Doole; Thickness and Grain Size Dependence of the Coercivity in Permalloy Thin Films, *J. of Applied Physics* Vol.81 (8), p4122~4124, 15 April, 1997.

#### **Conferences Attended**

The 2<sup>nd</sup> European Conference on Magnetic Sensors & Actuators, in Sheffield, U. K., July 1998,

Signed.....*Yong Qing Ma*.....  
Date.....15/12/98.....

## **ACKNOWLEDGEMENTS**

I would like to express my sincerest thank to all following people and organisations for their help and support during this study, in particular,

My supervisors, Professor D J Mapps and Dr M A Akhter, for their constructive supervision and guidance, constant support and steadfast encouragement throughout the project, and without whom this thesis would literally not have been possible.

Professor W W Clegg at the School of E.C.E.E, University of Plymouth for useful discussions and suggestions regarding this project.

All of the staff and my fellow researchers within the School of E.C.E.E., all of whose experience and expertise has been of help and benefit to me. Special thanks go to Mr P Brown and Mr S Warner for their technical skill & assistance and friendship in many ways, also Dr G Pan, Mr C Dong, Mr N Fry for their help and suggestions.

Dr A K Petford-Long and Mr R Doole, Department of Materials, University of Oxford, for their useful discussion and help in TEM observation.

Dr R Moate, Mr B Lakey and the staff at the Electron Microscopy Centre, the University of Plymouth, for training and the use of equipment including technical help.

Dr Z S Shan, Department of Physics, University of Nebraska, U.S.A. for useful discussions and suggestions relating to this project.

University of Plymouth for providing me with the studentship, particularly the School of Electronic, Communication and Electrical Engineering for giving a good study and research environment.

I wish to thank Ms P Blower at International office, University of Plymouth, who not only read a lot of the first draft of this thesis but also helped in point of academic writing, and her colleague, Ms E Fogg, for her help during this study.

China New Building Materials Industry Hangzhou Design & Research Institute and Journal of "New Building Materials" publishing house, for their understanding and providing me time to complete this study.

I hope to thank some of my friends, Dr Y Wang, Dr B Yang, Mr H Zhao, Dr J Luan, Dr Y Wang and Mr J Zhang, for their help and support, and Mr & Mrs Melhuish for giving a good self-study and living environment.

Finally, my most grateful thanks go to my parent and family for their love, support and encouragement throughout.

CONTENTS

Abstract ..... a

Declaration ..... b

Acknowledgement ..... c

Contents ..... l

List of Tables and Figures ..... i

**1 BACKGROUND ..... 1**

    1.1 Introduction ..... 1

    1.2 Sensors for detecting magnetic fields ..... 2

        1.2.1 Inductive coils (or search-coil magnetometer) .....3

        1.2.2 Flux-gate Magnetometers ..... 4

        1.2.3 Hall effect and sensors .....6

        1.2.4 SQUID magnetometers .....7

        1.2.5 Magnetoresistive sensors .....9

    1.3 Application limitations ..... 12

**2 THEORY ..... 14**

    2.1 Units and some basic magnetic parameters ..... 14

        2.1.1 Units ..... 14

        2.1.2 Definition of some basic magnetic parameters ..... 15

    2.2 Magnetic materials ..... 17

        2.2.1 Ferromagnetism ..... 17

        2.2.2 Fundamental Energy effects ..... 21

        2.2.3 Magnetic domains and domain walls ..... 25

        2.2.4 Mechanism of magnetisation ..... 27

        2.2.5 Barkhausen Effect ..... 29

    2.3 Magnetic thin films ..... 31

        2.3.1 Magnetic domain walls ..... 31

        2.3.2 Barkhausen effect in thin films ..... 34

        2.3.3 Theory of coercivity ..... 35

        2.3.4 The ripple theory ..... 41

    2.4 Anisotropic magnetoresistance ..... 43

        2.4.1 Anisotropic magnetoresistance effect ..... 43

        2.4.2 Basic theory ..... 43

        2.4.3 Transverse field detection ..... 46

        2.4.4 General field detection ..... 48

2.5	Switched-bias M-R sensors .....	49
<b>3</b>	<b>EXPERIMENTAL DEVELOPMENT .....</b>	<b>53</b>
3.1	Introduction .....	53
3.2	Fabrication technology of thin film M-R sensors .....	54
3.2.1	Thin film deposition by r.f. Sputter coating .....	54
3.2.2	Photolithography techniques .....	61
3.2.2.1	Details of M-R sensor mask design .....	62
3.2.2.2	Photo-resist .....	65
3.2.2.3	Aligner system .....	65
3.2.2.4	Etching process .....	66
3.2.3	Other methods relating thin film M-R sensor fabrication .....	71
3.2.4	Micro-fabrication of thin film M-R sensor .....	71
3.3	Microstructure and texture analysis for thin M-R films .....	79
3.3.1	Transmission Electron Microscopy (TEM) .....	79
3.3.1.1	Specimen preparation for TEM .....	80
3.3.1.2	Electron diffraction pattern and images .....	81
3.3.2	Domain Observation by Lorentz Microscopy .....	88
3.4	Measurements of properties of M-R films and sensors .....	91
3.4.1	Measurement magnetic properties of Permalloy films .....	92
3.4.1.1	Coercivity measurement by B-H loop plotting .....	92
3.4.1.2	Barkhausen noise analysis for M-R films .....	94
3.4.1.3	Resistance and Magneto-resistance measurement for M-R films.....	98
3.4.2	M-R response measurement for M-R sensors .....	102
3.4.3	Electronic drive and test system used to evaluate M-R sensor performance .....	105
3.4.3.1	Test procedure .....	105
3.4.3.2	Microprobe system .....	107
3.4.3.3	The coil system .....	108
3.4.3.4	Others .....	114
<b>4</b>	<b>RESULTS AND DISCUSSION .....</b>	<b>115</b>
4.1	Magnetic properties in very thin Permalloy films .....	115
4.1.1	The variation of coercivity in very thin Permalloy films .....	115
4.1.1.1	Thickness dependence .....	115
4.1.1.2	Underlayer effect .....	119
4.1.1.3	Temperature dependence .....	120
4.1.2	Magnetic domains .....	133
4.1.2.1	Domains in very thin $\text{Ni}_{81}\text{Fe}_{19}$ permalloy films .....	133
4.1.2.2	Ta underlayer effect .....	136
4.1.3	Barkhausen noise analysis .....	151
4.1.3.1	Thickness dependence .....	151
4.1.3.2	Ta Underlayer effect .....	152

4.1.3.3 Temperature effect .....	154
4.2 Switched-Bias Magneto-resistive sensors .....	161
4.2.1 M-R response .....	162
4.2.3 Ta underlayer effect on hysteresis .....	163
4.2.3 Sensitivity to applied d.c. fields .....	170
4.2.3.1 Effect of bias field on the output characteristics .....	170
4.2.3.2 Sensitivity to applied d.c. fields .....	173
4.2.4 Optimum sensitivity to a low fields in the nano-Tesla range .....	173
4.3 Discussions .....	178
4.3.1 Coercivity variations .....	178
4.3.2 Ta underlayer effects .....	188
4.3.3 Thermal effects .....	191
<b>5 CONCLUSION &amp; FUTURE WORK .....</b>	<b>194</b>
5.1 Conclusions .....	194
5.1.1 Coercivity .....	194
5.1.2 Domain walls and Barkhausen noise.....	194
5.1.3 Switched-bias sensor .....	195
5.2 Future Work .....	197
<b>• APPENDICES</b>	
Appendix A Publications .....	1
<b>• BIBLIOGRAPHY .....</b>	<b>i</b>

## **Figure list**

### **Chapter 1**

Figure 1-1 Dynamic range of various magnetic sensors .....	3
Figure 1-2 Search-coil magnetometer based on Faraday's Law of induction .....	4
Figure 1-3 Flux gate magnetometer operation .....	5
Figure 1-4 Hall Effect sensor measures the voltage that appears across a thin wafer of a semiconductor due to a magnetic field perpendicular to the plane of the material and a current is sent along its length .....	7
Figure 1-5 (a) Schematic diagram of the connection of two Josephson junctions in parallel to form a SQUID. (b) Current-voltage characters of a SQUID .....	8
Figure 1.6 Schematic diagram of a thin-film magnetoresistor showing the principle directions and quantities used in the theory .....	10

### **Chapter 2**

Figure 2.1 Ferromagnetism .....	18
Figure 2.2 Magnetisation curve of a ferromagnetic substance .....	19
Figure 2.3 A typical hysteresis loop .....	20
Figure 2.4 An atomic cube of iron under the influence of an external field $H$ .....	22
Figure 2.5 Domain structure in a specimen of iron with magnetostatic energy stored in fields at the domain extremities .....	23
Figure 2.6 Various possible domain configurations with zero magnetostatic energy .....	24
Figure 2.7 Some domain structures (a) single domain structure (b) Domain structure of a material with uniaxial anisotropy .....	25
Figure 2.8 Magnetisation curve and the classification of magnetisation mechanisms .....	27
Figure 2.9 Barkhausen noise (a) Magnetic energy versus magnetisation (b) magnetic energy and energy gradient versus domain wall position showing irreversible and reversible motion .....	30
Figure 2.10 Comparison between the energy densities of Bloch, Néel and cross-tie walls in $\text{Ni}_{81}\text{Fe}_{19}$ films of varying thickness .....	32
Figure 2.11 A Bloch wall in a thin film (a) strictly. (b) Néel's approximation .....	32
Figure 2.12 Structure of a Néel wall (a) strictly (b) Néel's approximation .....	33
Figure 2.13 A cross-tie wall (top view) .....	34

## *List of Figures and Tables*

Figure 2.14 (a) Schematic drawing of wall motion under influence of magnetic field. (b) increase of wall length as a result of the motion of a domain tip .....	36
Figure 2.15 Wall width as a function of permalloy film thickness .....	40
Figure 2.16 The magnetoresistive transfer characteristic used in magnetic recording .....	47
Figure 2.17 Diagram showing a typical switched-bias magnetoresistive sensor .....	50
Figure 2.18 (a) Peaked drive current waveform for overcoming hysteresis, (b) Exaggerated magnetoresistance loop showing sampling points over AB, PQ, CD, RS. ....	51
Figure 2.19 Operation principle of the switched-bias sensor .....	52

## **Chapter 3**

Figure 3-1 Schematic diagram of the Materials Research Corporation (MRC) Sputtering System .....	59
Figure 3-2 Formation of a thin film .....	60
Figure 3-3 Showing the geometric designs of sensor layer and biasing layer .....	64
Figure 3-4 Schematic diagram of the Commonwealth scientific ion beam etching system .....	69
Figure 3-5 Some Photographs of sensor showing the damaged features caused by over etching .....	70
Figure 3-6 A graph showing the coating thickness for EPON SU-8-5 photo-resist versus the speed of the spinner .....	75
Figure 3-7 A Photograph of the JEOL 2000 FX Transmission Electron Microscope System .....	82
Figure 3-8 The two basic operations of the TEM imaging system (a) projecting the diffraction pattern on the view screen and (b) projecting the image onto the screen ..	83
Figure 3-9 Simplified schematic diagram showing the forming of an Electron Diffraction Pattern .....	85
Figure 3-10 A EDP showing the there is a random texture and which is indexed by looking at the ratio of ring diameter (assuming the smallest ring is the [111] ring) .....	87
Figure 3-11 Fresnel and Foucault imaging used for revealing magnetic domain structure observation .....	90
Figure 3-12 Schematic diagram of a thin MR film or sensor B-H loop testing system ..	93
Figure 3-13 The experimental Basis of Barkhausen Noise Measurement .....	96



## List of Figures and Tables

Figure 3-14 Schematic diagram of Barkhausen Noise Measurement System .....	97
Figure 3-15 In-line four-point probe and a Square-probe array for resistance measurement .....	99
Figure 3-16 Schematic diagram of the anisotropic magnetoresistance test system .	101
Figure 3-17 Showing a typical plot of anisotropic magnetoresistance versus the applied field .....	103
Figure 3-18 Schematic diagram of the anisotropic magnetoresistance testing system (including high frequency external linearising field) .....	104
Figure 3-19 A schematic diagram of sensor electronic drive and test system .....	106
Figure 3-20 Geometry for calculation of the magnetic field on the axis of a one-turn rectangular coil .....	109
Figure 3-21 The magnetic field generated in a rectangular coil versus the input current .....	112

## Chapter 4

Figure 4.1(a) Graphs of coercivity versus film thickness for $\text{Ni}_{81}\text{Fe}_{19}$ thin films deposited on various surfaces .....	117
Figure 4.1(b) Graphs of coercivity versus film thickness in the range from 2.5 to 100 nm .....	118
Figure 4.2 The TEM bright field images showing the lateral grain size changed in (a) 5 nm Permalloy film, (b) 40 nm Permalloy film .....	123
Figure 4.3 The TEM bright images for 40 nm Permalloy thin films with same thickness (5 nm ) Ta and Cr underlayer deposited under the same conditions .....	124
Figure 4.4 Electron Diffraction Patterns of 7.5 nm $\text{Ni}_{81}\text{Fe}_{19}$ thin films (a) with 5 nm Ta underlayer, (b) without 5 nm Ta underlayer .....	125
Figure 4.5 Electron Diffraction Patterns of 30 nm $\text{Ni}_{81}\text{Fe}_{19}$ films (a) with 5 nm Ta underlayer, (b) without 5 nm Ta underlayer .....	126
Figure 4.6 Coercivity versus grain size as a function of thickness. Set one of for $\text{Ni}_{81}\text{Fe}_{19}$ films deposited at about 300°C. Set two of for $\text{Ni}_{81}\text{Fe}_{19}$ films deposited at 20°C .....	127
Figure 4.7 TEM bright field images and Electron Diffraction Patterns for 2.5 nm $\text{Ni}_{81}\text{Fe}_{19}$ films .....	128

## List of Figures and Tables

Figure 4.8 TEM bright field images and Electron Diffraction Patterns for 5 nm $\text{Ni}_{81}\text{Fe}_{19}$ films .....	129
Figure 4.9 TEM bright field images and Electron Diffraction Patterns for 7.5 nm $\text{Ni}_{81}\text{Fe}_{19}$ films .....	130
Figure 4.10 TEM bright field images and Electron Diffraction Patterns for 10 nm $\text{Ni}_{81}\text{Fe}_{19}$ films .....	131
Figure 4.11 High magnification TEM image of 10 nm $\text{Ni}_{81}\text{Fe}_{19}$ thin films.....	132
Figure 4.12 Magnetic domains in 7.5 nm $\text{Ni}_{81}\text{Fe}_{19}$ thin film. (a) domains (b) saturation state .....	140
Figure 4.13 Magnetic domains in 10 nm $\text{Ni}_{81}\text{Fe}_{19}$ thin films. (a) domains (b) saturation state .....	141
Figure 4.14 Lorentz TEM initial image for 5 nm $\text{Ni}_{81}\text{Fe}_{19}$ thin films with 5 nm Ta underlayer at zero field ( $H_0 = 0$ ) .....	142
Figure 4.15 Lorentz TEM initial image for 7.5 nm $\text{Ni}_{81}\text{Fe}_{19}$ films with 5 nm Ta underlayer at zero field ( $H_0 = 0$ ) .....	142
Figure 4.16 Lorentz TEM initial image for 10 nm $\text{Ni}_{81}\text{Fe}_{19}$ films with 5 nm Ta underlayer at zero field ( $H_0 = 0$ ) .....	143
Figure 4.17 Lorentz TEM initial image for 15 nm $\text{Ni}_{81}\text{Fe}_{19}$ films with 5 nm Ta underlayer at zero field ( $H_0 = 0$ ) .....	143
Figure 4.18 Lorentz TEM initial image for 30 nm $\text{Ni}_{81}\text{Fe}_{19}$ films with 5 nm Ta underlayer at zero field ( $H_0 = 0$ ) .....	144
Figure 4.19 Magnetic domains exist in 5 nm $\text{Ni}_{81}\text{Fe}_{19}$ films with 5 nm Ta underlayer at an applied field of - 0.72 Oe ( $H_a = -57$ A/m) .....	144
Figure 4.20 Images showing domain movement in 5 nm $\text{Ni}_{81}\text{Fe}_{19}$ films with 5 nm Ta underlayer .....	145
Figure 4.21 Images showing domain magnetisation in 10 nm $\text{Ni}_{81}\text{Fe}_{19}$ films with 5 nm Ta underlayer .....	146
Figure 4.22 Image showing cross-tie domain walls in 30 nm $\text{Ni}_{81}\text{Fe}_{19}$ films with a 5 nm Ta underlayer associated with defects .....	147
Figure 4.23 Lorentz TEM initial image for 7.5 nm $\text{Ni}_{81}\text{Fe}_{19}$ films without a 5 nm Ta underlayer at zero field ( $H_0 = 0$ ) .....	148
Figure 4.24 Lorentz TEM initial image for 30 nm $\text{Ni}_{81}\text{Fe}_{19}$ films without a 5 nm Ta underlayer at zero field ( $H_0 = 0$ ) .....	148

## List of Figures and Tables

Figure 4.25 Images showing typical domain structure and walls in 7.5 nm $\text{Ni}_{81}\text{Fe}_{19}$ films with and without a 5 nm Ta underlayer .....	149
Figure 4.26 Images showing typical domain structure and walls in 30 nm $\text{Ni}_{81}\text{Fe}_{19}$ films with and without a 5 nm Ta underlayer .....	150
Figure 4.27 Plots showing Barkhausen noise versus $\text{Ni}_{81}\text{Fe}_{19}$ film thicknesses from 5 nm to 25 nm .....	155
Figure 4.28 Plots showing Barkhausen noise in $\text{Ni}_{81}\text{Fe}_{19}$ films with and without Ta underlayer versus the film thickness (5 and 7.5 nm) .....	156
Figure 4.29 Plots showing Barkhausen noise in $\text{Ni}_{81}\text{Fe}_{19}$ films with and without a Ta underlayer versus the film thickness (10 and 15 nm) .....	157
Figure 4.30 Plots showing Barkhausen noise in $\text{Ni}_{81}\text{Fe}_{19}$ films with and without a Ta underlayer versus the film thickness (25 and 40 nm) .....	158
Figure 4.31 Graphs showing Barkhausen noise in $\text{Ni}_{81}\text{Fe}_{19}$ films with and without a Ta underlayer varied with the substrates .....	159
Figure 4.32 Graphs showing Barkhausen noise in $\text{Ni}_{81}\text{Fe}_{19}$ thin films varied with deposited temperature .....	160
Figure 4.33 Magnetoresistance change versus $\text{Ni}_{81}\text{Fe}_{19}$ thin film thickness .....	164
Figure 4.34 Magnetoresistance change versus film thickness for sensors with a 5 nm Ta underlayers .....	165
Figure 4.35 Magnetoresistance change versus film thickness for sensors without a 5 nm Ta underlayers .....	166
Figure 4.36 Graph showing the M-R response and hysteresis variation of 10 nm sensor (80 $\mu\text{m}$ wide) without a 5 nm Ta underlayers versus the frequency of linearising field (0.2 Oe and applied along the easy axis) .....	167
Figure 4.37 Graph showing the M-R response and hysteresis variation of 10 nm sensor (80 $\mu\text{m}$ wide) with a 5 nm Ta underlayers versus the frequency of linearising field (0.2 Oe and applied along the easy axis) .....	168
Figure 4.38 Graph showing the M-R response and hysteresis variation of 10 nm sensor (80 $\mu\text{m}$ wide) with 5 nm Ta underlayers versus the frequency of linearising field (0.2 Oe and applied along the hard axis) .....	169
Figure 4.39 Showing the output of a 80 $\mu\text{m}$ wide, 10 nm thick sensor with 5 nm Ta underlayer versus d.c. field for three bias fields .....	172

## List of Figures and Tables

Figure 4.40 The output response of an 7.5 nm sensor (80 $\mu$ m wide) for a $\delta H$ field of about 160 nano-Tesla (a) at zero field before switching on (b) at 160 nano-Tesla field after switching on .....	175
Figure 4.41 The output response of a 80 $\mu$ m wide, 10 nm thick sensor versus 250 Hz bias field (0.00906 Oe or 0.72 A/m per mA) for an applied field ( $\delta H$ ) of 160 nano-Tesla .....	176
Figure 4.42 The output response of a 80 $\mu$ m wide, 7.5 nm thick sensor versus 250 Hz bias field (0.00906 Oe or 0.72 A/m per mA) for an applied field ( $\delta H$ ) of 160 nano-Tesla .....	177
Figure 4.43 Showing the coercivity $H_c$ variation in the easy direction as a function of film thickness .....	181
Figure 4.44 Diagram showing the type of wall to be theoretically expected (solid lines) and experimentally observed (dashed lines) as a function of the angle $\phi_0$ (between magnetisation outside the wall and the hard direction) and the film thickness .....	182
Figure 4.45 The dependence of the structure constant on evaporation temperature for $Ni_{81}Fe_{19}$ films .....	192

## List of Tables

### Chapter 1

Table 1-1 Advantages of Magnetoresistive sensors .....	12
Table 1-2 Application Areas of Magnetoresistive Sensor .....	13
Table 1-3 Possible limitations in their applications .....	13

### Chapter 2

Table 2-1 The basic parameters used in magnetism in both SI and cgs units .....	14
---	----

### Chapter 3

Table 3-1 Typical parameter used in ion beam etching .....	78
Table 3-2 The ratios of diffraction ring for an cubic crystal of fcc structure .....	86

### Chapter 4

Table 4.1 Some Results for Coercivity versus Grain Size in $Ni_{81}Fe_{19}$ Thin Films .....	118
Table 4.2 Coercivity versus thermal history .....	122
Table 4.3 Domain structure and magnetisation properties observed in Permalloy films deposited with and without a 5 nm Ta underlayer .....	139
Table 4.4 Effect of frequency of bias field on the output of sensor .....	171

## PURSUING THE TRUTH

----The school motto of Zhejiang University

## **CHAPTER 1**

### **BACKGROUND**

#### **1.1 Introduction**

There is increasing interest in utilising very thin magnetoresistive films (typically in the range of a few nano-metres) to make magnetic sensors of a very small size and with a high signal-to-noise ratio [Mapps et al., 1997]. Much research has been carried out to explore the fundamental and application limitations of magnetoresistive sensors in their thin-film form [Kim & Silva, 1996] and some work has been performed using very thin magnetoresistive films to make recording heads [Tsang et al., 1996 & 1997].

In this thesis, a new type of magnetoresistive sensor is investigated which has a pair of very thin film M-R stripes whose magnetisation is switched alternately in opposite directions using bias fields from currents in overlay conductor films. The investigation considers, in particular, the Barkhausen noise in these sensors and its relationship with factors such as sensor film thickness.

Chapter 1 provides an introduction and background for this investigation with a review of various sensors for detecting magnetic fields. Some of these will be described in more detail together with their application limitations. In Chapter 2, the theories, including some basic parameters and concepts used in magnetism, magnetic materials and magnetic thin films are discussed. It also provides a detailed description of thin film magnetoresistive sensors. Some theories behind the experimental technology are also described in Chapter 2, the description of the experimental development is given in



Chapter 3. Results and a discussion of the relationship between these results and existing theories are given in Chapter 4. Chapter 5 includes conclusions and suggestions for future work.

## **1.2 Sensors for detecting magnetic fields**

Magnetic Sensors are devices which are able to transform an existing magnetic field into an electrical signal. They have been in use in one form or another for many years. They range from suspended magnets used for navigation to small thin film detectors which sense information in the form of magnetic reversals on magnetic computer disks. Magnetic fields are used almost universally in electrical motors and transducers to produce movement. They also give rise to concerns about their interaction with human beings and conversely, are used via magnetic resonance systems to scan inner parts of the human body not visible with X-rays.

Such a wide range of applications means that detection and measurement of magnetic fields is, therefore, of significant technical and commercial importance. A whole range of different detectors and systems have evolved to cover the range of magnetic fields of interest to society and industry in general [Mapps, 1994. & 1997] [ Heremans, 1993].

Figure 1-1 shows the various magnetic sensors used for sensing magnetic fields together with the approximate range of fields over which they detect. Most of them are quite different from each other in construction and cost, as well as in making comparisons. On the other hand, we must take account of the application, the accuracy desired and the physical size of the sensor being used.

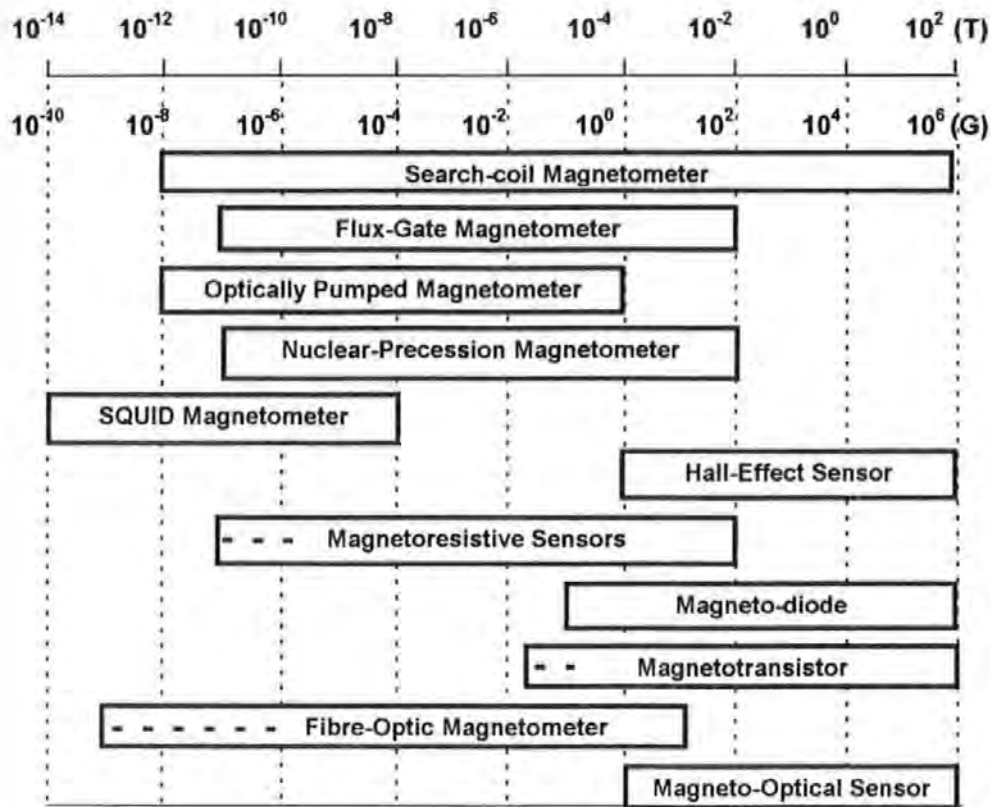


Figure 1-1 Dynamic range of various magnetic sensors  
(dashed range is possible) (after [Lenz, 1990]).

### 1.2.1 Inductive coils (or Search-coil magnetometer)

When there is a change in the magnetic flux passing through a coiled conductor, a current is induced in the coils and a voltage proportional to the rate of change of the flux is generated between its leads. This is Faraday's law of induction and is the principle behind the search-coil magnetometer. Equation 1.1 show the relationship between rate of change of flux ( $\Phi$ ) and the induced e.m.f. ( $V$ ).

$$V = -N \frac{d\Phi}{dt} \quad (\text{Equation 1.1})$$

If  $A$  is the cross-section area of the coil and  $N$  is the number of turns, the magnetic induction is then  $B = \Phi/A$  and



$$V = -NA \frac{dB}{dt} \quad (\text{Equation 1.2})$$

By measuring the magnetic flux passing through the coil  $\Phi$ , and from a knowledge of the cross-sectional area  $A$ , the magnetic induction  $B$  can be found.

A typical arrangement of a search-coil magnetometer is illustrated in Figure 1.2. The space inside the coil can be occupied by a material with a higher relative permeability than an air core. Such high permeability cores can be used to concentrate the surrounding magnetic field and increase flux density, and hence improve overall sensitivity. The sensitivity of the search-coil magnetometer is dependant on the following factors: (a)the permeability of the coil core material; (b)the area of the coil; (c) the number of turns; (d) the rate of change of the magnetic flux through the coil.

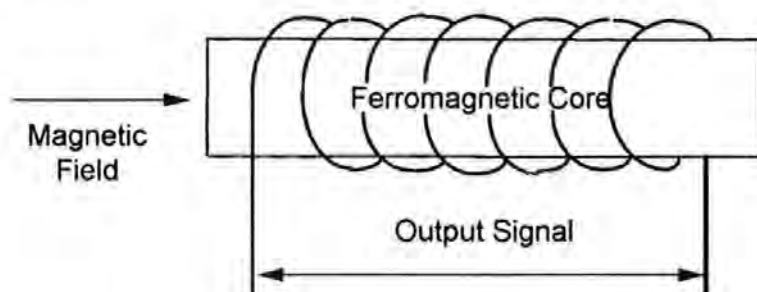


Figure 1-2 Search-coil magnetometer based on Faraday's Laws of induction

(after [Lenz,1990]).

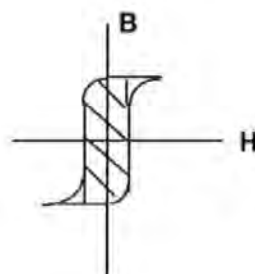
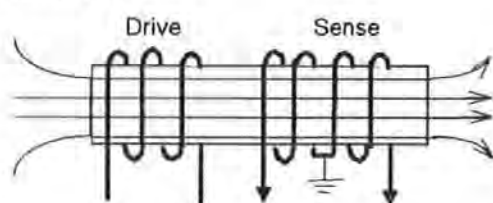
### 1.2.2 Flux-gate Magnetometer

The major limitation of the search coil is that there has to be a change in the flux passing through the coil to produce an e.m.f. at the coil's ends. This means that only a.c. fields can be detected. In contrast, the major advantage of flux-gate magnetometers over search coils is their ability to measure precisely direct current (d.c.) fields.

## Chapter 1: Background

A typical flux-gate magnetometer illustrated in Figure 1-3 consists of a ferromagnetic material wound with two coils, named a drive coil and a sense coil (a differential coil pair as shown in Figure 1-3) respectively. The drive coil is driven with an alternating waveform which magnetises the ferromagnetic core first in one direction and then the other. Early types of flux-gate were used to drive the coil hard into saturation in both directions. This would trace out a B-H loop as shown in Figure 1-3 for the core with its associated hysteresis. However this was not economical in terms of the power required by the drive coil to reach saturation.

Out of Saturation



In Saturation

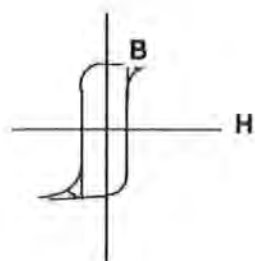
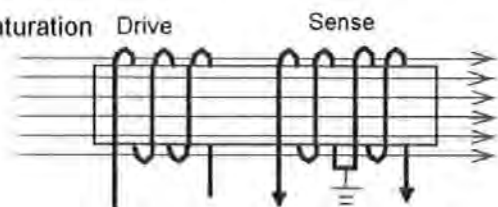


Figure 1-3 Flux gate magnetometer operation (After [Lenz, 1990])

New low power flux-gates do not operate over the major hysteresis loop, but instead drive the core around a minor hysteresis loop which does not enter saturation. These minor-loop flux-gate magnetometers are much more sensitive to the drive and readout electronics than the major-loop versions, which are mostly dominated by the core material's properties.

## Chapter 1: Background

Equation 1-3 shows the relationship between the flux-gate output  $V_{\text{sense}}$  and the external field.

$$V_{\text{sense}} \propto \left( \frac{dB_{\text{drive}}}{dt} + \frac{dB_{\text{external}}}{dt} \right) \quad (\text{Equation 1-3})$$

### 1.2.3 Hall effect and sensor

When a magnetic field is applied to a conducting material carrying an electric current, there is a transverse force (known as the Lorentz force) on the charge carriers (electrons) which can be given by

$$F = \mu_0 e v \times H \quad (\text{Equation 1.4})$$

The Lorentz force, which is perpendicular both to the electric current direction of motion and to the direction of the applied magnetic field, can be used to deflect the path of the electric current passing through a sample of the material. The effect is known as the Hall effect as illustrated in Figure 1-4 and is measured perpendicularly to both current and magnetic field. The relationship between Hall effect (the potential difference  $V$ ) and the passing distance  $L_x$  of the charge carriers may be given by,

$$V_{\text{Hall}} = \mu_0 R_H J \times \frac{H}{L_x} \quad (\text{Equation 1-5})$$

where  $R_H$  is the value of the Hall coefficient and is typically  $10^{-10} \text{ m}^3$  per Coulomb,  $J$  is the current density and  $H$  is the magnetic field strength [Lenz, 1990].

The Hall effect is very small in metallic conductors, but some semiconductors such as InAs or In Sb, will give a much larger effect. Since there are fewer conduction electrons in semiconductors, if the total current through it is the same as that through a metal, the electrons in the semiconductor must have a much higher drift velocity than those in the

## Chapter 1: Background

metal. The faster the electrons are moving, the stronger the force they experience and the greater the Hall voltage.

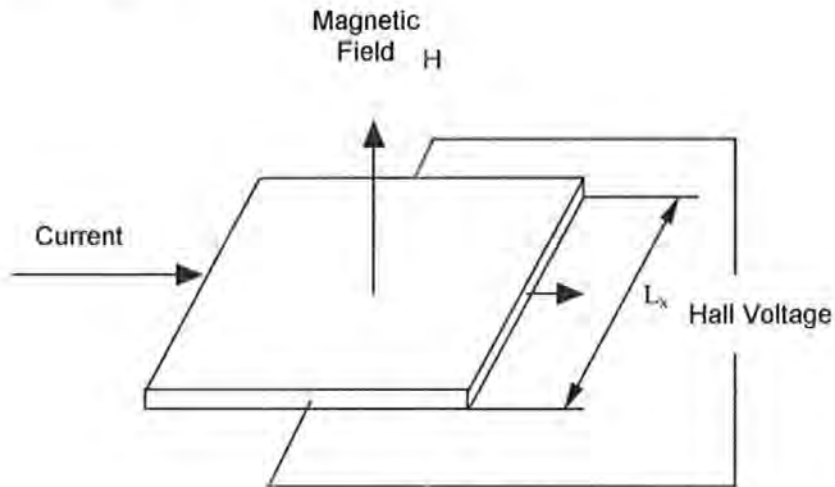


Figure 1-4 Hall Effect sensor measures the voltage that appears across a thin wafer of a semiconductor if there is a magnetic field perpendicular to the plane of the material and a current is sent along its length (after Lenz, 1990)

### 1.2.4 SQUID magnetometer

A 'SQUID' is a Super-conducting Quantum Interference Device, and has as its active element one or more Josephson junctions. A Josephson junction is a weak link between two superconductors that can support a super-current below a critical value  $I_c$ . The first type of SQUID was the two-junction d.c. SQUID (1964), later the one-junction SQUID (the r.f. SQUID) then appeared (1970).

In the d.c. SQUID, two Josephson junctions are connected in parallel as shown in Figure 1-5.

## Chapter 1: Background

As the magnetic flux  $\Phi$  threading the super-conducting loop changes the critical current of the two junctions, it oscillates with a period equal to that corresponding to the flux change. When the flux through the loop changes, the voltage-current characteristic oscillates smoothly as shown in Figure 1-5 (b). The SQUID is therefore a highly sensitive flux-voltage converter.

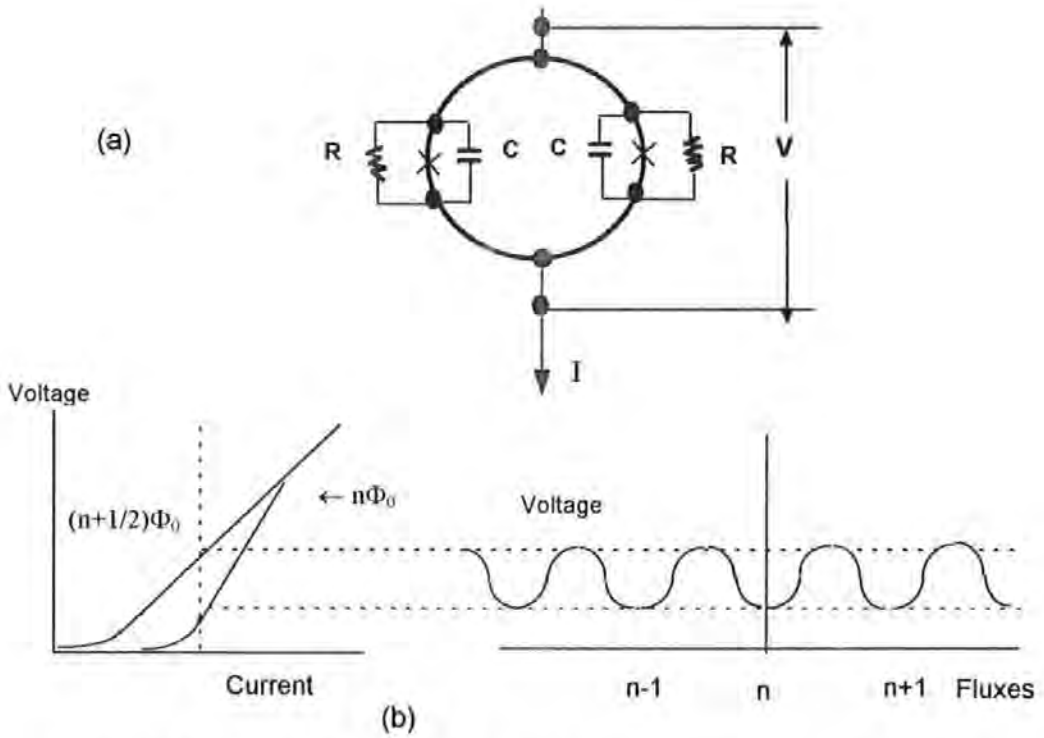


Figure 1-5 (a) Schematic diagram of the connection of two Josephson junctions in parallel to form a SQUID.

(b) Current-voltage characters of a SQUID. (after [Jiles,1991])

- The voltage is an oscillating function of the flux threading the circuit. The current-voltage characteristics are for a SQUID with fluxes  $n\Phi_0$  and  $(n + \frac{1}{2})\Phi_0$ . The variation of voltage across the SQUID with flux linking the circuit is shown on the right.

In general for practical field strength or induction measurements one usually needs a dynamic range somewhat greater than fractions of a flux quantum. In this case, the SQUID is often used as a null detector in a feedback circuit in which any change in

voltage across the SQUID is amplified and converted to a current through a coil coupled to the SQUID to produce an equal and opposite flux. This allows large magnetic fields to be measured to an accuracy of less than a flux quantum ( $2.067 \times 10^{-15}$  Wb, see [Jiles, 1991]). The SQUID can be said to be the most sensitive of all instruments for detecting a weak magnetic field.

### 1.2.5 Magnetoresistive Sensors

One magnetic sensor, in particular, has become popular because it occupies the mid-range of detection and can be made very small using photolithography fabrication methods common to the semiconductor industry. It also has small power consumption and relatively high resolution. This is the thin-film magnetoresistance sensor. Even now, it is only a quarter of a century after it was first reported in a paper by Hunt [Hunt, 1971]. More and more new application areas are being found and continue to be developed—most important among these are recording heads for magnetic storage devices, magnetic memory elements and position and speed sensors.

Magnetoresistive sensors are based on the magnetoresistive effect which is a change in resistance caused by an external magnetic field. The resistance of the magnetoresistive material (such as Permalloy) decreases as the direction of magnetisation rotates away from the direction in which the current flows because of the electron scattering.

- **Anisotropic Magnetoresistance**

A schematic diagram of a thin-film anisotropic magnetoresistor (AMR) showing the principle directions and quantities used in the theory is given in Figure 1-6.

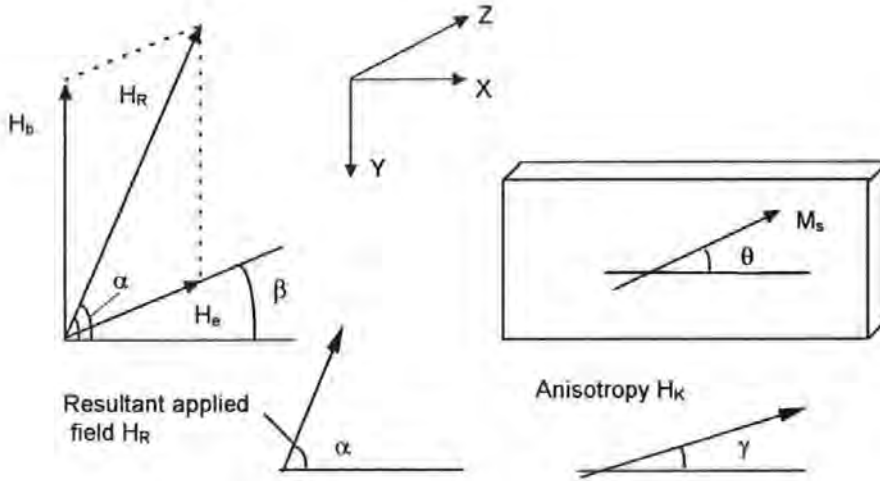


Figure 1.6 Schematic diagram of a thin-film magnetoresistor showing the principle directions and quantities used in the theory (After Mapps, 1997) .

Where, the film is assumed to be magnetised to saturation  $M_s$  at an angle  $\theta$  to its long axis which is also the one usually chosen for the direction of the electrical current flow.

$H_e$  is the earth's field and  $H_b$  is the bias field.  $H_R$  is the resultant applied field in which the sensor finds itself, and has a direction at an angle  $\alpha$  to the long axis. The anisotropy field  $H_k$  which is the direction of the lowest energy magnetisation direction of the material of the film, is at an angle  $\gamma$  to the long axis. The ultimate position of the magnetisation vector  $M_s$  is found as the resultant lowest energy magnetic state when the film experiences the applied field given the constraints mentioned above and also the demagnetising energy of the film in its own field. The relationship between the resistance change and the external magnetic field can be given by

$$\rho = \rho_0 + \Delta\rho \cos^2 \theta \quad (\text{Equation 1.6})$$

where,  $\rho_0$  is the isotropic resistivity and  $\Delta\rho_{max}$  is the maximum magnetoresistivity (saturation magnetoresistance).



## *Chapter 1: Background*

It is well known that the Anisotropic Magnetoresistance (or AMR), in general, is about 2% ~ 3% for most of common magnetoresistive materials such as permalloy or Co alloy. Research on magnetoresistance has been particularly active in recent years. Sensitivity has been especially improved using the Giant Magneto-resistance (GMR) effect in multilayers or granular films and their devices, Colossal Magnetoresistive (CMR) materials and devices, as well as Spin Polarised Tunnelling (SPT) junctions [Gallagher et al., 1997].

- Giant Magnetoresistance and sensors

The resistance of certain magnetic films may change by more than 20% for relatively small applied fields (GMR). This has been reported by many authors such as [White, 1982], [Mapps, 1994]. The dominant mechanism responsible for GMR is spin-dependent electron scattering. A GMR head for magnetic recording has been announced [Gallagher et al., 1997].

- Colossal Magnetoresistance

It has been discovered that certain perovskite materials (such as  $\text{LaMnO}_3$  doped with alkaline earth elements) display even larger (such as 80%) magnetoresistance, dubbed as 'colossal' magnetoresistance (CMR), but the effect only occurs in a large field and has a strong temperature dependence. The transport mechanism responsible for CMR is not well understood at the moment. The potential of CMR for low field, room-temperature applications has yet to be demonstrated [Gallagher et al., 1997].

- Spin Polarised Tunnelling Junctions

Another source of large magnetoresistance effects (on the order of about 20% at room temperature [Moodera et al., 1995]) have been reported in junctions, where electrons



tunnel through an ‘insulating’ barrier layer of, say, silicon oxide between two magnetic layers on either side. The tunnelling resistance depends on the relative magnetisation directions on either side of the junction. [Gallagher et al., 1997].

A summary of their advantages and application areas taken from reference [Mapps, 1997] is given in Table 1-1 and Table 1-2.

**Table 1-1 Advantages of Magnetoresistive sensors**

Main Advantages	More Details
High sensitivity	-allowing operation over relatively great distances
Low source resistance	-giving low sensitivity to electrical interference
High-temperature operation	-150°C continuous, 175°C peak (chip alone can withstand 175 °C continuous)
Operation over a wide frequency range	-from dc up to several MHz
Metal-film technology	-giving excellent long-term stability
Low sensitivity to mechanical stress	-facilitating mounting of the sensor and allowing its use in relatively rough environments.

### **1.3. Application limitations**

It may be hard to say which is the best sensor for detecting magnetic fields, due to the different needs for different applications. In general, factors such as temperature, sensitivity and S/N level, size and power consumption are of most importance and interest for selecting suitable sensors.

Table 1-3 shows the possible limitations of some sensors in their applications of detecting magnetic fields.

Note: The data shown in Table 1-3 can be found in Ref. [Lenz, 1990], [Jiles, 1991], [Wikswow, 1995], [Stewart, 1993] and [Heremans, 1993].

**Table 1-2 Application Areas of Magnetoresistive Sensor**

Main Areas	Application
Traffic control	<ul style="list-style-type: none"> <li>detection of vehicles</li> </ul>
Low-cost navigation	<ul style="list-style-type: none"> <li>allowing the production of simple compass systems with an accuracy of around 1° ideal for automotive applications</li> </ul>
Long-distance metal detection	<ul style="list-style-type: none"> <li>for the detection of, for example, military vehicles (tanks etc.) by measuring disturbances in the earth's magnetic field</li> </ul>
Motion detectors	<ul style="list-style-type: none"> <li>by measuring position changes relative to the earth's magnetic field.</li> </ul>
Current detection	<ul style="list-style-type: none"> <li>for example, earth-leakage switches</li> </ul>
General magnetic-field measurement	<ul style="list-style-type: none"> <li>from 10 A/m to 10 k A/m,</li> </ul>
Direct-current measurement	<ul style="list-style-type: none"> <li>starting currents in motor vehicles</li> </ul>
Angular or position measurement	<ul style="list-style-type: none"> <li>sensing of accelerator pedal or throttle position ( engine - management systems)</li> <li>position sensing in industrial automation systems</li> <li>(commercial sensor arrays that can measure positions with an accuracy of <math>\pm 30\mu\text{m}</math>)</li> <li>force/acceleration/pressure measurement using a moving magnet, for example: engine-intake-manifold pressure sensors, fluid-level sensors, low-cost weighing systems, geostatic (seismic) sensors, accelerometers.</li> </ul>
Mark detection and counting	<ul style="list-style-type: none"> <li>camshaft or flywheel position sensors for engine ignition systems.</li> <li>end-point sensors</li> <li>wheel-speed sensors for anti-blocking systems.</li> <li>rpm counters (0 to 20 kHz) for engine tachometers and for electronic synchromesh systems.</li> <li>flow meters</li> <li>zero speed detectors.</li> <li>rpm control in electric motors</li> <li>general instrumentation</li> </ul>
Magnetic Recording	<ul style="list-style-type: none"> <li>thin film reply heads for tape and disk systems, swipe readers for credit cards, bus tickets, door locks, etc.</li> </ul>

**Table 1-3 Possible limitations in their applications**

Sensor Type	Temperature (C°)	detectable range(Tesla) and S/N level	Frequency range (Hz)	Size mm or mm <sup>2</sup>	Power consumption (W)
Inductive coils	~0 to 40	$10^{-11} \sim 10^1$	1 ~ 1M	50 ~ 1250 mm	$1 \sim 10 \times 10^{-3}$ W
Flux-gate magnetometer	~0 to 40	$10^{-10} \sim 10^2$	d.c. ~ 10 k	10mm or 2.5 mm <sup>2</sup>	$5 \sim 50 \times 10^{-3}$
Hall effect	-273 ~ 200	$10^{-10} \sim 10^1$ 1%	up to 1 M	~7 mm <sup>2</sup>	0.1 ~ 0.2
SQUID magnetometer	4 ~ 77°K	$10^{-16} \sim 10^{-4}$ 1.4 pT / $\sqrt{\text{Hz}}$	$10^{-2} \sim 10^3$	~ 3 to 25 mm in diameter,	
AMR sensors	-55 ~ 200	$10^{-12} \sim 10^{-3}$	d.c. ~ 100 M	a few to a	$1 \sim 5 \times 10^{-4}$
GMR sensor	4.2 ~ 350 K	1.0 nT / $\sqrt{\text{Hz}}$ 1%		few tens mm <sup>2</sup>	

CHAPTER 2  
THEORY

2.1 Units and some basic magnetic parameters

2.1.1 Units

Some basic parameters used in magnetism are shown in Table 2-1. It should be noted that although the SI system of units is demanded in most of the current publications, the cgs (Gaussian) system of unit is still often used in practice. All of these parameters will be defined using the SI system of units in the following section. The SI system of units will be used throughout the remainder of this thesis and some conversion factors between both systems are given in Table 2-1.

Table 2-1 The basic parameters used in magnetism in both SI and cgs units

Quantity	Quantity Symbol	Unit in SI system	Unit in cgs system	Conversion Factors
Magnetic Field Strength	H	Ampere /metre (A/m)	Oersteds (Oe)	1 A/m = $4\pi/1000$ Oe or 1 Oe = $(1000/4\pi)$ A/m = 79.58 A/m
Magnetic flux	$\Phi$	Weber (Wb)	Maxwell	1 Wb= $10^8$ Maxwell or 1 Maxwell= $10^{-8}$ Wb
Magnetisation	M	Ampere/metre (A/m)	emu/cm <sup>3</sup>	1 A/m = $10^{-3}$ emu/cm <sup>3</sup> or 1 emu/cm <sup>3</sup> = 1000 A/m
Magnetic Induction	B	Tesla (T)	Gauss (G)	1 Tesla = $10^4$ Gauss
Magnetic moment	m	Ampere metre <sup>2</sup> (Am <sup>2</sup> )	emu	1Am <sup>2</sup> = 10 emu or 1emu = $10^{-1}$ Am <sup>2</sup>

### 2.1.2 Definition of some basic magnetic parameters

- **H** Magnetic field strength

A magnetic field is produced whenever there is electrical charge in motion. This can be generated by an electrical current flowing in a conductor, or produced by a permanent magnet. In the case of permanent magnet, there is no conventional electric current but there are the orbital motions and spins of electrons within the permanent magnet material which lead to a magnetisation within the material and a magnetic field outside.

The magnetic field strength (**H**), or magnetising force at a point is a vector quantity and is the measure of the effect of a field tending to produce magnetisation at that point. The unit of the magnetic field strength **H**, may be defined in a number of ways [Jiles, 1990]. It is measured in the ampere per metre, and can be simply defined as *the field strength produced by an infinitely long solenoid containing  $n$  turns per metre of coil and carrying a current of  $1/n$  ampere.*

- **Φ** Magnetic flux and **B** Magnetic induction or Magnetic flux density

Whenever a magnetic field is present in free space there will be a magnetic flux **Φ**. This magnetic flux is measured in units of Webers.

When a magnetic field **H** has been generated in a medium by a current, the response of the medium is its magnetic induction **B**. Sometimes it is called magnetic flux density, because it is based on the amount of flux passing through a given area of the medium in which the magnetic field exists. It is defined as  $\mathbf{B} = \Phi/A$ , and measured in Weber/m<sup>2</sup>, or equivalently, Tesla.

Magnetic induction is related to both magnetic field and magnetisation by a parameter known as the permeability  $\mu$  of the medium, measured in henrys per metre and generally calculated from B-H loop. Permeability defines the ability of a magnetic field passing through a medium to create an induction within the medium. In particular in free space,

$$B = \mu_0 H \quad (\text{Equation 2.1})$$

where  $\mu_0$  is a constant equal to  $4\pi \times 10^{-7}$  H/m. In another medium, however,  $\mu$  may not be a constant and hence  $B$  is not a linear function of  $H$ . This is particularly true in ferromagnets, where  $\mu$  varies rapidly. The relative permeability,  $\mu_r$  of a material is quoted, where

$$\mu_r = \frac{\mu}{\mu_0} \quad (\text{Equation 2.2})$$

- **m** Magnetic moment

The magnetic moment **m** is the most elementary unit of magnetism and one of the most important concepts for magnetic materials. In the case of magnetic materials, the electrical 'current' is caused by the motion of electrons within the solid, particularly the spins of unpaired electrons, which generate a magnetic moment even in the absence of a conventional current. It is measured in amperes metre<sup>2</sup>, and defined as: *A magnetic moment of 1 ampere metre<sup>2</sup> experiences a maximum torque of 1 Newton meter when oriented perpendicular to a magnetic induction of 1 Tesla.*

- **M** Magnetisation

The magnetic flux is caused by the presence of a magnetic field in a medium. The amount of flux for a given magnetic field depends on the properties of the medium in which the

field exists. To measure the response of a material (e.g. a medium) to the magnetic field, it is first necessary to define the quantities which represent the response of the materials to the field. The magnetisation  $M$  is a property of the material itself, and is generated by the resultant (uncompensated) spin and orbital angular momentum of electrons within the solid. The magnetisation of the material is measured in Amperes /metre.

When the magnetisation  $M$  and the magnetic field  $H$  are given, the magnetic induction  $B$  is now (Sommerfeld Convention)

$$B = \mu_0 \mu_r H = \mu_0 (H + M) \quad (\text{Equation 2.3})$$

## 2.2 Magnetic materials

### 2.2 1 Ferromagnetism

The atoms of any substance have an electronic structure in which electrons may be regarded as circulating in orbits about a central heavy nucleus. The electrons also have a gyroscopic spin. Both the orbital and spin motions of the electron charges can be considered like current in closed circuits, and with these permanently circulating currents magnetic moments may be associated. It is well known that the free atoms of some elements have zero magnetic moment because the various magnetic moments completely cancel each other, while the atoms of other elements have a resultant magnetic moment. The magnetic properties of any material in bulk depend, not only on the equivalent magnetic moments of the free atoms or molecules, but also particularly on temperature, that is on the thermal energy, and in solids on complicated inter-atomic forces in the crystals [Brailsford, 1966]. (Also see the Weiss Theory, page 20).



- Magnetisation curve

In the case of ferromagnetism, the electronic spins are aligned parallel to one another as a result of a strong positive interaction acting between the neighbouring spins as shown in Figure 2-1 (a). As the temperature increases, the arrangement of the spins is disturbed by thermal agitation, thus resulting in a temperature dependence of spontaneous magnetisation as shown in Figure 2-1 (b).

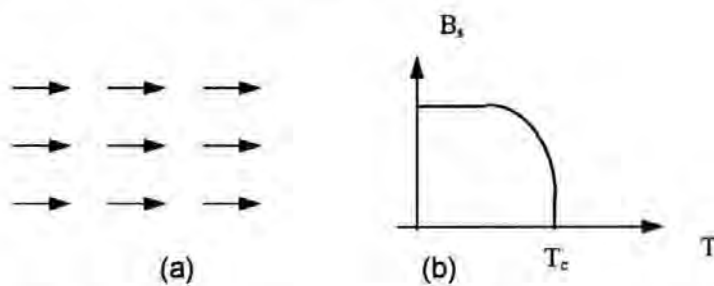


Figure 2.1 Ferromagnetism (after [Chikazumi,1964])

In spite of the presence of spontaneous magnetisation, a block of ferromagnetic substance is usually not spontaneously magnetised in the same direction but exists rather in an ‘overall’ demagnetised state. This is because the interior of the block is divided into many magnetic domains, each of which is spontaneously magnetised in different directions. If an external field is applied, the apparent magnetisation of the block is changed as shown in Figure 2-2 and finally reaches saturation magnetisation in the direction of the applied field. If the field is reduced, the magnetisation is decreased, but does not come back to the original value.

Such an irreversible process of magnetisation is called hysteresis. The presence of saturation magnetisation and hysteresis is an important feature of ferromagnetism.

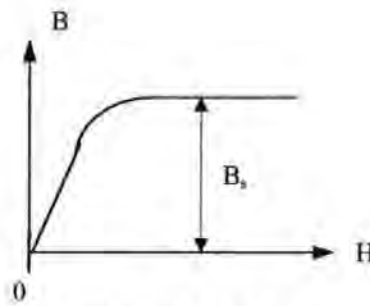


Figure 2.2 Magnetisation curve of a ferromagnetic substance

(after [Chikazumi, 1964])

- Hysteresis loop

A way to represent and compare the cyclic magnetic properties of a ferromagnetic material is by a plot of forward and reverse magnetic induction  $B$  for various field strengths  $H$ . This is called a hysteresis loop as shown in Figure 2.3. In particular, the output performance of ferromagnetic materials is closely related to the shape of the  $B$ - $H$  loops (both easy and hard directions). Various magnetic properties of interest in MR sensor applications, can be shown in their  $B$ - $H$  loop, such as

- The saturation magnetisation  $M_0$  is the upper limit to the magnetisation that can be achieved in which all magnetic moments are aligned parallel. At temperatures well below the Curie point the technical saturation  $M_s$  can be used instead. The saturation magnetisation is dependent only on the magnitude of the atomic moments  $m$  and the number of atoms per unit volume  $n$  and is given by  $M_0 = nm$ .
- The width of the  $M$ - $H$  loop across the  $H$  axis is twice the coercivity  $H_c$ . The coercivity is the magnetic field needed to reduce the magnetisation to zero from the remnant state.



- When the field is reduced to zero after magnetising a magnetic material, the remaining magnetic induction is called the remnant induction  $B_r$  and the remaining magnetisation is called the remnant magnetisation  $M_r$ .

The difference between B-H loop (e.g. Figure 2.3a) and M-H loop (e.g. Figure 2.3b and c) can be seen from Figure 2.3 and may also be explained theoretically from Equation 2.3  $B = \mu_0 (H + M)$ . The mechanism of hysteresis loop behaviour is technically related to the fundamental magnetisation curve [Jiles, 1991].

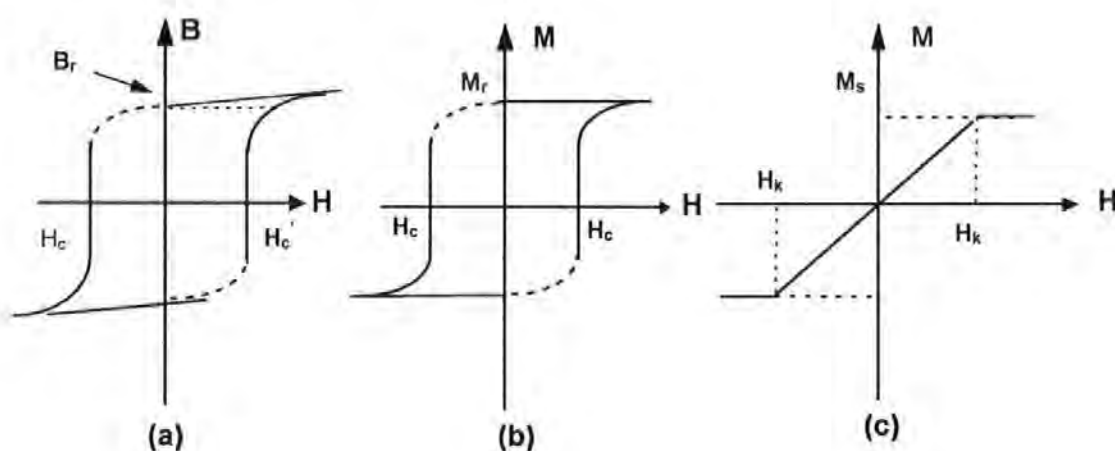


Figure 2.3 A typical hysteresis loop

- Weiss field theory

There is a transition temperature  $T_c$ , named the Curie point, in a ferromagnet, above which the material becomes paramagnetic and below which an ordered (the magnetic moments within domains are aligned parallel) ferromagnetic state exists. It can be explained phenomenologically by the Weiss theory.

Most ferromagnetic materials can be saturated by a magnetic field, which is considerable weaker than one required for paramagnets. The explanation for the relative ease with which ferromagnets may be magnetised is that there is an ‘internal’ field which causes all

atomic magnets to want to line up parallel to each other. It is normally considered to be an electric, not magnetic, effect which causes electrons in the 3d and 4s energy bands in certain materials to spin in the same direction as one another (instead of in opposite directions such as in most common materials). Thus the magnetic effects in adjacent atoms tend to be additive.

The interaction is such as to correspond to an applied field and this interaction, which Weiss introduced to explain the paramagnetic susceptibilities of certain materials, leads to the existence of a critical temperature below which the thermal energy of the electronic moments is insufficient to cause random paramagnetic alignment [Mapps, 1987] [Jiles, 1991].

### 2.2.2 Fundamental energy effects

One feature of ferromagnets is that they exhibit a complex change in their magnetisation upon the application of an external field. This is because there are many different kinds of energies and the energy interaction in ferromagnets. Basic energy terms in a ferromagnet can be summarised as follows [Jiles, 1991] [Miltat, 1994] [Mapps, 1987].

#### 1 Exchange energy

Exchange energy in a ferromagnet, as discussed previously, is based on the Weiss interaction theory. If the spins are forced to point in non-parallel directions there is an increase in magnetic potential energy. Since all magnetic systems behave as to reduce energy the system will have a minimum energy (all other things being equal) when the spins are parallel. This energy component is known as exchange energy. There may be a number of possible variations to the theme of the inter-atomic interaction or exchange,

only two of these, the mean-field approximation and a nearest-neighbour-only coupling will be mentioned. The exchange energy per moment due to above two interactions is

$$E_{ex} = -\mu_0 (mH_e + \alpha N m_i m_j) \quad (\text{Equation 2.4})$$

where,  $H_e$  is the interaction field which is proportional to the bulk magnetisation  $M$ .

$\alpha$  is the mean field parameter.  $m_i$  and  $m_j$  are neighbouring magnetic moments and  $N$  is the number of atoms per unit volume.

## II. Anisotropy energy

Suppose we have a single crystal of iron as shown in Figure 2.4 with an atom at each corner of the unit cube and one in the centre. It is found that if a field  $H$  is applied as shown, the material does not, surprisingly, magnetise along the direction of applied field. Instead, it magnetises along the nearest cube edge  $AB$  as shown. This is because of a spin-orbit coupling which produces a high-energy state for directions other than along cube edges. These are the so-called 'easy directions' in a crystal and coincide with a minimum in what is termed Anisotropy Energy.

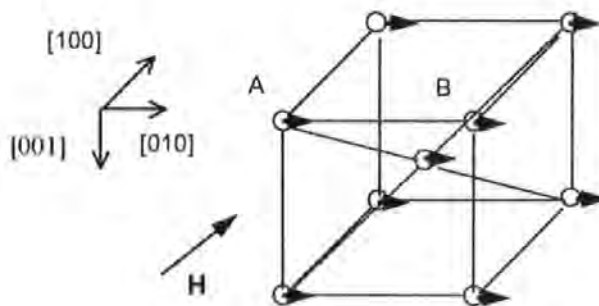


Figure 2.4 An atomic cube of iron under the influence of an external field  $H$  (after [Mapps, 1987])

### III Magnetostatic energy

If after  $H$  is applied in Figure 2.4 it is removed, the crystal appears like a magnet with a North Pole remaining at one end and a South Pole at the other. If left in this situation the crystal would have a large external field and this would consist high magnetostatic energy because all magnetic systems adjust themselves to try to reduce any external field. The tendency is for magnetisation to re-arrange itself to reduce the external field and this is one key factor in the creation of a multi-magnetic domain system.

### IV Domain wall energy

Once a single domain has split into multi-domains to minimise energy in a large crystal (containing millions of atoms) as shown in Figure 2.5, thin dividing regions between the domains are created. These regions are usually a few hundred atoms thick and are known as domain walls. They have an energy associated with their creation because magnetisation must reverse gradually through the thickness of walls and this will cause electron spins to point in non-parallel directions to each other and in non-easy directions leading to increases in exchange and anisotropy energy.

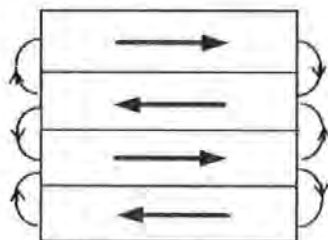


Figure 2.5 Domain structure in a specimen of iron with magnetostatic energy stored in fields at the domain extremities (after [Mapps, 1987])

## V Magnetoelastic energy

The magnetoelastic energy establishes a link between elastic strains and the direction of magnetisation in magnetic materials. Its origin is spin-orbit coupling. For example, it can be seen from Figure 2.6 (a), (b) and (c) that external field (and magnetostatic energy) can be virtually eliminated if the domain walls take up the positions shown. What, then is the magnetic difference between Figure 2.6 (a), (b) and (c) ?

The essential difference is via the phenomenon of magnetostriction whereby magnetic materials change their physical shape when magnetised. If we assume that the material of figure 2.6 (a) elongates along the direction of magnetisation by say 5% at saturation, then the angle ABC will cease to be  $90^\circ$  if the material ABC were free to expand. Since ABC is a part of the crystal it is prevented from expanding in this way causing the angle ABC to remain at  $90^\circ$ . Instead, mechanical strain energy is stored in the crystal-known as magnetoelastic energy.

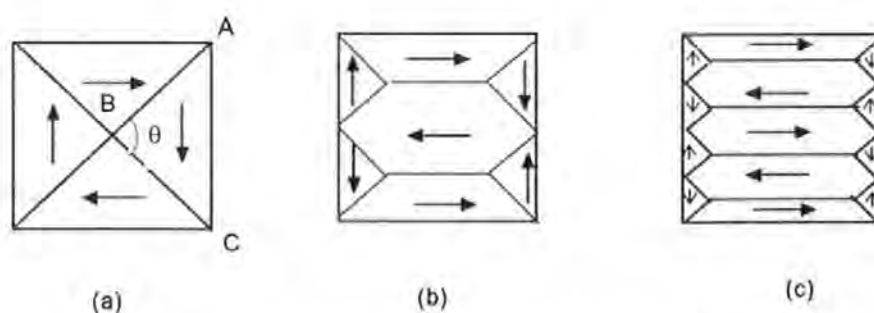


Figure 2.6 Various possible domain configurations with zero magnetostatic energy (after [Mapps, 1987])

The advantage of the structure in figure 2.6 (b) is that it has smaller triangular regions and therefore a lower magnetoelastic energy. It has, however, more domain walls and a higher domain wall energy.

Therefore, domains split and new domain walls are created until such time as there is a balance between domain wall and magnetoelastic energies, as might be indicated, for example, by figure 2.6 (c).

### 2.2.3 Magnetic domains and Domain Walls

- Domains

Domains in a magnetic body can be summarised as regions of very small or zero change in magnetic moment direction and were first suggested by Weiss in 1907. The concept of domains is now accepted. It was first experimentally verified both indirectly by Barkhausen in 1919 and directly observed by Bitter in 1931. Figure 2.7 shows some domain structures taken from ref. Chikazumi [Chikazumi, 1964].

Stable magnetic domains exist in ferromagnetic materials which can be treated as uniformly magnetised volumes in an overall minimum energy state.

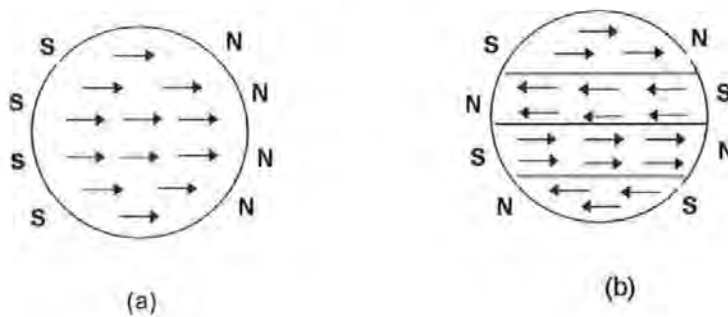


Figure 2.7 Some domain structures ((a) Single domain structure,  
(b) Domain structure of a material with uniaxial anisotropy (after [Chikazumi, 1964]))

- Domain walls

The first study of the transition layer between two magnetic regions (domains) with different directions of spontaneous magnetisation  $M$  was carried out by Bloch in 1932,

and it is after him that the 'Bloch wall' is named. The main concept associated with the understanding of this transition region is that the change in spin direction, between domains magnetised in opposite directions, does not occur suddenly across one atomic plane, but gradually, over many planes. In such a wall the effect of exchange interaction is to favour a transition over many planes because the smaller the angle between adjacent spins, the lower is the exchange energy between them. However, within this wall the magnetisation is in an unfavourable direction as determined by the magnetocrystalline anisotropy, so the widening effect of the exchange interaction is counteracted by the narrowing effect of the anisotropy [Prutton, 1964<sup>b</sup>].

- Energy minimisation and domain structure

In general, the essential reason for the existence of domains within a ferromagnetic material is that their formation reduces the magnetic free energy  $E$  associated with it. Thus, if all the necessary physical properties of the crystal and its surroundings are known, it should be possible in principle to deduce the optimum domain configuration so that the ferromagnetic material is in a state of minimum free energy, corresponding to a particular value of an applied field [Carey & Isaac, 1965].

However, the structure of domain walls depends on the relative importance of the energies such as the exchange anisotropy and magnetostatic contributions to the total energy. Hence wall structures depend not only on intrinsic magnetic properties but also on specimen dimension. Furthermore, there are generally marked differences between wall structures in thin films and bulk materials of the same composition [Chapman & Kirk, 1997].



It will be appreciated, however, that the difficulties of computation generally involved in such a problem will be enormous. As a result, only in certain simple cases, it is possible to determine with accuracy the sum of the energy terms associated with the domain [Carey & Isaac, 1965].

#### 2.2.4 Mechanism of magnetisation

When a ferromagnetic substance is put into an increasing magnetic field, its magnetisation is increased and it finally reaches saturation magnetisation. Such a process is essentially achieved by a change in the direction of domain magnetisation and domain size as domains with magnetisation more parallel to the field increase in size at the expense of domains with more anti-parallel magnetisation.

According to classical domain theory, the magnetisation process in a ferromagnet can be classified into three ranges as shown in Figure 2.8.

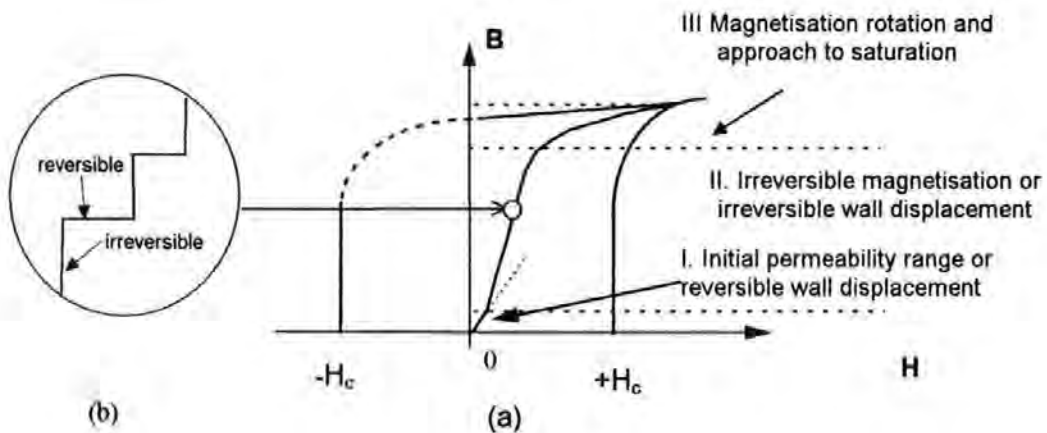


Figure 2.8 Magnetisation curve and the classification of magnetisation mechanisms (after [Chikazumi, 1964] and [Chen, 1977])



I. Initial permeability range or reversible displacements:

- Starting from the demagnetised state ( $B=0$  at  $H=0$ ), in which the magnetisation changes reversibly. Domain magnetisation in every domain rotates reversibly from their stable directions and/or domain walls are displaced reversibly from their stable positions. In this range, the reversible magnetisation is accomplished mainly by reversible displacements of domain walls. The ease of displacement of domain walls is essentially determined by the homogeneity of materials, the contribution of displacement of domain walls to an initial permeability is dependent on the kind of material studied.

II. Range of irreversible magnetisation or irreversible wall displacements

- If the magnetic field is increased beyond the initial range, the intensity of magnetisation will be increased further due to many small discontinuous changes in the magnetisation. At this stage, domain walls jump irreversibly past dislocations in the lattice structure by which they were initially held, referred to as the pinning sites. The occurrence of irreversible rotation of domain magnetisation is also expected in fine particles or in an extremely heterogeneous material which may contain many inclusions and precipitates. The magneto-thermal effect is also observed here due to the generation of heat accompanying magnetisation change. Barkhausen noise occurs mainly on the steep part of the magnetisation curve in this range as shown on an enlarged part of the curve (b) in the Figure 2.8.

III. Range of magnetisation rotation and approach to saturation.

- If the field is increased further, the magnetisation curve becomes less steep and its processes become reversible once more. In this range the displacements of domain walls have already been completed and magnetisation takes place by rotation of magnetisation. Beyond this range the magnetisation gradually approaches the saturation stage, in which it increases gradually in proportion to the intensity of the magnetic field as all the spins become perfectly aligned. It may be disturbed by thermal agitation to the thermal equilibrium state [Chikazumi, 1964].

#### 2.2.5 Barkhausen effect

The Barkhausen effect (also associated with Barkhausen noise) may be summarised as the phenomenon of discontinuous changes in the flux density  $B$  (or the magnetisation  $M$ ) within a ferromagnetic material as the magnetic field  $H$  is changed continuously, shown as (b) in Figure 2.8 [Jiles, 1991].

The effect was first observed in 1919 by Barkhausen [Barkhausen, 1919], when a secondary coil wound on a piece of iron was connected to an amplifier and loudspeaker. As the  $H$  field was increased smoothly, a series of clicks were heard (Barkhausen noise) over the loudspeaker, which were due to small voltage pulses induced in the secondary coil. These voltage pulses were caused through the law of electromagnetic induction by small changes in flux density through the coil arising from discontinuous changes (see section 2.2.4) in magnetisation  $M$  and hence in induction  $B$ .

Barkhausen effects are due to irreversible changes in the state of magnetisation. As can be seen from Figure 2.9 (a), there is a general energy minimum corresponding to the

central demagnetised state, but there are also many small minima. These can represent pseudo-stable states causing the magnetisation to lag behind the applied field, giving rise to the well-known phenomena of hysteresis and coercivity. This may be even more significant where the magnetisation is not a single magnetic domain. Figure 2.9 (b) is a plot of the rate of change of energy with distance moved of domain wall in a multi-domain state. This shows a series of irreversible jumps giving rise to a coercivity according to the equation

$$H_c = \frac{1}{2M_s} \frac{dE}{dx} \quad \text{(Equation 2.5)}$$

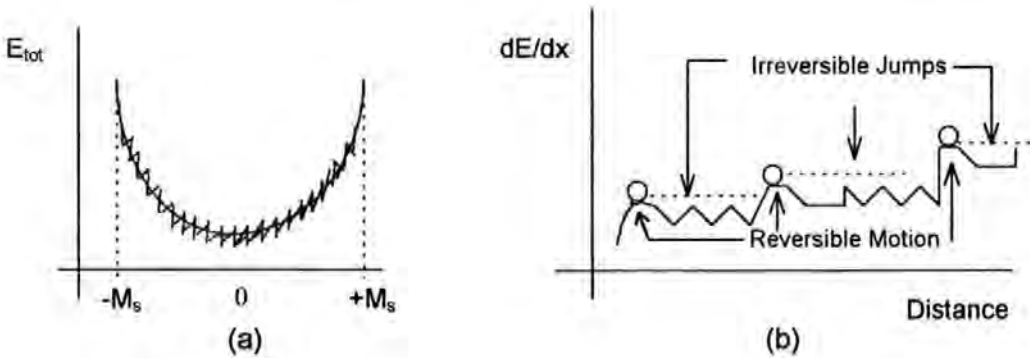


Figure 2.9 Barkhausen Noise (a) Magnetic energy versus magnetisation; (b) magnetic energy and energy gradient versus domain wall position showing irreversible and reversible motion (After [Mapps, 1997])

The Barkhausen effect is an extremely complex phenomenon and detailed studies are lacking. More detailed overviews about the Barkhausen effect, possible orientation, irreversible change in domain structure and experimental techniques have been summarised by many authors such as [McClure & Schroder, 1976], [Matzkanin et al., 1979], [Farrel, 1994] and [Mapps, 1997], and will be further discussed later.

## **2.3 Magnetic thin films**

As a consequence of the small thickness of 'thin' films, the magnetic energies, related domain structure and Barkhausen effect may be different from those in bulk material due to their thickness dependence. For example, the structure of domain walls depends on the relative importance of the exchange, anisotropy and magnetostatic contribution to the total energy. As film thickness is decreased the magnetostatic energy contribution becomes increasingly important and leads to other types of walls, such as Néel walls in the ultra-thin films, which are expected to be the norm [Néel, 1955], [Chapman and Kirk, 1997<sup>a</sup>].

### **2.3.1 Magnetic Domain walls**

The structure of domain walls in thin films was first investigated theoretically by Néel [Néel, 1955]. He predicted that the plane of spin rotation inside the wall will be changed from parallel to the wall surface to parallel to the thin film surface, and its magnetostatic energy should be reduced with a decrease of the film thickness due to reducing (their) volume interaction with the surface. More wavy type walls such as Néel wall and cross-tie walls have been observed in the thinner magnetic films.

Figure 2.10 shows the variation of wall energy density with film thickness for Bloch, Néel and cross-tie walls [Pruett, 1964<sup>a</sup>]. As can be clearly seen in Permalloy films, Bloch walls offer the lowest energy option for thicknesses greater than 90 nm, and Néel walls are dominant for thicknesses less than 30 nm. In the intermediate region, however, neither of these walls seem able to provide an advantageous energy state and the compromise cross-tie wall is observed.

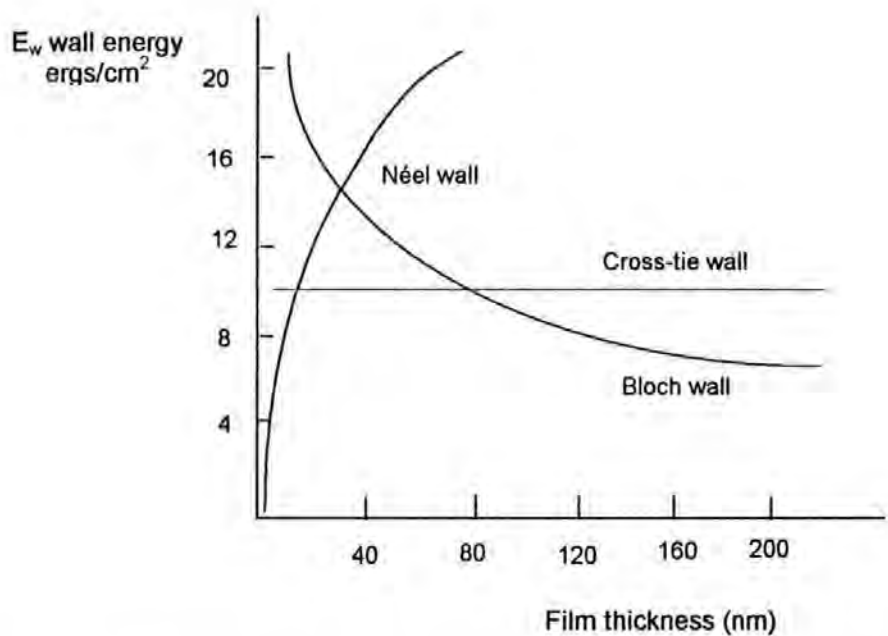


Figure 2.10 Comparison between the energy densities of Bloch, Néel and cross-tie walls in  $\text{Ni}_{81}\text{Fe}_{19}$  films of varying thickness (after Prutton, 1964<sup>b</sup>)

- Bloch wall

The Bloch wall is characterised by the magnetic moments in the wall rotating about an axis perpendicular to the plane of the wall itself as shown as in Figure 2.11. Both its energy and width depend only on the exchange and anisotropy constants and there is only a very small magnetostatic contribution [Chapman and Kirk, 1997<sup>a</sup>].

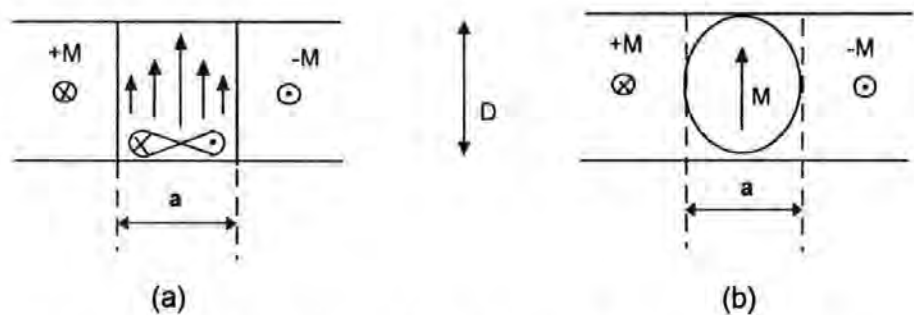


Figure 2.11 A Bloch wall in a thin film (a) strictly. (b) Néel's approximation (after Prutton 1964<sup>b</sup>)

- Néel walls

The Néel wall (see Figure 2.12) is energetically favoured once the film thickness decreases below a certain value, for example, around 30 nm in permalloy films, in which its energy becomes lower than the demagnetisation energy of the Bloch wall. In the Néel wall, the axis about which the magnetisation rotates is perpendicular to the film plane.

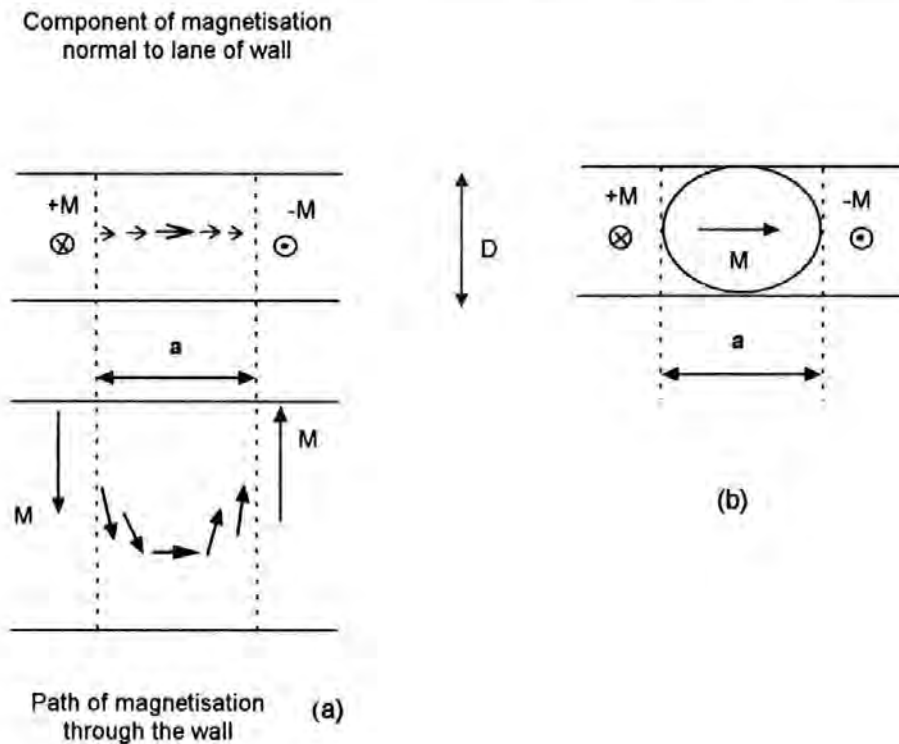


Figure 2.12 Structure of a Néel wall (a) strictly (b) Néel's approximation  
(after [Prutton, 1964<sup>b</sup>])

- Cross-tie walls

Cross-tie walls can be observed in the films thick enough to contain purely Bloch walls and films thin enough to contain purely Néel walls. Sometimes, they are observed together with Néel walls or Bloch walls. The magnetisation reversal may be achieved by

rotation of the magnetic moments both normal to and within the plane of the film, as illustrated in Figure 2.13. The character of these walls is such that close to the top and bottom surfaces they are Néel-like, thereby minimising the surface magnetic charge, whilst towards the centre of the film the way in which the moments rotate is more Bloch-like.

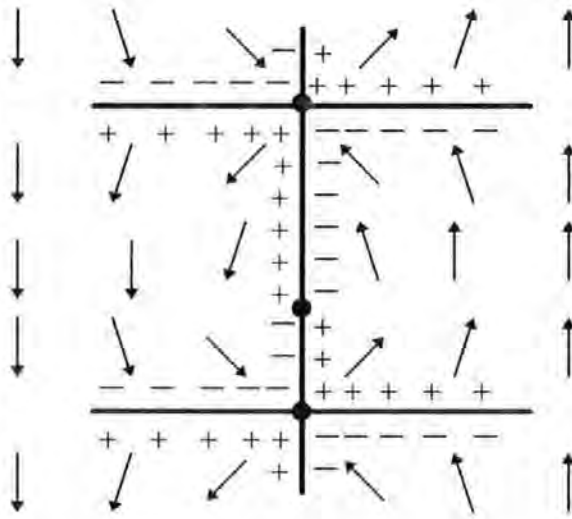


Figure 2.13 A cross-tie wall (top view) (after [Huo et al., 1998])

Many other wall types have been found in particular circumstances and some of them have been summarised by Chapman and Kirk [Chapman and Kirk, 1997<sup>a</sup>].

### 2.3.2 Barkhausen Effect in Thin Films

There are very few publications [Decker et al., 1981] concerning the thickness dependence of Barkhausen noise characteristics especially for the interesting thickness range in magnetic films down to a few tens of nanometres. In view of the structure of domain walls and its variation with the thickness, Barkhausen effect should be taken into account depending on the magnetic film form. Unfortunately, no theory has been yet



reported for quantitatively describing the variation of Barkhausen noise in the very thin magnetic films.

However, it is well known that Barkhausen noise is a result of irreversible jumps and is associated with the coercivity of thin films, so the less irreversible jumps, the smaller the coercivity and the lower the Barkhausen noise. Possible mechanisms and theories of coercivity will be described in the following section.

### 2.3.3 Theory of coercivity

Coercivity or coercive force is one of the most important properties for determining the magnetic behaviour of ferromagnetic films. It is directly related to the critical field required for the generation and movement of domain walls.

Experimental data show that coercivity is a parameter which also closely related to other structure-sensitive magnetic properties (e.g. magnetic anisotropy) [Prupton, 1964<sup>a</sup>] [Grundy, 1997]. There are many qualitative models have been developed for explanation of the variation of the coercivity in thin films. Some of them have been summarised and can be found in reference [Prupton, 1964<sup>b</sup>], [Chen, 1977]. The most well-known theories are:

#### I. Néel Model

Like other earlier theories (e.g. the strain theory developed by Bloch [1932] and Kersten [1938] and the inclusion theory by Kersten [1943]), The Néel model is based on the principle that irreversible movement of domain walls (only) is responsible for the coercivity.



Néel [Néel, 1956] described the coercive force (critical field ) variation with thickness of a thin film based on wall motion and this is given by,

$$H_c = \frac{c}{t^{4/3}} \quad (\text{Equation 2.6})$$

where,  $c$  is a constant and  $t$  is the thickness of the film. This is the well known '4/3' law.

## II. The wall motion model

Middelhoek constructed a general wall motion coercive force theory for thin NiFe films, in which the most important parameters (e.g. the change of the wall energy, film thickness variation and the wall length change) have been taken into account. Figure 2.14 is a schematic diagram of this wall motion model and is taken from reference [Middelhoek, 1961].

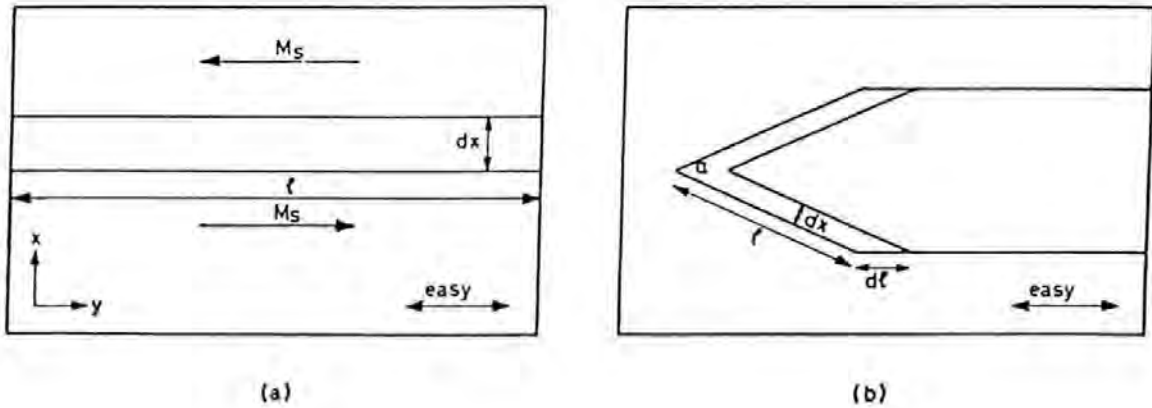


Figure 2.14 (a) Schematic drawing of wall motion under influence of magnetic field.

(b) Increase of wall length as a result of the motion of a domain tip

(after [Middelhoek, 1961])

In this model, for simplicity, it was assumed that the film is reversed by the shift of a wall parallel to the easy direction. The energy of the wall is a function of  $x$ , but constant

in the  $y$  direction. For a small shift  $dx$  of the wall parallel to itself the increase of the free energy of the system must be equal to the work performed on it.

$$2H_a M_s l dx = d(\gamma, t, l) \quad (\text{Equation 2.7})$$

where,  $H_a$  is applied field,  $M_s$  is saturation magnetisation,  $l$  is length of the part of the wall under consideration,  $t$  is thickness of the film,  $dx$  is distance over which the wall is shifted and  $\gamma$  is surface energy density of the domain wall.

The coercivity can be then written in more extended form as:

$$H_c = H_{a \max} = \frac{1}{2M_s} \left[ \frac{d\gamma}{dx} + \frac{\gamma}{t} \frac{dt}{dx} + \frac{\gamma}{l} \frac{dl}{dx} \right] \quad (\text{Equation 2.8})$$

From Equation 2.8, it seems that the wall motion coercive force can be ascribed to three roughly independent mechanisms:

- a) The change of the wall energy.
- b) Film thickness variations.
- c) Wall length and width changes [Middelhoek, 1961].

- The change of the wall energy

The first term in Equation 2.8 represents the coercivity associated with the change of the wall energy. As stated above, the structure of domain walls depends on the relative importance of exchange, anisotropy and magnetostatic (stray field) energy, so this can be written as,

$$\frac{d\gamma}{dx} = \frac{d\gamma_{\text{exchange}}}{dx} + \frac{d\gamma_{\text{anisotropy}}}{dx} + \frac{d\gamma_{\text{strayfield}}}{dx} \quad (\text{Equation 2.9})$$

The change of the wall energy is quite complex and relates to many factors and conditions, so it is quite hard to estimate and quantitatively calculate  $H_c$  by using

Equation 2.9. More detail analysis for certain cases can be found in reference [Middelhoek,1961].

- Film thickness variations

The part of the coercive force term which depends on the thickness of the film has the form [Middelhoek,1961]:

$$H_c(t) = \frac{1}{2M_s} \left[ \frac{\delta\gamma}{\delta t} \frac{dt}{dx} + \frac{\gamma}{t} \frac{dt}{dx} \right] = \frac{1}{2M_s} \left[ \frac{\delta\gamma}{\delta t} + \frac{\gamma}{t} \right] \frac{dt}{dx} \quad (\text{Equation 2.10})$$

For film thicknesses greater than 100 nm, Bloch wall formation is favoured. The total wall energy density for a Bloch wall [Middelhoek,1961] can be expressed by

$$\gamma_{Bloch} = A \left( \frac{\pi}{w} \right)^2 w + \frac{1}{2} w K + \frac{\pi w^2 M_s^2}{w + t} \quad (\text{Equation 2.11})$$

where  $A$  is the exchange stiffness,  $w$  the wall width,  $K$  the anisotropy constant,  $M_s$  film saturation magnetisation, and  $t$  is the film thickness.

For thick films,  $w \ll t$  and Equation 2.11 becomes:

$$\gamma_{Bloch} = \frac{\pi^2 A}{w} + \frac{\pi w^2}{t} M_s^2 \quad (\text{Equation 2.12})$$

Minimisation with respect to  $w$ , we have

$$w = \sqrt[3]{\frac{\pi A t}{2 M_s^2}}, \quad \gamma_{Bloch} = 12.7 \sqrt[3]{\frac{A^2 M_s^2}{t}}$$

and

$$\frac{\delta\gamma_{Bloch}}{\delta t} = -4.2 \sqrt[3]{\frac{A^2 M_s^2}{t^4}}$$

When we substitute this in the expression for  $H_c$ , we obtain:

$$H_c(t) = 4.2 \sqrt[3]{\frac{A^2}{M_s}} \frac{1}{t^{4/3}} \frac{dt}{dx} = \frac{c}{t^{4/3}} \quad (\text{Equation 2.13})$$

This is the well-known 4/3 law of Néel. This law is based on the assumption (a) the coercive force due to thickness variations dominates other effects and (b) that  $dt/dx$  is independent of the thickness itself. This calculation is valid only for thick films (e.g. 85 nm) where  $w \ll t$  and Bloch walls occur [Middelhoek, 1961].

For the Néel wall,

$$\gamma_N = A \left( \frac{\pi}{w} \right)^2 w + \frac{1}{2} w K + \frac{\pi w t}{(w + t)} M_s^2 \quad (\text{Equation 2.14})$$

and when  $t \ll w$ , the total wall energy only consists of the stray field energy and Middelhoek was suggested that the energy of the wall may depend only on the film thickness  $t$ .

$$\gamma_N \approx \frac{\pi \cdot w \cdot t}{(w + t)} M_s^2 = \frac{\pi \cdot t}{1 + \frac{t}{w}} M_s^2 = \pi \cdot t \cdot M_s^2$$

and

$$\frac{\delta \gamma}{\delta t} = \pi \cdot M_s^2$$

$$H_c(t)_{N\acute{e}el} = \frac{1}{2 M_s^2} \left[ \pi M_s^2 + \pi M_s^2 \right] \frac{dt}{dx} = \pi M_s \frac{dt}{dx} \quad (\text{Equation 2.15})$$

When, it was again assumed, that  $dt/dx$  is constant (no surface roughness), they found that the coercive force does not depend on the overall thickness ( $t$ ) of film at all [Middelhoek, 1961].

- Wall length, width and film crystallite size

As can be seen from Figure 2.10, there should only be Néel walls in the very thin  $\text{Ni}_{81}\text{Fe}_{19}$  films such as below 20 nm due to the fact that a Néel wall has much lower energy at lower film thickness.

Figure 2.15 is taken from reference [Middelhoek,1961] and shows the wall width of Bloch wall and Néel wall as a function of the permalloy film thickness.

In very thin films, it is usually assumed that the crystallite size of films is of the order of magnitude of the film thickness ( $\sim 20$  nm), whereas the width of Néel walls is of the order of 600 nm (see Figure 2.15), according to Middelhoek,

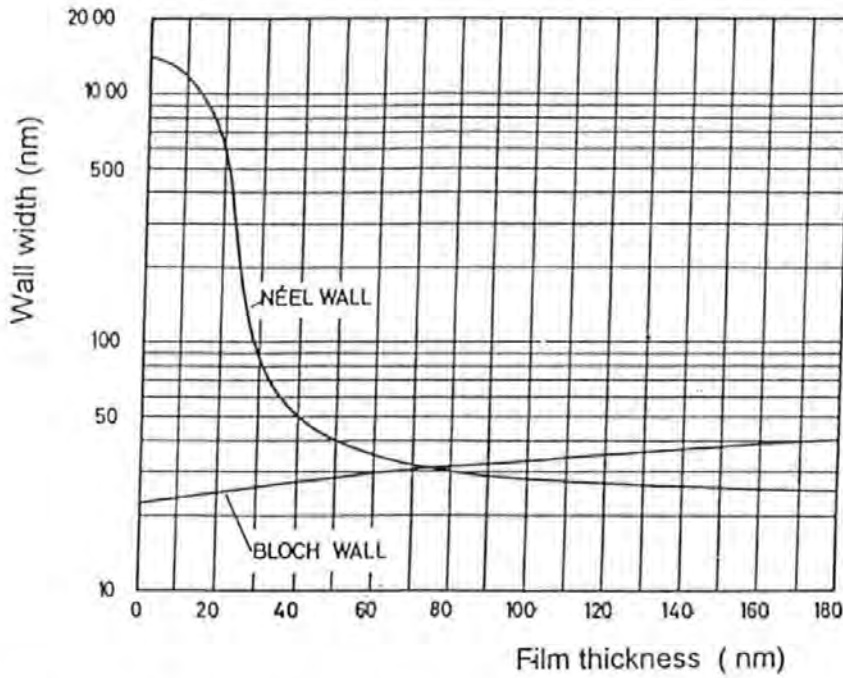


Figure 2.15 Wall width as a function of permalloy film thickness  
(after [[Middelhoek,1961]])

$$H_c = \frac{1}{2M_s} \frac{d\gamma}{dx} = \frac{1}{2M_s} \frac{dE}{dx} w \quad (\text{Equation 2.16})$$

where,  $\gamma$  is the surface energy,  $E$  is the energy density of the wall and  $w$  the wall width.

When the crystallite (grain) size is  $D$  ( $D > w$ ) the energy of wall change by  $\frac{\Delta E dx}{D}$  when

the wall is shifted over a distance  $dx$ , and thus

$$H_c = \frac{\Delta E}{2M_s} \cdot \frac{w}{D} \quad (\text{Equation 2.17})$$

When  $D < w$ , however, and the wall is shifted over  $dx$  and the relative energy increase is much smaller than the  $D > w$  case, as the energy increase must be averaged over many grains. When  $N$  is the number of the grains, the average energy increase is expressed by

$$\Delta E_{av} = \frac{\Delta E}{\sqrt{N}}$$

When we assume that the energy must be averaged over a wall length  $l$  which is given by  $l = qw$ , thus,

$$N = q \cdot \frac{w^2}{D^2} \quad \text{and} \quad H_c = q^{-\frac{1}{2}} \frac{\Delta E}{2M_s} \cdot \frac{D}{w} \quad (\text{Equation 2.18})$$

Equation 2.17 and 2.18 show that the coercivity is proportional to  $w/D$  when grain size is greater than the width of wall, but will become opposite when  $D \ll w$ . It is also plausible that the coercivity will have a maximum when  $w$  and  $D$  are of the same order of magnitude, which will be discussed later with experimental results in Chapter Four.

#### 2.3.4 The ripple theory

It is well known that all the magnetic properties of thin ferromagnetic films depend on the film structure. In the case of polycrystalline permalloy films the influence of film structure on magnetic properties was first explained by the micro-magnetism 'ripple' theory of differential susceptibility for two dimensional samples [Hoffmann, 1969].

In this theory the differential susceptibility was related to the structure of the film, determined by the thickness,  $t$ , the mean diameter of the crystallites,  $D$ , and the local

## Chapter 2: Theory

anisotropy constant,  $K_s$ , which is related to intrinsic stresses (e.g. due to substrate temperature), film composition, etc.

The ripple theory introduces a new material parameter, the structure constant  $S$  which gives a quantitative description of the film structure. For polycrystalline uniaxial permalloy films with low magnetostriction, this structure constant  $S$  has been calculated by [Hoffmann, 1964 and 1979] and was given by

$$S = \frac{K_s D \sigma_l}{\sqrt{n}} \quad (\text{Equation 2.19})$$

When uniaxial strains are neglected, which is true for most cases of sputtered permalloy films, Equation 2.19 becomes

$$S = \frac{D}{\sqrt{n}} \sqrt{\frac{8}{105} \left[ K_l + \frac{3}{8} (\lambda_{100} - \lambda_{111}) \sigma_m \right]^2 + \frac{7}{16} \left[ \frac{3}{2} (\lambda_{100} - \lambda_{111}) \sigma_m \right]^2} \quad (\text{Equation 2.20})$$

where,  $D$  is mean diameter of the crystallites, calculated from  $(\langle D^3 \rangle)^{1/3}$ ,  $K_s$  local anisotropy constant,  $n$  is the number of crystallites with different orientation through the film thickness and  $\sigma_l$  is the standard deviation of the angular function.  $\sigma_m$  is the intrinsic isotropy strain.  $K_l$  is the magnetocrystalline anisotropy constant,  $\lambda_{100}$  and  $\lambda_{111}$  are the magnetostriction anisotropy constants for single crystals [Kempter and Hoffmann, 1969, 1970] and [Hoffmann, 1964, 1979].

The successful extension of this theory has led to a quantitative understanding of various properties of permalloy thin films and future details can be found in reference [Hoffmann, 1979]. This will be further discussed with experimental results in Chapter Four.



## 2.4 Anisotropic magnetoresistance

### 2.4.1 Anisotropic Magneto-resistance Effects

Ferromagnetic materials may show an anisotropic magnetoresistance effect, which means that the electrical resistivity in such materials, e.g. nickel, iron and in particular, nickel-iron alloy, or ‘permalloy’ thin films, depends on the direction of their magnetisation vector and can be changed by an external magnetic field. This phenomenon is referred to as the anisotropic magnetoresistance effect, and was first observed in 1856 and later defined in 1857 by William Thomson [Bralisford, 1966]

If a ferromagnetic material is prepared in the form of a thin film, a layer in the thickness range 0 ~ 1000 nm, the anisotropic magnetoresistance effect may be restricted to lie in the plane of the film to a very good approximation due to the demagnetising effect. In this case, the effect is called the in-plane anisotropic magnetoresistance effect or simply, magnetoresistance effect.

### 2.4.2 Basic theory

There are three principle energy components in the magnetoresistive thin film as follows:

- *The potential energy  $E_p$*  created when the applied field exerts a twisting couple ( or magnetic moment) on the film magnetisation.

$$E_p = -M_s H_R \cos(\alpha - \theta) \quad (\text{Equation 2.21})$$

where

$M_s$  is the saturation magnetisation of the ideal (single domain) state of magnetisation;



$H_R$  is the applied field in which the magnetic thin film is placed and has a direction at an angle  $\alpha$  to the long axis of the film (the so-called easy axis).  $\theta$  is the angle between the magnetisation and the easy axis

- *The additional anisotropy energy* which arises when the magnetic vector lies in a direction other than the lowest free magnetisation direction.

$$E_A = +\frac{1}{2} M_s H_K \sin^2(\gamma - \theta) \quad (\text{Equation 2.22})$$

where,  $H_K$  is the thin film anisotropy field which where the lowest energy magnetisation direction of the material of the film, is at an angle  $\gamma$  to the long axis.

- *The demagnetising energy  $E_D$*  where atomic spins in the material lattice interact with each other negatively to reduce the effect of applied field in aligning them. This is sometimes described as being like the effect of free magnetic poles at the extremities of the film which produce an internal reverse field. Such a field is not due to ‘free poles’ which do not exist in fact, but such a concept is useful for mathematical analysis.

$$E_D \equiv +\frac{1}{2} M_s^2 N_D \sin^2 \theta \quad (\text{Equation 2.23})$$

where  $N_D$  is the demagnetising factor relating to the field opposite to the direction of  $M_s$ . ( $\sim t/h$  where  $t$  is the film thickness and  $h$  is the width of the film)

If three energy components are added together and then differentiated for a minimum of energy with respect to  $\theta$ , a condition can be found wherein the energy is a minimum, i.e.

$$H_R \sin(\alpha - \theta) - \frac{1}{2} H_K \sin 2(\gamma - \theta) - \frac{1}{2} N_D M_s \sin 2\theta = 0 \quad (\text{Equation 2.24})$$

Equation 2.24 determines the relationship between the applied field  $H_R$  in which the sensor finds itself, and the angle  $\theta$  between the magnetisation and the easy axis (the original lowest energy magnetisation direction in the film).

It should be noted that this energy analysis is based on a single domain model, in which the magnetisation in a single domain film is caused by its domain magnetisation rotation. The integrals and this analysis assume this domain magnetisation rotates coherently with there only ever being a single angle  $\theta$  between the magnetisation vector and the current direction. Achieving a single domain state, however may be sometimes difficult in practice and has resulted in numerous ideas and configurations in practical designs [Mapps, 1994].

The basic equation for magnetoresistance in thin films was stated by P. R. Hunt in 1971 [Hunt, 1971] in an application related to the detection of field on magnetic tape. He noted that in magnetoresistive thin film materials such as un-oriented polycrystal films with isotropic resistance, the resistivity has an un-axial anisotropy with a symmetry axis parallel to the direction of magnetisation (see Figure 1.6 taken from ref. [Mapps, 1994]), which obeyed a  $(\cosine)^2$  law, thus

$$\rho = \rho_0 + \Delta\rho \cos^2 \theta \quad (\text{Equation 2.25})$$

where,

$\rho_0$  is the isotropic portion of the resistivity;

$\Delta\rho$  is the maximum value of the magnetic field related resistivity change (saturation magnetoresistance);

$\theta$  is the angle between the magnetisation  $M_s$  and the electric current  $I$ .

For materials such as permalloy, their  $\Delta\rho$  and  $H_k$  are known. The induced anisotropy field (typically 6 Oe or about 480 A/m) can be fixed during film production so that its direction is clearly defined.

Referring to Figure 1.6, if an external magnetic field is applied in the film plane and perpendicular to the easy axis, the lowest energy magnetisation direction of the thin magnetoresistive film, will be when the magnetisation vector  $M_s$  in the thin film has rotated by an angle  $\theta$  towards the applied field in order to remain in the lowest energy magnetic state. The electrical resistance of the magnetoresistance film can be changed and modulated by the external magnetic field. See Equation 2.25.

If other constants are known, a relationship between the fractional magnetoresistance and the magnitude and direction of applied field can be developed by eliminating  $\theta$ . This is the basis of the theory of the thin film magnetoresistive sensor.

The magnetoresistance effect in thin magnetoresistive films has been well investigated for many years. Intensive studies have been made on magnetoresistive thin films for their application in sensors and recording heads [Lenz,1990]. The theory of the magnetoresistance effect may be slightly different in each application.

#### 2.4.3 Transverse field detection

In magnetic recording applications, a small current is passed through the thin film along its length which also happens to be the same as the direction of the magnetisation vector (easy axis) in the film. It means that  $\alpha = \beta = 90^\circ$  and  $\gamma = 0$  in Equation 2.24, which can then be reduced to

$$\sin \theta = \frac{H_R}{H_K + N_D M_s} \quad \text{or}$$

$$\sin \theta = \frac{H_R}{H_0} \quad (H_0 = H_K + N_D M_s) \quad (\text{Equation 2.26})$$

from Equation 2.25,

$$\rho = \rho_0 + \Delta \rho \left[ 1 - \left( \frac{H_R}{H_0} \right)^2 \right] \quad (\text{Equation 2.27})$$

Since  $H_0$  is a constant for a given film with given dimensions, the graph of percentage resistance change versus transverse field is typically as shown in Figure 2.16 [Mapps, 1994].

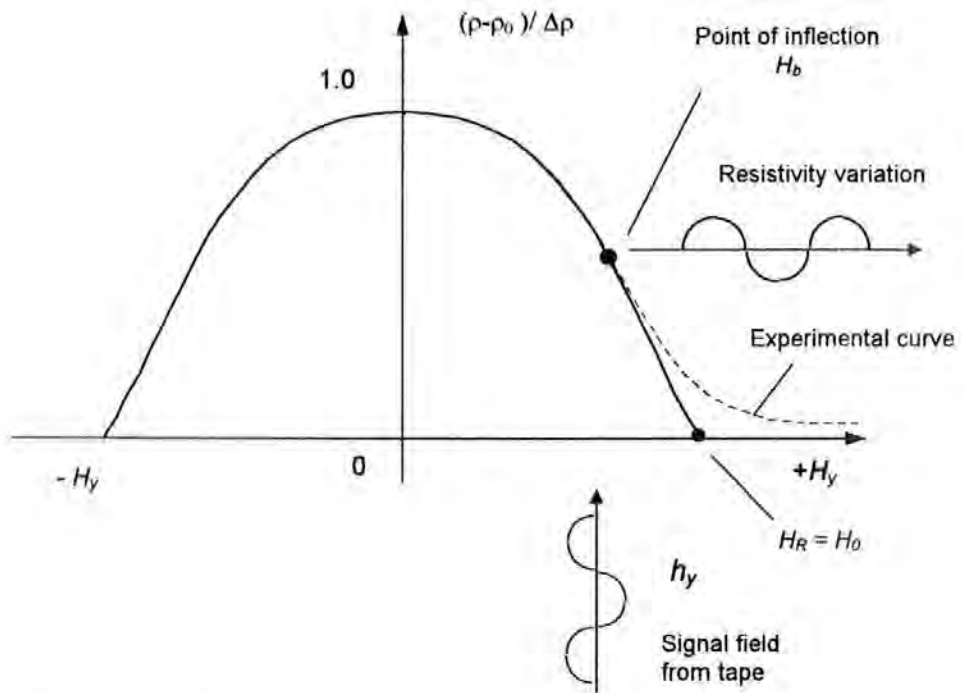


Figure 2.16 The magnetoresistive transfer characteristic used in magnetic recording (after [Mapps, 1994])

In practice, it is usual to apply a steady biasing field to the film in the vertical direction so that the operating point moves to the linear part of the magnetoresistance curve (point of

inflection). A small sinusoidal signal field ( $h_y$ ) will produce a similarly sinusoidal change in resistance of the magnetic medium, giving a sinusoidal voltage variation across the film for a constant-current operating condition. Equation 2.27 then becomes,

$$\rho = \rho_0 + \Delta\rho \left[ 1 - \left( \frac{H_b}{H_0} \right)^2 - \left( \frac{2H_b h_y}{H_0^2} \right) - \left( \frac{h_y}{H_0} \right)^2 \right] \quad (\text{Equation 2.28})$$

Assuming  $H_R = H_b + h_y \ll H_0$  and integrating over the device dimensions to get an output voltage  $V$ ,

$$V = 2IR_0 \cdot \frac{\Delta\rho}{\rho_0} \cdot \frac{H_b}{H_0^2} \iint h_y(y, z) \frac{d_y}{h} \cdot \frac{d_z}{l} \quad \text{volts} \quad (\text{Equation 2.29})$$

where  $h$  and  $l$  are the height and length of the magnetoresistor respectively.  $I$  is the constant current [Mapps, 1994].

#### 2.4.4 General field detection

In the magnetic recording application the *direction* of a transverse magnetic field relative to an M-R film can be assumed constant due to the high demagnetising field perpendicular to the film plane. In the general field detection such as the earth's field, the *magnitude* of detected field stays relatively constant but the *direction* may be changed to any direction.

In practice, the angle between the anisotropy field and the long axis  $y$  can be set at zero during film fabrication. Equation 2.24 then becomes [Mapps et al., 1985]

$$H_R \sin(\alpha - \theta) - H_k \cos\theta \sin\theta - N_D M_S \sin\theta \cos\theta = 0 \quad \text{or}$$

$$\sin(\alpha - \theta) = \frac{H_k + N_D M_S}{H_R} \sin\theta \cdot \cos\theta \quad (\text{Equation 2.30})$$

For thin film sensors, the anisotropy field  $H_K$  is much greater than the demagnetising field  $H_D$ , and the resultant field  $H_R$  acting on the film can be a function of detected fields (such as the earth's field) and the biasing field. As can be seen from Figure 1.6, a relationship can be developed [Mapps et al., 1985] and given by

$$H_R = \sqrt{(H_b + H_e \sin \beta)^2 + (H_e \cos \beta)^2} \quad (\text{Equation 2.31})$$

therefore,

$$\sqrt{(H_b + H_e \sin \beta)^2 + (H_e \cos \beta)^2} \cdot \sin(\alpha - \theta) = H_K \cos \theta \cdot \sin \theta \quad (\text{Equation 2.32})$$

where

$$\alpha = \tan^{-1} \left[ \frac{H_b + H_e \sin \beta}{H_e \cos \beta} \right]$$

## 2.5 Switched-bias MR sensors

A switched-bias sensor as described in ref. [Mapps et al., 1987] consists of a pair of identical MR thin-film sensors which are subjected to transverse fields applied via currents in two overlaid thin-film bias conductors as shown in Figure 2.17. There is an insulating layer between the MR layer and the bias conductor layers, therefore, an insulated shunt-biasing method is also employed here.

Where,  $t_1$  is the thickness of the bias conductive layer,  $t_2$  is the thickness of the insulating layer and  $t_3$  is the thickness of the Permalloy layer.  $L_b$  and  $W_b$  are the length and the width of the bias conductive layer respectively.  $L_s$  and  $W_s$  are the length and the width of the sensor layer respectively.

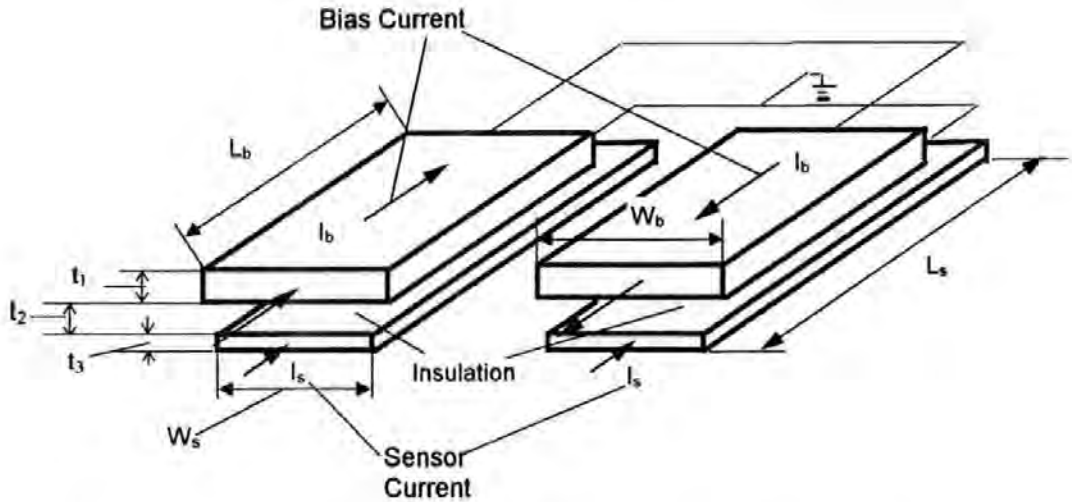


Figure 2.17 Diagram showing a typical switched-bias magnetoresistive sensor

- Switched-bias field

The transverse field from these bias conductors are in opposite directions but are provided from the same current  $I_b$  so that when  $I_b$  is reversed ( $I_b$  is a square-wave alternating current) the transverse bias field also reverses so that the bias point for each sensor switches to the other side of the MR characteristic and vice-versa.

The leading edge of each half-cycle of square-wave ideally has a steep pulse on it so that the sensor can be driven into transverse saturation before sampling data if the biasing field is smaller than the saturation field required. As can be seen in the exaggerated hysteresis diagram (Figure 2.18), with a modified square-wave, the sensors are always being sampled at X and Y making the outputs virtually independent of hysteresis effects.

- Differential output

If the sensor current is applied as part of a bridge circuit the differential output (subtraction of the two sensor output voltages as seen from Figure 2.19,  $\Delta U_{s1} = -\Delta U_{s2}$ ) from the sensors is zero in a zero applied magnetic field. The sensor output is also free



from temperature effects. If the sensor is placed in a steady applied field (e.g. the  $\delta H$  of a 80 nano-Tesla field) the bridge is unbalanced and the output signal is a square wave whose amplitude is proportional to the steady field. Figure 2-19 shows the operating principle of the switched-bias sensor and assumes the hysteresis of sensor can be neglected.

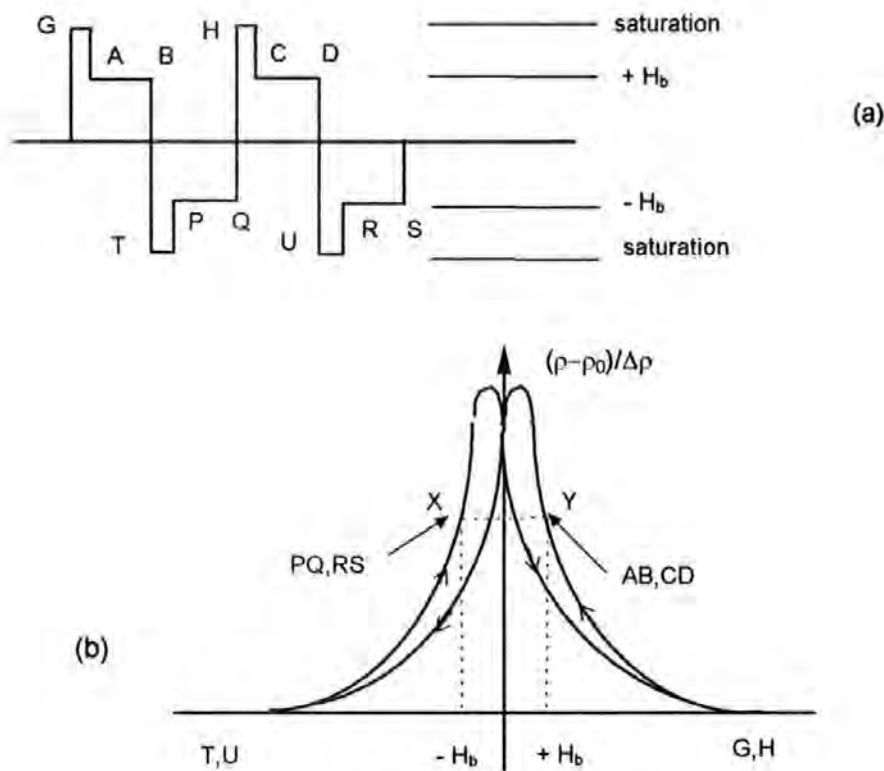


Figure 2.18 (a) Peaked drive current waveform for overcoming hysteresis;  
(b) Exaggerated magnetoresistance loop showing sampling points  
over AB, PQ, CD, RS (after [Mapps et al., 1987]).

- Lock-in amplifier technique

One advantage of this kind of sensors is that lock-in amplifier techniques can be used to extract the output signal almost totally free of noise, so making the sensor very effective for detecting small steady fields in noisy environments [Mapps et al., 1998].

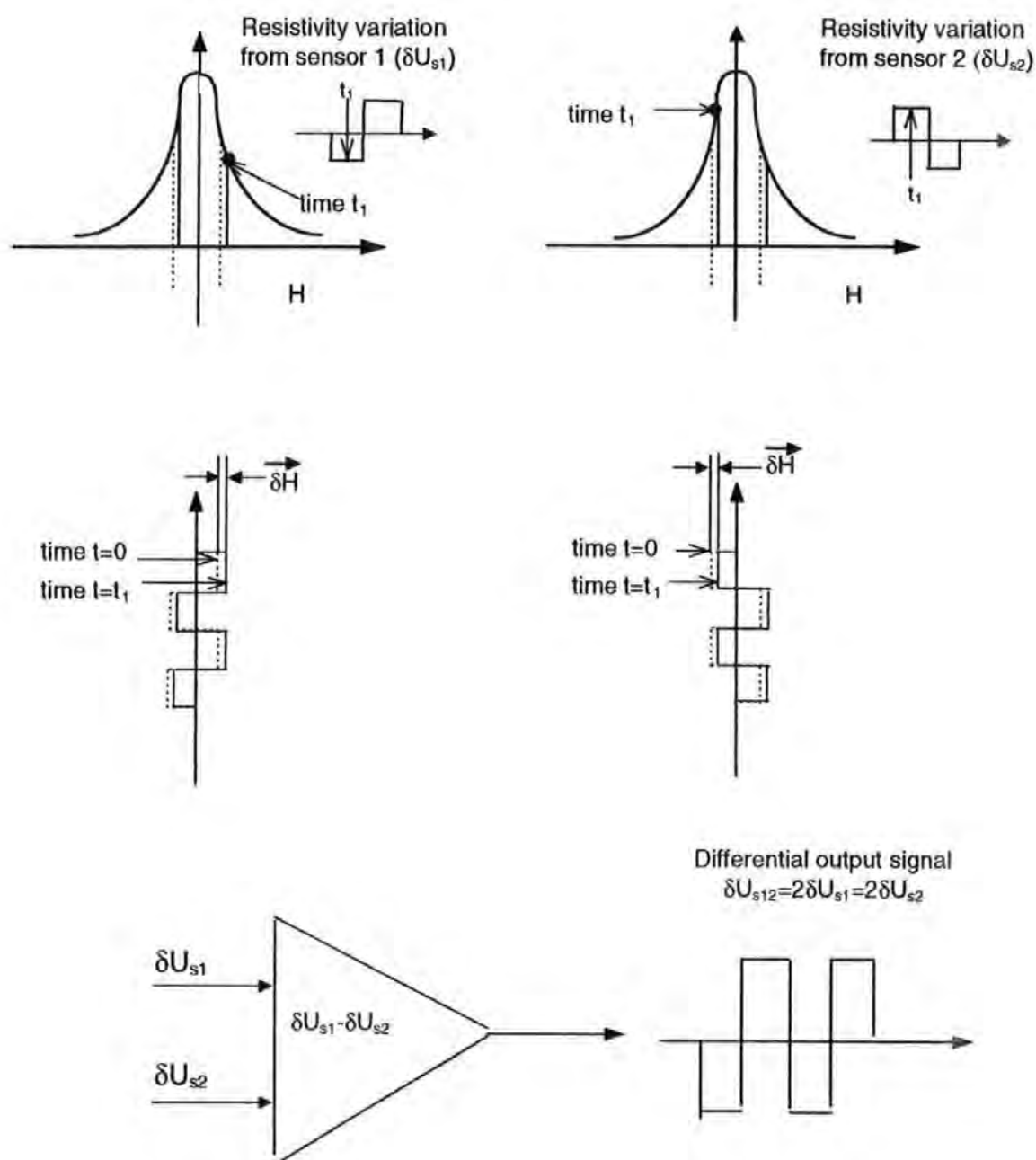


Figure 2.19 Operation principle of the switched-bias sensor

- ..... In a zero applied magnetic field
- In a steady applied field of  $\delta H$

## **CHAPTER 3.0**

### **EXPERIMENTAL DEVELOPMENT**

#### **3.1 Introduction**

This chapter will discuss techniques, procedures and experimental steps required to develop a novel dual stripe, switched bias, permalloy magneto-resistive (MR) sensor for detection of weak magnetic fields.

The Sputter coating technology employed to create thin films at the heart of the sensor will be discussed.

Design of photo-masks used to produce sensors, covering layers and bias conductors will be described along with associated photo-lithographic techniques.

Ion-beam etching techniques to fabricate sensors from thin metal layers are described.

Microstructure investigation of Permalloy films by Transmission Electron Microscopy (TEM) methods and observation of magnetic domains by Lorentz microscopy are discussed.

In conclusion, the main experimental methods and test systems used or developed for this study are discussed. Barkhausen noise investigation in magnetoresistance films and sensors, MR effect and hysteresis measurement are described

A test system developed for measuring output performance of switched bias sensors is also described.

## **3.2 Fabrication Technology of Thin Film MR Sensors.**

### **3.2.1 Thin Film Deposition by r.f. Sputter Coating**

Production of thin metal layers for this investigation required a suitable coating technique. Sputter coating was used as this method produces thin layers with similar characteristics to those of the source materials. Additionally, this technology allows thin layers to be produced from materials which may be difficult to deposit using other methods. Deposited layers are largely free from contaminants, which may be found in films created by techniques such as electro-plating.

There are several variations of sputtering techniques with systems available using d.c., r.f., ion-beam, electron-beam and micro-wave power sources. Developments have occurred within the technology with variations such as magnetically enhanced cathodes, substrate heating and bias sputtering, which improve deposition rate and quality of sputtered films.

A Materials research corporation (MRC) 8632 r.f. system of the “sputter down” type was used for the work. Schematic diagram of the Materials Research Corporation (MRC) system is given in Figure 3.1. This machine features a 1.25 kW power supply operating at 13.56 MHz. There are three 15.2 cm (6”) target stages (cathodes) each with water cooling. Each target can be connected separately to the power source by a selector switch.

There are three substrate holders (anodes) which are water cooled, these can be positioned below each target as required. One of these three anodes features a substrate heating stage which may be used to improve the quality of deposited films. On the second stage a switching network allows either electrode to be independently energised

### *Chapter 3: Experimental development*

for target or substrate etching. Also on this stage a fixed 9:1 power divider network allows material to be deposited using bias sputtering. There is a sputtering electrode without any additional features at the third position. Substrate to target separation can be varied to alter deposition characteristics by raising or lowering the anode.

Finally a rotatable shutter is located centrally between the target and substrate positions to allow each surface to be etch-cleaned before deposition with reduced risk of cross-contamination affecting other electrodes in the chamber.

Sputtering systems are based on vacuum chambers evacuated by suitable pumps. They feature specially constructed electrodes which face each other with a separation gap of about 7 cm which is adjustable. These electrodes are electrically insulated from the chamber and one-another.

Inert gas (usually Argon of 99.95% purity) is used as the process gas and is supplied to the chamber through a needle valve. Oxygen Free Nitrogen (OFN) is used to flood the chamber after 'breaking' the vacuum when loading or un-loading the chamber.

The source material is attached to one electrode and is known as the "target". This electrode is connected to the negative terminal of the r.f. power supply and is therefore known as the "cathode".

Target material is usually specified at the highest purity, it is common to use "five nines" (99.999 %) or "four nines" (99.99 %) purity materials.

With r.f. sputtering systems a matching network and blocking capacitor are connected between the generator and the chamber. The matching network is used to "tune" the chamber impedance to that of the generator output impedance (usually 50 Ohms), ensuring maximum power transfer for sputtering is made to the chamber. The blocking

### *Chapter 3: Experimental development*

capacitor is part of the tuning network and can be connected to improve tuning if the altering the electrode spacing pushes the chamber tuning out of the range of matching network.

The substrate is attached to the other electrode, called the anode. The anode may be allowed to “float” to a high voltage determined by the sputtering power being used. On the other hand, it may be grounded or have a tuning network similar to that used on the cathode.

Sputter coating machines which have the cathode mounted above the anode are known as “sputter down systems”. When the cathode is mounted below the anode they are called “sputter up systems”. There are variations where the electrodes are mounted on the sides of the chamber, these are known as “sideways” sputtering systems.

In use the chambers are pumped to high vacuum, typically  $2 \times 10^{-7}$  Torr. The process gas is fed into the chamber, metered through a needle valve this raises the process pressure to around  $5 \times 10^{-6}$  Torr. Regulation or “throttling” of the high vacuum pump is carried out during sputtering to reduce pumping speed. This stabilises the argon through-put and chamber pressure to create stable conditions required to maintain a plasma.

Energetic electrons collide with argon atoms in the chamber. If the collision energy is high enough a electron is dislodged from the argon atom creating a ion and two electrons. If these two electrons collide with further argon atoms more ion and electron generation takes place and the process multiplies.

As the system r.f. power source is connected to the cathode the target surface achieves positive and negative bias on alternate half cycles. This causes the ions and electrons in

### *Chapter 3: Experimental development*

the plasma, which are readily influenced by electric fields, to be accelerated towards the target surface.

A particle striking the surface of the target can cause the following events to occur:

- It may be reflected and possibly neutralised.
- It may strike causing a electron called a “secondary electron” to be ejected.
- It may implant itself in the target.
- It may cause structural alteration of the target.
- It may cause the ejection of an atom of material.

A minimum of two collisions, called a collision cascade, within the target are required for ejection of material. The phenomenon is relatively inefficient and generally only 1% of incident energy appears at the target surface as sputtered material.

The material arrives at the substrate in atomic or molecular form. The particles may begin to “condense” on the surface or may re-evaporate. After a period of time two particles may combine to form a “doublet”, a form which is more stable and less mobile than single atoms, making it less likely to be re-evaporated. After a further period of time “triplets” and “quadruplets” form then the films reaches the “nucleation” stage where “islands” of material form. These islands may be single crystal structure or polycrystalline, although only a few crystals may be found in the structure. After a time the islands on the substrate surface grow large enough to touch and reach the stage called agglomeration or coalescence. This stage proceeds until continuity is reached when the film is complete. Figure 3.2 shows the formation of a thin film forming as the deposition process proceeds [Chapman,1980].



### *Chapter 3: Experimental development*

Improving the performance of the Permalloy sensor layer is a important task in this project. It is well documented that magnetic properties of permalloy thin films are very sensitive to preparation methods and conditions. Optimisation of sputtering conditions was carried out in this study to reduce Oxygen and other contaminants possibly trapped in the film. Pumping of the vacuum system was continued until to a low base pressure of about  $6 \times 10^{-7}$  Torr was recorded before sputtering. Pumping to this base pressure was considered useful in removing expected contaminants but many workers report higher base pressures (up to  $2 \times 10^{-6}$ ) prove just as effective [Krongelb & Electron, 1973]. Sputtering with a suitable negative substrate bias (e.g. -75 Volts for 200 W and -90 Volts for 300 W) is also effective in removing unwanted components trapped in the film, improving the film quality [Flur, 1967].

The type of substrate and surface temperature are important in determining the nature of the film [Chapman,1980]. The influence of the substrate on thin film structure depends on the condition & nature of the surface, the substrate temperature and the chemical nature of the substrate (i.e. crystallographic structure & impurity content). This will be outlined later in section 3.2.4.

Normally in permalloy films the anisotropy is self-selecting when depositing on glass substrates. For the purpose of this study an in-plane field of about 40 Oe was applied during deposition (via a 'magnetic' substrate holder) to "select" anisotropy direction. The anisotropy direction was marked on each substrate. The main parameters used in the deposition of each layer of the sensor will be given in the section 3. 2.4.

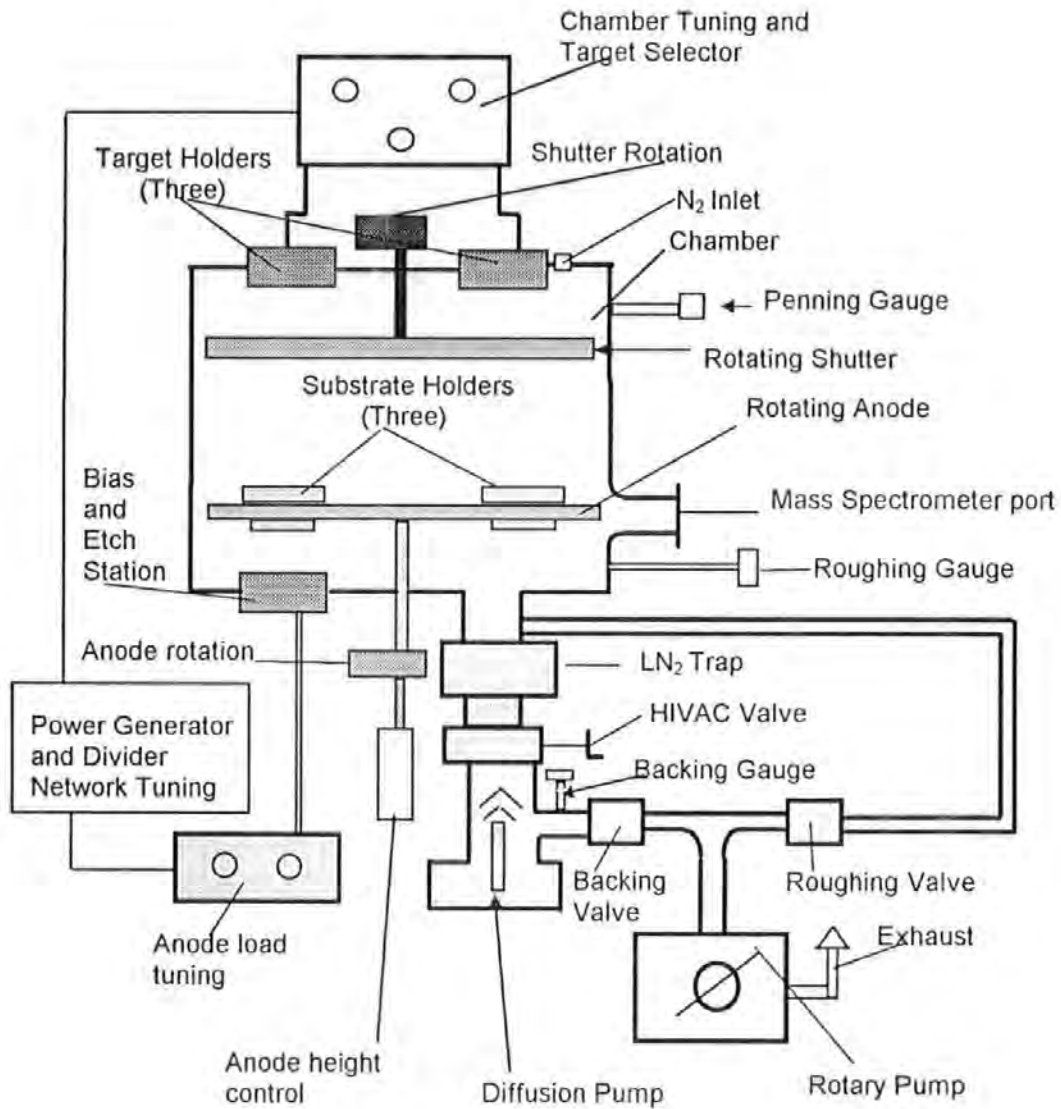


Figure 3-1 Schematic diagram of the Materials Research Corporation (MRC) Sputtering System

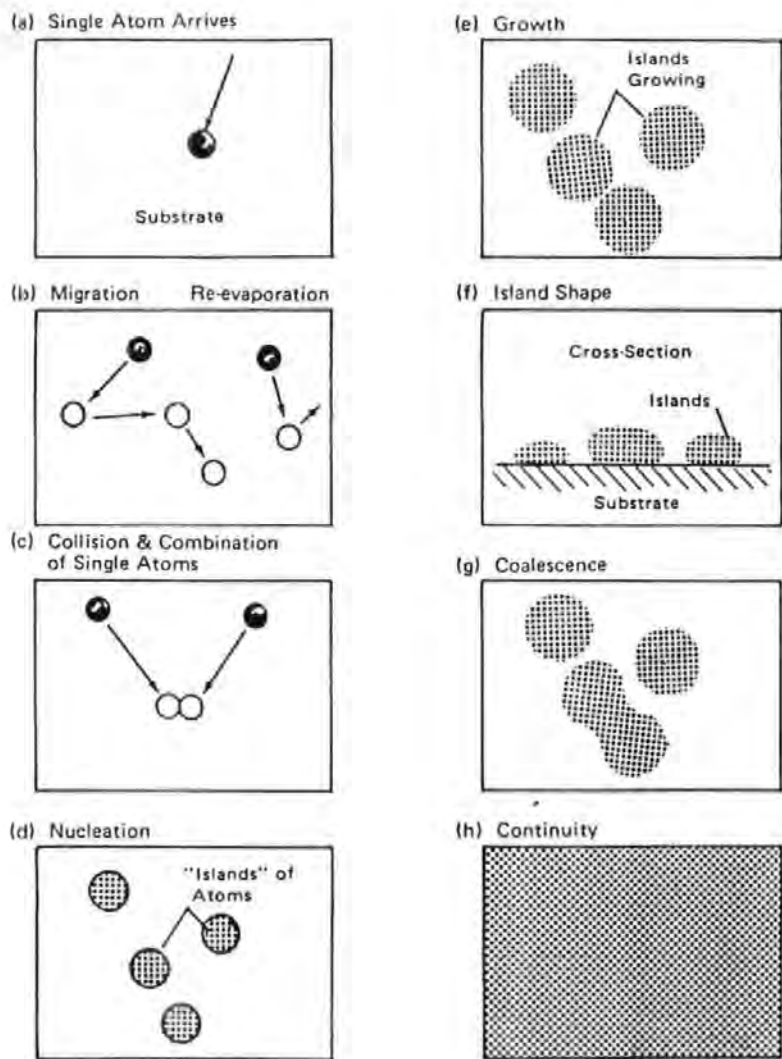


Figure 3.2 Formation of a thin film (after [Chapman, 1980])

### **3.2.2 Photolithography techniques**

Photo-lithographic techniques used to create sensors patterns for this work are similar to those employed in contact printing photographic negatives. Once the substrates have been coated with a particular layer, an ultra-violet light-sensitive chemical called photo-resist is applied to the surface. The substrate is placed in a vacuum chuck in a special high speed spin coater. A controlled amount of photo-resist is applied to the substrate surface using a calibrated hypodermic syringe. The vacuum chuck is rotated at 4000 rpm causing the photo-resist to spin out and distributing on the substrate surface in a thin planar layer. A typical photo-resist material used is the Microposit 1800 series, manufactured by Shipley Europe Limited, type 1813. The last two digits mean that this resist deposited using a coater running at 4000 rpm will produce a layer 1.3  $\mu\text{m}$  thick.

A number of chromium-coated high quality glass plates, (mask set) are designed specifically for the project and contain the pattern of the sensor to be fabricated. Usually there are several masks in the set, especially if multi-layer devices are being constructed.

The patterned side of the mask is brought into contact with the photo-resist layer on the substrate in a mask aligner. These systems feature a powerful u.v (ultra-violet) light source, typically of 200 W. This light is directed onto the mask/substrate assembly through a mirror and collimating lens assembly which creates a parallel beam of even illumination. Clear areas on the mask allow u.v. light to fall on the photo-resist layer altering the chemical structure. The areas of photo-resist effected by u.v. light can be washed off in a dilute solution of sodium hydroxide (developer), leaving the areas of photo-resist covered by the mask as a pattern on the previously deposited film.

### *Chapter 3: Experimental development*

The substrate can then be placed in a chemical etch solution or ion beam etching machine to remove the exposed metal film. Once etching is completed the required sensor pattern covered by photo-resist is left on the substrate. The photo-resist layer can now be removed if necessary. As additional layers are added the mask aligner is used to line up special target marks on the previously etched layers with similar marks on the next mask. This ensures the developing layers in a multi-layer device are held in alignment.

#### **3.2.2.1. Details of MR Sensor Mask Design**

Effective sensor performance depends on quality mask design and careful attention to detail in the many steps to produce the sensor.

Mask manufacture is usually entrusted to a commercial producer to ensure a quality product for the important steps in the lithography process

Eight photo mask designs are required for this project and all are incorporated on two mask plates. A novel quartering method is employed to reduce the number of masks plates and consequently reduce costs. Sensor arrays are constructed on 51 mm (2"square) substrate. Masks are manufactured on 100 mm (~ 4"square) plates. During photolithography the masks are aligned above the substrate. As the device layers build up the substrate is rotated below the mask to each quarter in turn.

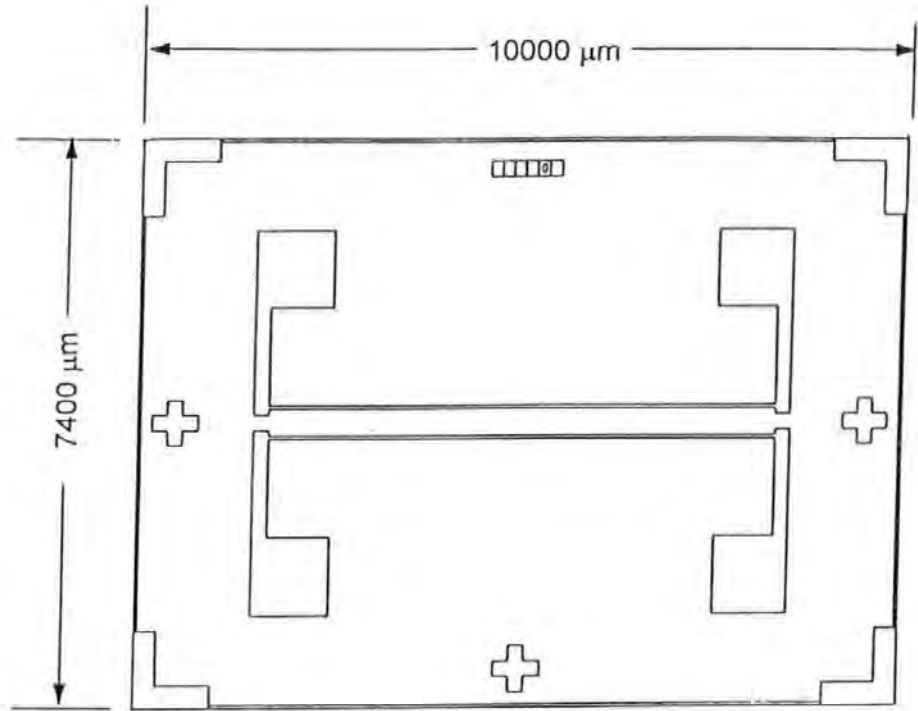
The MR sensor consists of two "active" elements of permalloy, overlaid with a chrome / copper / gold laminate to create conductors for carrying the sensor bias current. Electrical connections are brought out to pads which can have wires conveniently soldered to them for testing. Testing of sensors whilst they are still part of the substrate can be carried out, using a "microprobe" IC wafer test system, applied to these connecting pads as described later in this work.

### *Chapter 3: Experimental development*

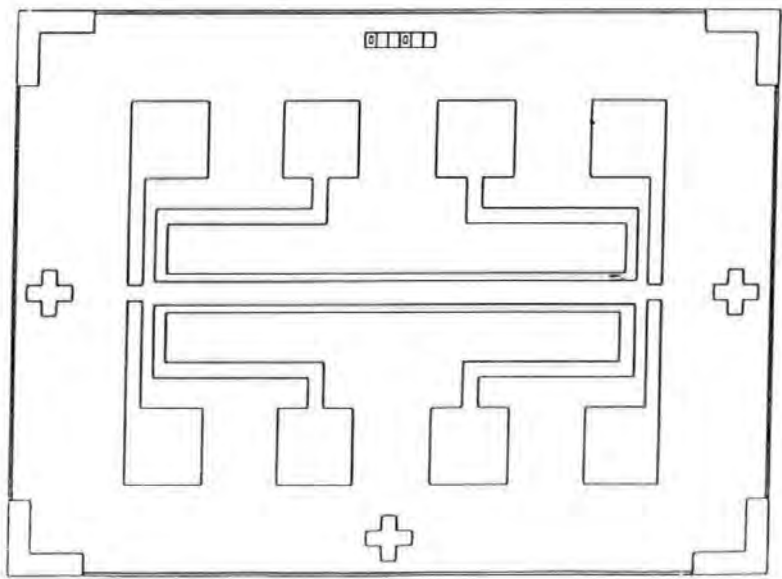
A combination of positive and negative mask design has been employed in this project. This has made it possible to use a range of fabrication techniques including the “lift-off” method for certain details, as described later in this work.

A range of sensor elements with different widths have been included on the mask, these include dimensions of 10, 20, 40, 60 and 80  $\mu\text{m}$ . The bias conductor has a width of 100  $\mu\text{m}$ , allowing it to be used with all widths of sensor as it is approximately 12% larger than the widest sensor after etching. The geometric designs of the sensors are shown in Figure 3.3. The choice of sensor width is restricted by the micro-manufacturing and testing system, such as the limits of the mask-aligner system (smallest feature size is  $\sim 5$   $\mu\text{m}$ ), acceptable resistance of each sensor for the bridge circuit (e.g. about 0.5 k $\Omega$  to 10 k $\Omega$ ) and the geometric dimensions of the microprobe test system. The length of the sensor stripe is 6600  $\mu\text{m}$ . The length of bias stripe is 6000  $\mu\text{m}$ . The four sections or quadrants corresponding to four separate mask designs on each photo plate are the same size, 25 mm (1”) square. The sections are placed symmetrically about the centre of the mask plate. There are 6 pairs of sensors or bias strips in each mask and overall dimensions of individual strip pairs are 10000  $\times$  7400  $\mu\text{m}$ . The off-set between strips is 500  $\mu\text{m}$ . A list of detailed cell-graphs for each mask can be found in Ref. [Ma,1997].

The CAD language used in the mask design was developed by Mentor Graphics Corporation for the manufacture of VLSI (Very Large Scale Integration) circuits. The program allows the designer to define a series of points, lines, and shapes, to create the various feature elements and electrical conductors and connections. A design rule checker and utilities converts the database into a commonly used graphical data format such as GDS II. This information is then sent directly to the mask manufacturer.



(a) Sensor layer



(b) Biasing layer

Figure 3.3 Showing the geometric designs of sensor layer and biasing layer



### 3.2.2.2 Photo-resist

The pattern transfer process is accomplished by spin-coating the substrate with a thin photo-resist layer as previously described. The photo-resist material is sensitive to ultra-violet light and is available in positive and negative types depending on their chemical structure. For positive resists, the area exposed (through the mask) is affected by u.v. radiation and becomes soluble in sodium hydroxide solution during the “developing” stage of the process. The image created in the positive resist is the same as the pattern on the mask. For negative resists, the exposed regions affected by u.v. light make the chemical structure resistant to the developer solution. In this case, the photo-resist protected by the mask is removed during developing.

The Microposit 1800 series photo-resist are high resolution positive photo-resists capable of resolving features at less than 1.0  $\mu\text{m}$ . For S1813 photo-resist, the typically thickness at 4000 rpm is about 1.3  $\mu\text{m}$ .

### 3.2.2.3 Aligner system

The Precima MAS12 contact mask aligner system was used for the photo-lithographic work. This machine features a high pressure mercury arc light source. A concave mirror behind the light source and a condenser lens assembly placed in front of it produce a powerful collimated ultra-violet beam of 0.2~0.3  $\mu\text{m}$  wavelength with an intense, evenly illuminated “footprint”. The system is capable of reproducing minimum line / gap widths of 5  $\mu\text{m}$  with suitable masks.

A stable substrate mounting system with vacuum clamping for the mask / substrate pair prevents errors caused by vibration during exposure. This mounting system is able to

### *Chapter 3: Experimental development*

accommodate 51 mm (2") substrates. Three micrometer controlled movements (X, Y and rotation) allow the user to align the features on a mask with those previously etched on a substrate. The mask holder is designed for 102 mm (4") square, high quality photo mask plates. The ultra-violet source has a shutter with adjustable timer to control light exposure.

#### 3.2.2.4 Etching process

After resist exposure and development, device patterning is completed by an etching process to remove unwanted metal layers. Both chemical etching (or wet etching) and ion beam etching (or dry etching) have been considered.

Chemical etching has been widely used for thin film devices. It is economical and straightforward to use on the majority of materials (with some disadvantages). Etch geometry is important when creating the sensor layers. The etchant recipe must be the same for each etching task on a particular material so that characteristics are repeatable. Etching takes place vertically and horizontally in a layer. The rate at which the etching takes place in each direction is called the "aspect ratio". Horizontal etching can lead to degradation of the edges beneath the photo-resist possibly leading to a reduction in sensor performance. Variation of time and temperature can affect the etch so care must be taken to repeat the same conditions each time a particular material is etched.

Tantalum layers are used in the sensor as an underlayer and capping layer. This material is difficult to etch using chemical methods. To overcome these problems, ion beam etching has been employed.

Ion-beam etching provides excellent etch resolution and is accurate and repeatable. This etching method is not selective since any material presented to the beam will be etched.

### *Chapter 3: Experimental development*

Careful monitoring of the process must be carried out and etching stopped when the necessary material has been removed . If this is not done important components of the device may be damaged or removed from the substrate.

Ion beam etching is based on momentum exchange. Neutral atoms or molecules of the process gas (argon) are fed into the discharge chamber inside the ion beam gun. Energetic electrons from the gun cathode collide with these atoms or molecules producing ions. Ions pass through a screen grid forming 'beamlets' and are attracted to the negative potential of the accelerator grid. Most ions pass through this grid without striking it because the holes in the screen and accelerator grid are aligned. A Ion beam is formed from the combination of individual 'beamlets' after they leave the accelerator grid. The beam is neutralised by electrons from the neutraliser cathode which creates a beam with equal quantities of ions and electrons. The energetic electrons, ions and other low energy electrons in the discharged chamber form a electrically conductive gas or plasma.

The plasma potential is very stable varying only from 1 to 5 Volts. The anode is operated at a potential  $V_b$  close to the origin potential of the ions. The target potential is close to the vacuum chamber ground so the ion energy at the target corresponds to the beam supply potential  $V_b$ .

Most of the energy in a ion beam is transferred to the material removed from the surface of the substrate by this ion bombardment. A momentum exchange takes place within the surface material to be removed similar to that of sputtering.

In order to create geometric shapes of sensors on the substrate, the required areas of material must be protected by an etch resistant material (photo resist) patterned using

### *Chapter 3: Experimental development*

photolithographic techniques. Usually this photo resist layer should be three times thicker than the layer to be etched so that etch patterning of the sensors is completed before the etch resisting material is removed.

A schematic drawing of the ion-beam etching system used in this work is shown in Figure 3-4. This system consists of a stainless steel chamber with a 3 cm diameter ion source ( the maximum output current is about 100 mA and the total voltage which includes the beam and accelerator voltage should be limited to a maximum of 1200 V). The substrate mounting system features high rate water cooling, variable speed rotation and adjustable beam incidence. The machine has an IBS-250 power supply with automatic or manual control and digital readout of the power supply parameters. It provides up to 1500 eV ions in a 250 mA beam. The power supply has microprocessor control linking the various sections providing an easy-to-use driver for the ion source. The uniformity of etch with this system is  $\pm 5\%$  across the 76 mm (3") diameter and 51 (2") mm square substrate.

With dry etching, the roughness of the substrate becomes very important. It may only take a few seconds to etch off a layer, where the film thickness is only a few nanometers. Figure 3-5 (a) and (b) shows broken lines in a joint feature which is believed to be caused by over etching in a mis-matched area of a sensor. An overlap joint structure in the mask design would eliminate this fault. Use of an ideal substrate (e.g. 7059 Corning glass) helps to avoid damage to the features previously patterned. The main parameters will be given in section 3.2.4

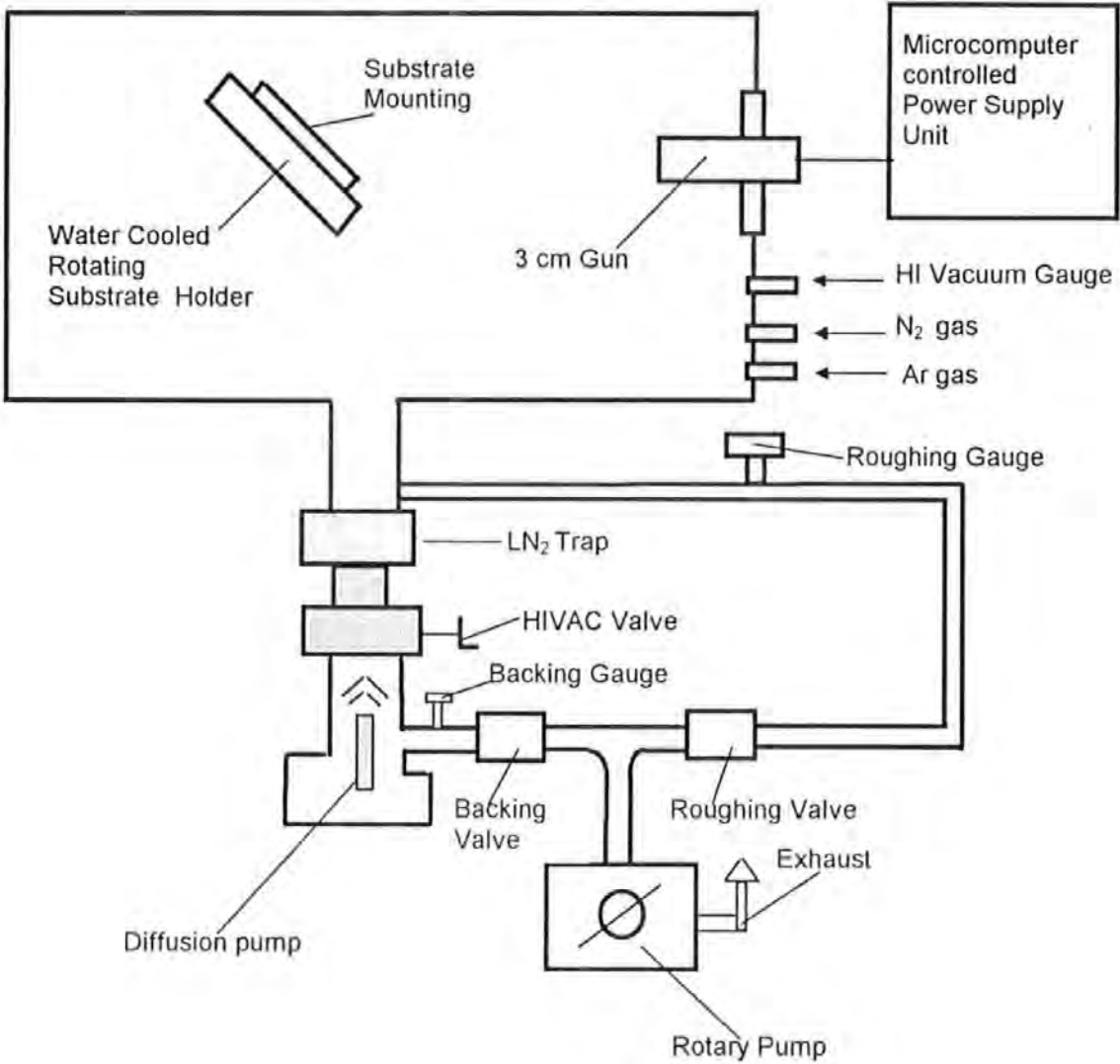
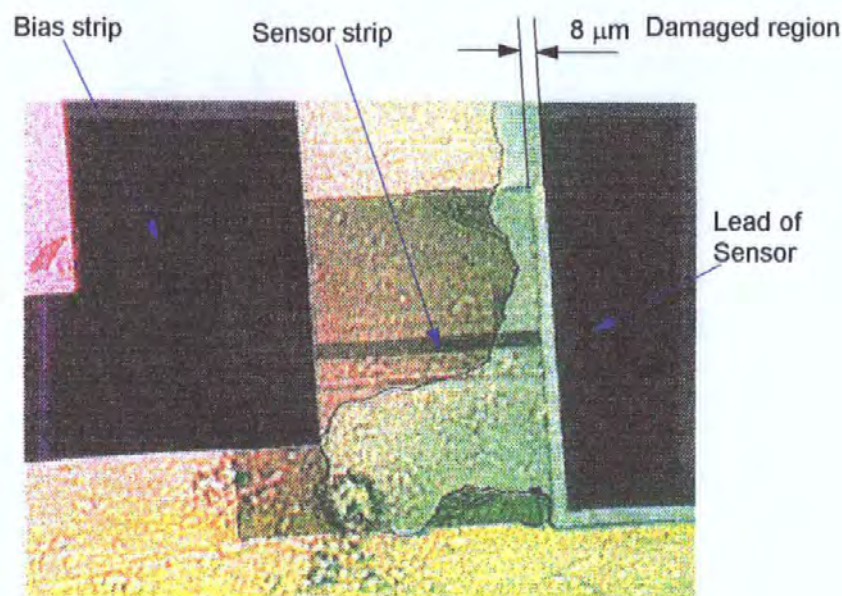
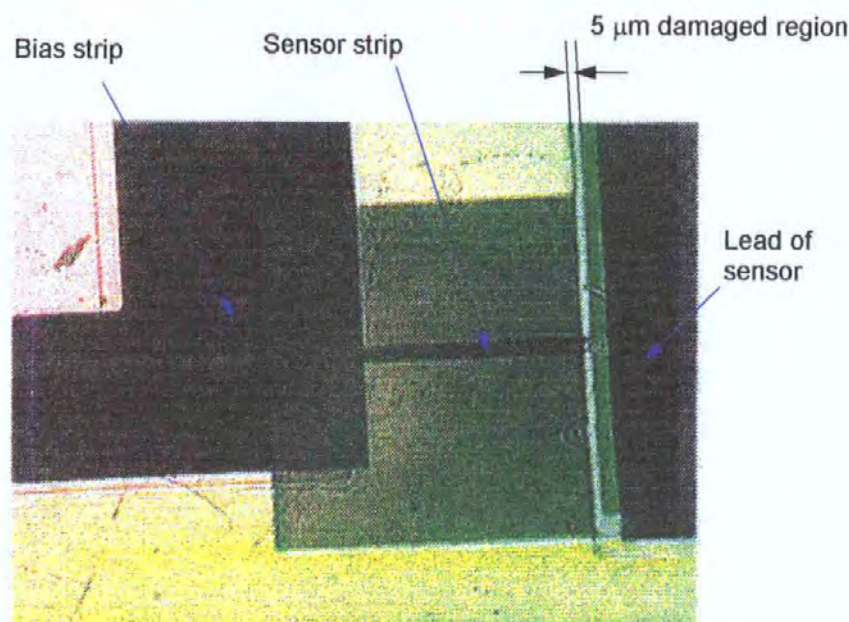


Figure 3-4 Schematic diagram of the Commonwealth Scientific Ion Beam Etching System.





(a) broken sensor end



(b) half broken sensor end

Figure 3.5 Some photographs of sensor showing the damaged features caused by over etching.

### 3.2.3 Other Methods Relating Thin Film MR Sensor Fabrication

#### (a) Film Thickness Measurement by Taly-step Instrument

The control of film thickness is an important feature of micro-sensor fabrication, in particular when sensor thickness is a few nano-metres. A precision (Taly-step 1) stylus measuring instrument with an accuracy of  $\pm 4\%$  was used to measure the film thickness (full-scale reading is 50 nm, each division is 2 nm). Each value of thickness for the various films used to make up the sensors, conductors and insulating layers was averaged for five measurements.

#### (b) Lift-off technique

The lift-off technique is another related patterning process used. A positive resist and its matched negative mask is used to form the end of MR sensor pattern. This layer (about 5 nm Cr & 30 nm Au) is deposited over the resist and substrate, this layer thickness is much less than that of resist. The portion of metal film sputtered onto resist is removed by selectively dissolving the resist layer in an appropriate liquid etchant (e.g. Acetone) so that the overlying film is lifted off and removed. Many thin film fabrication processes can be simplified by using the lift-off technique.

### 3.2.4 Micro-Fabrication of Thin Film MR sensor

A major advantage of thin film MR sensors is that they can be constructed from different functional thin film layers on the same substrate using deposition, coating and photolithography techniques, which are commonly used and well developed in the semiconductor and micro-devices industry.



### *Chapter 3: Experimental development*

The fabrication procedure for the new MR sensor, basically consists of over 50 steps. The main stages and the main difficulties in MR sensor fabrication will be described. The dimensions and geometric design of the MR sensor and its layer structure are shown in Figure 2-17 and Figure 3.3.

The fabrication procedure of the MR sensor can be divided into four main stages.

#### **(1) Deposition and Patterning of under layer, MR layer and Capping layer**

- The preparation of the substrate surface for thin film deposition is of key importance in obtaining good adhesion. Therefore, in each case the substrates were prepared by ultrasonically cleaning in a 2% solution of Neutracon, a laboratory cleaning fluid, for at least 15 minutes at 65°C, rinsing in deionised water, degreasing in an acetone bath, re-rinsing in deionised water and force drying in an oxygen free nitrogen jet.
- The substrates were then dehydrated by being baked in an air convection oven at about 200° for at least 15 minutes to remove residual water contamination of the substrate surface.
- To align the easy axis of the material of the magnetoresistive stripes in a predetermined direction, three magnetic substrate holders were used and provided a constant direction magnetic field of about 40 Oe across the substrate during sputtering. The direction of the anisotropy was marked on each substrate.
- Three thin film layers, underlayer (5 nm Ta), permalloy ( $\text{Ni}_{81}\text{Fe}_{19}$  from 5 nm to 40 nm), and capping (5 nm Ta) layer are sputter-deposited first.
- Ion beam etching of these three layers is carried out after a photo-resist layer is applied, pre-baked, exposed to u. v. light through No 1<sup>#</sup> or No 7<sup>#</sup> chrome photo-mask, and developed to provide the sensor shape required.

### *Chapter 3: Experimental development*

- Finally, the substrate with MR pattern is cleaned after removal of the photo-resist using acetone.

(2) Removal of the MR layer from the bonding leads region of the MR sensor and first deposition of the bonding lead.

It is necessary to remove the permalloy film from the joint area between the end of MR sensor and the conductor bonding leads and deposit the first conducting layer (relatively thin, about 50 nm) in this joint area. This can be carried out by the following steps:-

- The No 2<sup>nd</sup> mask is designed to apply to a photo-resist layer on top of the sensor layer and to open the windows in the joint area which is to be etched.
- The Ta capping layer and permalloy layer are removed from this window area by ion beam etch. The photo-resist applied to substrate for this step must be removed by acetone and the substrate cleaned again. It was convenient for the process to employ this layer even at 5 nm thickness. If the MR sensor is constructed without a Ta underlayer, a difficulty of mask alignment occurs in the next assembly stage because no visible layer is left in the window area.
- A lift-off method and No 3<sup>rd</sup> mask is then used to form the first electrical connection layer after applying further photo-resist and patterning layers of 5 nm Chromium and about 30 nm Au then were deposited over the photo-resist. The use of a chrome under-layer beneath the gold on the electrical connector for the sensors improves the adhesion of these features to the substrate. This Cr layer can also be used as an interface layer to improve the adhesion between the insulating layer and copper bias layer in the next stage.

### *Chapter 3: Experimental development*

- The Cr/Au layer is then patterned by using a lift-off method as previously described in section 3.2.3.

#### (3) Deposition and Patterning of the insulating layer

For switched-bias type thin film MR sensors, the performance of the insulating layer is very important and is a key problem in the fabrication. To achieve enough bias field from the bias current, it is necessary to have a small thickness of the insulating layer.

Three kinds of insulating material, SiO<sub>2</sub>, Photo-resist S1813 and EPON SU8 photo-resist (both supplied by Shipley Europe Limited), were tested for the insulating layer.

- SiO<sub>2</sub> is quite a good candidate for the insulating layer and has been widely used in the semiconductor industry but it is difficult to deposit and etch. Problems occur such as pinholes, cracks and broken joint lines due to over heating during sputtering which may be very difficult to improve by using the present sputtering equipment. It can be improved a little by sputtering the SiO<sub>2</sub> film for a longer time and at lower power such as 100 ~ 200 watts, or sputtering with interruption. Even so it was not good enough to achieve success both for pinholes or broken joint lines.
- EPON SU8 photo-resist supplied by Shipley Europe Limited was another candidate, as it can be hard baked at lower temperature (e.g. a few hours at about 105°C using a hot plate) and good dielectric property (the dielectric constant for EPON SU-8 is about 3). The basic component of this photo-resist is a solid epoxy and a range of thickness can be obtained in one spin by varying the speed of the spinner and changing the viscosity of the resist by altering the quantity of solvent contained in it [Lorenz et al., 1996]. It is convenient to use as it is easy to coat and pattern without fear of damage to the features of MR sensors' previous pattern. The main problem is that

*Chapter 3: Experimental development*

EPON SU8 photo-resist was designed for thick films (typically in the range from 5  $\mu\text{m}$  to 200  $\mu\text{m}$ ) applications. The commercially stated minimum thickness of EPON SU 8-5 is about 5  $\mu\text{m}$  at 2500 rpm. The experiment for reducing the thickness of EPON SU 8-5 was carried out with results as shown in Figure 3-6.

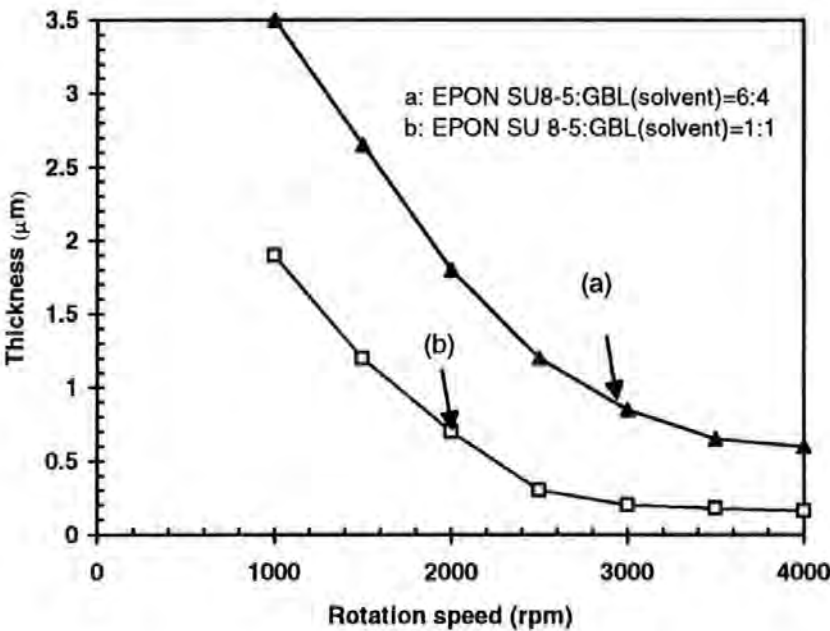


Figure 3.6 A graph showing the coating thickness for EPON SU 8-5 photo-resist versus the speed of the spinner

- A thickness of less than 1  $\mu\text{m}$  can be obtained at about 3 000 rpm and with a volume ratio of EPON SU 8-5 : GBL (Gamma-butyrolacton) solvent of about 6:4. It was found that when the thickness of EPON SU 8-5 was less than 1  $\mu\text{m}$ , there were many pinholes in the film after being hard baked on a hot plate, possibly caused by the high solvent content. Further experimental results also show there are other problems in later fabrication steps of the sensors if the EPON SU 8-5 photo-resist has been used

### *Chapter 3: Experimental development*

as an insulating layer, such as surface re-cleaning and insulating layer re-melting due to the lower hard-bake temperature.

- The latest candidate used is Microposit S1813 Photo Resist, which is the same photo-resist used for other patterns in this work. It was reported that photo resist can be used as an insulating layer if it is hard baked at up to  $200 \sim 250^{\circ}\text{C}$  for a few hours although there are some problems (such as cracking off and poor adhesion property of the top conducting layer) [Stewart, 1992]. By carefully graduated hard-baking and deposition of the interface layer, this photo-resist has been successfully used as an insulating layer in this work. The number 2<sup>#</sup> mask (negative ) was used. The thickness of the hard-baked photo-resist insulating layer can be produced and controlled in the order of about  $1 \pm 0.05 \mu\text{m}$ , which allows the conducting bias layer above it to be quite effective. It was found that the most effective hard baking temperature range is around  $220^{\circ}\text{C} \pm 10^{\circ}\text{C}$ .

#### (4) Deposition and patterning of the bias layer

- In the final fabricating stage, a  $0.55\mu\text{m}$  thick copper and 50 nm gold cap is sputter deposited and used as a current bias layer. To improve the adhesion property between the hard baked photo-resist insulating layer and copper bias layer, 5 nm of Chromium is deposited. The use of the 50 nm gold cap also improves the stability of the copper and reduces its oxidation problem whilst wire-bonding and during use.
- The main difficulty in this stage is the problem of mis-matched bias features relating to the aligning precision of the exposure system and the over-etching problem which relates to the roughness of the substrate and that of the multiple-film array. By using a

### *Chapter 3: Experimental development*

high quality substrate, optimising the multiple-film structure and carefully controlling the etching rate and time, a switched-bias MR sensor can be successfully made.

The sputtering details for each layer are:

- a) Tantalum: Target sputter cleaned for 20 minutes at 200 watts after changing target, or sputter cleaned for 10 minutes at 200 watts after changing substrate. 5 nm Ta is sputtered for 29 seconds at 200 watts (forward power) and zero watts (reverse power). Forward power refers to the power delivered to the target. Reverse power refers to the power delivered to the substrate platen.
- b)  $\text{Ni}_{81}\text{Fe}_{19}$ : Target sputter cleaned for 20 minutes at 200 watts after changing target, or sputter cleaned for 10 minutes at 200 watts after changing substrate. The sputtering rate for  $\text{Ni}_{81}\text{Fe}_{19}$  is about 0.28 nm per second at 200 watts (forward power) and zero watts (reverse power). Bias voltage set to -75 volts.
- c) Chromium: Target sputter cleaned for 20 minutes at 200 watts after changing target, or sputter cleaned for 10 minutes at 200 watts after changing substrate. 5 nm Chromium is sputtered for 20 seconds at 200 watts (forward power) and zero watts (reverse power).
- d) Copper: Target sputter cleaned for 20 minutes at 200 watts after changing target, or sputter cleaned for 10 minutes at 200 watts after changing substrate. The sputtering rate for Copper is about 30 nm per minute at 200 watts forward power and about 50 nm per minute at 300 watts (forward power) with zero watts (reverse power).
- e) Gold: The sputtering rate for gold is about 10 nm per minute at 200 watts forward power and about 15 nm per minute at 300 watts (forward power) with zero watts (reverse power).



*Chapter 3: Experimental development*

- f) The thickness of all films is controlled by depositing at a selected forward power for a particular length of time.

Other main parameters used in the fabrication of thin film MR sensors are as follows:-

- A typical parameter program used for ion beam etching process (Table 3-1).

**Table 3-1 A typical parameter used in ion beam etching**

Cathode (Amps)	Discharge (Amps)	Beam Current (mA)	Beam Voltage (Volts)	Accelerator (Volts)	Neutralise (mA)
12.9	2.71	30	500	460	28.8

- A typical hard baking procedure for using S1813 photo-resist as an insulating layer:
  - a) Clean and gradually heat the substrate from ambient temperature up to 250° (keep constant for more than 15 minutes).
  - b) Spray about 2 ml S1813 photo-resist on a 2" substrate and spin at a speed of 4000 rpm.
  - c) Soft bake for about 5 minutes at 110°C, then expose in ultra-violet light and develop to obtain the insulating layer features required.
  - d) Put in an air convection oven to heat gradually the substrate from ambient temperature up to 220°C  $\pm$  10 °C ( keep for 3 ~ 4 hours).
  - e) Gradually cool down to ambient temperature.



### **3.3 Microstructure and texture analysis for thin M-R film**

#### **3.3.1 Transmission Electron Microscopy**

There are two types of electron microscope in common use, the Scanning Electron Microscope (SEM) and the Transmission Electron Microscopy (TEM).

The SEM is perhaps the most useful and widely used instrument for the study of surface or cross section micro-morphology of materials. It also allows ease of specimen preparation. The various SEM techniques are differentiated on the basis of what is subsequently detected and imaged. By mean of scanning the probe, the image can be built up point by point in a way similar to that generated in a television display. The information detected and imaged by an SEM is therefore limited and the information about the crystallographic structure of specimen may not be provided.

Unlike SEM, the Transmission Electron Microscope (TEM), as the name implies, is used to obtain structural information from specimens that are thin enough to allow electron transmission. It is therefore like a true microscope, in the sense that all the image information is acquired simultaneously or in parallel. With high resolution TEM, it is possible to obtain detailed information about the microstructure of grains and grain boundaries near atomic level, e.g. a sub-50 nm scale, which is of great interest in the detailed investigation of many materials [Chapman & Kirk, 1997].

The modern TEM is a powerful tool for the study of a wide range of magnetic materials currently under development. It offers very high spatial resolution because of the large number of interactions that take place when a beam of fast electrons hits a thin solid specimen. It provides detailed insight into compositional, electronic, as well as structural and magnetic, properties. The achievable resolution of a TEM depends largely on the

### *Chapter 3: Experimental development*

information sought and may be limited by the specimen itself. Typical resolutions achievable for structural imaging are 0.2 ~ 1.0 nm, for the extraction of compositional information 1 ~ 3 nm and for magnetic imaging 2 ~ 20 nm [Chapman & Kirk, 1997]

Both SEM and TEM have been used in this study. Although SEM was used to observe the morphology and features of the sensor, most microstructure and texture analysis such as grain size, was performed by TEM, therefore, the TEM technique will be discussed here in more detail. Figure 3-7 is a picture of the JEOL 2000 FX Transmission Electron Microscope system used in this study. The accelerating voltage of this TEM can be up to 200 kV, and has been varied from 100 kV to 200 kV during observation as the changing in the thicknesses of specimens.

#### **3.3.1.1 Specimen preparation for TEM**

The principal disadvantage of a TEM is that it can be used only to study thin specimens. In most cases of thin films, the TEM specimen preparation may not be a serious problem except that the bulk substrate has to be removed. Usually this process can be successfully performed by using a carbon film (typically, 30 to 50 nm thick) pre-coated on the substrate as a transfer film. The films to be observed are deposited on this carbon film, and then floated off from the substrate by water (or other solvents) and placed in foldable Copper grids for TEM observation.

It was found that when the thickness of films becomes very small, for example, below 10 nm, it is very hard to prepare the specimen by using the transfer method because the thin film is very likely to disintegrate in the water. Direct deposition of the thin films on Copper TEM grids was also tried but failed because the thin films cannot be supported by a grid alone.

### *Chapter 3: Experimental development*

To overcome this problem, a support film, of 'Formvar', was then used for the preparation of specimens. Formvar is a polyvinyl formaldehyde resin and can very easily and quickly form a film on the surfaces of a substrate. The easiest way to prepare a thin film TEM specimen using Formvar is to put several TEM grids on a piece of paper, which has been first adhered to the substrate (e.g. a glass slide). A few drops of a solution of 0.5 percent Formvar in chloroform is then placed on the grids and a glass rod is used to wipe these drops uniformly over the whole slide to form a continuous film on the grids. The substrate with grids coated with Formvar can be used directly as a substrate to deposit thin film for examination. Afterwards, each grid together with a thin film specimen can be easily lifted off from the slide and placed in a TEM specimen holder for observation. Experiments showed that the film structure in the TEM Sample was not affected by using both (carbon or Formvar films) specimen preparation methods.

#### 3.3.1.2 Electron diffraction pattern and images

There are two basic operations of the TEM imaging system, one is to project the diffraction pattern on the viewing screen (diffraction mode) and another is to project the image onto the viewing screen (image mode). Both operations are useful for the study of magnetic thin films and have been employed in this study. To see the diffraction pattern you have to adjust the imaging system lenses so that the back focal plane of the objective lens acts as the object plane for the intermediate lens. Then the diffraction pattern is projected onto the viewing screen, as shown in Figure 3.8 (a). In image mode, the intermediate lens is readjusted so that its object plane is the image plane of the objective lens. Then an image is projected onto the viewing screen, as shown in Figure 3.8 (b) [Williams & Carter, 1996].

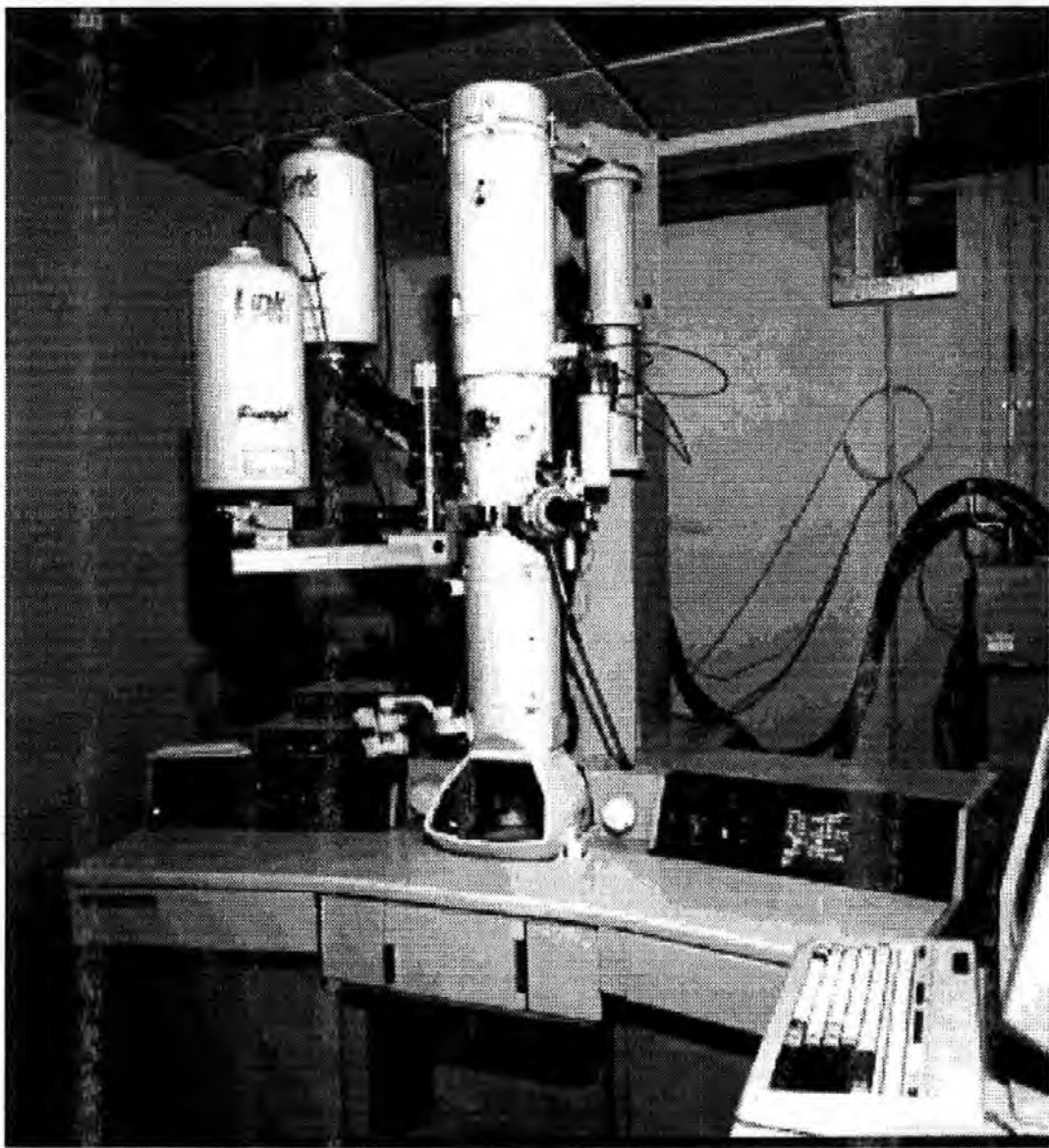


Figure 3-7 A Photograph of the JEOL 2000FX Transmission  
Electron Microscope System

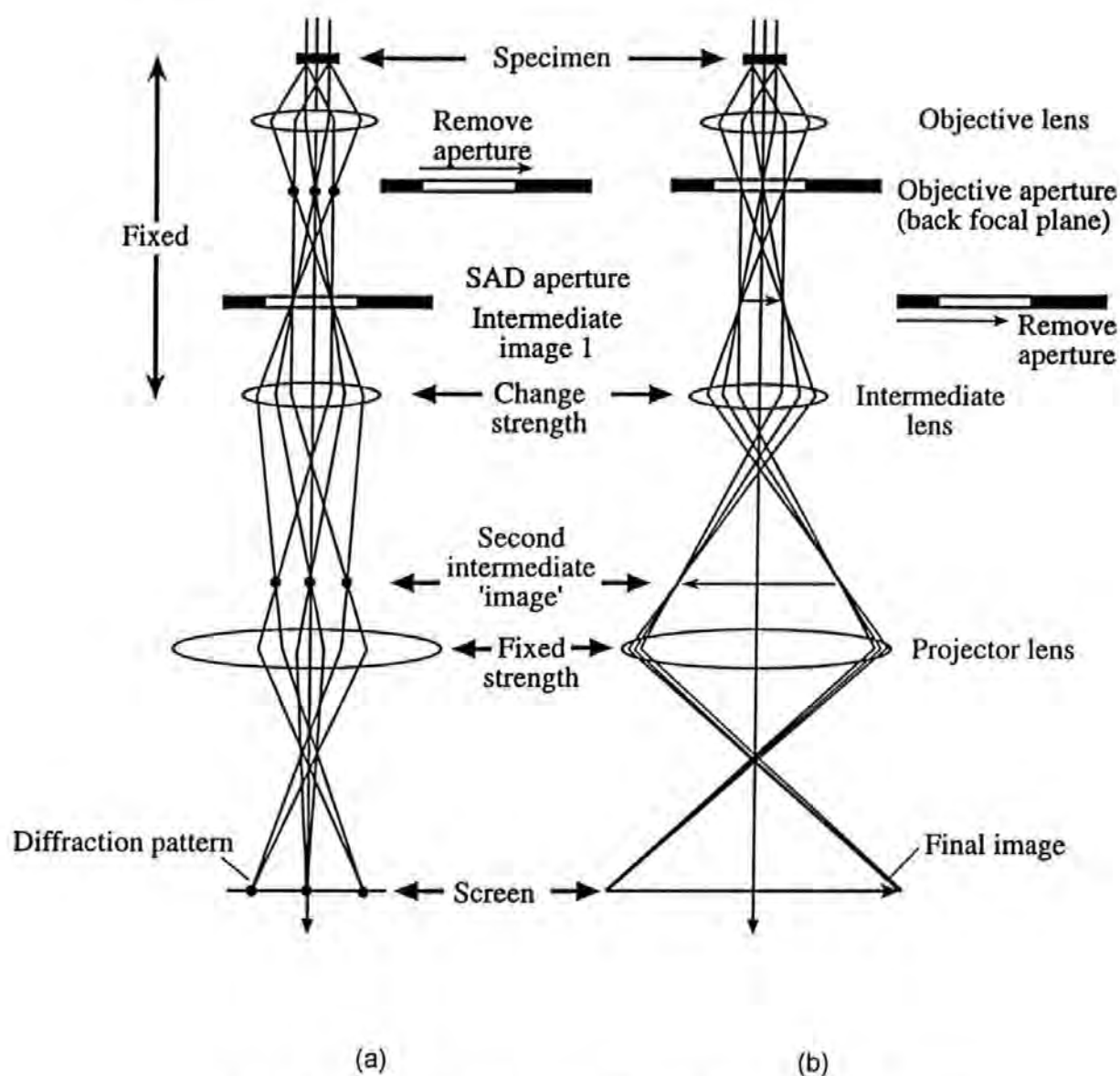


Figure 3.8 The two basic operations of the TEM imaging system

(a) projecting the diffraction pattern on the view screen and

(b) projecting the image onto the view screen.

(after [Williams & Carter, 1996] )

- Electron Diffraction Pattern and Selected-Area Diffraction

The electron diffraction mode is based on the fact that electrons are scattered by the film material and this can be used to form a picture (Electron Diffraction Pattern) of the scattered electrons distribution in the TEM imaging system. As can be seen from Figure 3.8 (a), the diffraction pattern contains electrons from the whole area of the specimen illuminated by the beam. Such a pattern is not very useful because the specimen will often be buckled. Furthermore, the direct beam is often so intense that it will damage the viewing screen. In practical operation, Selected-Area Diffraction is performed by making the beam smaller or inserting an aperture above the specimen which would only permit electrons that pass through it to hit the specimen [Williams & Carter, 1996].

This method can be used to get a qualitative measure of any crystallographic texture present in the film, by looking at the relative intensity of diffraction rings.

In principle, the index of a diffraction ring can be determined by Bragg's Law, and is depicted in simplified form in Figure 3-9.

When an electron beam with wavelength  $\lambda$  strikes a specimen with incident angle  $\theta$ , a diffraction pattern is formed on a photographic plate in the TEM screen, at a distance  $R$  from the centre of the diffraction pattern. The distance between the specimen and the screen plate (the camera length) is designated  $L$ . According to Bragg's law,

$$\lambda = 2d \sin \theta \quad (\text{Equation 3.2})$$

and by simple geometry, equation 3.2 becomes,

$$\tan 2\theta = R/L \quad (\text{Equation 3.3})$$

For very small  $\theta$ ,  $\tan 2\theta \cong 2\sin \theta$ , and equation 3-3 becomes,



$$Rd = \lambda L \quad (\text{Equation 3.4})$$

With equation 3.4, if  $R$  can be measured from a particular diffraction ring,  $L$  can be calibrated by a known crystalline specimen, e.g. a gold sample, and  $\lambda$  can be obtained from the accelerating voltage of the electron beam, then the  $d$ -spacing of the set of lattice planes giving rise to the diffraction ring can be determined [Williams & Carter, 1996].

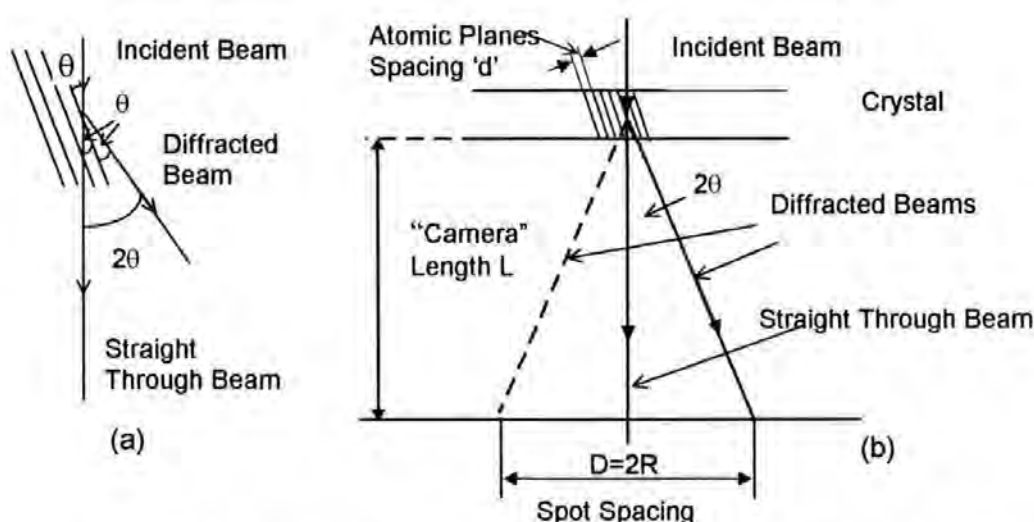


Figure 3-9 Simplified schematic diagram showing the forming of an Electron Diffraction Pattern (after [Pan, 1993])

When the type of film structure (e.g. fcc cubic for NiFe) is known, another easy way can be introduced to determine the index of the diffraction rings. For example, it is well known that  $\text{Ni}_{81}\text{Fe}_{19}$  films have a cubic crystal of an fcc structure and therefore, the allowed reflections for an fcc structure should correspond to the diffraction ring diameters of  $\text{Ni}_{81}\text{Fe}_{19}$  obtained by TEM. It is much better to investigate the RATIO of ring diameters assuming the smallest ring to be the [111] ring and so on. For an fcc structure, the ratios of ring diameters can be illustrated in Table 3-2 [Petford-long, 1996].



Figure 3-10 is an example of EDP for a 10 nm  $\text{Ni}_{81}\text{Fe}_{19}$  thin film, which was indexed in this simple way. By means of the electron diffraction pattern and by comparison with typical intensity ratios of the diffraction rings of textured polycrystalline samples, more information about the texture of thin films may be obtained. This is because the relative intensities of the different rings depend on whether the grains are randomly aligned or have a crystallographic texture along the film in the normal direction. For example, the diffraction pattern in Figure 3-10 shows that there is a random texture in this sample.

Table 3-2 Diffraction ring ratios for an cubic crystal of fcc structure

[hkl]	[111]	[200]	[220]	[311]	[222]	[400]	[331]
Ring Diameter Ratio	1.0	1.16	1.63	1.92	2.0	2.31	2.52

- TEM Images

A TEM image can be formed in a number of ways. By changing the objective aperture, two basic images, bright-field (BF) image and dark-field (DF) image can be obtained. The former is formed by placing suitably sized apertures in the back focal plane of the objective lens, and in this case, only the central direct beam can be selected. A DF image is formed by magnifying a single beam, which is chosen by means of an aperture that blocks the central direct beam and some other diffracted beams. The BF and DF images can be viewed at any magnification simply by adjusting the intermediate lenses of the microscope. Typical magnification ranges will be  $25,000\times \sim 100,000\times$ . They can be used for the measurement of microstructure details such as the grain size, whether homogeneous and continuous. The Bright-field image was used in this study and will be further described in Chapter Four.

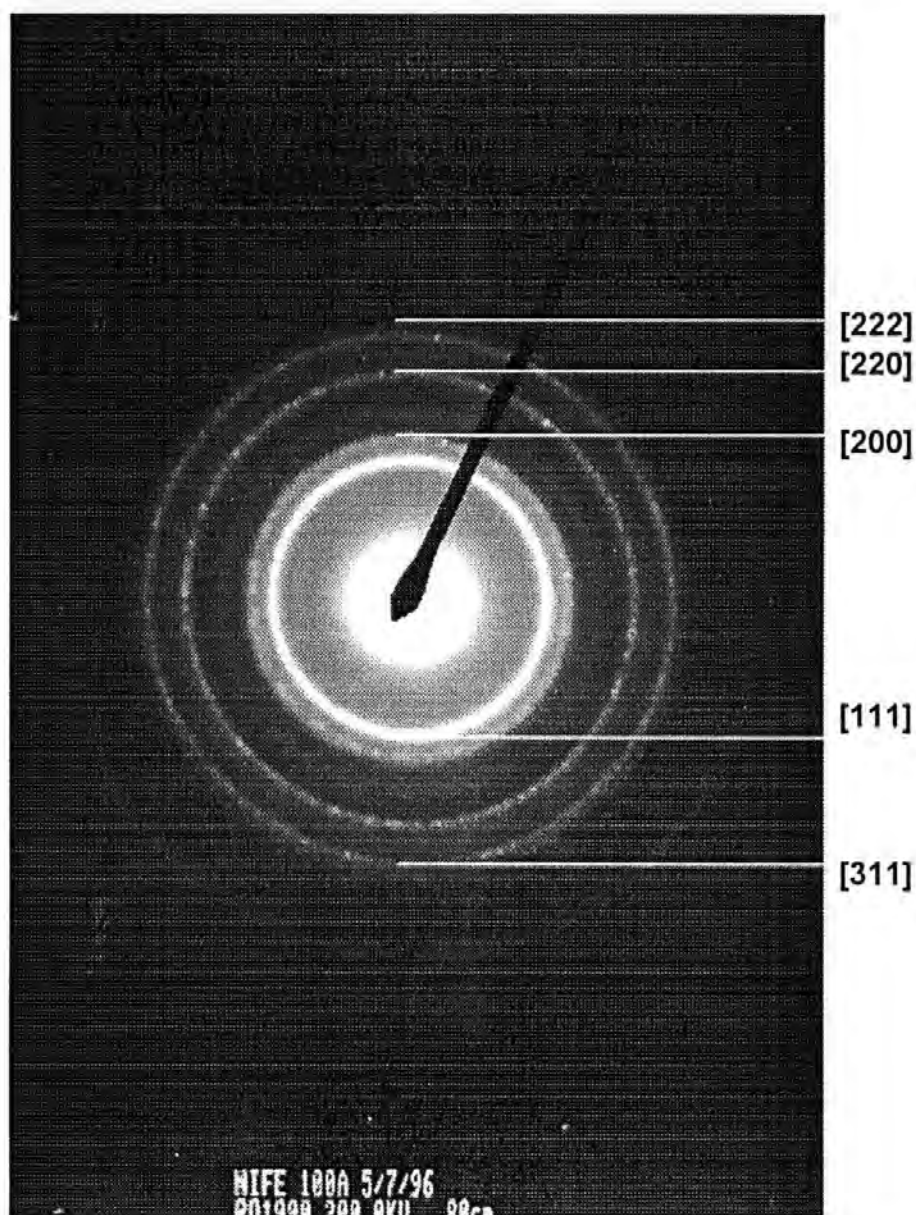


Figure 3-10 An EDP or SAD showing there is a random texture and which is indexed by looking at the ratio of the ring diameters (assuming the smallest ring is the [111] ring) (after[Petford-long, 1996])

### 3.3.2 Domain Observation by Lorentz Microscopy

Any feature of a transmission microscope specimen which deflects the electron beam can be translated into image contrast. Electrons are also deflected by internal magnetic and electric fields in the specimen, and the distribution of these fields can be made visible and used to detect the magnetic domain structures. Magnetic domain structures in thin films may be revealed in a number of ways in the transmission electron microscope, and are most commonly revealed using one of the modes of Lorentz microscopy. Since the observed contrast can be understood qualitatively in terms of the Lorentz force, this branch of electron microscopy is known as Lorentz microscopy [Chapman, 1984].

All imaging modes in which contrast is generated as a result of the deflection experienced by electrons as they pass through a region of magnetic induction, are called Lorentz images modes. The angular deflection of the electrons in ferromagnetic materials such as iron is typically  $0.01^\circ$  [Jiles, 1991].

The most commonly used modes for revealing magnetic domain structures are the Fresnel (or defocus) and Foucault imaging modes, because they are generally fairly simple to implement and they provide a clear picture of the overall domain geometry and are a useful indication of the directions of magnetisation in (at least ) the larger domains [Chapman, 1997].

A schematic drawing of how magnetic contrast can be generated in Fresnel and Foucault imaging modes is shown in Figure 3-11. Fresnel is particularly useful for revealing domain boundaries and Foucault gives an indication of the areas in the sample with a similar component of magnetic induction vector [Daykin & Petford-long, 1995]. The

### *Chapter 3: Experimental development*

Fresnel image was mainly employed in this study because the domain boundaries and walls were of most interest.

The principal difficulty encountered when using a TEM to study magnetic materials is that the specimen is usually immersed in the high magnetic field (e.g. about 1000 Oe for JEOL 2000FX) of the objective lens. This is sufficient to eradicate completely or severely distort most domain structures of interest, particularly for soft magnetic thin films. A number of strategies have been devised to overcome this problem [Chapman and Kirk, 1997]. A modified TEM in which the specimen can be sited in a field-free region of the microscope is required and employed for this observation [Daykin and Petford-Long, 1995].

The domain wall images presented in this thesis were observed at 400 kV in a JEOL-4000 EX TEM with an AMG 40 (low field) pole-piece using Fresnel imaging in the 'long camera length' mode. This was carried out at Oxford University. The applied field can be varied in the range of  $\pm 380$  Oe. Most magnetic domain images presented here are approximately 25  $\mu\text{m}$  in diameter and full details will be discussed in Chapter Four.

The preparation of specimens for Lorentz TEM observation is similar to that stated above. In order to know the direction of the anisotropy in the TEM grid, a field of about 40 Oe was used (via a magnetic substrate holder) during deposition and the direction of anisotropy was marked on each slide. This was marked again on each grid prior to being placed into the TEM grid holder for observation.

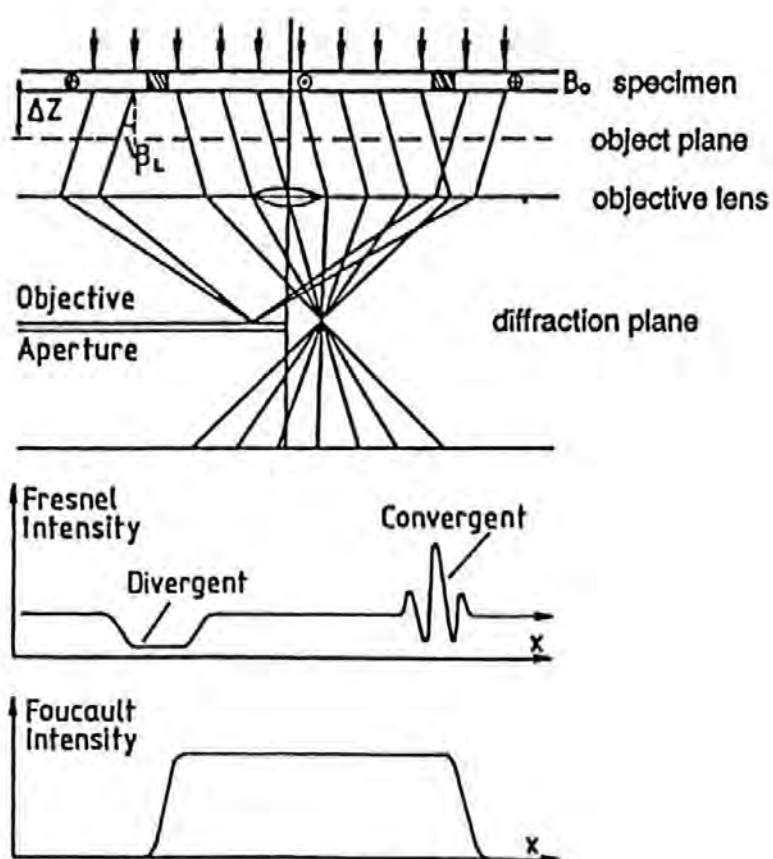


Figure 3-11 Fresnel and Foucault imaging used for revealing magnetic domain structure observation (after [Chapman, 1997] )

### **3.4 Measurements of magnetic properties of M-R Films and sensors**

As previously described, the deposition of the permalloy thin films is optimised in many ways, providing a reliable means of producing high quality magnetoresistive permalloy thin films for use in the fabrication of sensors. However, in order that the sensors produced from such films are able to provide the highest possible magneto-resistive (M-R) response, the lowest coercivity and Barkhausen noise, lower hysteresis and the highest possible sensitivity, several of their fundamental magnetic properties have to be investigated and optimised.

1. Film coercivity is interesting, not only for inclusion in the theoretical description of the sensors' dynamic response, but as a fundamental property of the films.
2. The resistivity and magnetoresistivity of the complete films and sensors needs to be measured so that the maximum magnetoresistive response can be calculated. Additionally the change in resistance versus applied field, resulting from the anisotropic Magnetoresistance of the whole film and complete sensors, provides qualitative information on their magnetic behaviour such as hysteresis.
3. Barkhausen noise in the films has to be measured in order to explain the variation in coercivity and magnetic domain structure.
4. The sensitivities of the switched bias sensors and variation in sensor sensitivity with magnitude of switched-biasing field should be studied so that information about the highest possibility sensitivity, frequency response and output performance of the sensors can be provided and evaluated.



### 3.4.1 Measurement of the magnetic properties of Permalloy films

#### 3.4.1.1 Coercivity Measurement by B-H loop plotting

The coercivity measurement by B-H loop plotting (hysteresis loop plots) has been widely used to observe the magnetisation of thin films for many years. It was based on the fact that the magnetisation reversal in thin ferromagnetic films can be produced by a magnetic field which may change slowly (typically, at times much longer than about 100 microseconds) in relation to the switching time of the films. This technique enables highly sensitive electronic circuits to be used to amplify and integrate the very small signal generated as a result of the small flux change occurring when a magnetic film is switched [Prupton, 1964<sup>b</sup>].

Figure 3-12 is a schematic diagram of a thin film B-H loop testing system used in this study. This sensitive instrument consists of two pairs of coils, one power generator and its amplifier, one X-Y plotter (or printer), a signal amplifier and integrator (which behaves as a low pass filter), as well a storage oscilloscope. The power amplifier provides an alternating current to a Helmholtz coil pair which generates a uniform field in the film sample. The film specimen is inserted in one of the inner sense coils (pick-up coil). The current passing through the coils generates a voltage across a known resistor in series with coils, which is amplified and taken to the X axis of an oscilloscope. The flux change in the film sample will induce a voltage in its sense coil. The air flux contribution to this voltage is compensated by connecting the coil in series opposition with another pick-up coil, which is of similar cross-sectional area but without a film sample. This voltage is an amplified, integrated induction signal and is taken to the Y



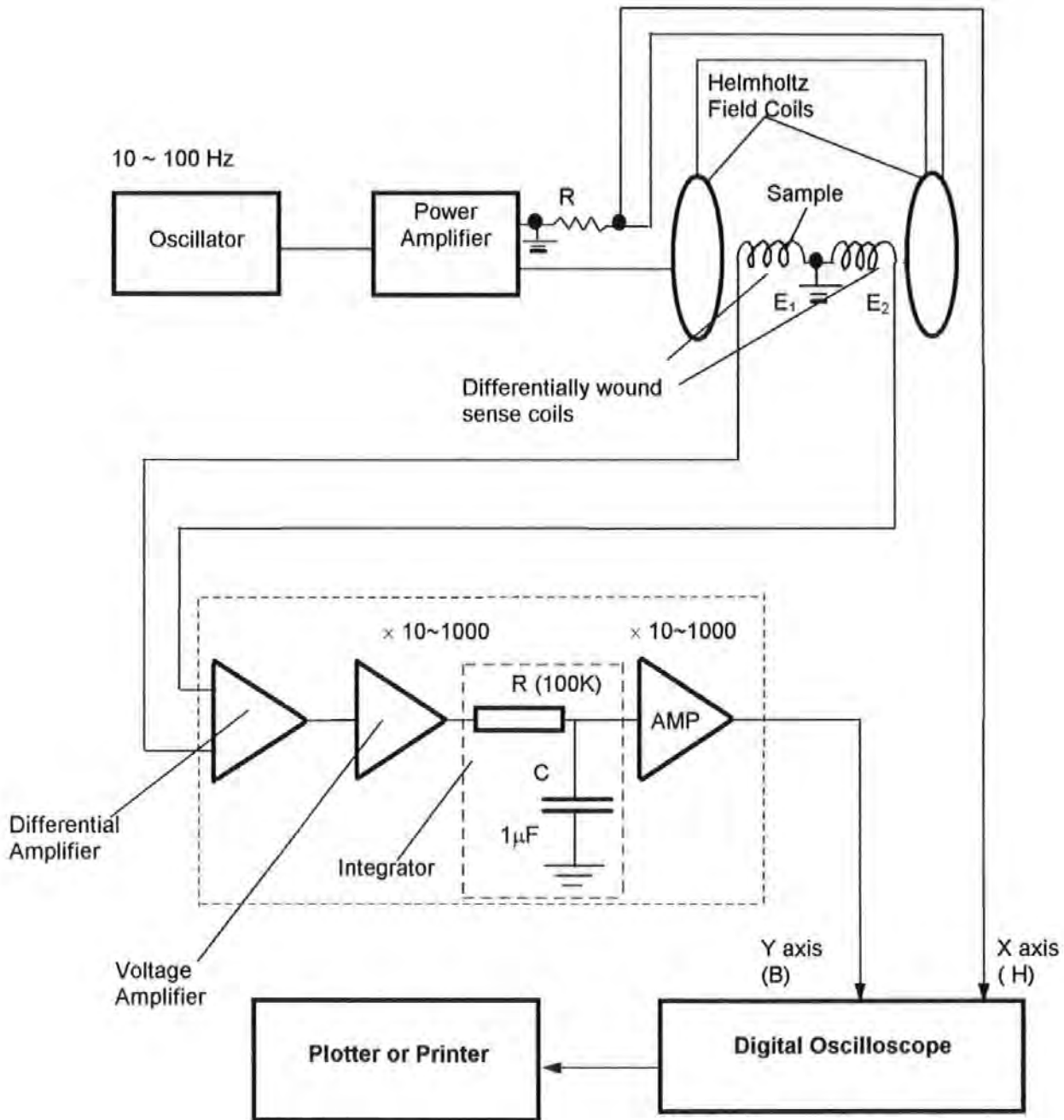


Figure 3.12 Schematic drawing of a thin MR film or sensor B-H loop testing system

### *Chapter 3: Experimental development*

axis plate of the oscilloscope. A typical frequency around 77 Hz was used in this study to avoid any mains generated noise at 50 Hz.

The Helmholtz drive coils consist of 400 turns of copper wire with an average diameter of about  $20 \times 10^{-2}$  m. The resistance of each coil is 4.3 ohms and the inductance is 48.4 mH in the zero field. They can produce a maximum field of about 5.6 kA/m (about 70 Oe) and are typically calibrated at 480 A/m (6 Oe) for soft magnetic thin film measurement. The sense (pick up) coil consists of about 1172 turns copper wire with an average wire diameter of about 0.16 mm. The resistance of each coil is 22.3 ohms and the inductance is 2.043 mH in the zero field. A standard sample of coercivity 115.2 A/m (1.44 Oe) is used to calibrate the testing system prior to each measurement. The coercivity data for the films was averaged for five readings.

The easy direction coercivities of  $\text{Ni}_{81}\text{Fe}_{19}$  films varies in the range from about 10 to 1000 A/m. In the hard direction, the coercivities become very small, and may be less than a few A/m in the case of very thin films. The measurement became very difficult as the flux change in such thin films may be too weak. Most of the coercivity measurement results presented and discussed here are taken from the easy direction of the films.

#### **3.4.1.2 Barkhausen Noise Analysis for MR Film**

It is well known that Barkhausen noise has been a major problem in MR sensor design and application for many years. Barkhausen noise measurement also provides basic information on magnetisation processes of magnetic thin films.

The Barkhausen Noise measurement for MR thin films in this study was based on analysing the voltage induced by flux changes in the films as a result of sweeping them with a field of 77 Hz. The difference between this and the B-H loop measurement system

was only in the output signal amplifier and integrating circuit. The experimental basis for the measurement is also shown in Figure 3-13. A schematic diagram of this test system is given in Figure 3-14.

The theory of Barkhausen noise measurement is based on Faraday's law of electromagnetic induction, and may be described as follows:

For the differential sense coils arrangement shown in Figure 3-14, in a constant field, without a sample present, the induced field B is

$$B = \mu_0 H_{coil1} - \mu_0 H_{coil2} = 0 \quad (\text{Equation-3.5})$$

If a sample with magnetisation M is now introduced into coil 1,

$$B = \mu_0 (H_{coil1} + M) - \mu_0 H_{coil2} = \mu_0 M \quad (\text{Equation-3.6})$$

where,  $\mu_0 = 4 \pi \times 10^{-7} \text{ H/m}$ .

The e.m.f. induced in a circuit is equal to the product of the number of coil turns and the rate of change of flux linking the circuit

$$e = -N \frac{d\Phi}{dt} \quad (\text{Equation 3.7})$$

If A is the cross-sectional area of the coil (e.g.  $10^{-3} \text{ m}^2$ ) and N is the number of turns the magnetic induction (e.g. N=1172 turns) is then  $B = \Phi/A$

$$e = V = f(\Phi) = -N \frac{d\Phi}{dt} = -NA \frac{dB}{dt} = -NA\mu_0 \frac{dM}{dt} \quad (\text{Equation 3.8})$$

As can be seen from Equation 3.8, the induced voltage is proportional to the rate of change of magnetic induction or magnetisation. And thus, by connecting the sense coils to a suitable signal capture system, it is possible to observe the rate of change of magnetic induction or magnetisation,  $dB/dt$  or  $dM/dt$ , as a function of applied field.

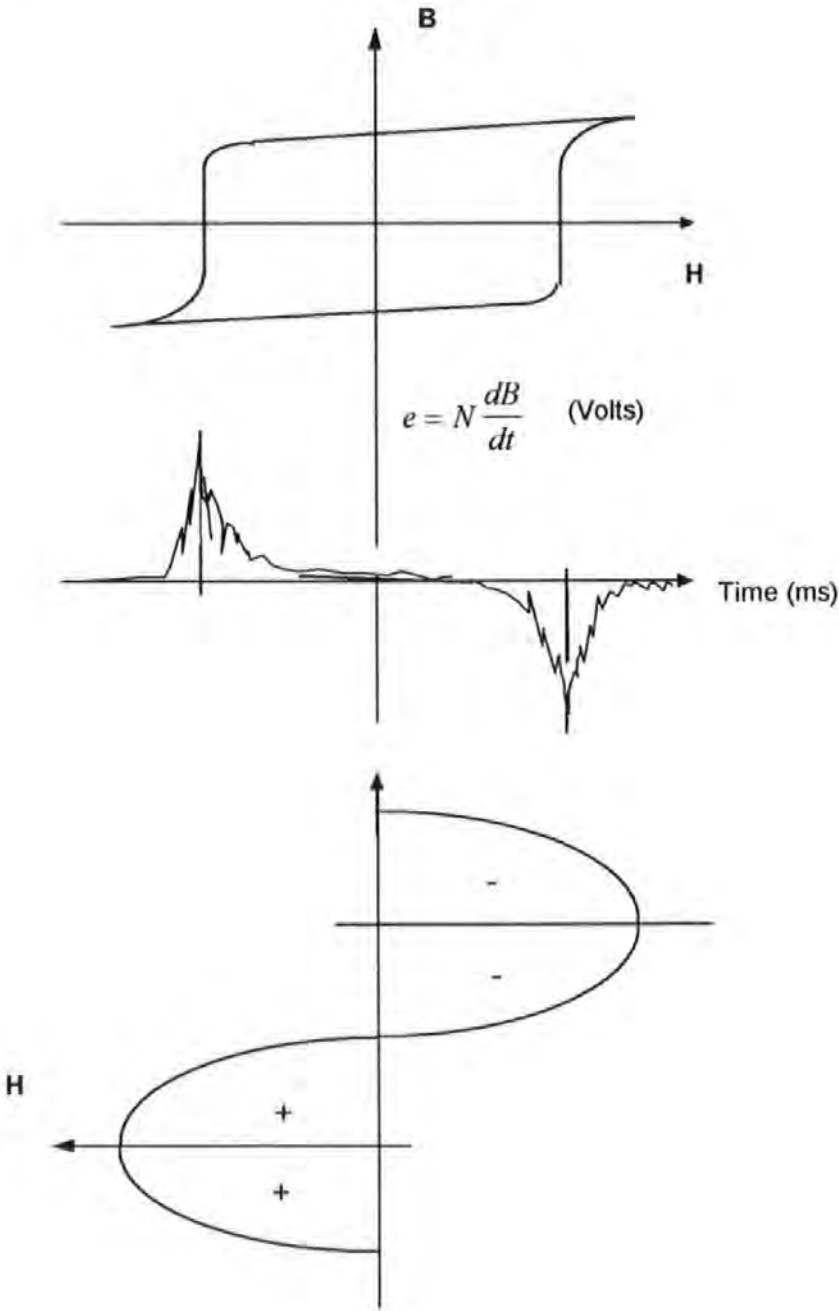


Figure 3.13 The experimental basis of Barkhausen Noise measurement

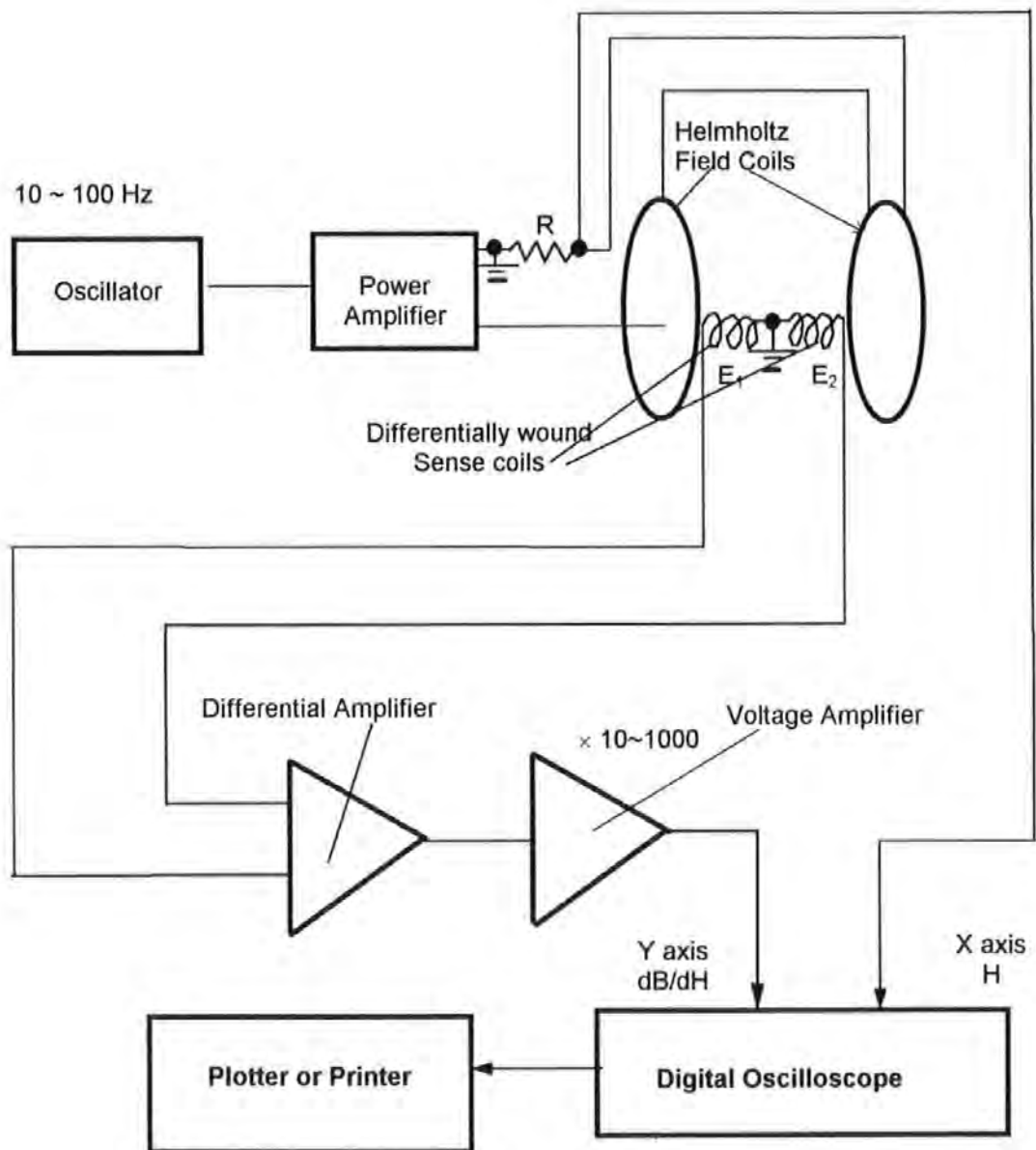


Figure 3.14 Schematic diagram of Barkhausen Noise measurement system

### Chapter 3: Experimental development

#### 3.4.1.3 Resistance and Magnetoresistance Measurement for MR Films

- Sheet Resistance

Sheet resistance is a very useful quantity that is widely used for comparing thin films particularly those of the same material deposited under similar conditions. The resistance of a rectangular shaped section of film can be defined by

$$R = \frac{\rho \cdot l}{d \cdot b} \quad (\text{Equation 3.8})$$

where,  $l$  and  $b$  are the side lengths of the rectangular section of film, and  $d$  is the thickness of film.

If  $l=b$ , equation (3-8) then becomes  $R=\rho/d =R_s$  and is independent of the size of the square, depending only on the resistivity and thickness of the film.

An in-line four-point probe method and a square-probe array method (such as shown in Figure 3-15) have been used to measure the sheet resistivity of MR films. These methods are based on using a four probe (contact) potentiometric circuit and more details can be found in refs. [Maissel and Glang, 1970] and [Jenkins, 1995].

In the former method, a constant current is passed between an outer pair of contact probes. An inner pair of contacts is then used to measure the voltage dropped across a portion of film between these outer probes. When the probes are placed on a material of semi-infinite volume, the resistivity is given by

$$\rho = \frac{V}{I} \cdot \frac{2\pi}{1/S_1 + 1/S_2 - 1/(S_1 + S_2) - 1/(S_2 + S_3)}$$

When  $S_1 = S_2 = S_3 = S$ , this reduces to

$$\rho = \frac{V}{I} 2\pi \cdot S$$

### Chapter 3: Experimental development

If the material on which the probes are placed is an infinitely thin slice resting on an insulating support (e.g. glass substrate), then,

$$\rho = \frac{Vd\pi}{I \ln 2} \quad \text{or} \quad \frac{\rho}{d} = R_s = 4.532 \frac{V}{I}$$

For the square-probe array, current  $I$  is fed in through any two adjacent probes and the voltage  $V$  generated across the other two is then measured. With both methods, the sheet resistance of films can be obtained by

$$\rho = \frac{Vd\pi}{I \ln 2} \quad \text{or} \quad \rho = 4.532 \frac{V}{I} d \quad \text{for the four-point method} \quad (\text{Equation 3.9})$$

and

$$\rho = \frac{V \cdot 2\pi \cdot d}{I \cdot \ln 2} = \rho = 9.06 \frac{V}{I} d \quad \text{for the square-probe method} \quad (\text{Equation 3.10})$$

where,  $I$  is a constant current fed into the probe,  $V$  is a voltage generated across the probes, and  $d$  is the thickness of film. The units of  $\rho$  are  $\Omega\text{-m}$  or  $\mu\Omega\text{-cm}$ .

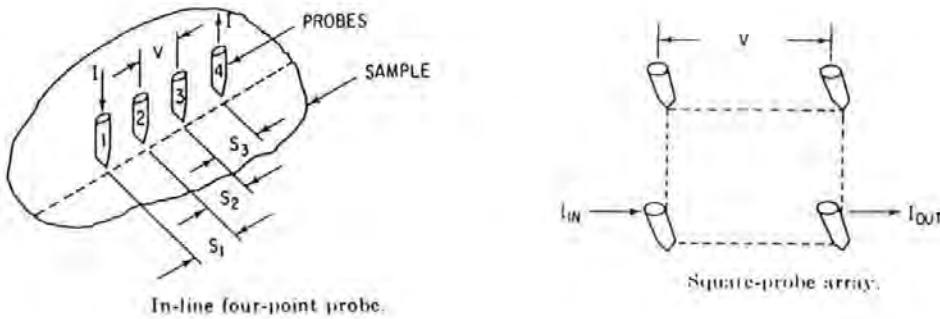


Figure 3-15 In-line four-point probe and a square-probe array for resistance measurement (after [Maissel and Glang, 1970])

In practice, it is difficult to make a perfect geometry for the probe arrangement, the reading accuracy of about 1%–5 % can be obtained by using a d.c. constant-current



source in a suitable potentiometric circuit and with good connection between the probes and film. The values of film resistance may be changed in a wide range. For thinner films having high resistance a balance point can be found using reasonable values for the standard resistance and adjusting the bridge output to zero volts.

- The anisotropic magnetoresistance measurement

It is necessary to accurately measure the anisotropic magnetoresistance of the films after deposition before lithography to ensure that films will be suitable to be made into sensors. To measure the anisotropic magnetoresistance of a film, an external magnetic field has to be applied to rotate its magnetisation moment relative to the current direction. The physical arrangement of the various elements of the anisotropic magnetoresistance measurement system are given in Figure 3-16. This consists of a pair of Helmholtz coils, one generator with amplifier, a pressure pad with two probes, a standard resistance box and an X-Y plotter.

The Helmholtz coils are fixed to the sample holder plate and used to generate an external magnetic field in the range from 800 A/m to 8 000 A/m. For soft magnetic films such as permalloy, the peak applied field is calibrated at  $\pm 1600$  A/m ( $\pm 20$  Oe). This is typical for most measurements in this study. The ramp generator supplies a current to the drive coil, providing a very slowly varying triangular waveform oscillating about zero volts at about 0.1 to 1 Hz. The direction of the magnetisation vector in the film can be rotated by this field and the resistance of films also changes due to their anisotropic properties. With this applied field, the magnetisation in a film is saturated first in one direction, and then after passing through zero, saturated in the other direction. A potentiometric circuit is used to measure the change in the resistance of the film sample.

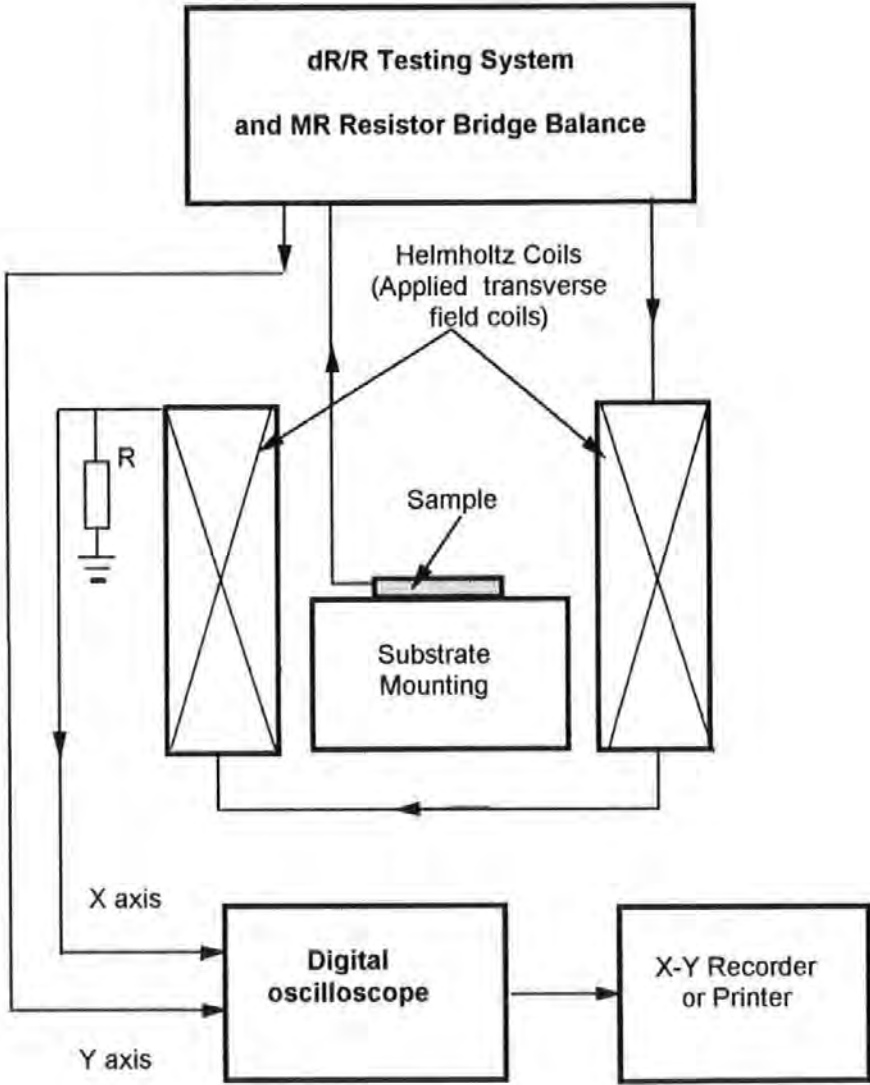


Figure 3.16 Schematic diagram of the anisotropic magnetoresistance testing system

### *Chapter 3: Experimental development*

There are two identical current sources in this potentiometric circuit, which supply currents to the film sample and a standard resistance box. The connection between the film and circuit is performed by using a pressure pad with two probes. The sample film and a standard resistance box are connected to a bridge and the bridge output fed to a differential amplifier. The resultant output from this amplifier is fed to the vertical terminals of an X-Y plotter (or oscilloscope). A voltage proportional to the current in the field coils is also introduced to the horizontal terminals of the plotter. A record of the magnetoresistive change in the sample film can be produced.

Figure 3-17 is a typical magnetoresistance plot produced using the testing system as shown in Figure 3-16. The change in resistivity (along the Y axis) can be determined by reducing the external field to zero, and then altering the value of the standard resistance box in fixed standard increments to obtain the same change in the bridge output observed by the deflection of the plotter pen) as that produced by the magnetoresistive change of the MR film.

#### **3.4.2 MR Response Measurement for MR Sensor**

For the completed sensors, magnetoresistance can be measured with the testing system shown in Figure 3-16. The only difference is that the pressure-pad probes are connected to the ends of sensors to be examined. This time the M-R response may be changed in the sensors made from the same substrate film but with different geometry (for example, different width) due to the transverse demagnetising field.

It was found that, there are two peaks (see Figure 3-17) on the magnetoresistance loop in some samples. The double peaks may be introduced by hysteresis related to the

dispersion in the magnetoresistive films. Like Barkhausen noise, hysteresis also needs to be eliminated or overcome in sensor applications. It has been reported that the hysteresis and Barkhausen noise can be reduced by means of applying a constant longitudinal field in Ref. [Tsang, 1984], [Watson,1986], [Flynn, 1994]. It can also be seen from Figure 3.17, that the double peaks are also not symmetrical and there is over-cross in some parts of curve, which may be caused by the error movement of pen.

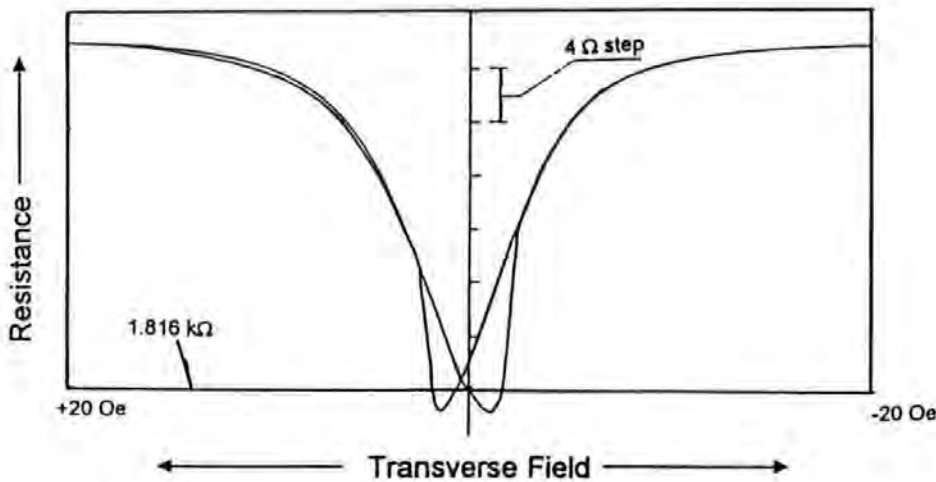


Figure 3-17 Showing a typical plot of the anisotropic magnetoresistance versus the applied field ( $\pm 20$  Oe, or 160 A/m)

An alternative method was adopted in this study using an additional high-frequency external 'linearising' field perpendicular to the saturating (drive) field. In this case, a well defined direction can be obtained for the sensors magnetisation to relax and these double magnetoresistance peaks (the hysteresis) can be pulled together. This high-frequency field also has the effect of producing the maximum possible magnetoresistive change by improving the original state of magnetisation in the sensors [Watson,1986]. A schematic diagram of the M-R response test system (including high-frequency external linearising field) is shown in Figure 3.18

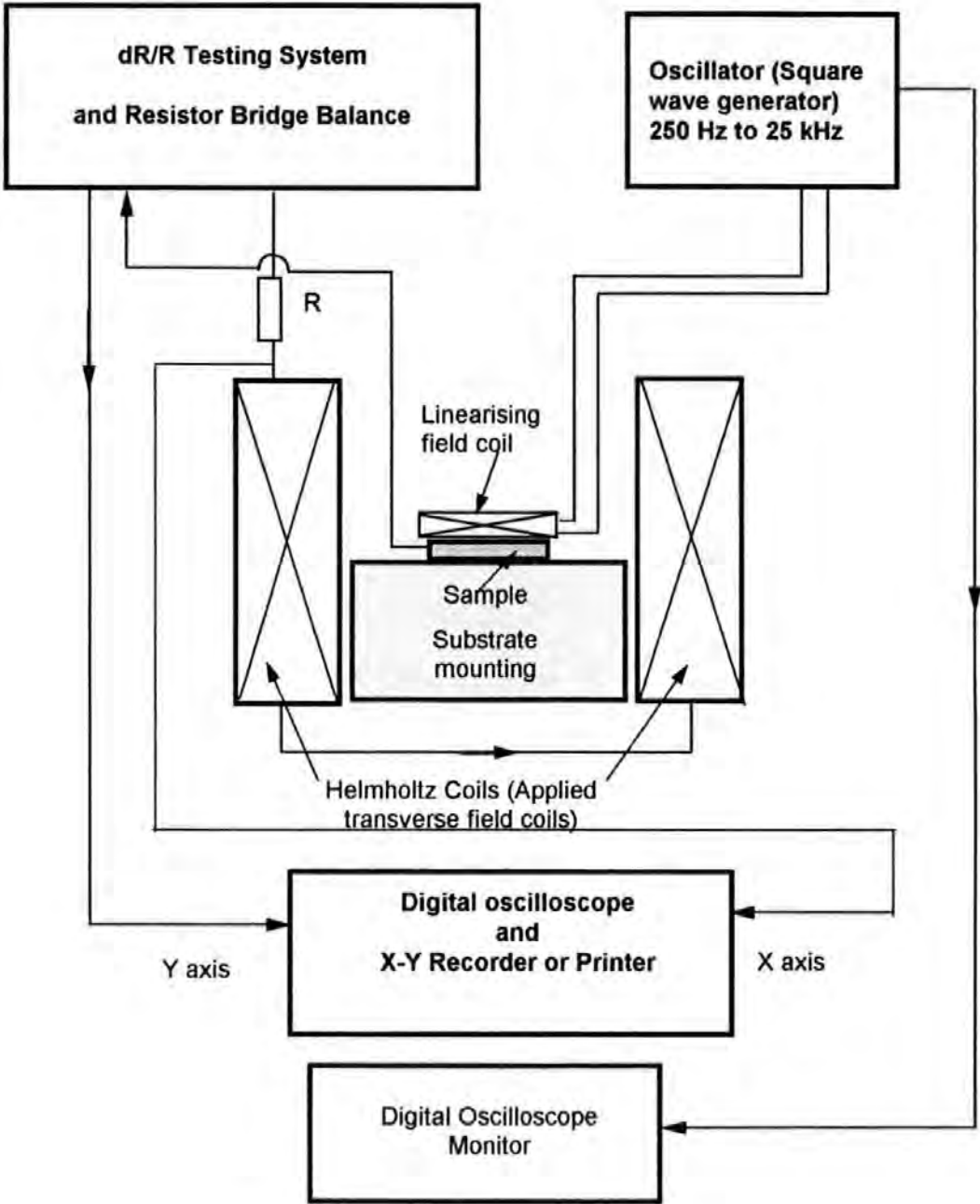


Figure 3.18 Schematic diagram of the anisotropic magnetoresistance testing system (including high-frequency external linearising field)

### 3.4.3 Electronic drive and test system used to evaluate MR Sensor performance

There are very few publications concerning the fundamental magnetic properties of very thin e.g., a few nano-metres thick, MR sensors [Flynn,1994]. Also, no systems have been reported for evaluating the output performance of thin, switched-bias MR sensors. Figure 3-19 is a schematic diagram of the sensor electronic drive and test system, which has been developed and successfully used in the evaluation of the sensors in this study. Because of its importance, it is described here in more detail.

#### 3.4.3.1. Test procedure

The two sensors are connected to a bridge and the bridge output to a differential amplifier. It is well known [Mapps,1997] that if the sensor current is applied as part of a bridge circuit the differential output ( subtraction of the two sensor output voltages) from the sensor will be zero in a zero applied magnetic field. The sensors are always biased in opposite directions so that any d.c. field ( $\delta H$ ) such as from a pair of 10-turn Helmholtz coils can unbalance the bridge. The output from the differential amplifier is a square wave containing some noise if the sensor is used to detect small fields. This output is fed into a lock-in amplifier and compared with a reference signal from the bias current. This square-wave reference ensures that only signals of this same shape and repetition frequency will be registered in the output of the lock-in amplifier. This output is a d.c. level proportional to the applied field  $\delta H$ .

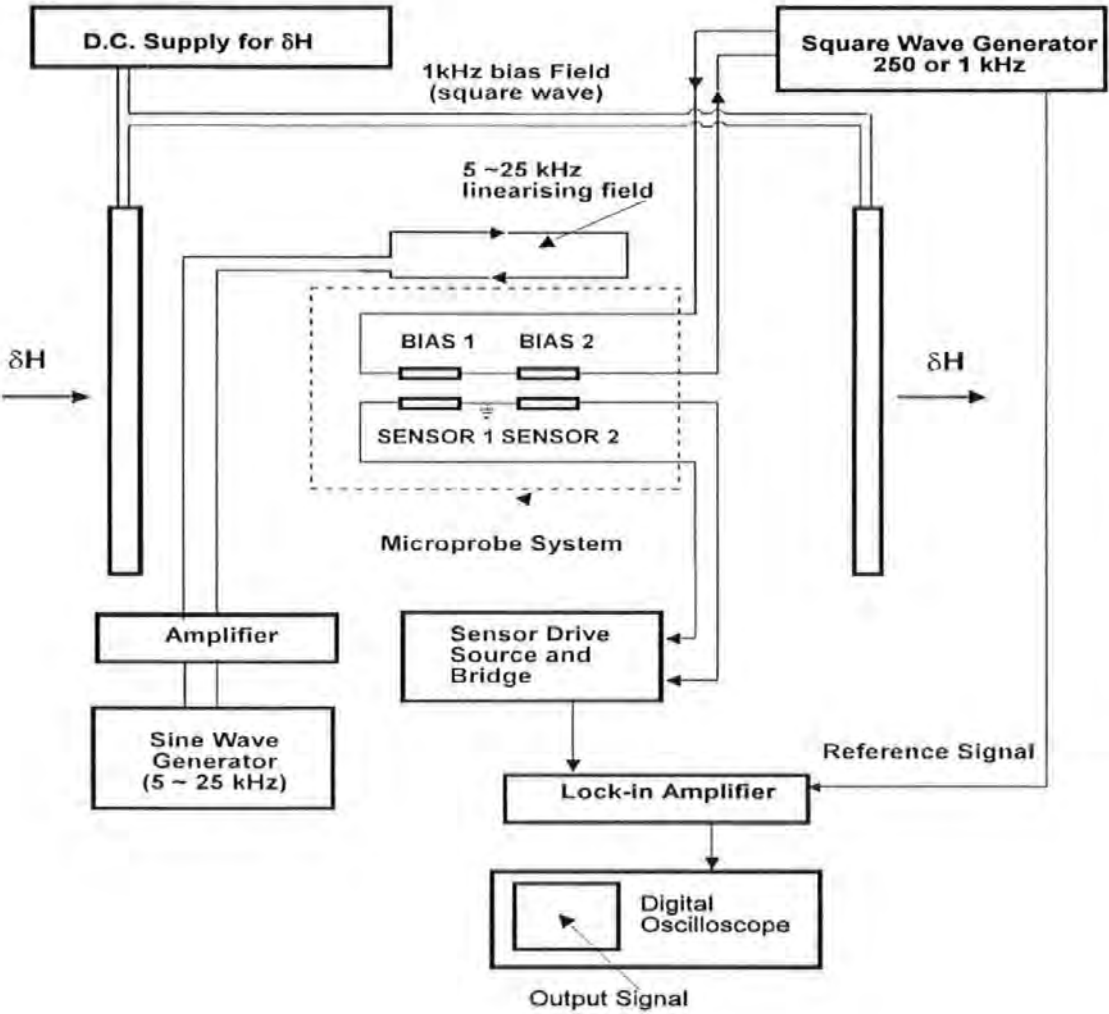


Figure 3-19 A schematic diagram of sensor electronic drive and test system.



### Chapter 3: Experimental development

In addition to the applied field and sensor switching bias field (which can be, say from zero to 1 kHz and typically 250 Hz) an additional high-frequency bias field can be supplied from another set of Helmholtz coils (shown in ‘longitudinal’ field mode in Figure 3-19). This field reduces hysteresis and Barkhausen effects. The output from the lock-in amplifier is fed to an oscilloscope with an averaging capability to reduce any fluctuations in the output.

The value of  $\delta H$  can be varied precisely from zero to 300 nT. The peak switched-bias current is typically from 0 to 140 mA (field approx. 100 A/m) but can be varied to find the best operating point of the sensor. All data is averaged for five measurements.

#### 3.4.3.2. Microprobe system

In the test system the sensor substrate (which contains many prototype sensors) is mounted in a non-magnetic microprobe system so that each dual sensor can be accessed by tungsten probes mounted on a microprobe card, for supplying bias current and sense current. There are 18 pairs of sensors in a 2 inch square substrate. Using the microprobe system, it is easy to examine all the sensors very quickly.

The contact area of the tungsten micro-probe is about 15 ~ 16  $\mu\text{m}$  in diameter and this means the area size is about 180  $\mu\text{m}^2$ . Assuming the maximum bias current to be about 200 mA (corresponding to about  $0.4 \times 10^{10} \text{ A/m}^2$  current density for the Cu bias film) the maximum current density in micro-probe tip is given by

$$\sigma_{\text{max}} = \frac{I_{\text{max},b}}{A_{\text{max}}} = \frac{200 \times 10^{-3}}{180 \times 10^{-10}} = 1.11 \times 10^9 \text{ A/m}^2 \quad (\text{Equation 3.11})$$

### *Chapter 3: Experimental development*

This is safe for the tungsten probes and copper & gold bias films [Ciureanu, 1992]. In practice, it is very important to make sure of good contact between each probe and the end leads prior to each measurement, because any bad contact may cause contact resistance to rise.

To reduce any noise coupling into any metal part in the micro-probe system, all connections are screened and all metal parts (including spare filaments in the microprobe card) are connected to the system earth.

#### 3.4.3.3. The coil system

The field coils must be designed so that the field over the whole of the sample is substantially uniform. Also, the constant of proportionality between field and current was calculated as well as calibration being performed by measuring the field with an accurate gaussmeter [Prupton, 1964<sup>b</sup>]. To meet this need, three sets of coils were designed and used in this test system.

Because of the physical space limit within the microprobe system, two pairs of rectangular coils were used both for a d.c. field ( $\delta H$ ) and for another applied field (e.g. the M-R response measurement). The calculation of magnetic field from a pair of rectangular coils is explained as below.

Considering one turn of the rectangular coil as shown in Figure 3-20.

here

$$\sin \alpha = \frac{b}{\sqrt{b^2 + r^2}}$$

where,  $r^2 = a^2 + d^2$

$$\sin \alpha = \frac{b}{\sqrt{b^2 + a^2 + d^2}}$$

and, 
$$\sin \gamma = \frac{a}{\sqrt{a^2 + d^2}}$$

from the Biot-Savart law,

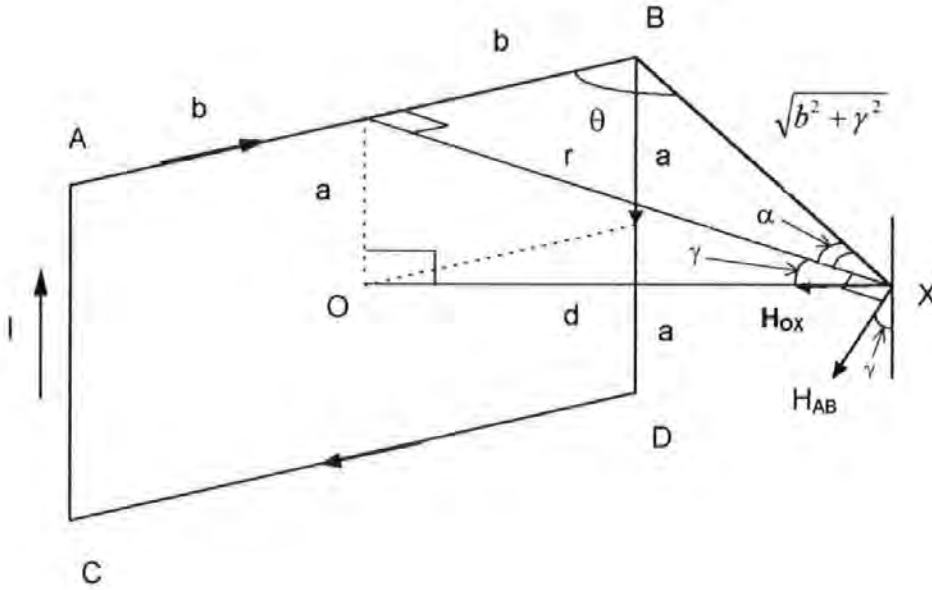


Figure 3-20 Geometry for calculation of the magnetic field on the axis of a one-turn rectangular coil

$$dH_{AB} = \frac{I}{4\pi r} \cos \alpha \cdot d\alpha$$

$$H_{AB} = \frac{I}{4\pi r} \int_{-\alpha}^{+\alpha} \cos \alpha \cdot d\alpha = \frac{I}{4\pi r} [+\sin \alpha]_{-\alpha}^{+\alpha} = \frac{I}{4\pi r} \cdot 2 \sin \alpha$$

$$= \frac{I}{2\pi r} \cdot \frac{b}{\sqrt{b^2 + a^2 + d^2}} \quad \text{(Equation 3.12)}$$

### Chapter 3: Experimental development

and since  $r = \sqrt{a^2 + d^2}$

therefore  $H_{AB} = \frac{I}{2\pi} \times \frac{b}{\sqrt{(a^2 + d^2)(a^2 + d^2 + b^2)}}$

to get  $H_{OX}$  we must resolve  $H_{AB}$  along the axis  $XO$ ,

i.e.  $H_{OX} = H_{AB} \cdot \sin \alpha$  where  $\sin \alpha = \frac{a}{\sqrt{a^2 + d^2}}$

$$\begin{aligned} H_{OX} &= \frac{I}{2\pi} \times \frac{a \cdot b}{\sqrt{(a^2 + d^2)^2 (a^2 + d^2 + b^2)}} \\ &= \frac{I}{2\pi(a^2 + d^2)} \times \frac{a \cdot b}{\sqrt{(a^2 + d^2 + b^2)}} \end{aligned}$$

For two conductors AB and CD we get  $2 \times H_{OX}$

Similarly, for conductors DA and BC we get

$$2 \times \frac{I}{2\pi(b^2 + d^2)} \times \frac{a \cdot b}{\sqrt{a^2 + d^2 + b^2}}$$

therefore, total field

$$H_{OX} = \frac{I \cdot a \cdot b}{\pi(a^2 + d^2)\sqrt{(a^2 + d^2 + b^2)}} + \frac{I \cdot a \cdot b}{\pi(b^2 + d^2)\sqrt{a^2 + d^2 + b^2}}$$

$$H_{OX} = \frac{I \cdot a \cdot b}{\pi\sqrt{(a^2 + d^2 + b^2)}} \left[ \frac{1}{(a^2 + d^2)} + \frac{1}{(b^2 + d^2)} \right] \quad A/m/turn \quad (\text{Equation-3.13})$$

for one coil with  $N$  turn, we get

$$H_{total} = \frac{N \cdot I \cdot a \cdot b}{\pi\sqrt{(a^2 + d^2 + b^2)}} \left[ \frac{1}{(a^2 + d^2)} + \frac{1}{(b^2 + d^2)} \right] \quad (\text{Equation-3.14})$$

Practical sizes of the rectangular coils used are:

### Chapter 3: Experimental development

#### (1) The drive coil

The drive coils consist of 300 turns of enamelled copper wire in a rectangular form to produce a field along the sensor long axis as shown in Figure 3-19. The dimensions are,

$$N=300, \quad d=9.5 \text{ cm}=9.5 \times 10^{-2} \text{ m},$$

$$b=7 \text{ cm}=7 \times 10^{-2} \text{ m},$$

$$a=3.7 \text{ cm}=3.7 \times 10^{-2} \text{ m},$$

using 
$$H_{total} = \frac{NIab}{\pi \sqrt{(a^2 + d^2 + b^2)}} \left[ \frac{1}{(a^2 + d^2)} + \frac{1}{(b^2 + d^2)} \right],$$

If  $I=1A$ , then

$$\begin{aligned} H_{total} &= \frac{300 \times 3.7 \times 10^{-2} \times 7 \times 10^{-2}}{3.14 \times \sqrt{(3.7^2 + 9.5^2 + 7^2)} \times 10^{-4}} \left[ \frac{1}{3.7^2 + 9.5^2} + \frac{1}{7^2 + 9.5^2} \right] \times \frac{1}{10^{-4}} \\ &= \frac{77.7 \times 10^4}{3.14 \times 12.37} \left[ \frac{1}{103.94} + \frac{1}{139.25} \right] = 335.5 \text{ (A/m)} = 4.194 \text{ Oe} \end{aligned}$$

The calibration for this coil has been performed by measuring the field with an accurate gauss-meter.

Figure 3-21 shows the magnetic field generated in the rectangular coil versus the input current. The solid curve is for the theoretical result and the broken curve is the calibration. The difference may be as a result of the coil resistance changing with temperature and that the theory assumes that every turn of the coil is in one place (which is impossible in practice).

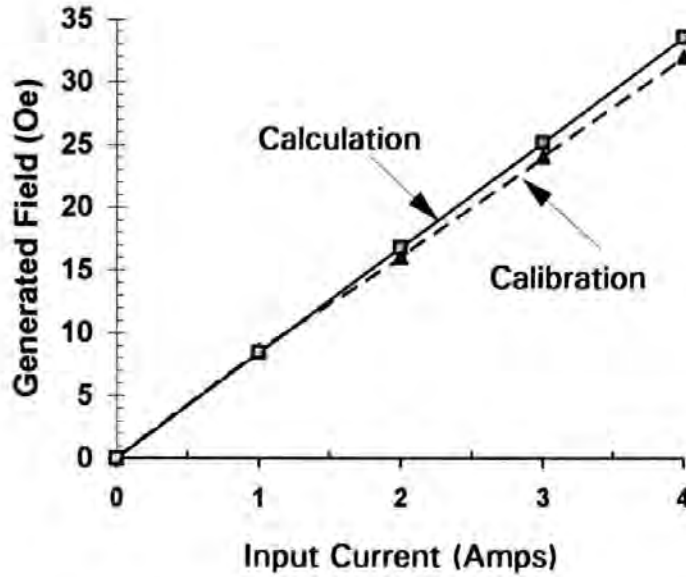


Figure 3-21 The magnetic field generated in a rectangular coil versus the input current. (the solid curve is for the theoretical calculation and the dotted curve is the calibration, 1 Oe=79.6 A/m).

(2) The sense coil

The dimension are  $N=10$ ,  $d=9.5 \text{ cm}=9.5 \times 10^{-2} \text{ m}$ ,  $b=5.4 \text{ cm}=5.4 \times 10^{-2} \text{ m}$  and

$a=2.2 \text{ cm}=2.2 \times 10^{-2} \text{ m}$ , for a pair coils  $N=2 \times 10=20$

from Equation 3-14,

$$\begin{aligned} \frac{H_{total}}{I} &= \frac{2 \times N \times a \times b}{\pi \sqrt{(a^2 + d^2 + b^2)}} \left[ \frac{1}{(a^2 + d^2)} + \frac{1}{(b^2 + d^2)} \right] \\ &= \frac{2 \times 10 \times 2.2 \times 10^{-2} \times 5.4 \times 10^{-2}}{3.14 \times \sqrt{(2.2^2 + 5.4^2 + 9.5^2) \times 10^{-4}}} \left[ \frac{10^4}{2.2^2 + 9.5^2} + \frac{10^4}{5.4^2 + 9.5^2} \right] \\ &= \frac{2 \times 11.88 \times 10^3}{3.14 \times 11.15} \left[ \frac{1}{95.09} + \frac{1}{119.41} \right] = 6.408 \times 2 = 12816 \text{ m}^{-1} \end{aligned}$$

if  $I = 1 \text{ mA}$ ,

$$\begin{aligned}
 H_{total} &= 12.816 \times 10^{-3} \text{ A/m} = \frac{12.816 \times 10^{-3}}{\left(\frac{1000}{4\pi}\right)} \text{ Oersteds } (\cong \text{ Gauss}) \\
 &= \frac{12.816 \times 10^{-3}}{\left(\frac{1000}{4\pi}\right) \times 10^4} \text{ Tesla} = \frac{12.816 \times 10^{-3}}{\left(\frac{1000}{4\pi}\right) \times 10^4} \times 10^9 \text{ nano-Tesla} \\
 &= 16.1 \text{ nano-Tesla per mA}
 \end{aligned}$$

The corresponding current  $I$  for 1 nano-Tesla ( $I_{nT}$ ) is,

$$I_{nT} = \frac{1}{16.1} = 0.062 \text{ mA}$$

This means that a one nano-Tesla field can be generated by applying a current of 0.062 mA to the  $\delta H$  coil. However, the applied field was set at about 9.95 mA (about 160 nano Tesla), and used for most measurements of  $\delta H$ .

Initially, the  $\delta H$  coils were supplied by an a.c. power supply but this proved unsatisfactory because of unexpected noise at 50 Hz. A 12-Volt battery was therefore employed, together with a potentiometer for measurement and variation of current. In this way a noise-free and precise sense field of a few tens or hundreds (e.g. 160 nT) nano-Tesla could be applied.

### (3) Ring coil supplying a high-frequency 'linearising' field

The high-frequency linearising field coil consists of about 140 turns of enamelled copper wire wrapped on a ferrite ring with an air gap 5mm long. It is mounted with epoxy on the top of a plastic cover and placed on the micro-probe card. The field direction provided by this coil is along the sensor long axis, and perpendicular to the  $\delta H$  applied field and the switching bias field. The distance between the sensor and the gap of the ring is set at  $1.2 \times 10^{-2}$  m. The resistance and inductance of this ring coil are  $2\Omega$  and 7.8 mH



### *Chapter 3: Experimental development*

respectively. The magnetic field generated at the sample is linear with input current at about 1.6 A/m per mA.

It was found that the field required for the linearising effect is small, of the value of a few to a few tens of A/m. This is because the sensors have been optimised for lowest coercivity and Barkhausen noise.

#### 3.4.3.4. Others

Except for micro-probe and coils, there are two functional power generators, one amplifier, one sensor drive source and bridge box, one precision lock-in amplifier and one or two digital oscilloscopes in this system. In practice, the electrical behaviour of this system is complicated by some effects (e.g. noise) which may be related to the connection arrangement. For example, if the sensor drive and bridge box is put on the top of the switching bias field generator, the output of sensor noise level will rise even in the case when they have screens connected to earth.

In order to properly evaluate the output of sensor, all precautions and pre-checking should be done prior to measurement, e.g. proper screening and good connection, using high-quality elements.

By means of its switched-bias nature the sensor can be used with a precision lock-in amplifier together with low pass and high pass filters. An output signal which excludes any extraneous noise at frequencies other than the bias switching frequency of the sensor can be produced. The noise level on this output is about 1 mV when set up to produce 24 mV from about 160 nano-Tesla.

## **CHAPTER 4**

### **RESULTS AND DISCUSSION**

This chapter will present the results obtained from the experimental development described previously. Comparisons between theoretical and experimental values will emphasise discussion of the correlation of magnetic properties such as coercivity with microstructure, thickness dependence, underlayer effects and temperature influence. The ultimate aim of the study is to make new kinds of M-R sensor with lower Barkhausen noise and lower demagnetising field. The sensor's output results will be presented initially together with some selective review of the related subjects so as to discuss some of my own work and that of others. This highlights the effect of microstructure on the magnetic properties of thin film M-R sensors. Special attention is paid to the Ta underlayer effect on hysteresis, the effect of bias field and the optimum sensitivity to a low field of about 80 nano-Tesla.

#### **4.1 Magnetic properties in very thin Permalloy Films**

##### **4.1.1 The variation of coercivity in very thin Permalloy films**

###### **4.1.1.1 Thickness dependence**

Figure 4.1 (a) shows the results of coercivity measured from B-H plots as a function of  $\text{Ni}_{81}\text{Fe}_{19}$  permalloy film thickness in the range from 2.5 nm to 30 nm. Four sets of multi-layer structures were studied,  $\text{Ni}_{81}\text{Fe}_{19}$  films deposited on glass (a) at a substrate temperature of 20°C (b) at a substrate temperature of 300°C (c) with 5 nm of  $\text{SiO}_2$  as underlayer at a substrate temperature of 20°C (d) with a 5 nm Ta underlayer at a

substrate temperature of 20°C. As can be seen from figure 4.1(a), there is a similar minimum in coercivity at 7.5 nm film thickness of permalloy in each case.

Figure 4.1 (b) shows the extended results of coercivity variation of permalloy films in the thickness range from 2.5 nm to 100 nm, which were deposited at substrate temperatures of 20 °C and 300°C. These correspond with sets **a** and **b** in Figure 4.1.a.

As can be more clearly seen from Figure 4.1 (b), there is a similar minimum in coercivity at 7.5 nm but there are also two peaks in coercivity at film thicknesses of about 27.5 nm and 50 nm. These cases may relate to the change of domain wall structure and the micro-structure of the films. This will be discussed later.

- Grain size

Table 4.1 shows some results for coercivity versus grain size in  $\text{Ni}_{81}\text{Fe}_{19}$  Permalloy thin films. As can be seen from the change in coercivity against the thickness and the change in grain size for such thin films, higher coercivity does not mean greater grain size. Other factors such as underlayer and deposition temperature may also affect the coercivity.

For example, No. 1 and No. 2 (see Table 4.1) permalloy films have the same thickness, but a different deposition temperature resulted in a different grain size and gives the same coercivity. No. 5 and No. 6 samples have same thickness but different underlayer. The No. 6 film deposited on 5 nm Ta underlayer has smaller grain size (less than half) and less coercivity (about half) than those of film (No.5) with 5 nm Cr underlayer [Ma, 1996]. More details about such factors are given below.

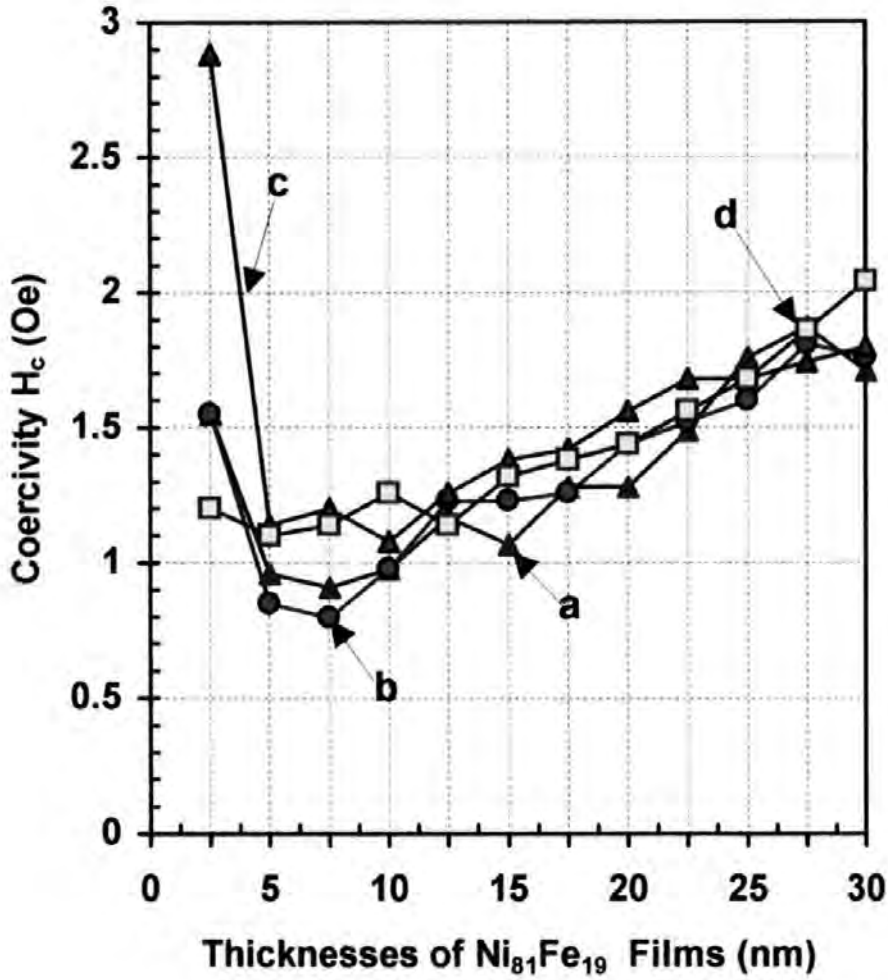


Figure 4.1: Graphs of coercivity versus. film thickness for  $Ni_{81}Fe_{19}$  thin films

deposited on various surfaces (after [Ma,1996]).

(a) for  $Ni_{81}Fe_{19}$  Thin Films Deposited on Glass at a Substrate Temperature of 20°C and (b) for films at 300°C

(c) for  $Ni_{81}Fe_{19}$  Thin Films Deposited on Glass with a 5 nm of  $SiO_2$  Underlayer at a Substrate Temperature of 20°C and (d) for films with a 5 nm of Ta Underlayer.

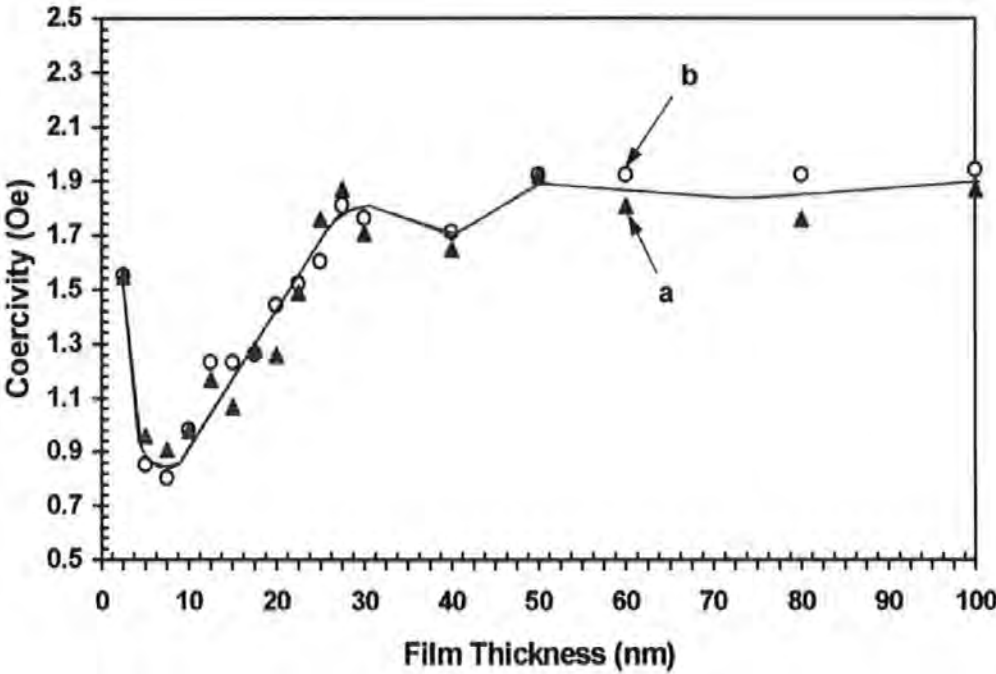


Figure 4.1b: Graphs of coercivity versus film thickness in the range from 2.5 to 100 nm (▲ for films deposited at 20°C and ○ for 300°C)

Table 4.1 Some Results for Coercivity versus Grain Size in  $\text{Ni}_{81}\text{Fe}_{19}$  Permalloy Thin Film

No	Film layers and Thickness (nm) and Depositing Temperature	Average Grain Size (nm)	Coercivity (A/m)
1	$\text{Ni}_{81}\text{Fe}_{19}$ ( 10 nm, 20°C )	4.8	75.5
2	$\text{Ni}_{81}\text{Fe}_{19}$ ( 10 nm, 300°C )	7.5	75.5
3	$\text{Ni}_{81}\text{Fe}_{19}$ ( 30 nm, 20°C )	12	135
4	$\text{Ni}_{81}\text{Fe}_{19}$ ( 40 nm, 20°C )	12 ~15	131
5	Cr (20 nm) + $\text{Ni}_{81}\text{Fe}_{19}$ ( 30 nm, 20°C )	35 ~40	207
6	Ta (20 nm) + $\text{Ni}_{81}\text{Fe}_{19}$ ( 30 nm, 20°C )	12 ~15	111
7	Cr (5 nm)+ $\text{Ni}_{81}\text{Fe}_{19}$ (10 nm 20°C)	25 ~35	127
8	Ta (5 nm) + $\text{Ni}_{81}\text{Fe}_{19}$ (10 nm, 20°C )	5 ~7	95

- Lateral grain size examined by TEM

Figure 4.2 shows TEM bright field images: (a) for a 5 nm Permalloy film and (b) for a 40 nm Permalloy film. As can be clearly seen, the 5 nm Permalloy film shows much smaller grain size than the 40 nm film. The bright field image of the 5 nm film also shows that at such a thickness the film is not yet continuous and this may be a reason for its higher observed coercivity.

#### 4.1.1.2 Underlayer effect

- Underlayer materials

An experimental study of very thin  $\text{Ni}_{81}\text{Fe}_{19}$  permalloy films deposited on various underlayers such as Ta, Cr,  $\text{SiO}_2$  was undertaken. Some results show that both grain size and texture of Permalloy thin films are strongly affected by underlayers. As can be seen from Table 4.1, the coercivity is lower in Permalloy thin films with Ta underlayer but higher with Cr underlayer. This results is in good agreement with results reported by [Galtier et al., 1993].

- Grain size and texture

For comparison, the TEM bright images for 40 nm Permalloy thin films with the same thickness (5 nm) Ta and Cr underlayer deposited under the same conditions are given in Figure 4.3. The bright field image for the Ta underlayer shows a small lateral grain size of about 10 to 15 nm and no particular lateral shape. In the Cr case, the average grain size is much bigger (it may be up to 50 nm) and is more likely to be randomly oriented.

## *Chapter 4: Results and Discussion*

This may suggest that the lower coercivity observed for films with a Ta underlayer, corresponds to relatively smaller grain size and a more circular grain shape.

- **Electron diffraction study**

In order to understand the textural relationship between the  $\text{Ni}_{81}\text{Fe}_{19}$  permalloy films and Ta underlayers, film thicknesses such as 5 nm, 7.5 nm, 10 nm and 30 nm with 5 nm Ta underlayers were studied by TEM diffraction pattern. Two pairs of electron diffraction pattern images, for 7.5 nm and 30 nm  $\text{Ni}_{81}\text{Fe}_{19}$  permalloy films with and without Ta underlayers, are given in Figure 4.4 and Figure 4.5 respectively.

In the Electron Diffraction Pattern of permalloy films grown with Ta underlayers, the innermost ring corresponds to bcc Ta [110], and the next two rings being Permalloy [111] and [200], then a rather fuzzy Ta [211] ring. The rest are Permalloy [220], [311] and [222] respectively. In this case, there is some degree of (111) in-plane texture in permalloy film which may be favoured by the presence of Ta. The films grown without Ta underlayer had all rings showing typical  $\text{Ni}_{81}\text{Fe}_{19}$  permalloy fcc structure and there is a random crystallographic texture [Petford-long, 1996].

### **4.1.1.3 Temperature dependence**

- **Grain size and substrate temperature**

An estimation of grain size for  $\text{Ni}_{81}\text{Fe}_{19}$  permalloy films in the thickness range from 2.5 to 10 nm was made and a plot of grain size as a function of film thickness vs. its coercivity is given in Figure 4.6. There are two sets of curves in Figure 4.6, one for a  $\text{Ni}_{81}\text{Fe}_{19}$  permalloy film deposited at about 300°C, another for a  $\text{Ni}_{81}\text{Fe}_{19}$  permalloy film deposited



at 20°C . It can be clearly seen that the grain size of films increases with increasing thickness. The average grain size of the set deposited at 300°C is greater than for 20°C. The coercivity results show that films deposited at 300°C have relatively lower coercivity independent of their grain size. This result suggests that a suitable elevated substrate temperature can be used to improve the film quality and obtain lower coercivity. Possible reasons are reduced initial anisotropy dispersion and increase in thermal stability and related to the [111] crystal orientation. These have been discussed by many authors such as [Engelman & Hardwick, 1963], [Prupton, 1964] and [Jhingan et al., 1984].

- TEM bright field images and EDP observation

Figures 4.7 to 4.10 show two sets of TEM bright field images and corresponding electron diffraction patterns for very thin permalloy films (2.5 nm, 5 nm, 7.5 nm and 10 nm) deposited at 300°C and ambient temperature respectively. A higher magnification image for a 10 nm film deposited 20°C is given in Figure 4.11.

The films deposited at higher substrate temperature have greater grain size and stronger intensity of the diffraction ring at the same film thickness. The size of the continuous regions of these permalloy films increases with increasing film thickness and is greater in the films deposited at higher temperature.

Films deposited at higher substrate temperature have a large crystal size. As film thickness increases, the degree of crystallisation is raised and their fcc structure becomes more clear. The ring diameter ratios are in good agreement with an fcc structure of random texture. From Figure 4.11, it can be seen that a  $\text{Ni}_{81}\text{Fe}_{19}$  permalloy film of 10 nm

thickness is polycrystalline, continuous and has small grain size. However, thinner films (such as 2.5 nm and 5 nm) may be less continuous.

- Thermal history

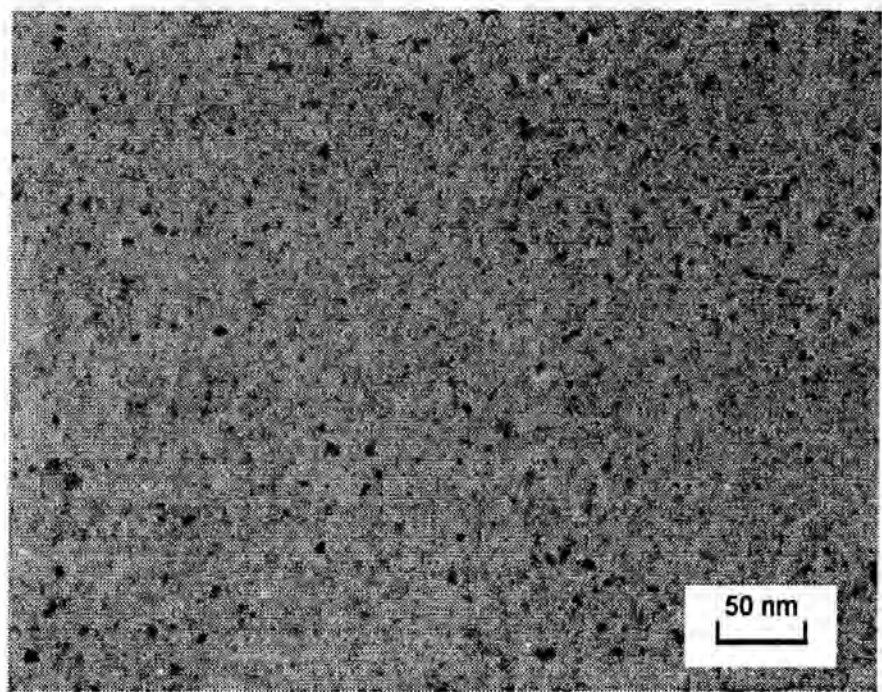
It was found that the coercivity of permalloy film is dependant not only on substrate temperature during deposition but also thermal history during fabrication. In particular, if the film was deposited at room temperature, the coercivity value may be slightly varied during or after fabrication.

Table 4.2 shows some experimental data of film coercivity, where  $H_{cf}$  is the initial (continuous film sheet) coercivity of the film and  $H_{cs}$  is for the etched sensor. These films were very thin in the range of several nm.

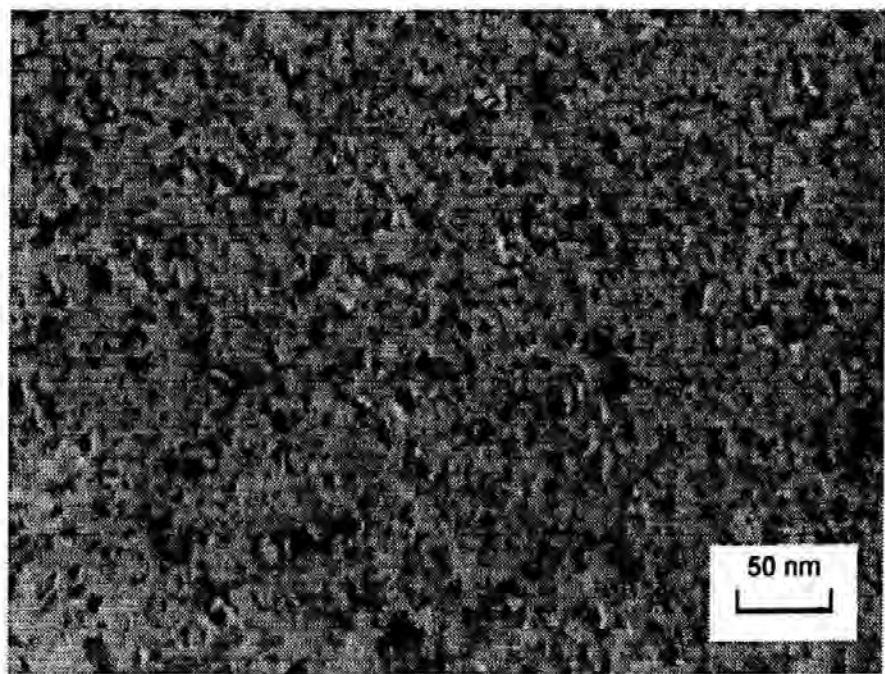
**Table 4.2 Coercivity versus thermal history**

Sample No	1	2	3	4	5
$H_{cf} (A/m)$	80.5	76.1	96.7	98.6	105
$H_{cs} (A/m)$	79.5	74.0	93.8	98.6	101

It was found in this work that the thermal effect on the coercivity of ultrathin soft magnetic films such as permalloy (several nm) is substantial and the coercivity obtained at room temperature by means of quasistatic methods such as VSM, B-H loop and SQUID, may not be equal to the intrinsic coercivities [Hou et al., 1997]. However, insufficient data has been reported on this subject.

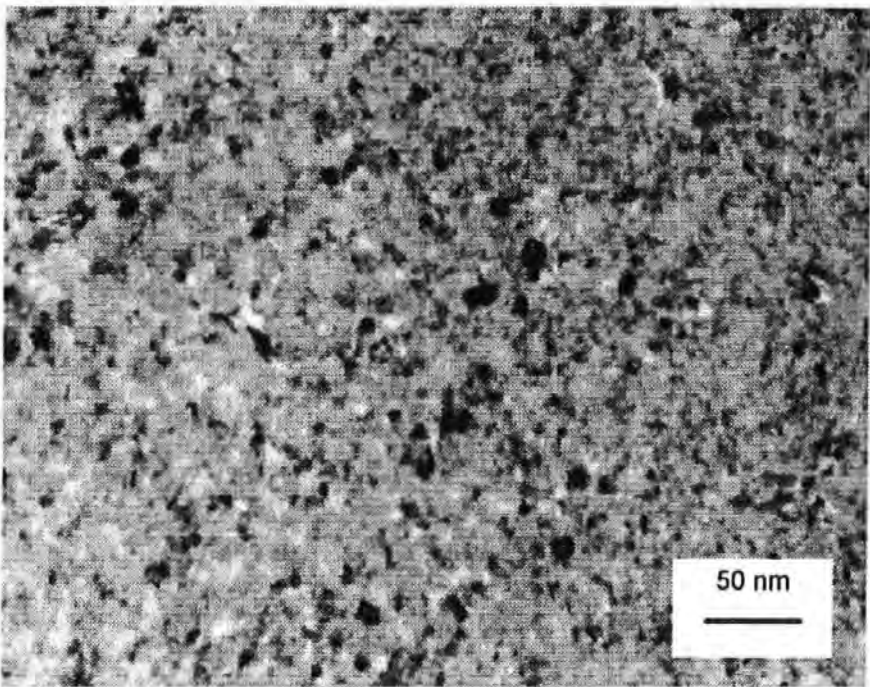


(a) 5 nm Permalloy film

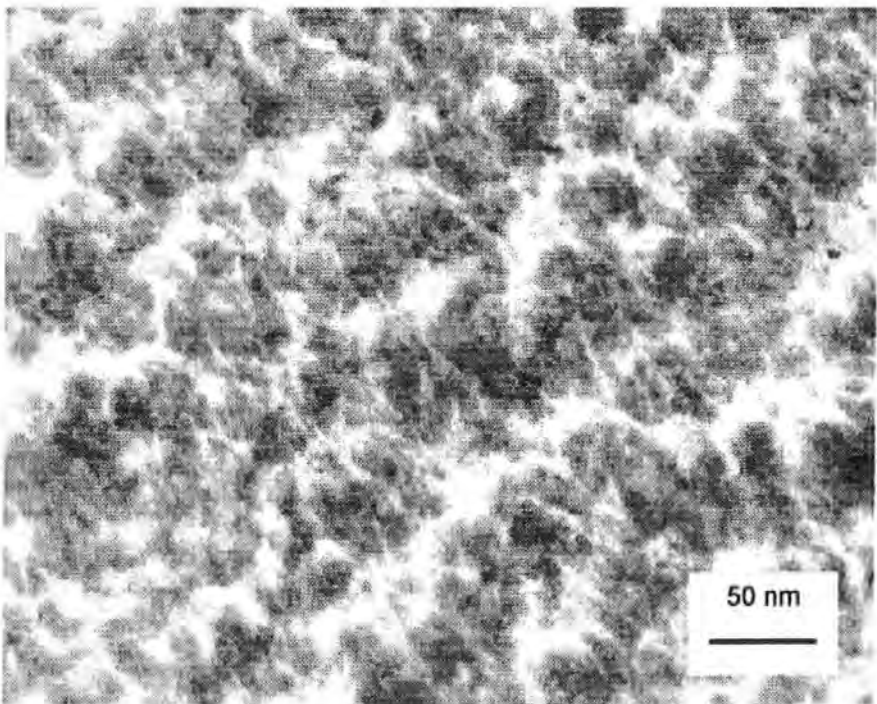


(b) 40 nm Permalloy film.

Figure 4.2 The TEM bright field images showing the lateral grain size versus film thickness (the dark areas correspond to the crystalline grains of deposited film-'light' areas are amorphous)

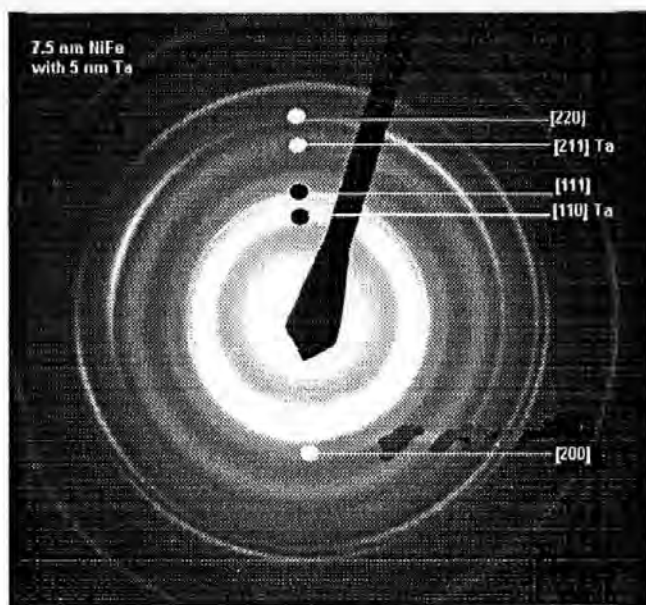


(a) with 5 nm Ta underlayer

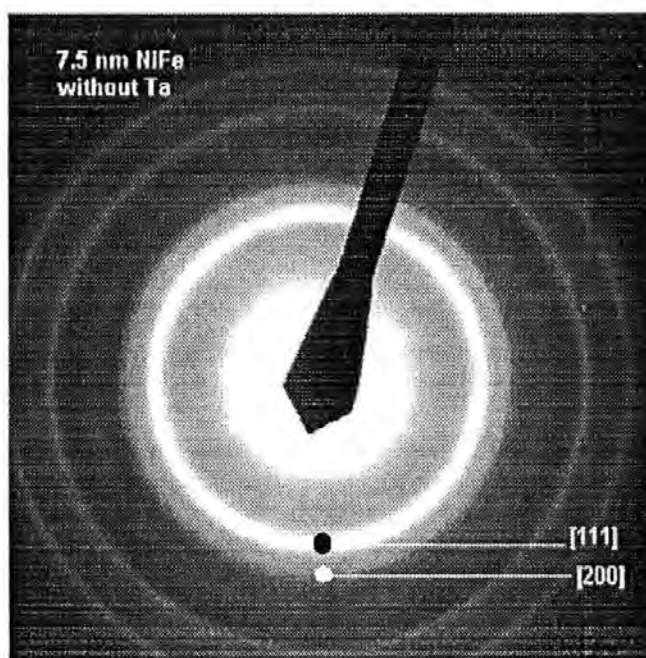


(b) with 5 nm Cr underlayer

Figure 4.3 The TEM bright images for 40 nm Permalloy thin films with same thickness ( 5 nm) Ta and Cr underlayer deposited in the same condition (the dark areas correspond to the crystalline grains of deposited film -'light' areas are amorphous)



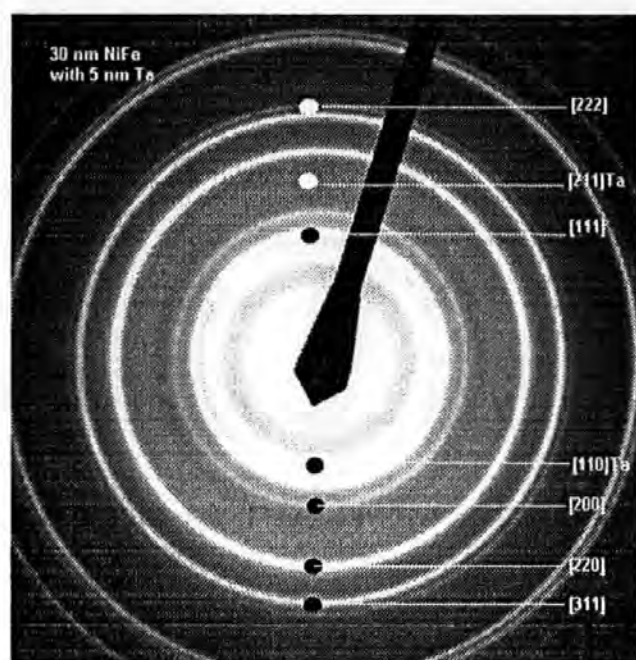
(a) with 5 nm Ta underlayer



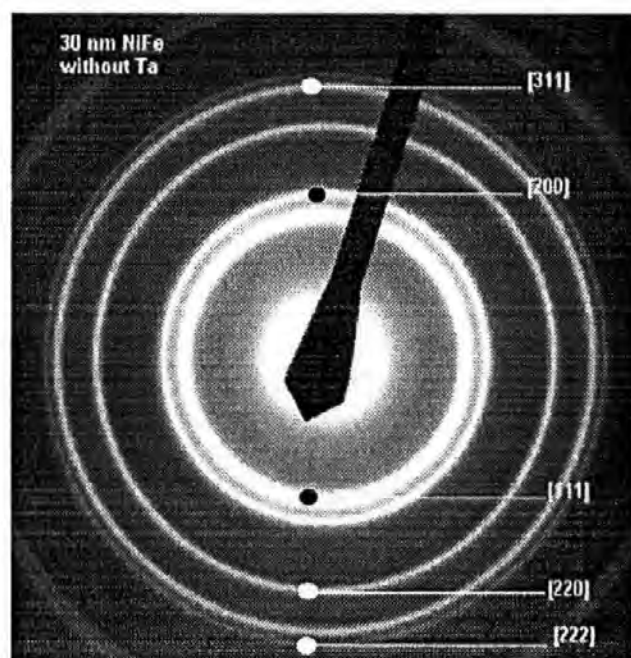
(b) without Ta underlayer

Figure 4.4 Electron Diffraction Patterns of 7.5 nm  $\text{Ni}_{81}\text{Fe}_{19}$  thin films





(a) with 5 nm Ta underlayer



(b) without Ta underlayer

Figure 4.5 Electron Diffraction Pattern of 30 nm  $\text{Ni}_{81}\text{Fe}_{19}$  films

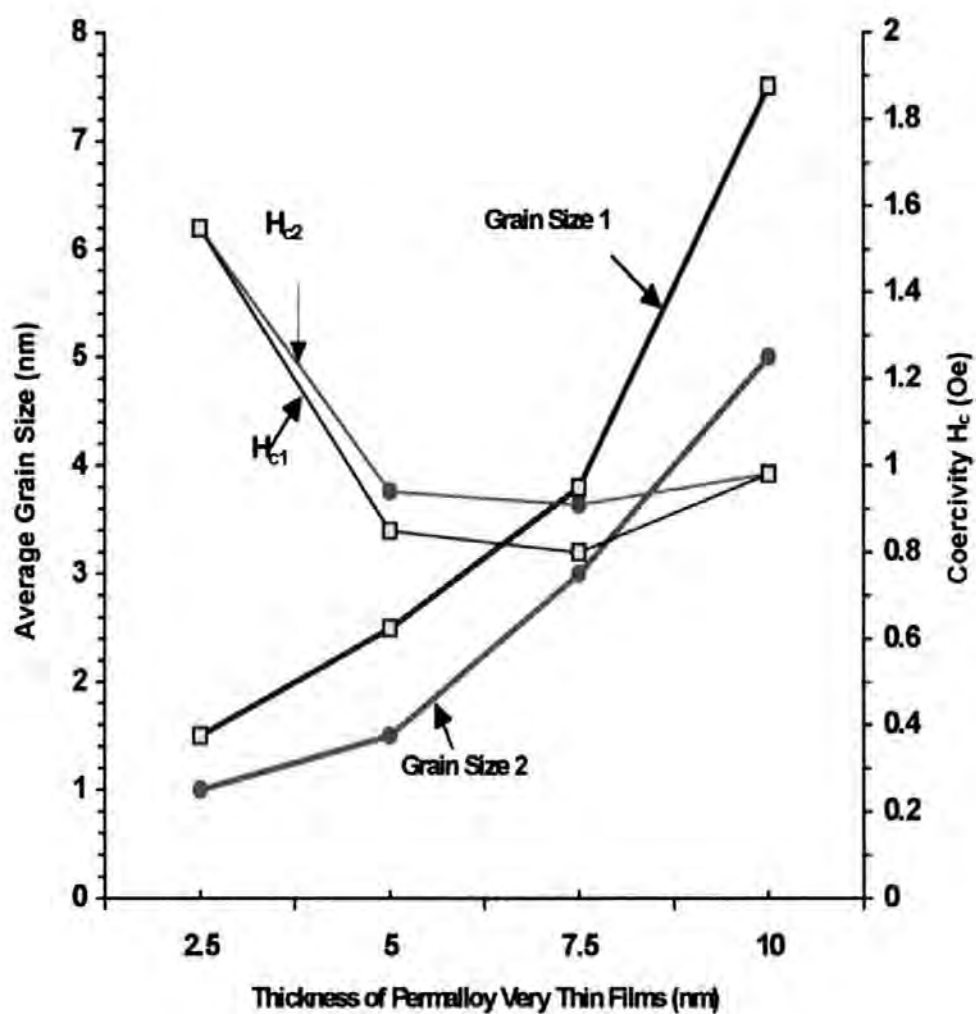


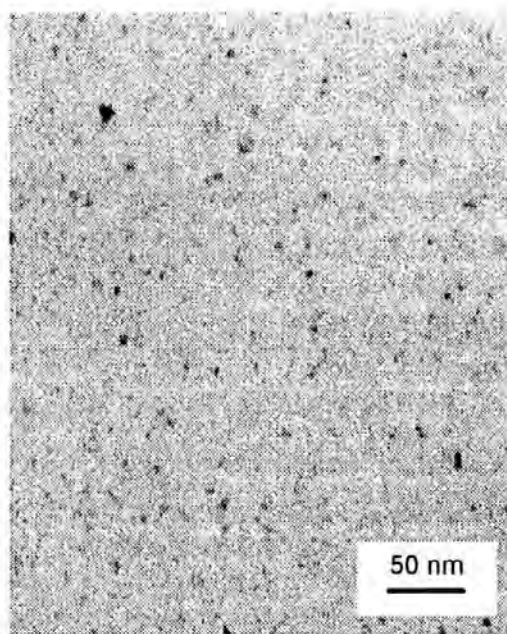
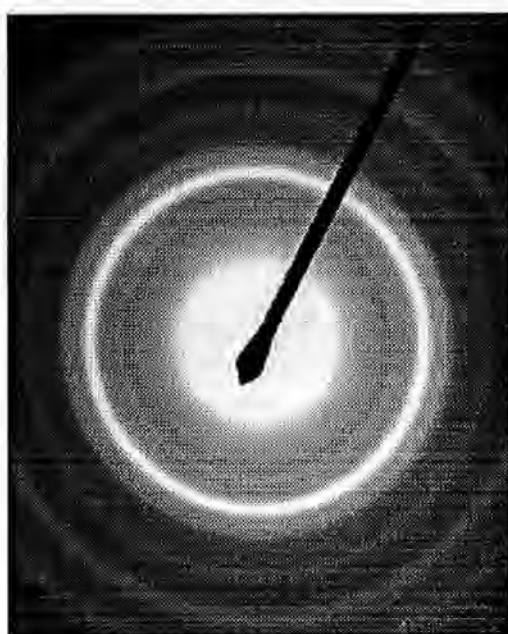
Figure 4.6, Coercivity verse grain size as a function of thickness.

(after [Ma, 1996])

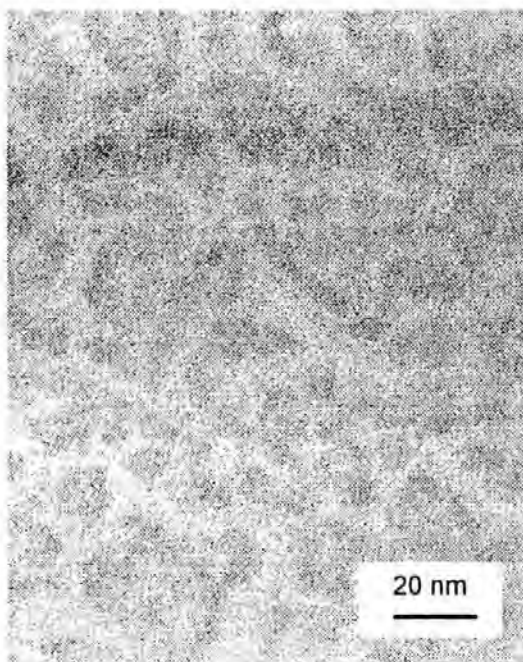
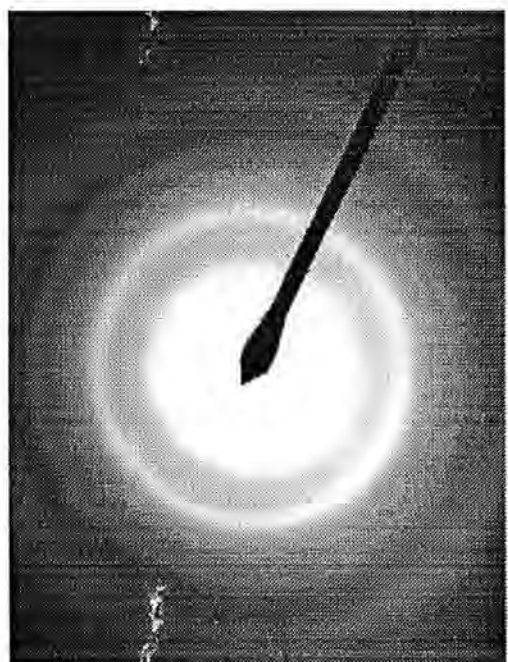
Set one for  $\text{Ni}_{81}\text{Fe}_{19}$  film deposited at about  $300^{\circ}\text{C}$ .

Set two for  $\text{Ni}_{81}\text{Fe}_{19}$  film deposited at  $20^{\circ}\text{C}$ .



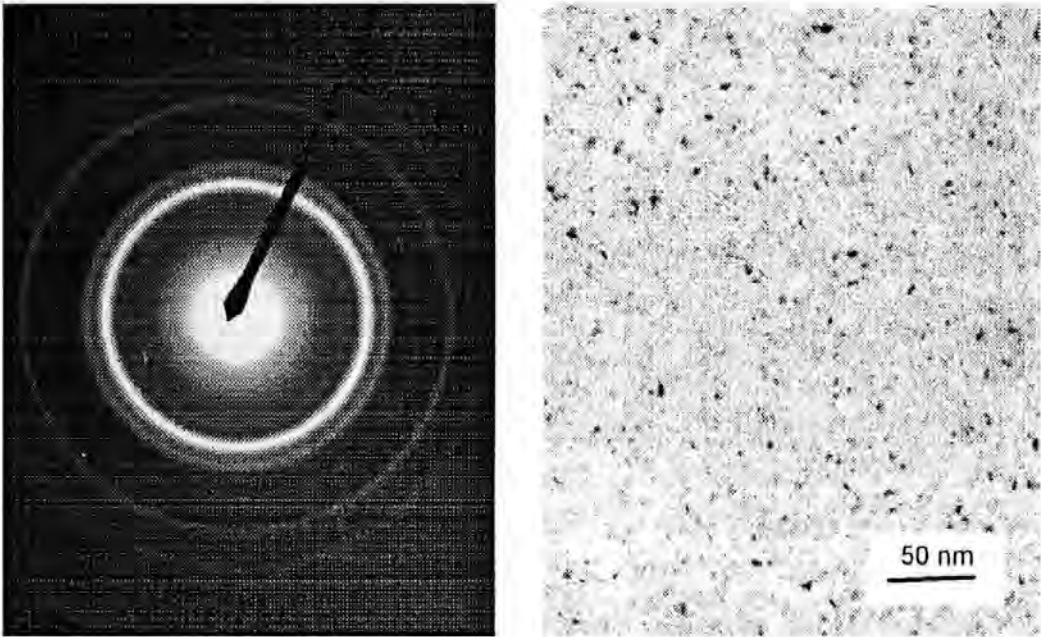


(a) deposited at 300°C

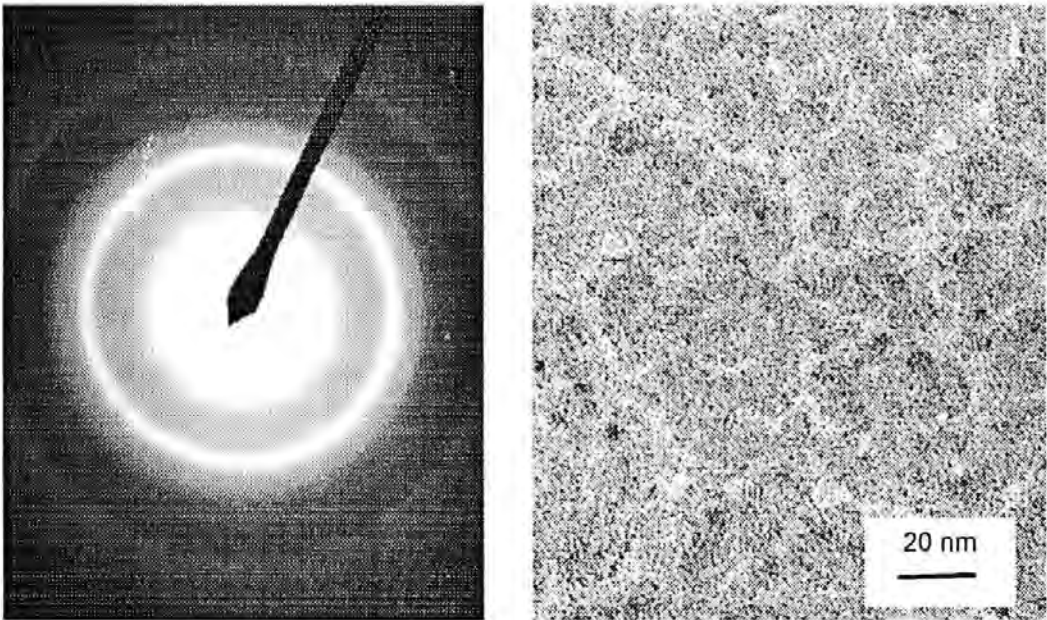


(b) Deposited at 20 °C

Figure 4.7 TEM bright field images and Electron Diffraction Patterns for 2.5 nm  $\text{Ni}_{81}\text{Fe}_{19}$  films

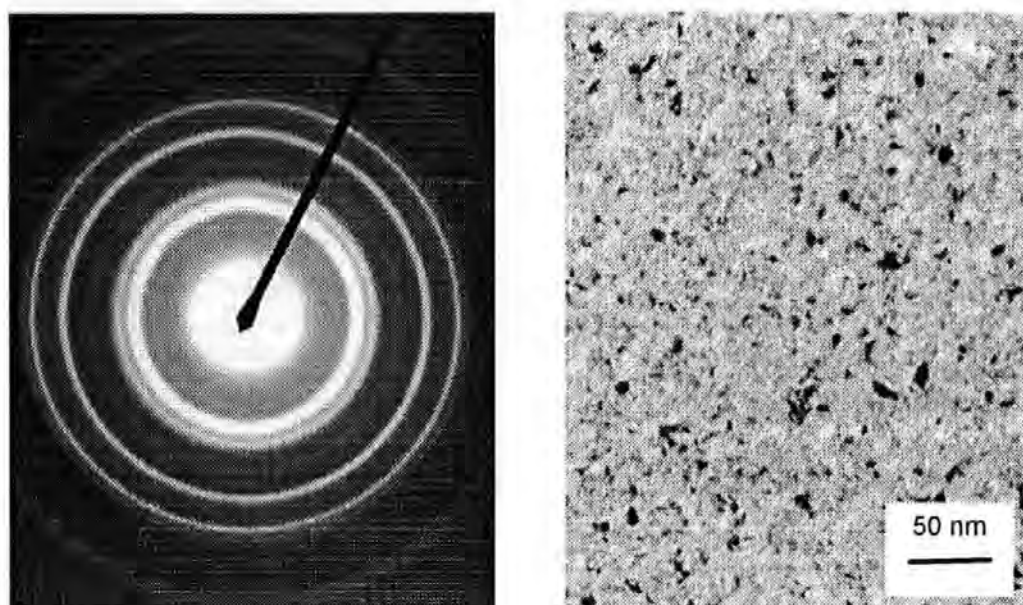


(a) Deposited at 300°C

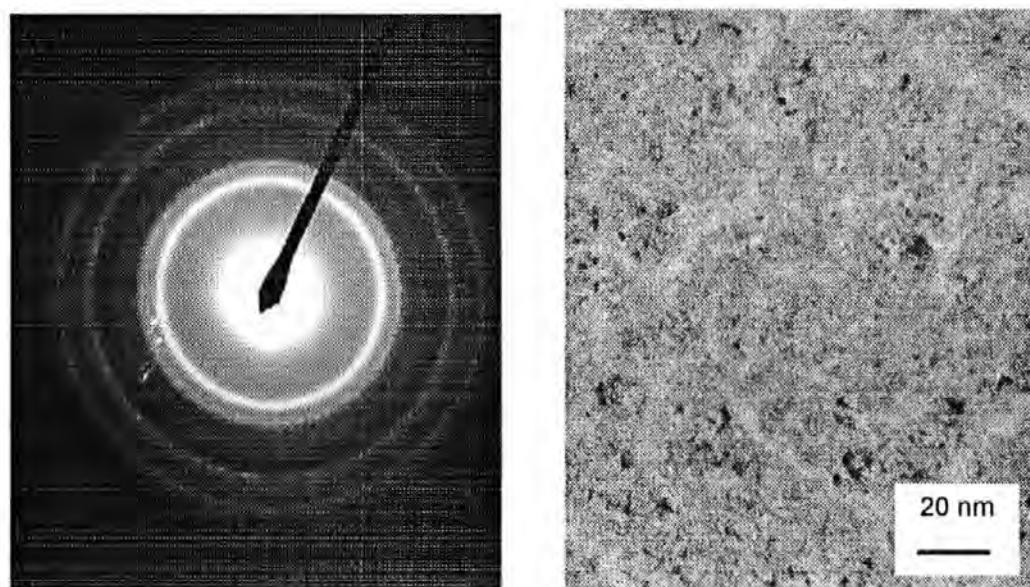


(b)deposited at 20°C .

Figure 4.8 TEM bright field images and Electron Diffraction Patterns  
for 5 nm  $\text{Ni}_{81}\text{Fe}_{19}$  films

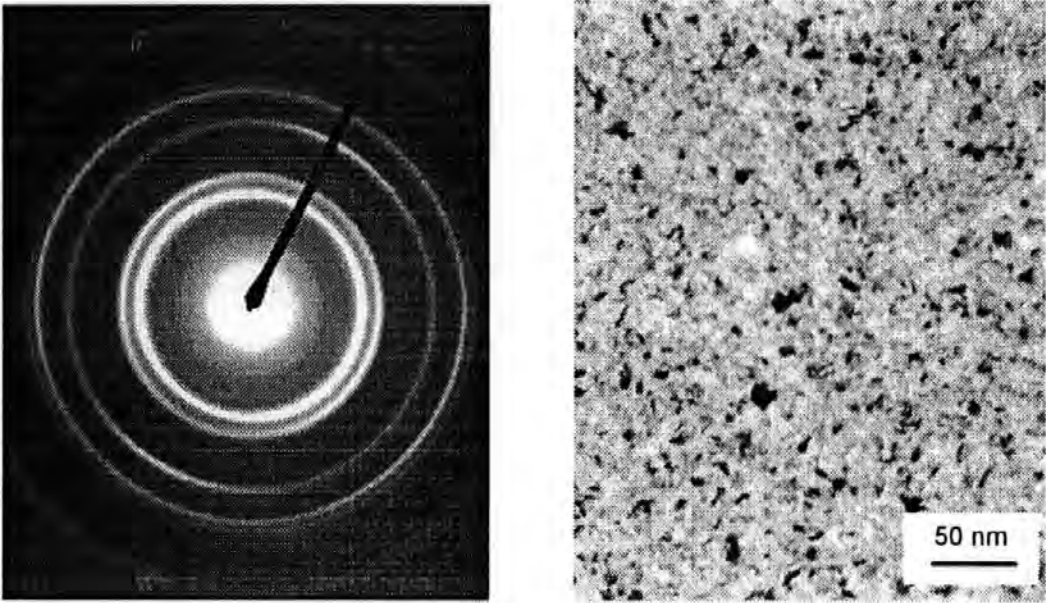


(a) Deposited at 300°C

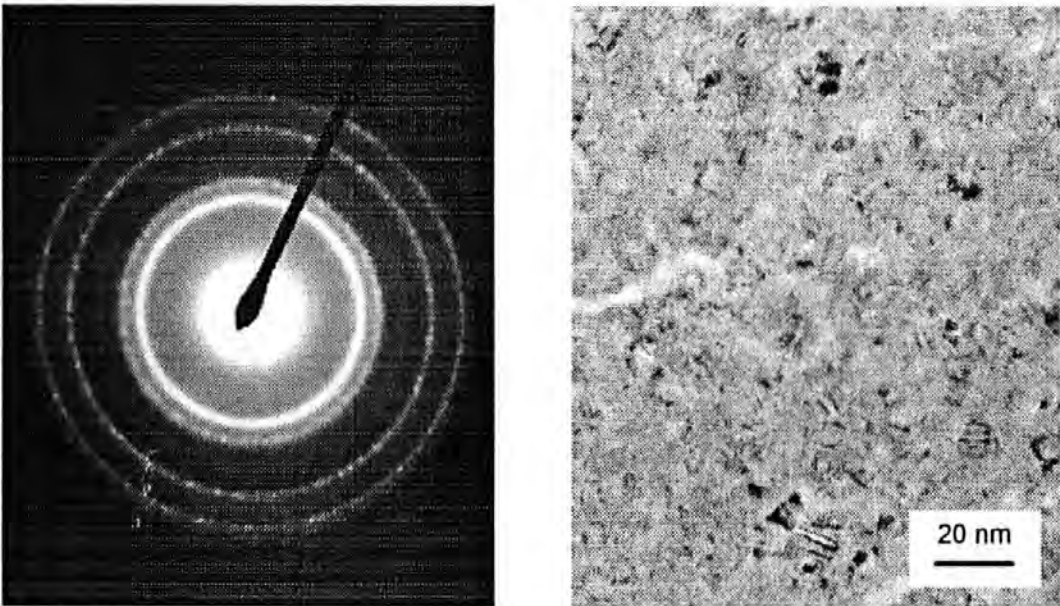


(b) deposited at 20°C

Figure 4.9 TEM bright field images and Electron Diffraction Patterns for 7.5 nm  $\text{Ni}_{81}\text{Fe}_{19}$  films



(a) deposited at about 300°C,



(b) deposited at 20°C

Figure 4.10 TEM bright field images and Electron Diffraction Patterns  
for 10 nm  $\text{Ni}_{81}\text{Fe}_{19}$  films



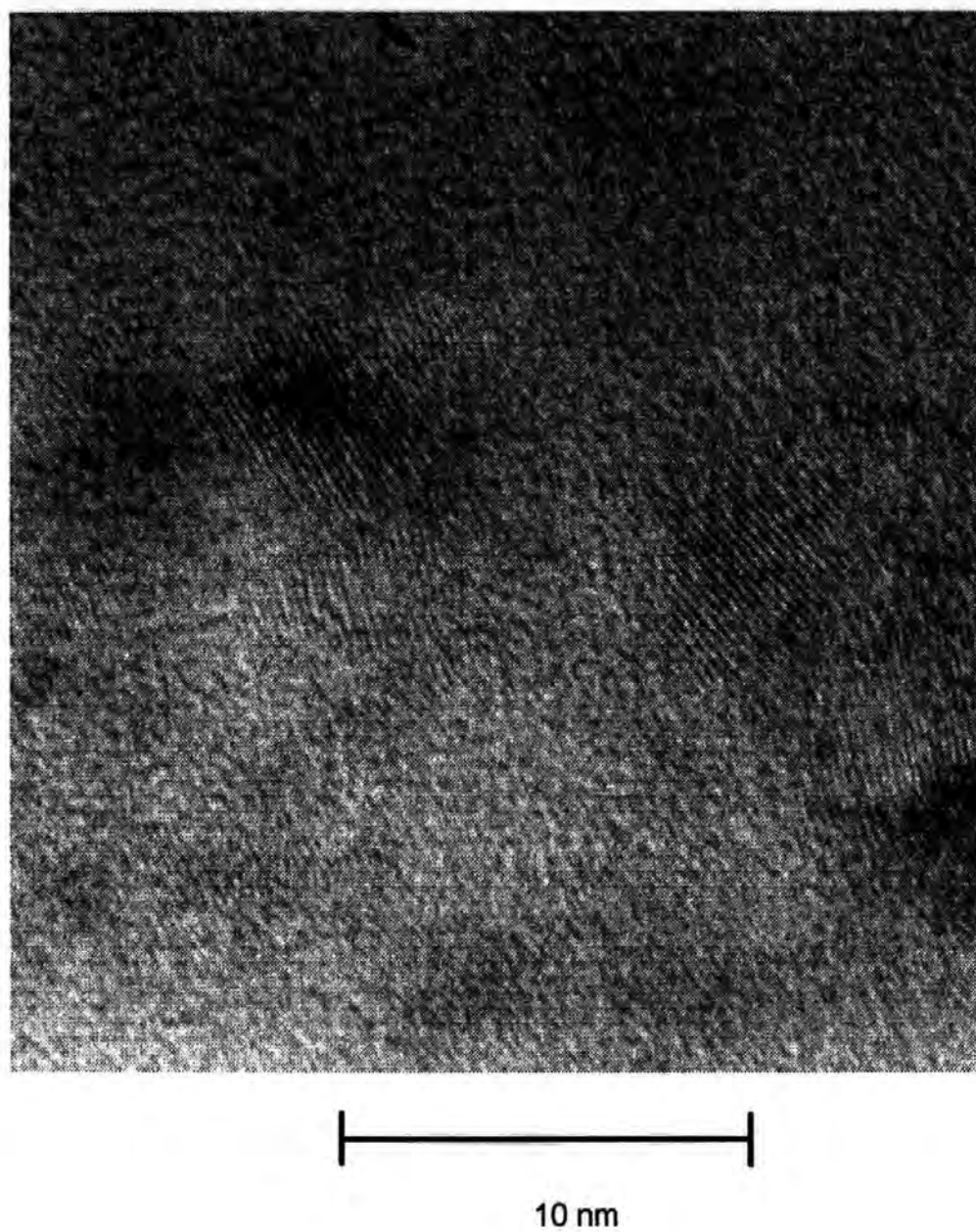


Figure 4.11 High magnification TEM image of 10 nm  $\text{Ni}_{81}\text{Fe}_{19}$  thin film

#### 4.1.2 Magnetic domains

Earlier experimental results for  $\text{Ni}_{81}\text{Fe}_{19}$  films (section 4.1.1.1) show that there is a minimum coercivity at a thickness of 7.5 nm. The main sources of coercivity in magnetic thin films are rotation against magnetic anisotropy, domain nucleation and wall pinning. In order to obtain more insight into the behaviour of the coercivity in this most interesting range, magnetic domain observations by Lorentz TEM were carried out.

##### 4.1.2.1 Domains in very thin $\text{Ni}_{81}\text{Fe}_{19}$ film

Lorentz TEM studies of  $\text{Ni}_{81}\text{Fe}_{19}$  films with thicknesses in the range from 30 to 100 nm have been reported by many researchers such as [Pruett, 1964] [Middelhoek, 1961 and 1963], [Lo and Hanson, 1969]. However, sample thickness was smaller in this study. The films were observed at 400 kV in a JEOL 4000 EX TEM at the Department of Materials, University of Oxford. An applied field varying over a range of  $\pm 380$  Oe (30.21 k A/m) was employed during observation. Most magnetic domain images presented here are approximately 25  $\mu\text{m}$  in diameter and all using Fresnel image mode.

The preparation of specimens was the same as described in section 3.3.1.1. Two sets of specimens of  $\text{Ni}_{81}\text{Fe}_{19}$  films (2.5, 5, 7.5 and 10 nm) were prepared for this observation.

The films were directly deposited on a Cu grid with a formvar support film.

In the second case, films were deposited on glass or mica substrates (at about 300°C) with  $\sim 80$  nm carbon underlayer. Specimens were prepared at Oxford University and obtained from the larger pieces. The quality of the specimens was poor with high structural contrast making it quite difficult to see the magnetic contrast. In this case, the

#### *Chapter 4: Results and Discussion*

angle of zero degrees of the applied field in the microscope corresponded to this field being applied parallel to the easy axis of the sample [Petford-Long, 1996].

- 2.5 nm films

The first sample (2.5 nm thick) film did not show any clear magnetic contrast at all. The second one showed magnetisation ripple perpendicular to the anisotropy easy direction. There were no domain walls visible in this case [Petford-Long, 1996].

- 5.0 nm films

The first of 5 nm film sample was with very low magnetisation, and magnetic contrast was only seen at near zero to a few Oe fields. Very fine and fuzzy domain walls (like ripple) were seen at a field of 5 Oe (400 A/m). These were very unstable and the sample was almost saturated at a field of about 6.5 Oe (520 A/m). In the second sample case, the film also shows uniaxial anisotropy with an easy direction in which the domain (ripple) is at a direction perpendicular to this. When a magnetic field was applied, a sudden change in contrast was seen but it was not possible to observe a moving domain wall [Petford-Long, 1996].

- 7.5 nm films

In the first 7.5 nm film, magnetic domains can be more clearly seen and the film saturated at a field of  $\pm 46$  Oe (or 3.68 k A/m). Figure 4.12 (a) and (b) shows domain wall images and the saturation state. In the second sample case, the film also shows uniaxial anisotropy with an easy direction whose domain (ripple) is in a direction perpendicular to this (but still in the plane of the film). The ripple rotates and suddenly changes in contrast but no domain wall was seen [Petford-Long, 1996].



- 10 nm films

In the 10 nm film, the specimen showed very strong magnetic contrast with domains clearly seen in the 'as grown' state. Figure 4.13 (a) shows a domain wall's image in a 10 nm film at zero field. Figure 4.13 (b) shows a domain wall image in a 10 nm film at a field of 7.5 Oe (600 A/m). There was a slight increase in ripple contrast near zero field which gradually strengthened until at a field of between 6 and 7.5 Oe (480 and 600 A/m) domain walls suddenly formed. The saturation field was at about 28 Oe (2.24 kA/m). For the second sample, no clear anisotropy was seen [Petford-Long, 1996].

The observation results indicated that visible domains and domain walls in very thin  $\text{Ni}_{81}\text{Fe}_{19}$  films cannot be observed below a critical thickness such as 5 nm, due to weak magnetic contrast (image contrast). This is also strongly dependent on specimen quality and preparation method.

In such thin films, magnetic domains show fine ripple with thin walls of irregular shape and closely spaced. The domain magnetisation is in a direction usually perpendicular to the ripple axis (90 or 180° domain) and still in the film plane. The magnetisation of domains seems to vary in angle from 90° to 180°. Domain walls seem very unstable and will be suddenly formed or disappear with a small change of applied field. Domain structure and domain walls can be more clearly seen above thicknesses of 7.5 nm. The results suggest that the domains of  $\text{Ni}_{81}\text{Fe}_{19}$  permalloy films in this range seem to be of Néel wall type only with in-plane magnetisation and no cross-tie walls [Petford-Long, 1996].

#### 4.1.2.2 Ta underlayer effect

One set of  $\text{Ni}_{81}\text{Fe}_{19}$  films with 5 nm Ta underlayer thickness was prepared for Lorentz TEM observation. The thickness of permalloy films was in the range from 2.5 nm to 100 nm. Five of these samples, with thicknesses at 5, 7.5, 10, 15 and 30 nm, were selected for examination. All results reported here are taken from experimental data recorded by [Doole, 1997].

- Domain structure and magnetisation

Magnetic domains and walls have been observed for each thickness (including for 5 nm thick permalloy). Figures 4.14 to 4.18 show the initial images of magnetic domain structure in each sample, which were obtained at zero field.

As can be seen from these images, the structure and shape of domains and domain walls seem quite different with those of films deposited without Ta underlayer.

In the 5.0 nm film, the grown film has very faint ripple contrast but no domain wall can be seen (see Figure 4.14), but the domain wall can be found when applying a field (see Figure 19). The records show that the domain wall in this case is less stable and easily changed by the very small field. Figure 4.20 is three images showing the domain magnetisation, which rotates through  $90^\circ$  across the wall. The change of value of applied field between each image is only about 0.356 Oe or 28.3 A/m. The field required to rotate the film magnetisation to 90 degrees is about 2.5 Oe or 200 A/m.

In the 7.5 nm thick film, domains are well defined with straighter and wider walls (see Figure 4.15). The domain wall width is approximately 300 nm. The size of the domain is

quite large-it may be over  $100\ \mu\text{m}^2$ . A field of about 4.3 Oe or 342 A/m is required to rotate the film magnetisation to  $90^\circ$ .

The 'as-grown' film has clear walls with very large domains as shown in Figure 4.16 for a 10 nm permalloy film. There are some pinned walls in this film and these can remain up to 128 Oe of applied field. The field required to rotate magnetisation through  $90^\circ$  in this case, is about 10 Oe or 800 A/m. In some areas, the ripple seems to rotate through  $150^\circ$  without any domain walls forming. In an area with stronger defects, the domain magnetisation process has been observed. Ripple is rotated within a domain and starts to break up into 'Vee' ripples after which a definite domain is formed as shown in Figure 4.21 (a). The walls then start rotating in the outer domains with increasing applied fields (see Figure 4.21 b). The direction of magnetisation will be changed by some angle when the walls meet defects (see Figure 4.21 c) during this time. Ripple still rotates within domains with increasing applied field, but domain walls eventually cancel each other until only ripple is left (see Figure 4.21 d). The remaining ripple rotates until magnetisation is aligned with applied field.

The initial domain and domain wall images for a 15 nm Permalloy film with 5 nm Ta underlayer are shown in Figure 4.17. The shape and structure of domains in this case is similar to that for 10 nm film. The field required to rotate magnetisation  $90^\circ$  is about 15.7 Oe or 1255 A/m. No cross-tie walls were found in this film.

In 30 nm thick permalloy films with 5 nm Ta underlayers, large domains and some cross-tie walls have been observed in zero field as shown as Figure 4.18. It was found that there are more cross-tie walls near a 'bent' area in the main domain wall. Cross-ties near a bend in a wall are shown in Figure 4.22. The domain wall is still quite wide and

#### *Chapter 4: Results and Discussion*

about 300 to 350 nm. The field required to rotate magnetisation  $90^\circ$  is about 13.9 Oe or 1110 A/m.

- **Comparing with films without Ta**

To compare with permalloy films without Ta underlayer, two Permalloy film samples, 7.5 nm and 30 nm thick respectively, were examined by Lorentz TEM.

In 7.5 nm films without Ta, there was no clear domain wall found. The domains have many fine ripples with irregular shape as shown in Figure 4.23. The field needed to change the ripple and rotate the ripple  $90^\circ$  to the original direction is about 14.3 Oe or 1144 A/m. The magnetisation in the film changed suddenly.

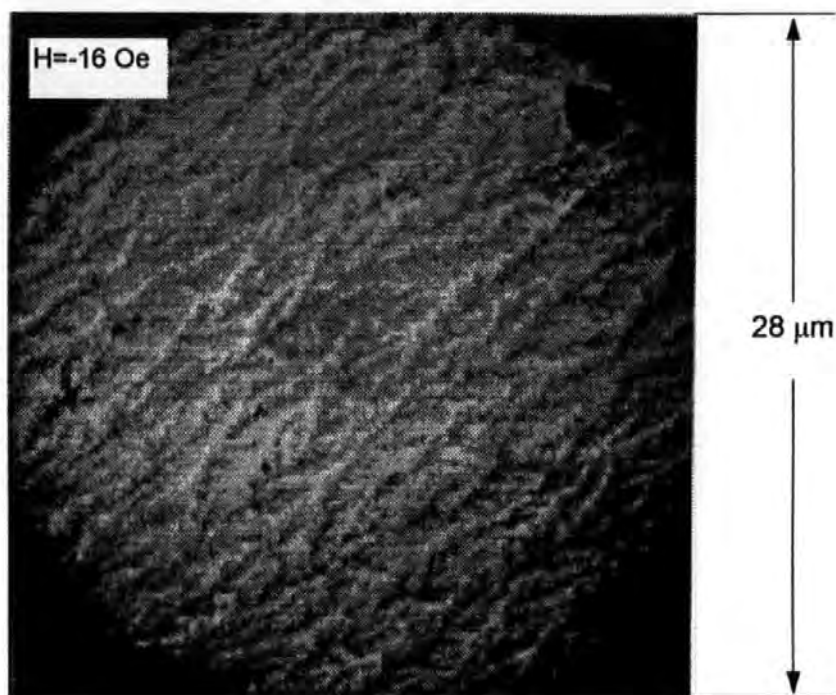
Larger domains and a clearly defined domain wall (see Figure 4.24) were observed in 30 nm permalloy films without Ta underlayers. The domain walls are very thin, say less than 100 nm. They are irregular, are closely spaced and have cross-ties. The domain magnetisation in adjacent domains varies in angle from  $90^\circ$  to  $180^\circ$  and with strong rippling. The field required to rotate domain walls  $90^\circ$  to the original direction is around 14.3 Oe or 1144 A/m, similar to the 7.5 nm film. This varied sometimes for different observations.

Typical magnetic domain wall images for 7.5 nm and 30 nm with and without Ta underlayer are shown in Figures 4.25 and 4.26 respectively. The domain structure and walls are very different in both cases.

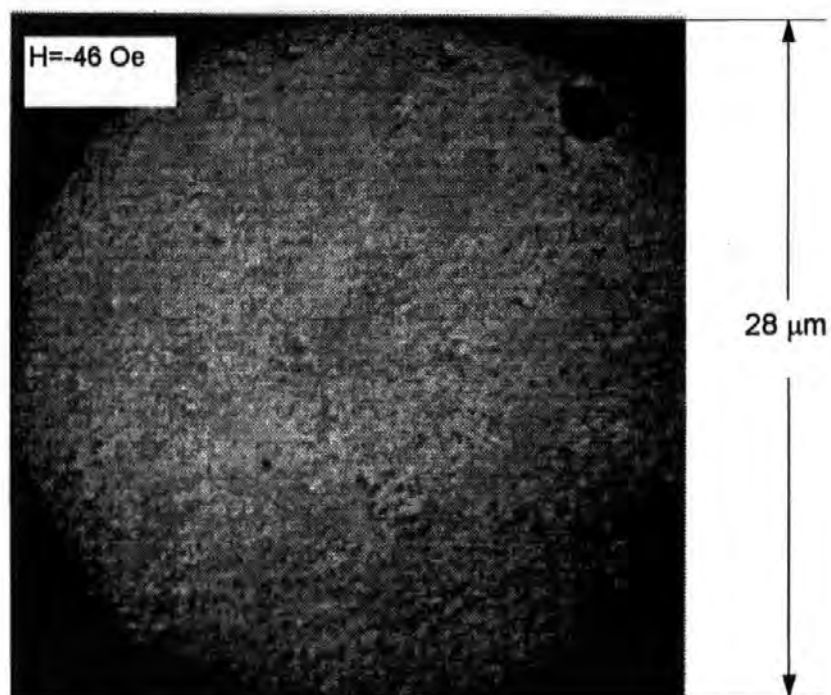
Table 4.3 is a simple comparative summary of the main differences in the permalloy films deposited with or without Ta underlayer.

Table 4.3 Domain structure and magnetisation properties observed in Permalloy films deposited with and without a 5 nm Ta underlayer

Sample	7.5 nm Ni <sub>81</sub> Fe <sub>19</sub> / 5 nm Ta	7.5 nm Ni <sub>81</sub> Fe <sub>19</sub>	30 nm Ni <sub>81</sub> Fe <sub>19</sub> / 5 nm Ta	30 nm Ni <sub>81</sub> Fe <sub>19</sub>
Domain shape	large and regular, definite	fine, closely spaced, irregular and hard to see	large, definite, regular, a few cross-ties	closely spaced, irregular, many cross-ties
Domain size	may be over 100 $\mu\text{m}^2$	may be a few $\mu\text{m}^2$	may over 100 $\mu\text{m}^2$	varied from 10 to over 100 $\mu\text{m}^2$
Domain wall width	about 300 nm	may be a few tens nm	may over 300 nm	around 100 nm
Domain magnetisation	domain rotates through 90° across the wall domains formed suddenly	ripple rotates with strong rippling effect. Unstable	ripple rotates and splits into V-shape and then rotates within domain through 90° across the wall. Walls may cancel each other and form a new domain	strong ripple starts to split into a 'V-shape'. Magnetisation in adjacent domains varies in angle from 90° to 180° to form domains with a jumping effect
The field for 90° magnetisation	about 340 A/m	about 1144 A/m	about 1104 A/m	about 1144 A/m



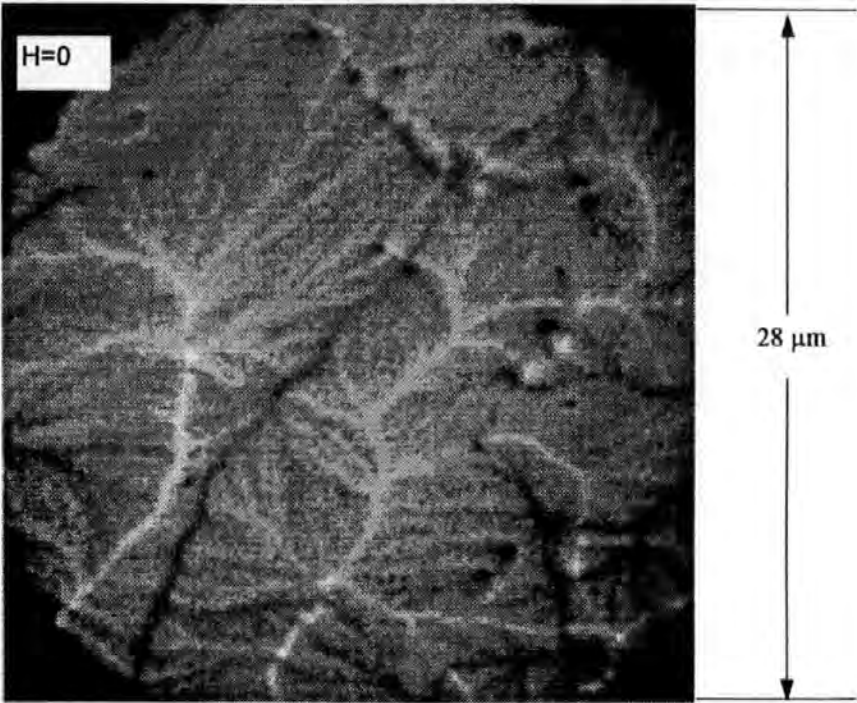
(a) domains



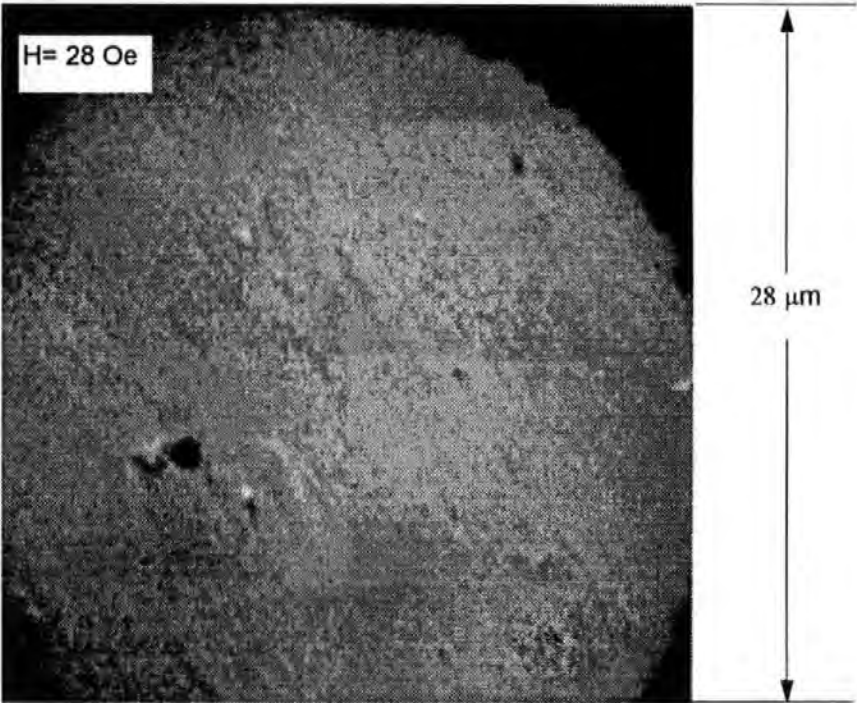
(b) saturation state

Figure 4.12 Magnetic domains in a 7.5 nm  $\text{Ni}_{81}\text{Fe}_{19}$  thin film





(a) domains



(b) saturation state

Figure 4.13 Magnetic domains in an 10 nm  $\text{Ni}_{81}\text{Fe}_{19}$  film



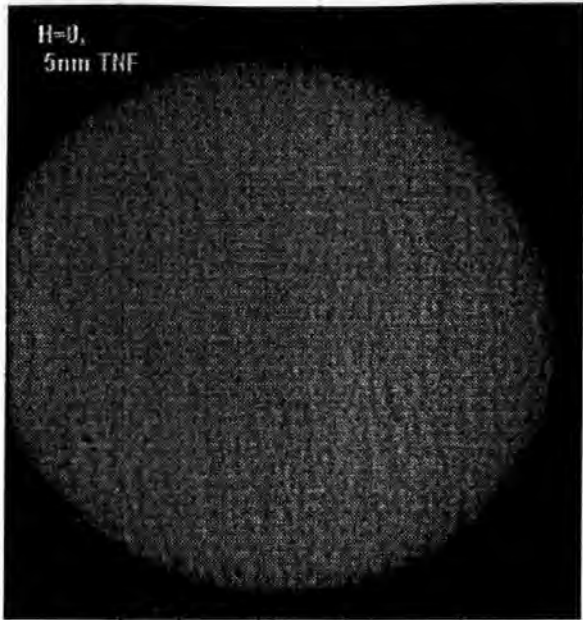


Figure 4.14 Lorentz TEM initial image for 5 nm  $\text{Ni}_{81}\text{Fe}_{19}$  film with 5 nm Ta underlayer at zero field ( $H_0=0$ ) and the average diameter of image is 25  $\mu\text{m}$ .

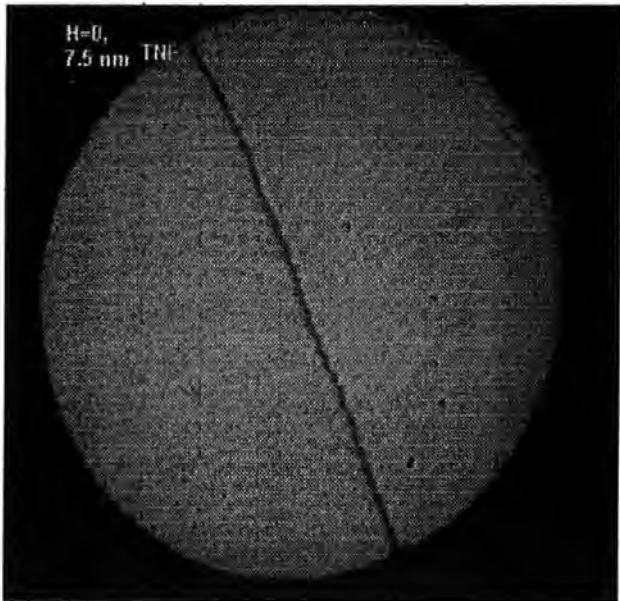


Figure 4.15 Lorentz TEM initial image for a 7.5 nm  $\text{Ni}_{81}\text{Fe}_{19}$  film with a 5 nm Ta underlayer at zero field ( $H_0=0$ ) and the average diameter of image is 25  $\mu\text{m}$ .

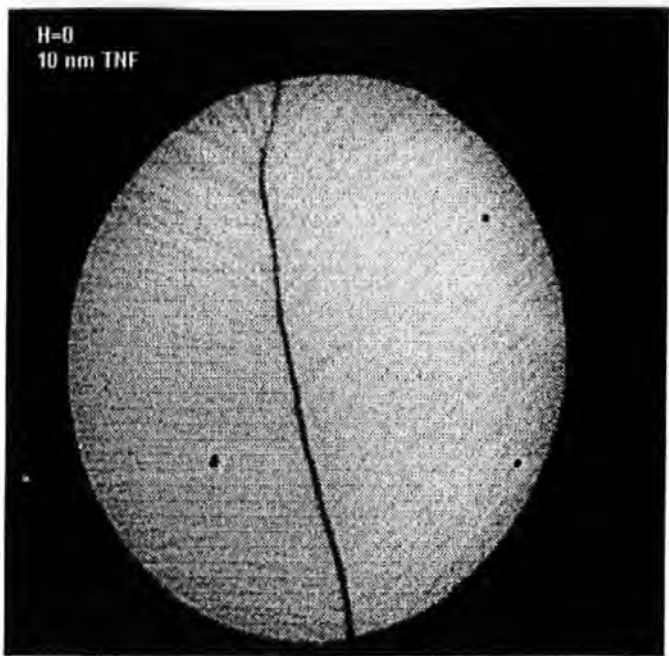


Figure 4.16 Lorentz TEM initial image for an 10 nm  $\text{Ni}_{81}\text{Fe}_{19}$  film with a 5 nm Ta underlayer at zero field ( $H_0=0$ ) and the average diameter of image is 25  $\mu\text{m}$ .

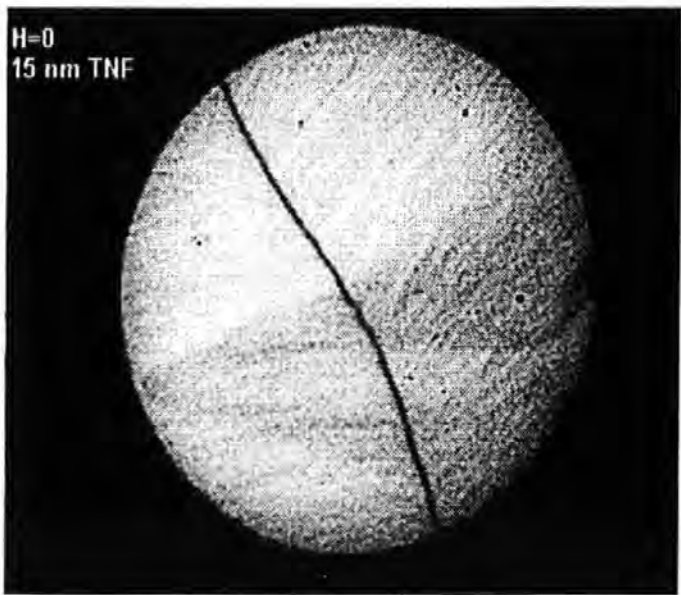


Figure 4.17 Lorentz TEM initial image for an 15 nm  $\text{Ni}_{81}\text{Fe}_{19}$  film with a 5 nm Ta underlayer at zero field ( $H_0=0$ ) and the average diameter of image is 25  $\mu\text{m}$ .

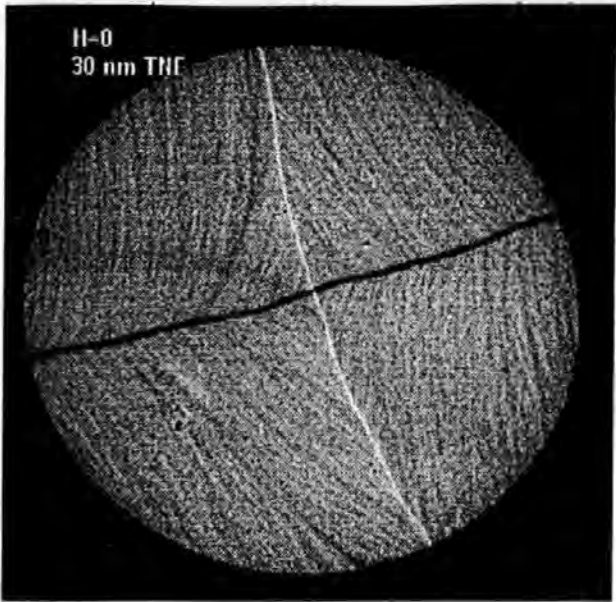


Figure 4.18 Lorentz TEM initial image for a 30 nm  $\text{Ni}_{81}\text{Fe}_{19}$  film with a 5 nm Ta underlayer at zero field ( $H_0=0$ ) and the average diameter of image is 25  $\mu\text{m}$ .

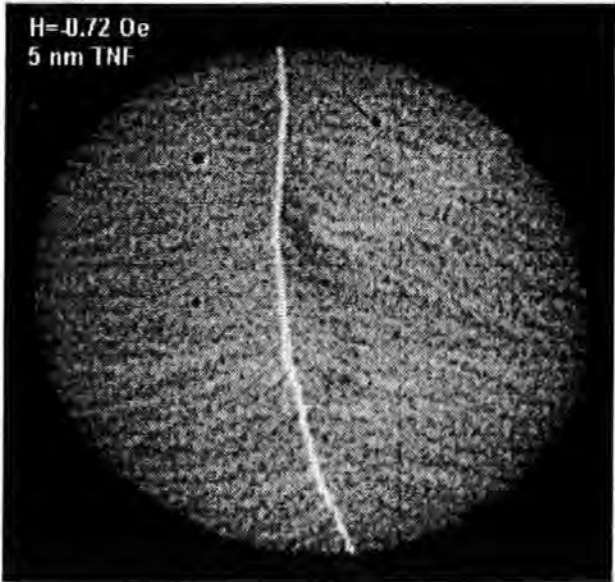
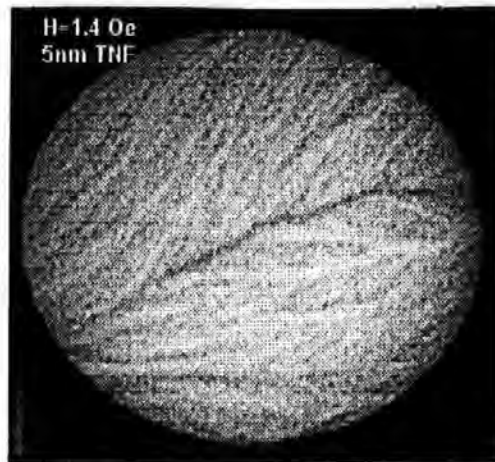


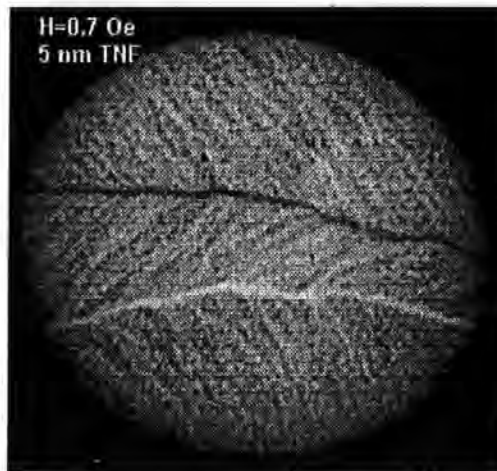
Figure 4.19 Magnetic domains exist in a 5 nm  $\text{Ni}_{81}\text{Fe}_{19}$  film with a 5 nm Ta underlayer at an applied field of - 0.72 Oe (-57 A/m) and the average diameter of image is 25  $\mu\text{m}$ .



(a) Showing walls at  $H_a = 1.4$  Oe or 112 A/m



(b) Showing domain walls at  $H_a = 1.1$  Oe or 84 A/m



(c) Showing 'jumped' walls, large domain overall area recorded at  $H_a = 0.7$  Oe or 56 A/m.

Figure 4.20 Images showing domain movement in a 5 nm  $\text{Ni}_{81}\text{Fe}_{19}$  film with a 5 nm Ta underlayer and the average diameter of image is 25  $\mu\text{m}$ .

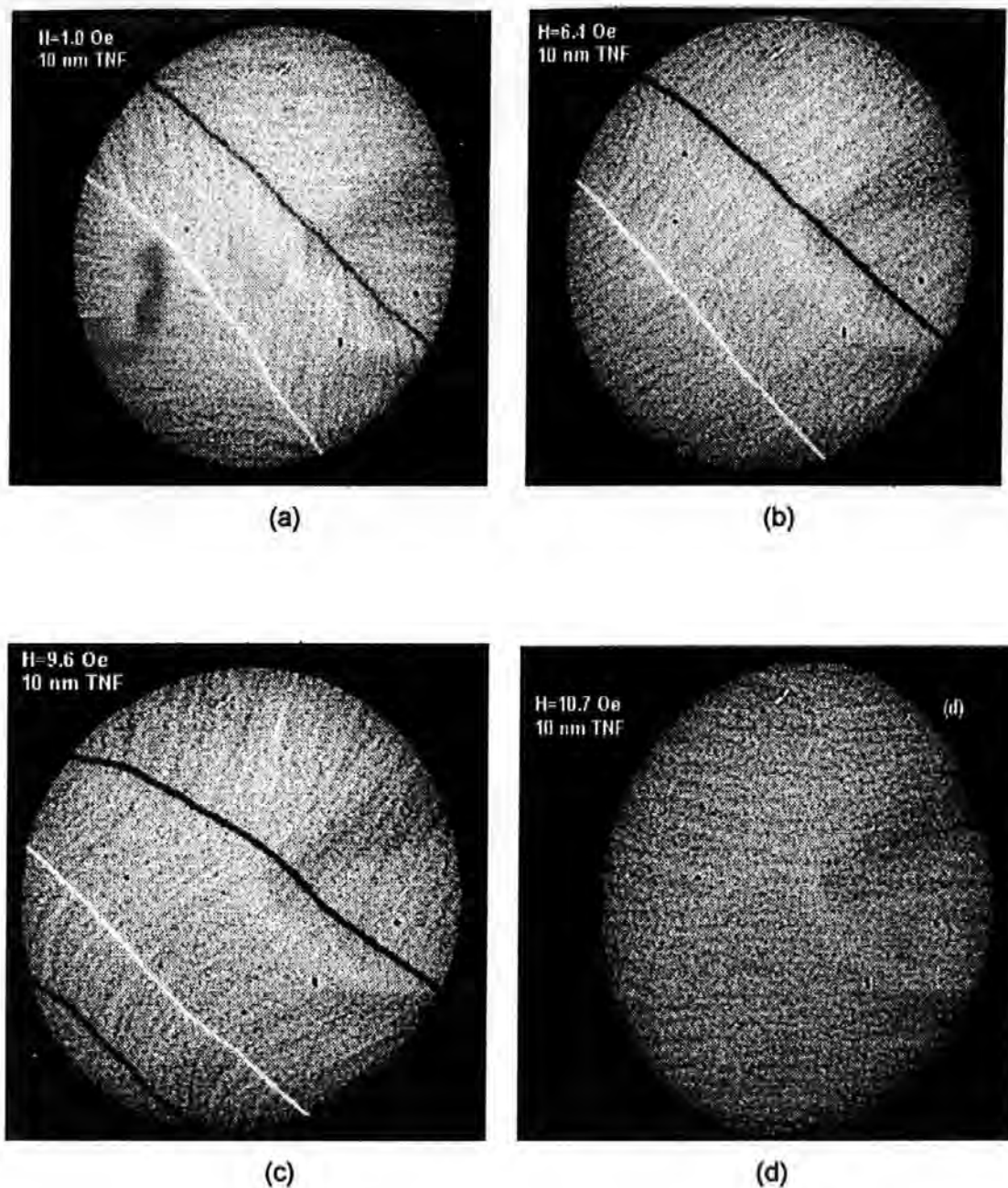


Figure 4.21 Images showing domain magnetisation in 10 nm  $\text{Ni}_{81}\text{Fe}_{19}$  / 5 nm Ta film and the average diameter of image is 25  $\mu\text{m}$ .

- (a) Domain walls at  $H_a = 1.75$  Oe or 140 A/m;
- (b) Rotated ripple in outer domain at  $H_a = 6.4$  Oe or 510 A/m;
- (c) Change in angle of magnetisation at  $H_a = 9.6$  Oe or 764 A/m
- (d) Ripple only and magnetisation aligned with applied field at 10.7 Oe or 800 A/m.

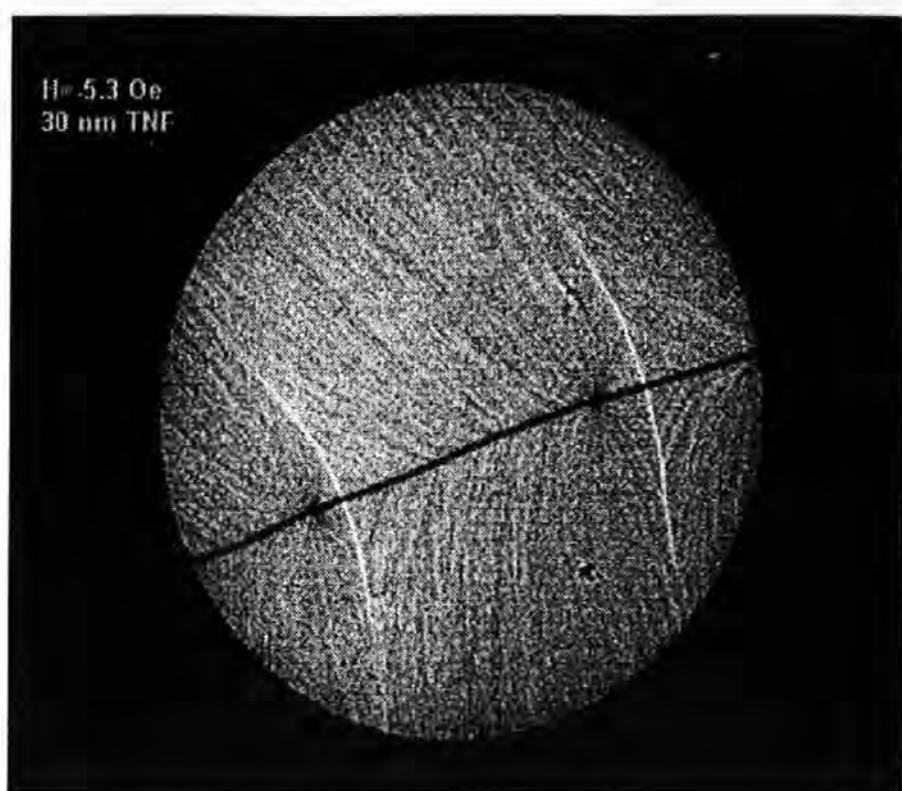


Figure 4.22 Image showing cross-tie domain walls in 30 nm  $\text{Ni}_{81}\text{Fe}_{19}$  film with 5 nm Ta underlayer near a bend in the wall and the average diameter of image is 25  $\mu\text{m}$ .



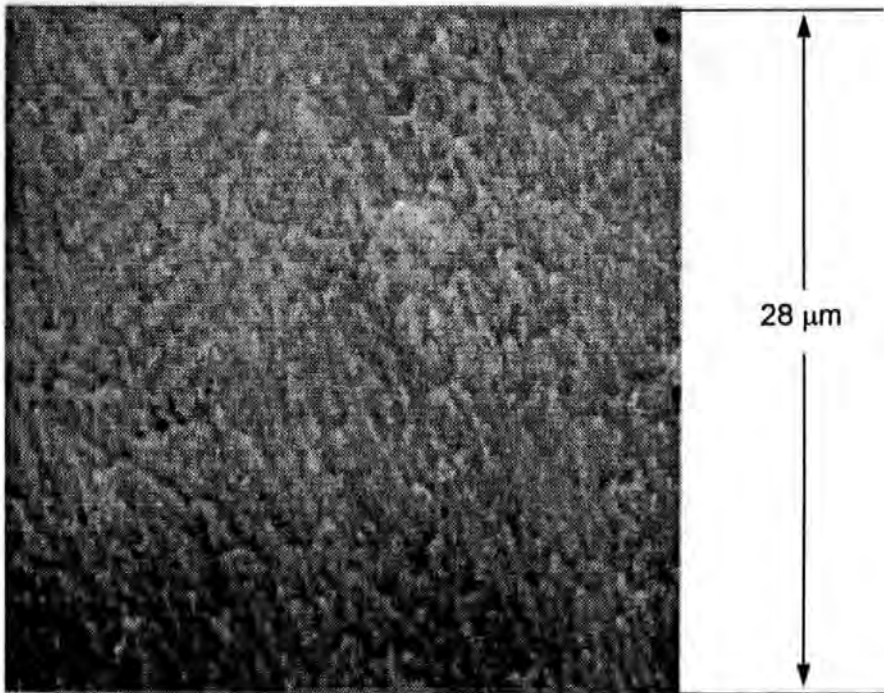


Figure 4.23 Lorentz TEM initial image for a 7.5 nm  $\text{Ni}_{81}\text{Fe}_{19}$  film without a 5 nm Ta underlayer at zero field ( $H_0=0$ )

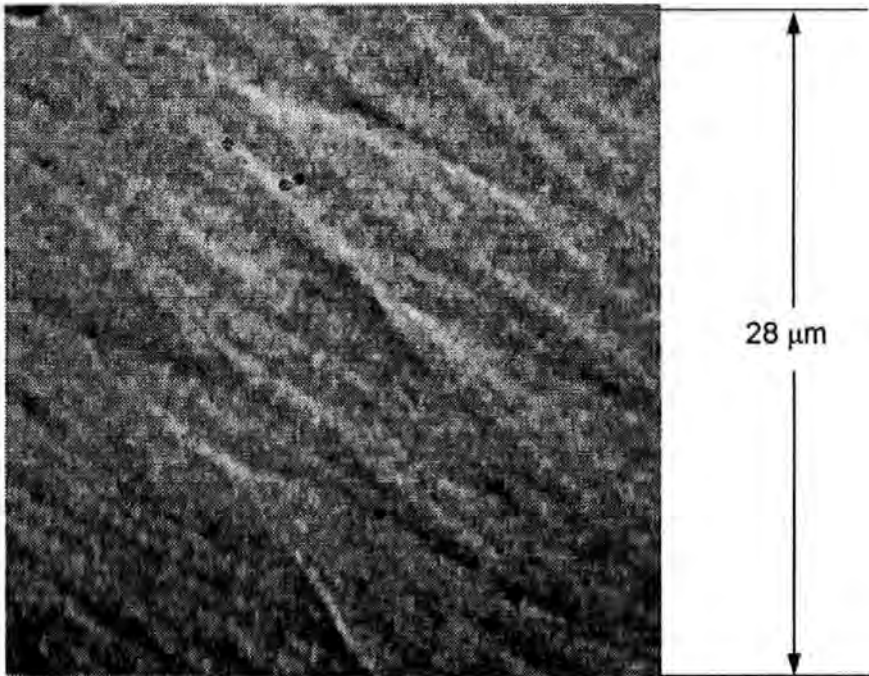
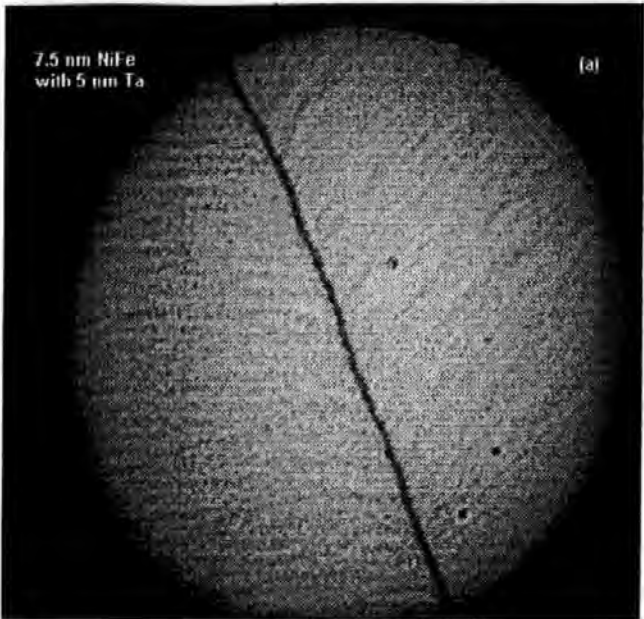
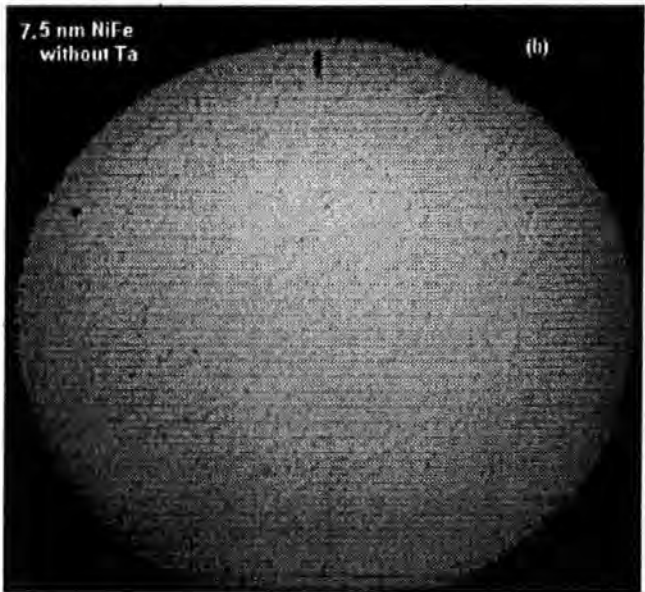


Figure 4.24 Lorentz TEM initial image for a 30 nm  $\text{Ni}_{81}\text{Fe}_{19}$  film without a 5 nm Ta underlayer at zero field ( $H_0=0$ )



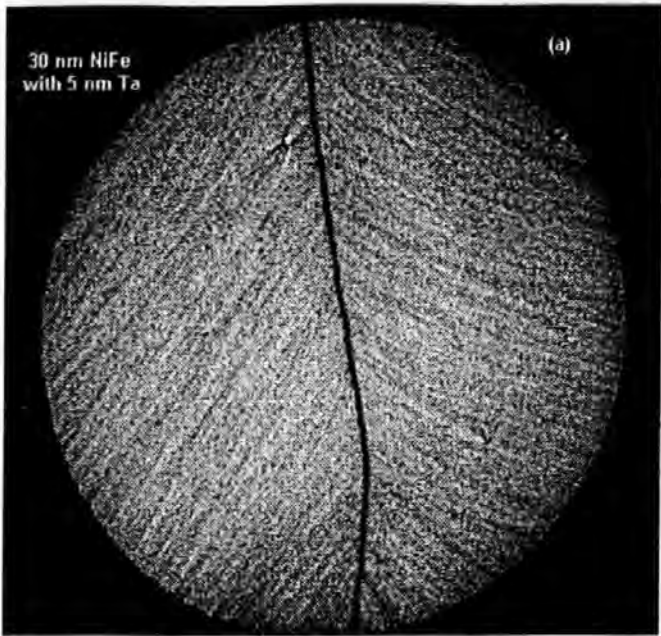


(a) with 5 nm Ta underlayer

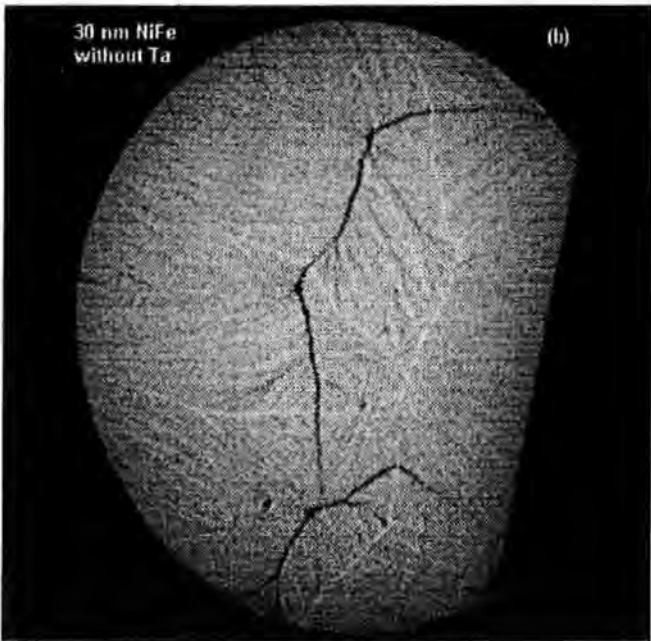


(b) without 5 nm Ta underlayer

Figure 4.25 Images showing typical domain structure and wall in 7.5 nm  $\text{Ni}_{81}\text{Fe}_{19}$  films with and without 5 nm Ta underlayer and the average diameter of image is 25  $\mu\text{m}$ .



(a) with 5 nm Ta underlayer



(b) without Ta underlayer

Figure 4.26 Images showing typical domain structure and wall in 30 nm  $\text{Ni}_{81}\text{Fe}_{19}$  films with and without 5 nm Ta underlayer, and the average diameter of image is 25  $\mu\text{m}$ .

#### 4.1.3 Barkhausen noise analysis

As already stated in chapter 3.4.1.3, a Barkhausen noise study of very thin  $\text{Ni}_{81}\text{Fe}_{19}$  Permalloy films has been extensively carried out as a function of the thickness, substrate temperature and underlayer effect of the film.

The main measurement of Barkhausen noise was carried out by sweeping an 77 Hz ac field ( $\pm 480$  A/m) through the permalloy films and recording the induced output voltage due to the flux change on a digital storage oscilloscope. A number of plots (about 50) were examined in each measurement. Typical plots for the rate of change of flux as a function of time were recorded from the oscilloscope.

The Barkhausen effect of such films was also observed by MR & hysteresis measurement. The MR & hysteresis loop for each sample was obtained from a in-house MR test instrument. The maximum transverse field for the MR loop is set at  $\pm 20$  Oe and the typical current flowing in each sample was 1 mA. These results will be presented later.

##### 4.1.3.1 Thickness dependence

Figure 4.27 is a series of the plots showing results of Barkhausen noise in very thin  $\text{Ni}_{81}\text{Fe}_{19}$  films, which were measured by differentiating the B-H characteristic. These films were deposited on glass substrates at normal temperature, with thicknesses of 5, 10, 15, 15, 20 and 25 nm respectively. These plots are single test results but are representative of about 50 similar plots from a number of thin film samples for each case.

The main peak is due to the magnetisation reversal of the films and is proportional to the induced voltage, the rate of change of flux linking the circuit  $V = N \frac{d\Phi}{dt} = NA \frac{dB}{dt}$ . The

shape of this peak and the remaining part of the curve differs for each film and gives a qualitative insight into the Barkhausen noise. As can be clearly seen from Figure 4.27, the Barkhausen noise became stronger with increasing film thickness, and, in particular, when film thickness is greater than 20 nm. Similar results were obtained from two sets of very thin films, one set deposited at about 300°C and the other on 5 nm Ta underlayers. The thickness range was from 2.5 nm to 30 nm.

#### 4.1.3.2 Ta Underlayer effect

For comparison, the Barkhausen noise analysis of permalloy thin films with and without 5 nm Ta underlayers (which were prepared for sensor fabrication), are presented in Figures 4.28, 4.29 and 4.30. The average sampling for each record is 128.

The films with 5 nm Ta underlayer exhibited less Barkhausen noise and have a relatively stable and sharp response in the thickness range from 5 nm to 40 nm.

In the films without Ta, the behaviour of the Barkhausen effect seems quite complicated. The maximum rate of change of flux (or say the maximum induced voltage) may sometimes be less than the ones with Ta. The width of the peak being greater than the case with Ta. This means that more irregular jumps happen for these films. With a 5 nm Ta underlayer, the phenomenon of Barkhausen effect in Permalloy thin films exhibits more stability and less noise.

The early experimental results also show that the effect of Ta underlayer on the reduction of Barkhausen noise may not be very strong in very thin  $\text{Ni}_{81}\text{Fe}_{19}$  films such as below 20 nm [Akhter et al., 1997]. However, some later experimental results (see Figure 4.31) show the Ta underlayer may also have considerable effect on Barkhausen noise in very thin films of several nanometers thickness.

#### *Chapter 4: Results and Discussion*

The results given in Figure 4.31 were obtained from the substrates of sensors. There are 18 pairs of sensors created on about 3/4 area in each 2 inch square substrate. A triangular wave was used for this measurement so that the distance between two peaks is a reflection of the coercivity in the film examined. The average sampling rate for each test sample is 128 per second and the persistence time is 5 seconds.

The structure of these films ( presented in Figure 4. 31) are as below:

- (a) 7.5 nm film on high quality 7059 glass substrate;
- (b) 7.5 nm film on microscope glass slide;
- (c) 7.5 nm film with 5 nm Ta underlayer on 7059 glass substrate;
- (d) 7.5 nm film with 5 nm Ta underlayer on microscope glass slide.
- (e) 10 nm film with 5 nm Ta underlayer on 7059 glass substrate;
- (f) 10 nm film with 5 nm Ta underlayer on microscope glass slide

In the films without Ta underlayer, the coercivity of film deposited on 7059 Corning glass substrates is smaller (about 1.01 Oe or 80 A/m) than the one (about 1.3 Oe or 104 A/m) deposited on a microscope glass slides due to the effect of surface roughness. The shape of the peak is similar in both cases but the width of peak in the film with Ta underlayer is slightly narrower than the other.

For the films with 5 nm Ta underlayer, the coercivities of films increase with increasing film thickness on both substrates. It should be noted from Figure 4.31, the curve shape and height in the films deposited on 7059 glass (curve c and e) are very different with those of films deposited on a microscope glass slides (curve d and f).

The results show that Barkhausen jumps in the films deposited on 7059 glass may be bigger but they happen less often, while for the films deposited on microscope glass

slides, the jumps may be small but many. Why there is such difference needs to be examined in more detailed experiments. The difference that occurs by using 7059 glass may be disadvantageous because of substrate cost but offers opportunities for better films based on better fabrication.

#### 4.1.3.3 Temperature effect

As can be seen from Figure 4.1, one set of films deposited at about 300°C shows weaker coercivity than those deposited at ambient temperature. The measurement of Barkhausen noise in these films was carried out and the results are in fair agreement with the variation of their coercivity (see Figure 4.32).

A number of experimental results obtained in this study show that the films deposited at elevated temperature have lower coercivity, less Barkhausen noise and more stable magnetic properties. A possible explanation for the coercivity behaviour in terms of free energy is the fact that the films deposited at elevated substrate temperature may have their initial minimum surface free energy state related to deposition temperature. This initial minimum state will be quite stable if their later thermal experience is below the deposition temperature. One should note that the elevated temperature may cause other thermal effects such as increasing the dispersion of the magneto-crystalline easy axis [Flur, 1967] so that a suitable value should be carefully chosen.



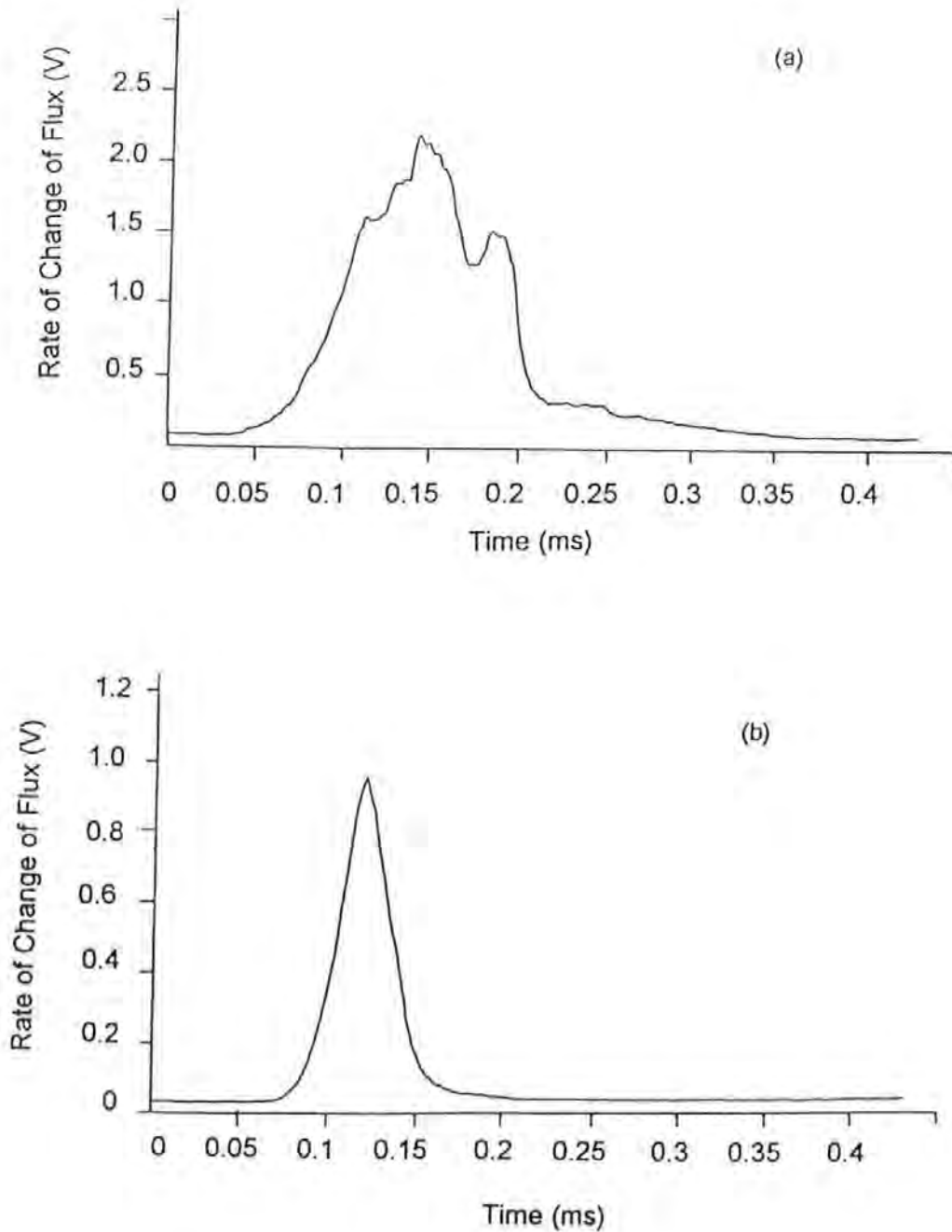


Figure 4.27. Plots showing Barkhausen noise versus  $\text{Ni}_{81}\text{Fe}_{19}$  film thicknesses from 5 nm to 25 nm

(Rate of change of flux is obtained from a sense coil with 1170 turns and the applied field on the sample is sinusoid of zero to peak value of 6.1 Oe under the frequency of 77 Hz)

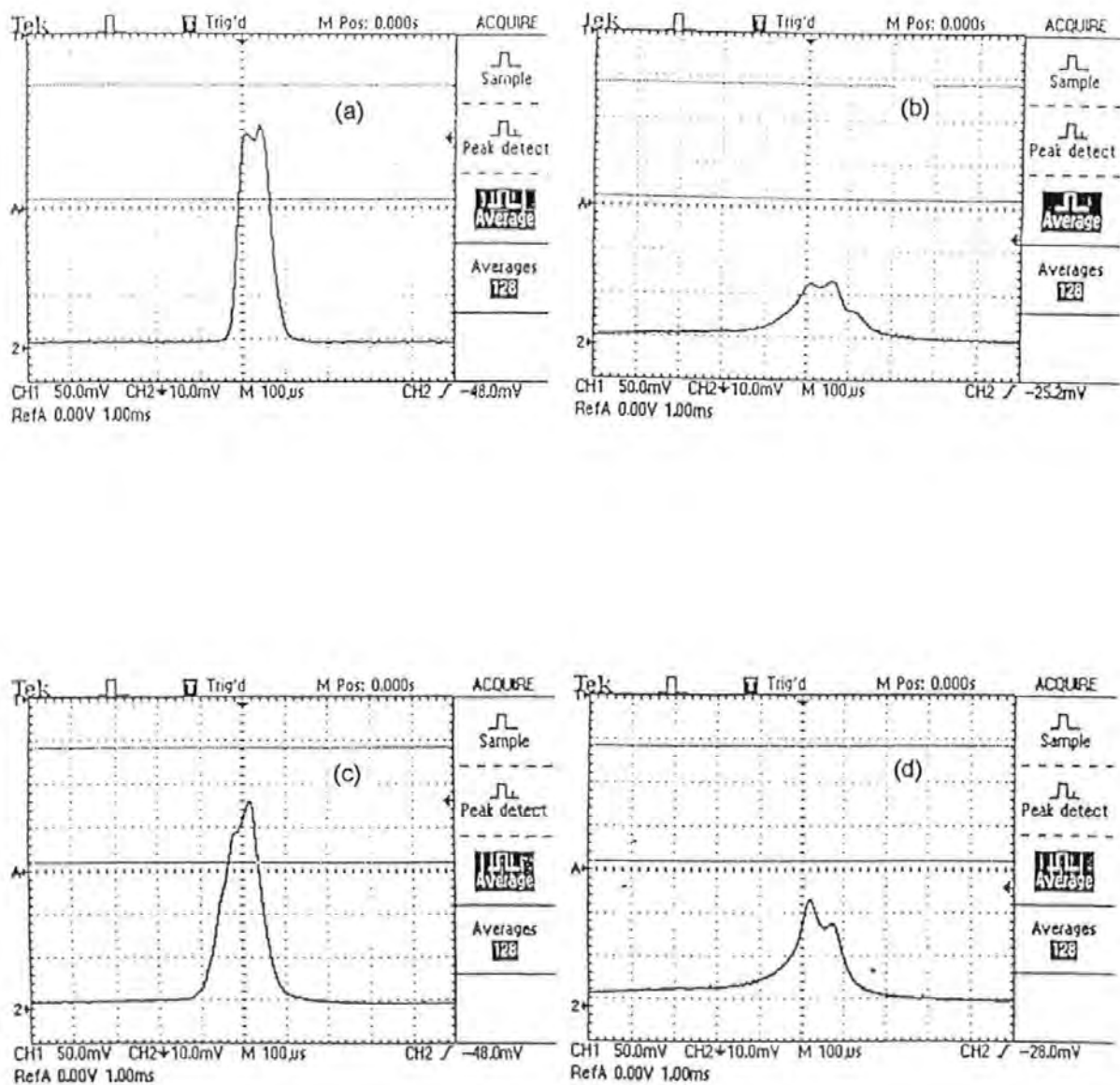


Figure 4.28. Plots showing Barkhausen noise in the  $\text{Ni}_{81}\text{Fe}_{19}$  films with and without Ta underlayer versus the film thickness

- (a) 5 nm film with 5 nm Ta underlayer;
- (b) 5 nm film without 5 nm Ta underlayer;
- (c) 7.5 nm film with 5 nm Ta underlayer;
- (d) 7.5 nm film without 5 nm Ta underlayer;

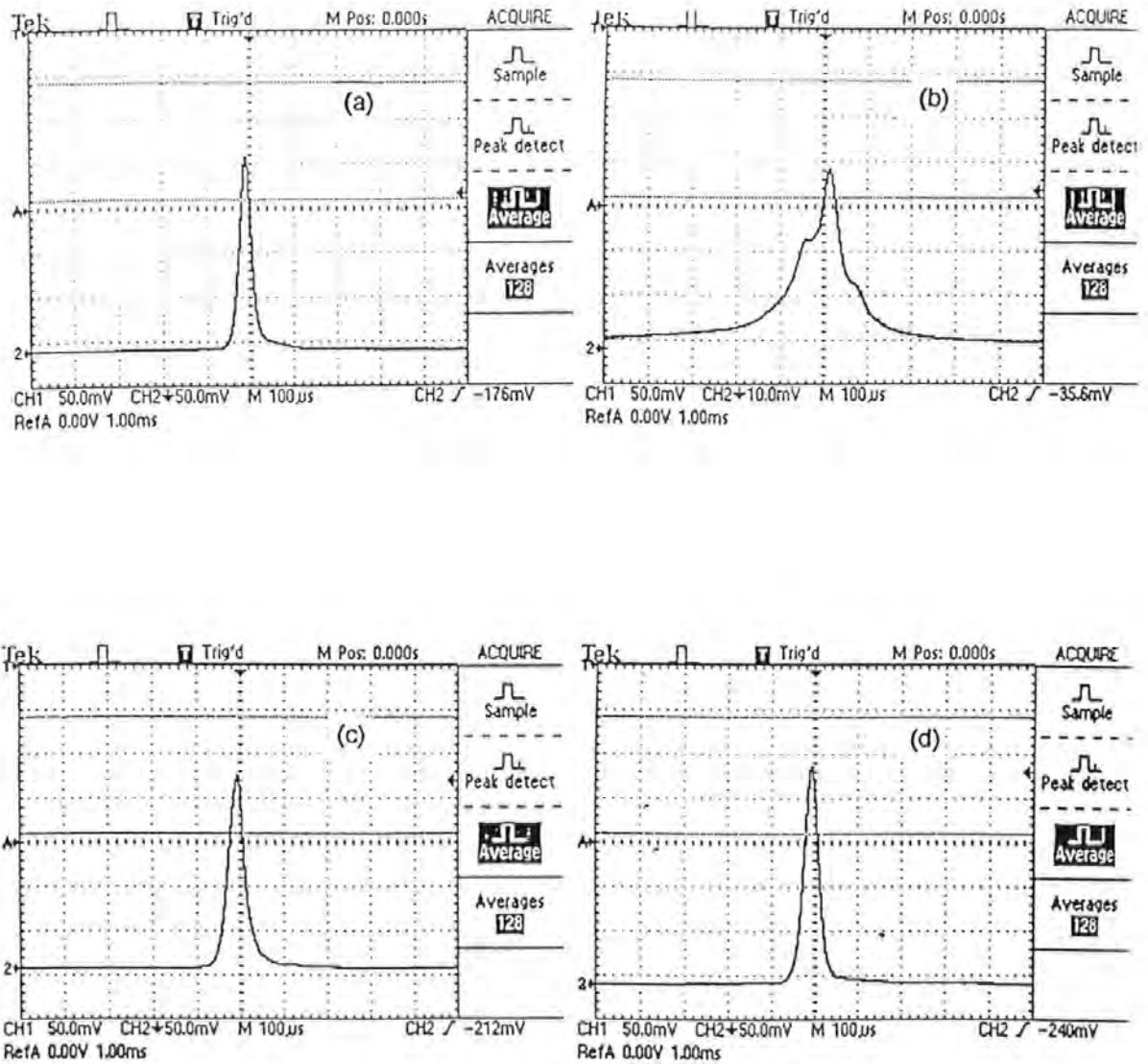


Figure 4.29. Plots showing Barkhausen noise in the  $\text{Ni}_{81}\text{Fe}_{19}$  films with and without Ta underlayer versus the film thickness

- (a) 10 nm film with 5 nm Ta underlayer;
- (b) 10 nm film without 5 nm Ta underlayer;
- (c) 15 nm film with 5 nm Ta underlayer;
- (d) 15 nm film without 5 nm Ta underlayer;

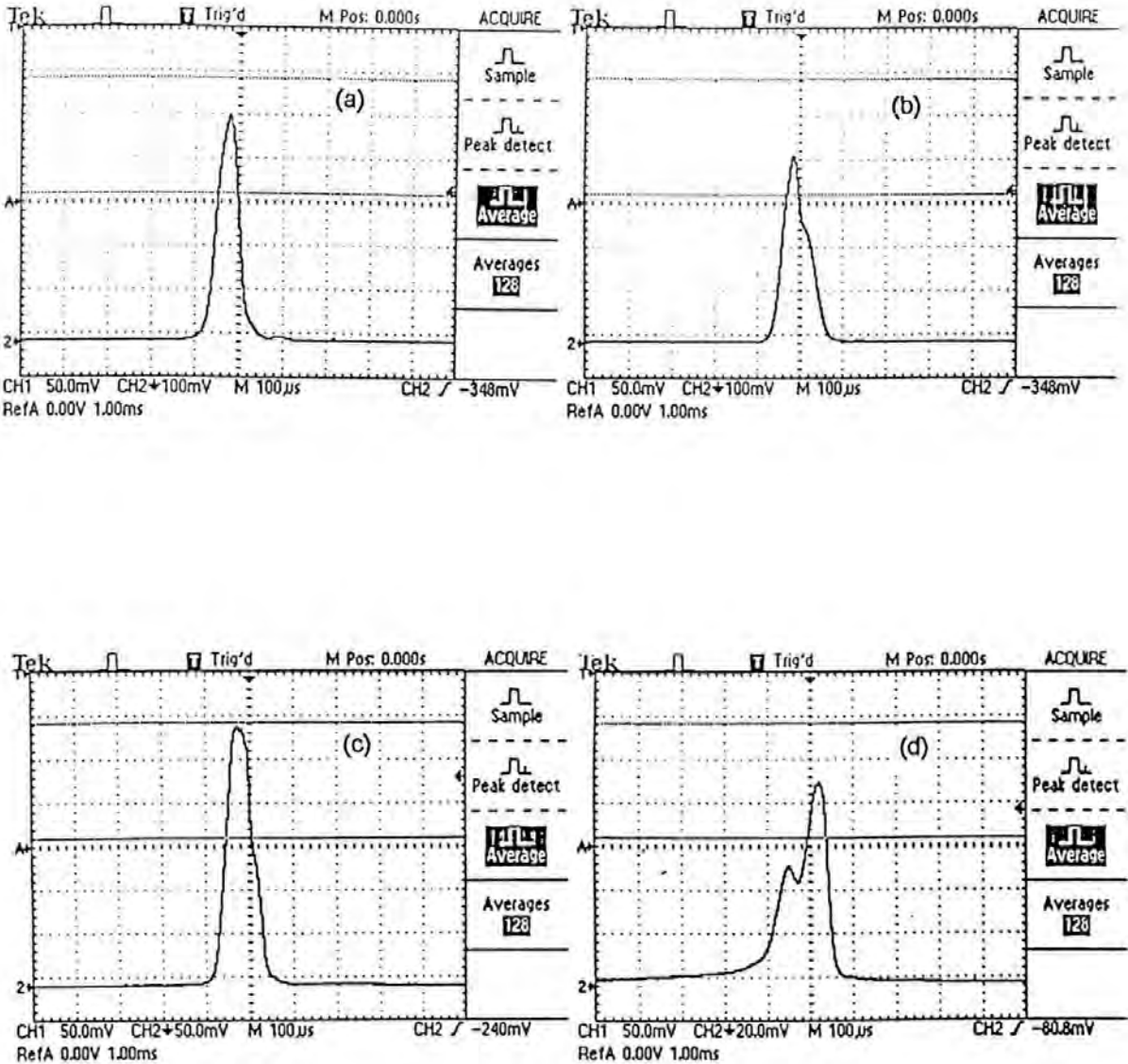


Figure 4.30. Plots showing Barkhausen noise in  $\text{Ni}_{81}\text{Fe}_{19}$  thin films with and without Ta underlayer versus the film thickness

- (a) 25 nm film with 5 nm Ta underlayer;
- (b) 25 nm film without 5 nm Ta underlayer;
- (c) 40 nm film with 5 nm Ta underlayer;
- (d) 40 nm film without 5 nm Ta underlayer;

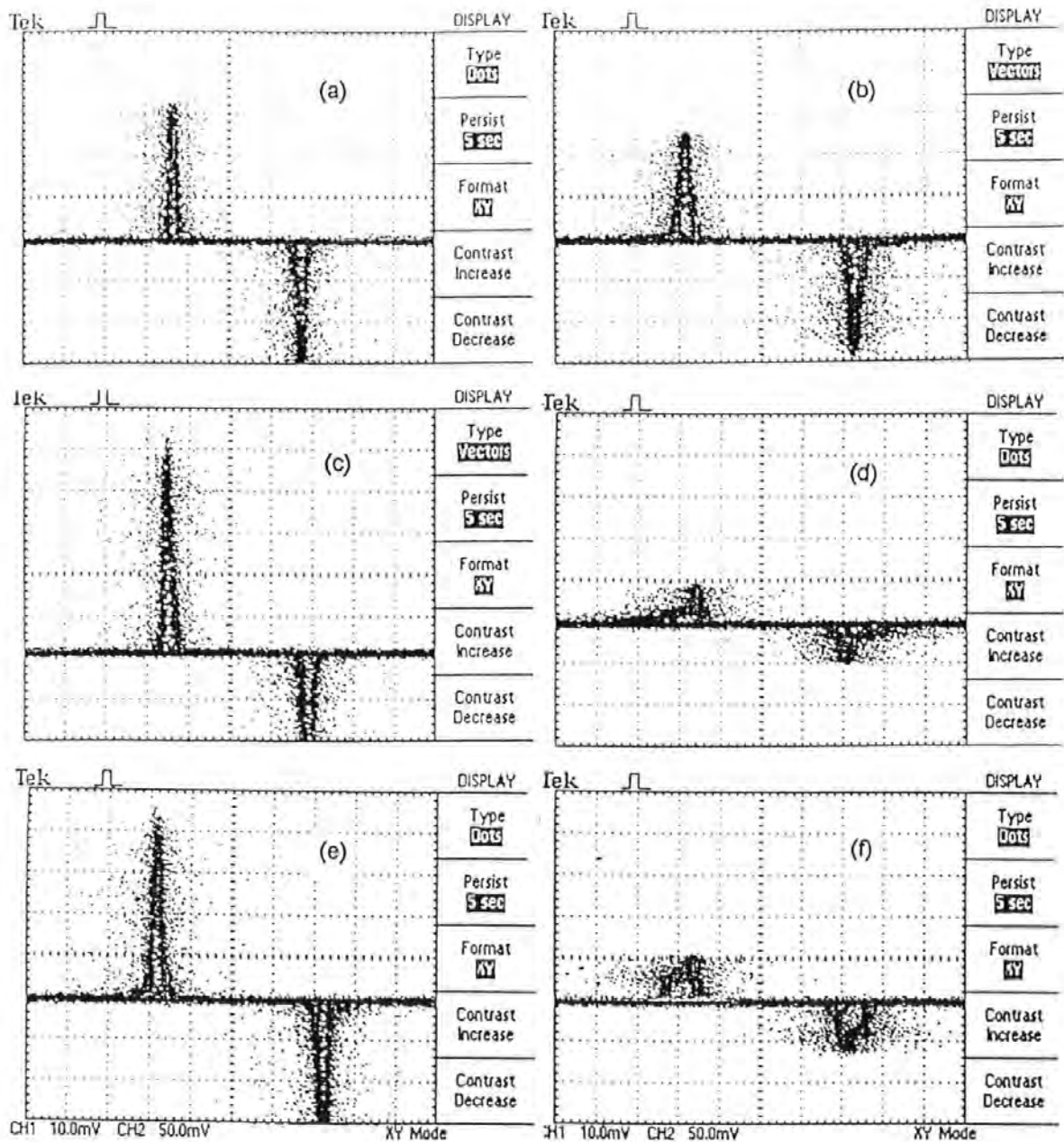


Figure 4.31 Graphs showing Barkhausen noise in  $\text{Ni}_{81}\text{Fe}_{19}$  thin films with and without Ta underlayer varied with the substrates.

7.5 nm films on 7059 glass substrate (a) and on normal microscope glass substrate (b).

7.5 nm film (c) and 10 nm film (e) with 5 nm Ta underlayer on 7059 glass substrate.

7.5 nm film (d) and 10 nm film (f) with 5 nm Ta on microscope glass substrate.

#### Chapter 4: Results and Discussion

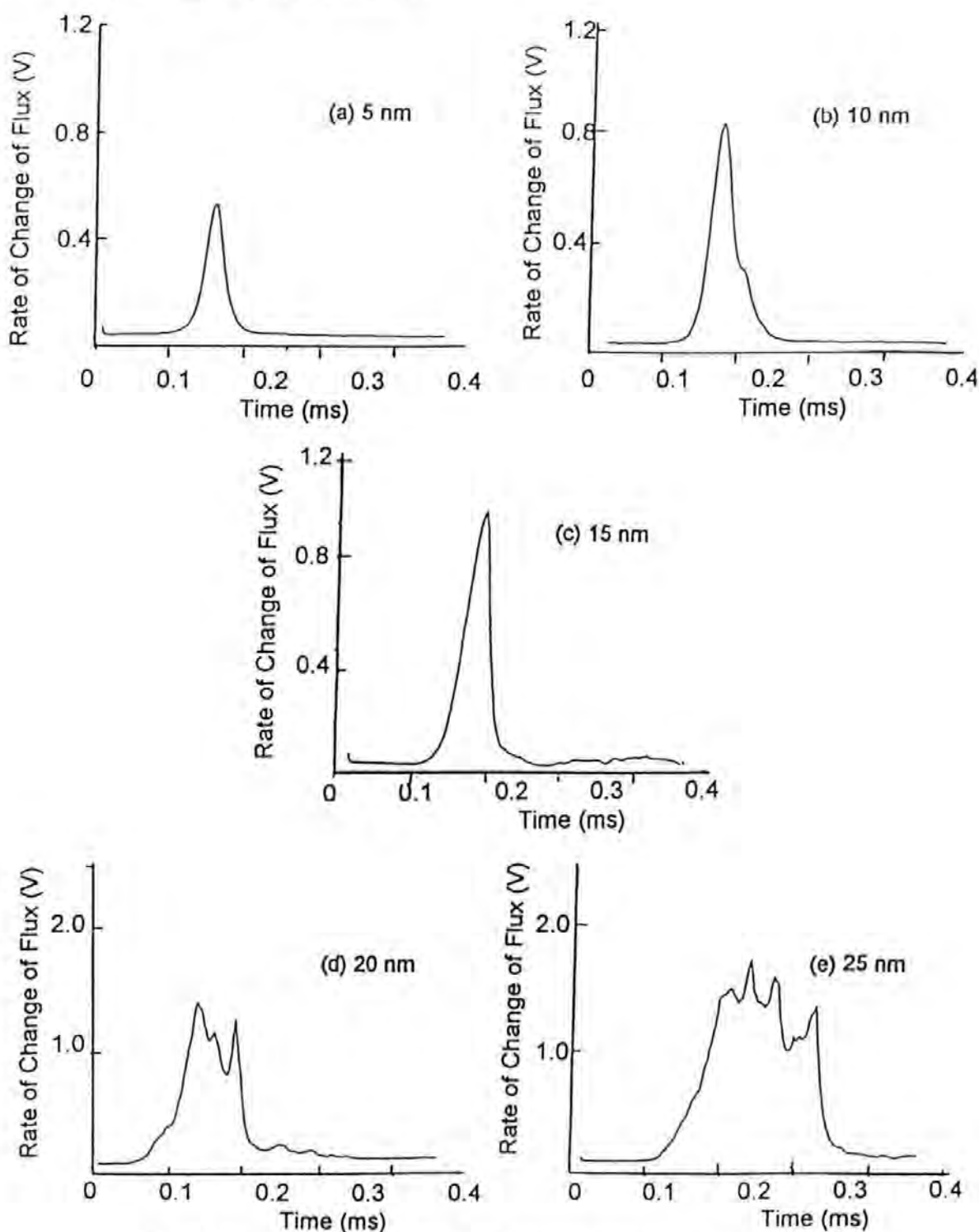


Figure 4.32 Graphs showing Barkhausen noise in  $\text{Ni}_{81}\text{Fe}_{19}$  thin films varied with deposited temperature

(a) 20 nm film deposited at ambient temperature. (b) 20 nm film deposited at  $300^{\circ}\text{C}$   
(Rate of change of flux is obtained from a sense coil with 1170 turns and the applied field on the sample is sinusoid of zero to peak value of 6.1 Oe under the frequency of 77 Hz)



## **4.2 Switched-bias magnetoresistive sensors**

As stated previously, the total fabrication procedure consists of about 55 steps for each substrate and one set of eight photo-masks has been designed and used for the fabrication. A number of sensors (about 30 substrates or 540 pairs of sensors) with film thickness of 5 to 40 nm, stripe widths varying between 10 to 80  $\mu\text{m}$  and a standard length of 6 mm, have been completed in this study. After the fabrication of sensors, measurements of their output performance was carried out and some of results are presented here.

The anisotropic M-R response or hysteresis loop for each completed sensor is measured by an M-R or B-H test instrument, purpose built for thin-films. The transverse field for the M-R loop is set at  $\pm 20$  Oe and a typical current flowing in the sensor or film is 1 mA. Barkhausen noise and the corresponding hysteresis are studied by analysis of the MR response of various sensors together with their magnetoresistive hysteresis. In order to reduce hysteresis in the sensors, a high-frequency external 'linearising' field method is used. This high-frequency field (5 to 20 kHz) oscillates the magnetisation in the sensor so that the sensor magnetisation finds the lowest magnetic energy condition for all magnetisation conditions. In our experiments a high-frequency field of various amplitudes is applied both along the sensor long axis and transverse to it.

Variation in the sensitivity of the sensor to the magnitude of a switched-biasing field was measured by applying a very small alternating field (variable from 80 nT to 24000 nT) and varying a transverse dc field component ( $H_x$ ). The effect of biasing field frequency and external linearising field on the sensitivities of these MR sensors is studied using an in-house built measurement system..

## *Chapter 4: Results and Discussion*

### **4.2.1. M-R response**

For comparison, the results of anisotropic magnetoresistance coefficient for  $\text{Ni}_{81}\text{Fe}_{19}$  thin films deposited under different conditions as a function of film thickness are plotted in Figure 4.33. The results of anisotropic magnetoresistance for sensors with stripe widths of 20, 40 and 80  $\mu\text{m}$  and a standard length of 6 mm, as a function of their thickness are given in Figure 4.34 and Figure 4.35. Figure 4.34 is for sensors with 5 nm Ta underlayer and Figure 4.35 is for sensors without Ta underlayer.

Figure 4.33 shows that as the film becomes thinner, the  $\Delta\rho/\rho_s$  decreases due to the additional resistivity which is known to occur in very thin films [Krongelb, 1973]. The change in M-R response is almost the same in the thinner films but in the  $\text{Ni}_{81}\text{Fe}_{19}$  permalloy film thicknesses above 10 nm, the change is slightly higher in the films grown on Ta underlayers. The change of M-R response is also more stable in the films with Ta. The saturation anisotropic magnetoresistance for these sensors in the thickness range from 5 to 40 nm varied between about 1% to 2 %, with the exception of the 5 nm film. The variation in sensor widths seems to only have a slight effect on the change of M-R response due to the very large aspect ratio ( $l/w$  varying from 75 to 600). In the case of sensors with Ta underlayer, similar effects still can be seen and the results show that a Ta underlayer favours the magnetic properties of these sensors.

It should be noted that the M-R change of the 5 nm sensor seems not to be stable and has an unexpected high value. The reasons for this are not clear yet but data has been repeated 5 times. It was found that the measurement of M-R response becomes quite difficult in very thin films (below 15 nm) due to high resistance.

The variation of  $\Delta\rho / \rho$  for sensors with Ta underlayer exhibits oscillatory characteristics in the film thickness below 15 nm, which may be caused by the presence of Ta and seems to have a similar tendency on the change of their coercivity. However, the maximum anisotropic magnetoresistance change in very thin sensors of thickness about 7.5 nm (about 1.88 %) or even 10 nm (about 1 %) is still useful for their application.

#### 4.2.2 Ta underlayer effect on hysteresis

MR/field characteristics are useful for checking the response of an MR sensor in respect of hysteresis and Barkhausen noise.

In order to reduce hysteresis in the sensors, a high-frequency external ‘linearising’ field method is used. This high-frequency field oscillates the magnetisation in the sensor so that the sensor magnetisation finds the lowest magnetic energy condition for all magnetisation conditions. In our experiments the high-frequency field of various amplitudes is applied both along the sensor long axis and transverse to it.

An indicator of hysteresis is the separation of the forward and reverse curve around the vertical axis as shown by the apparent ‘coercivity’ in Figure 4.36 and Figure 4.37.

In the case of Figure 4.36 the curves are from a 10 nm-thick sensor deposited directly on the glass substrate. In this case, with no high-frequency ‘linearising’ field applied, the separation of forward and reverse curves reaches a value of 1.5 Oersteds (119 A/m). Application of the high-frequency field along the sensor long axis reduces this but some Barkhausen jumps are seen in the characteristics even when no hysteresis is present.

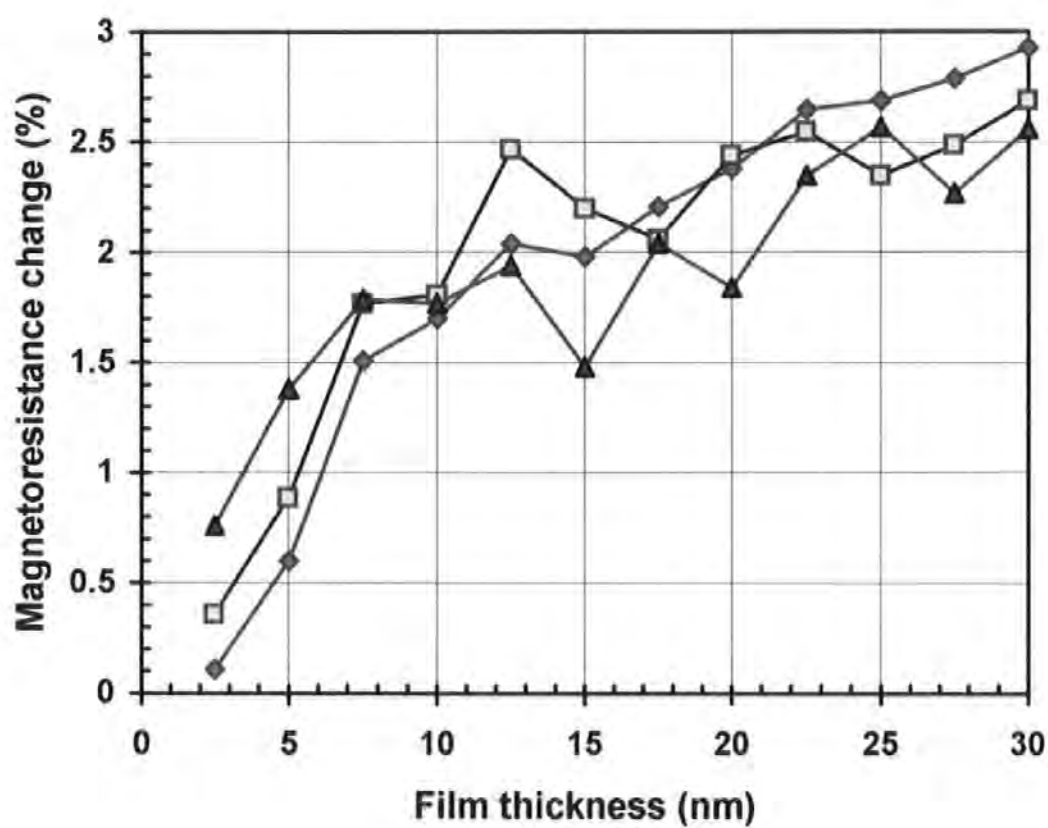


Figure 4.33 Magnetoresistance change versus  $\text{Ni}_{81}\text{Fe}_{19}$  thin film thickness  
 (▲) on glass substrate deposited at ambient temperature;  
 (◆) on glass substrate with 5 nm Ta underlayer deposited at ambient temperature  
 (□) on glass substrate deposited at about 300° C.

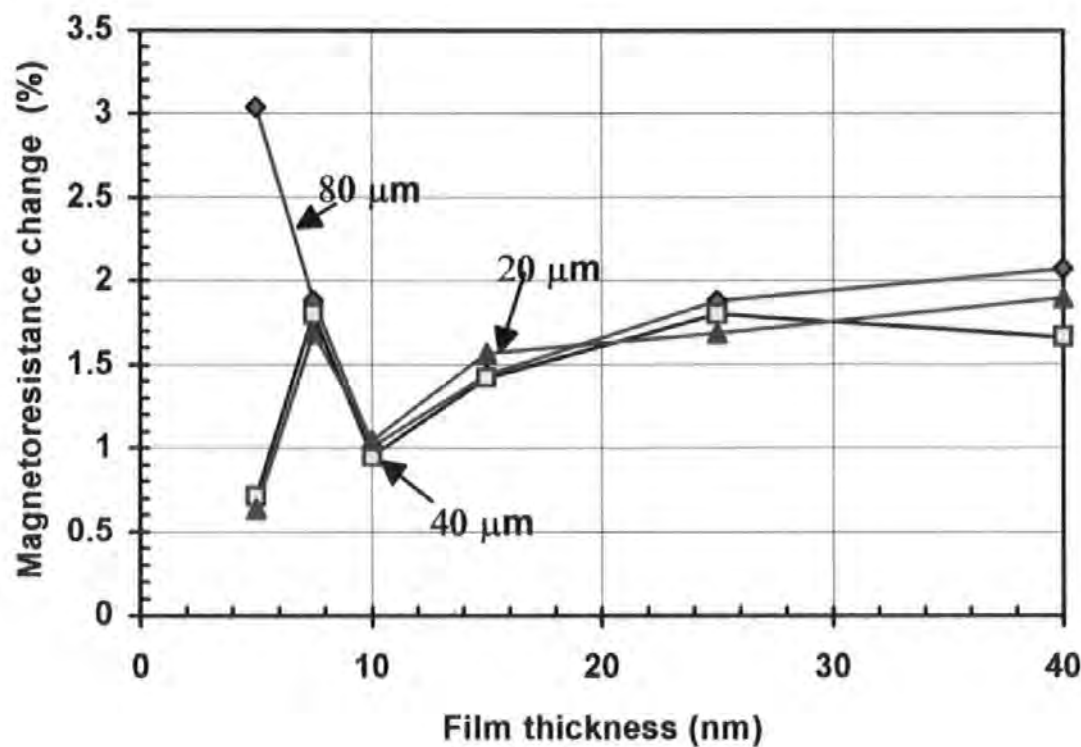


Figure 4.34 Magnetoresistance change versus film thickness for sensors with 5 nm Ta underlayer (♦) 80 μm (□) 40 μm, (▲) 20 μm

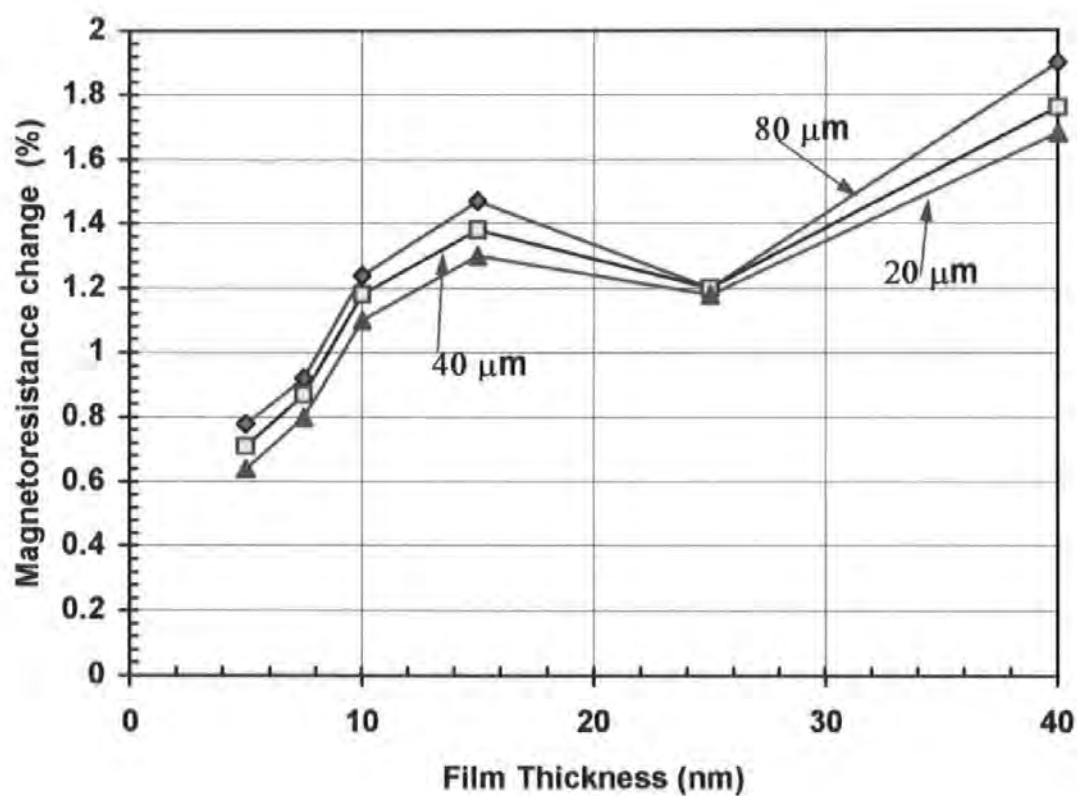


Figure 4.35 Magnetoresistance change versus film thickness for sensors without 5 nm Ta underlayer ( $\blacklozenge$ ) 80  $\mu\text{m}$ , ( $\square$ ) 40  $\mu\text{m}$ , ( $\blacktriangle$ ) 20  $\mu\text{m}$



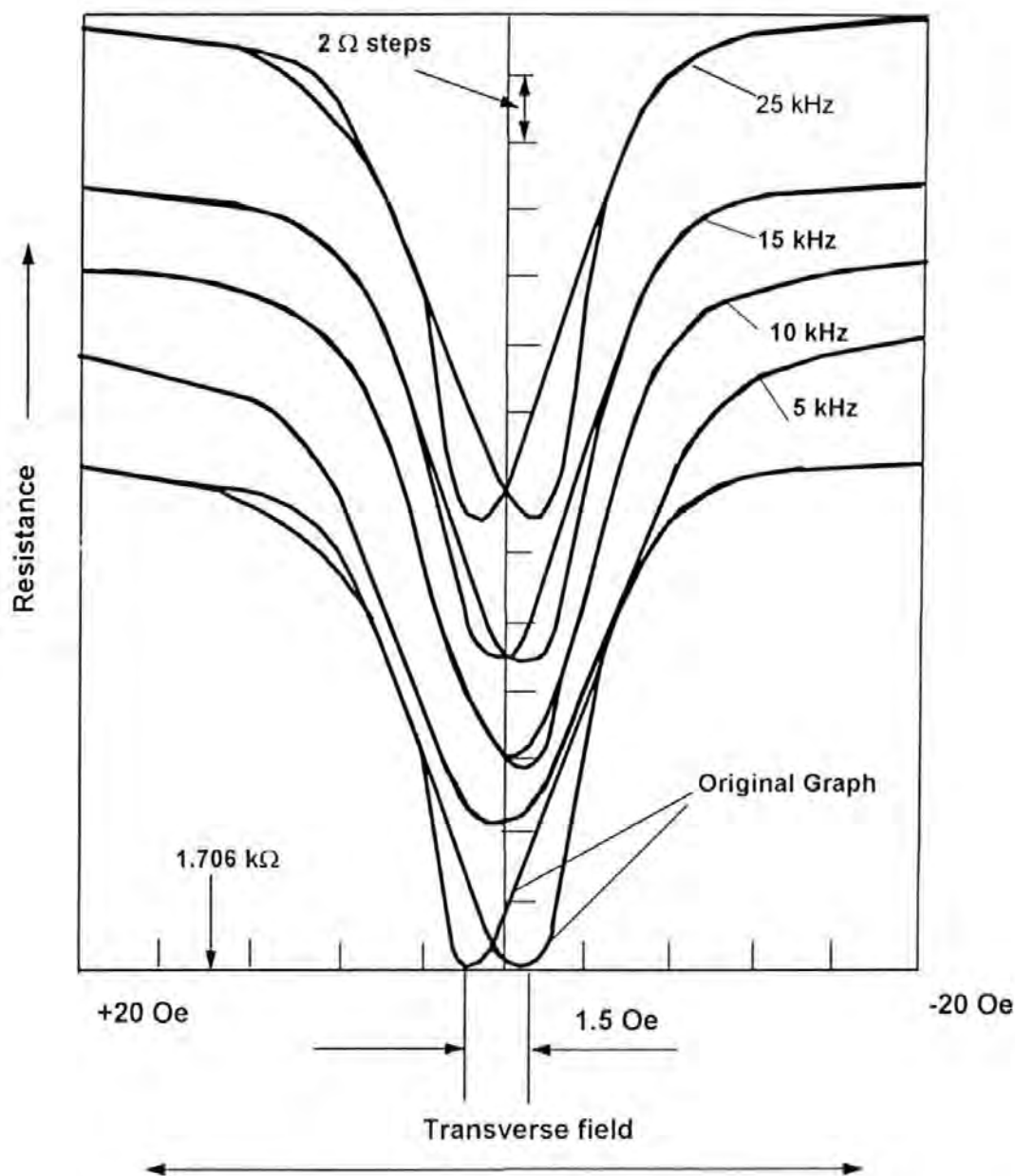


Figure 4.36 Graph showing the M-R response and hysteresis variation of 10 nm sensor (80  $\mu\text{m}$  wide) without 5 nm Ta underlayer versus the frequency of linearising field (0.2 Oe and applied along the easy axis)

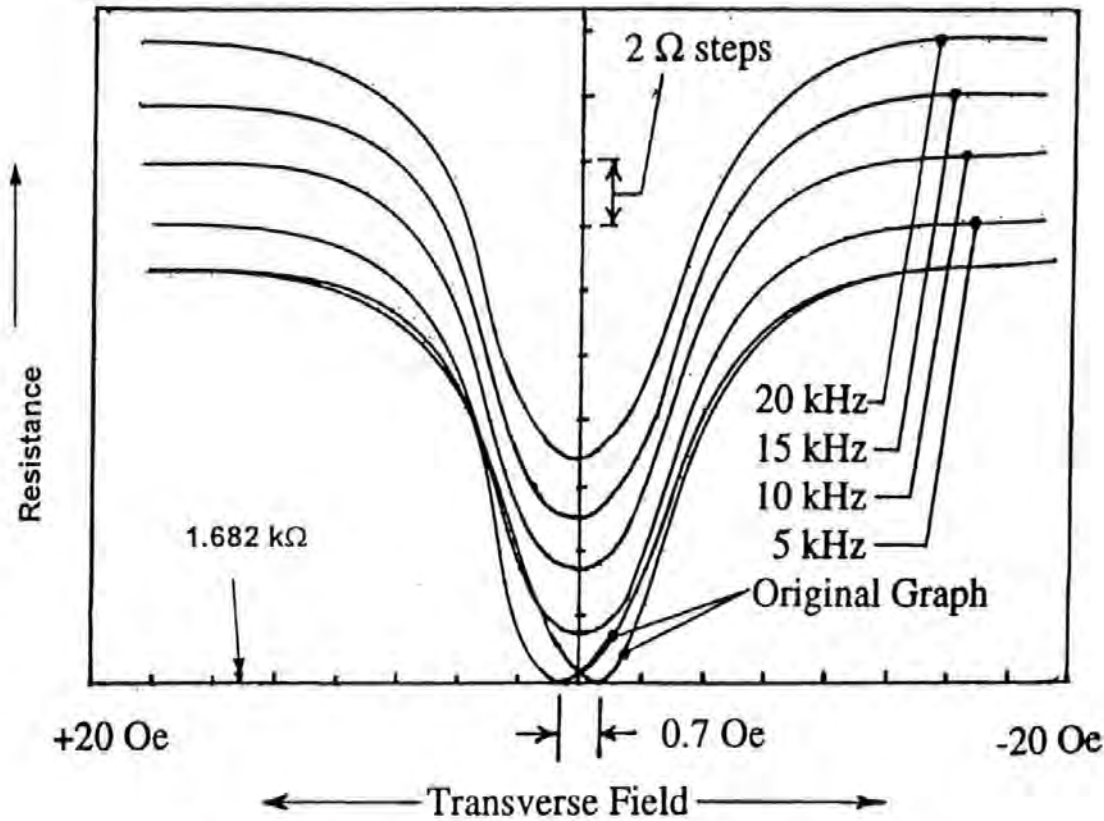


Figure 4.37 Graph showing the M-R response and hysteresis variation of 10 nm sensor (80  $\mu\text{m}$ ) wide) with 5 nm Ta underlayer versus the frequency of linearising field (0.2 Oe and applied along the easy axis)

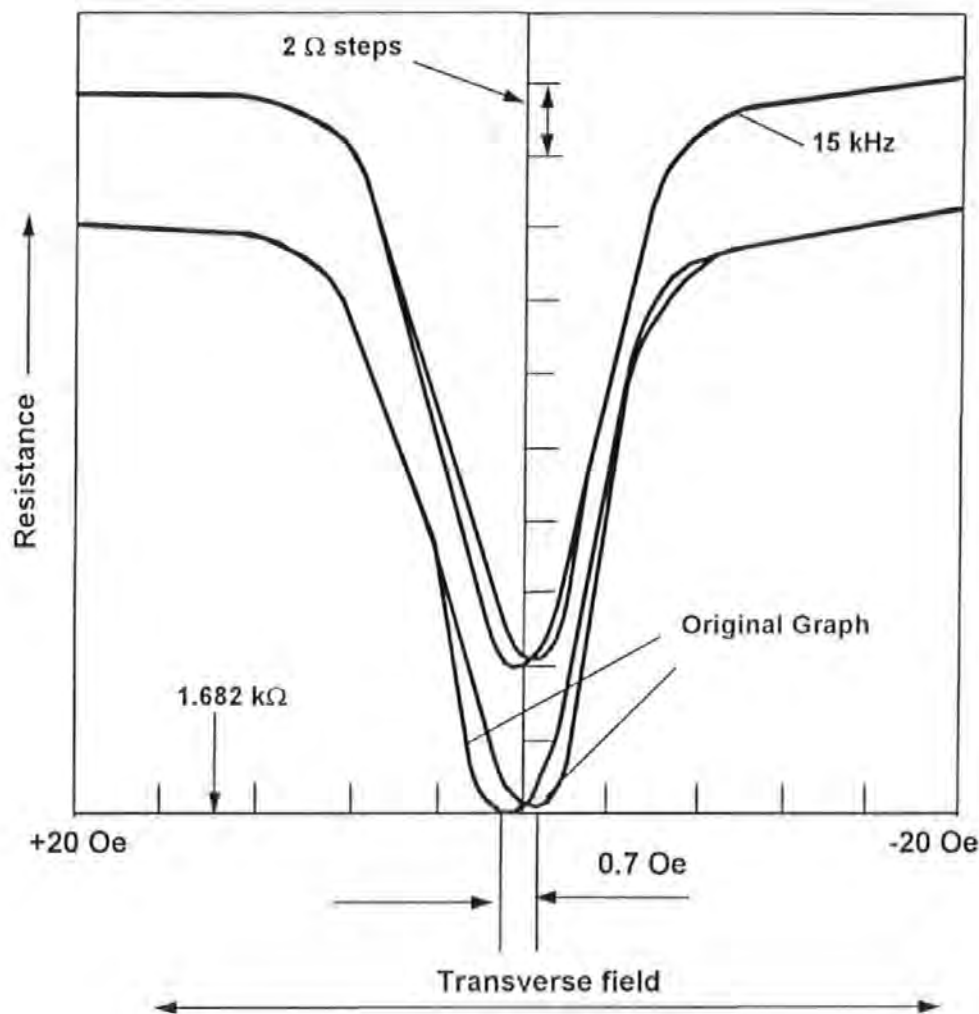


Figure 4.38 Graph showing the M-R response and hysteresis variation of 10 nm sensor (80  $\mu\text{m}$  wide) with 5 nm Ta underlayer vs. the frequency of linearising field (0.2 Oe and applied along the hard axis)

## *Chapter 4: Results and Discussion*

In the case of Figure 4.37, an identical sensor is used except that it has been deposited on a tantalum underlayer. For this case the 'coercivity' separation field is reduced to 0.7 Oe (55 A/m) and there are almost no Barkhausen effects visible for frequencies up to 20 kHz. The best linearising frequency appears to be about 10 kHz when the forward and reverse MR curves coincide although linearising fields at nearby frequencies are almost as effective.

The result of Figure 4.37 can be explained if it is realised that the effect of the tantalum underlayer is to promote microstructure growth in the  $\text{Ni}_{81}\text{Fe}_{19}$  film with its (111) crystallographic plane (Miller indices) parallel to the film surface. This leads to a more isotropic magnetic behaviour as reported in ref. [Akhter et al., 1997 & 1998].

It was found that the direction of this external linearising field is more effective when aligned with the easy axis than with the hard axis as shown in Figure 4.38. The results also confirm that the field required to significantly reduce the hysteresis of such sensors is very small such as about 1.6 A/m or 0.02 Oe. Similar results can be found in ref. [Decker and Tsang, 1980], [Mapps et al., 1985] and [Flynn, 1994], and was thought due to enhancement of single domain behaviour.

It should be noted that the initial magnetisation state of such a sensor is easily changed by applying an external field during measurement due to its low demagnetising field. This suggests that each sample should be carefully demagnetised to ensure the initial magnetising state of each sensor is the same.

### 4.2.3. Sensitivity to applied d.c. field

#### 4.2.3.1 Effect of bias field on the output characteristics

- Amplitude of bias field  $H_b$

For a magnetoresistor with easy axis parallel to the current flow the change in resistivity (and the output voltage  $V$ ) can be determined from a magnetic model based on minimisation of the free energy assuming a single domain system [Flynn, 1994]. This output voltage is proportional to a steady field, which is transverse to the film easy axis direction and in-plane.

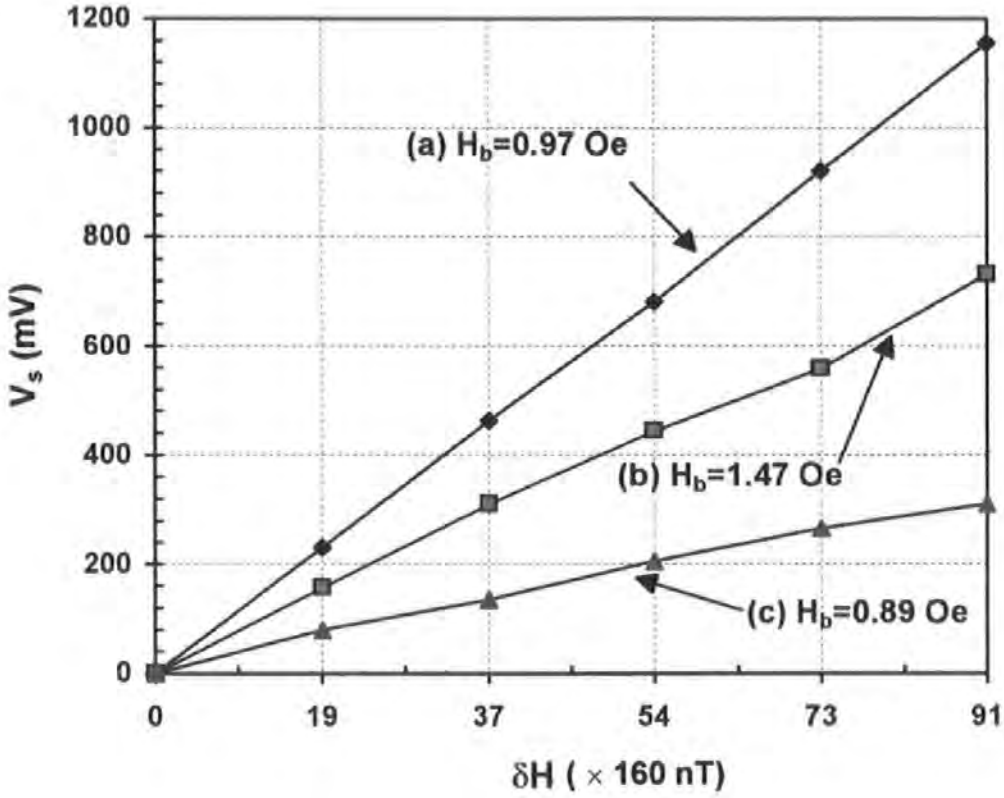
Figure 4.39 shows the output characteristics of a 10 nm  $\text{Ni}_{81}\text{Fe}_{19}$  sensor with 5 nm Ta underlayer as a function of d.c. field for three bias fields. It can be seen that the output of the sensor is highly dependent on the magnitude of the switched-bias field, this is to be expected from the (bell) shape of the M-R response characteristic seen in Figures 4.36 and 4.37.

- Frequency of bias field  $H_b$

The frequency of bias field was set at 1 kHz for the first measurements. It was found that the best frequency of bias field for the sensor is at a lower frequency e.g. 250 Hz. The variation of the output of the sensor as a function of frequency of bias field is given in Table 4.4. In this case the external field change is set at about 2960 nT and bias field is set at about 80 A/m or 1 Oe.

Table 4.4 Effect of frequency of bias field on the output of sensor

Frequency of $H_b$ (Hz)	70	100	200	300	400	500	600	700	800	900	1000
The output of sensor (mV)	10	20	20	16.5	16	14	13	12	11	10	10



10 nm NiFe Sensor with 5 nm Ta Underlayer  
( $f_b=1$  kHz,  $f_L=5$  kHz,  $H_L=1.2$  Oe)

Figure 4.39 Showing the output of a 80  $\mu$ m wide, 10 nm sensor thick with 5 nm Ta underlayer versus d.c. field for three bias fields

- (a)  $H_b=0.97$  Oe or 77 A/m;
- (b)  $H_b= 1.47$  Oe or 117 A/m;
- (c)  $H_b=0.89$  Oe or 71 A/m

This effect was thought to be caused by the filter at the front end of the Lock-in amplifier. There are two low pass filters in this Lock-in amplifier, one is  $F < 30$  kHz and the other is  $F < 1$  kHz. The test results show that there is some change on the output of sensor using each one, but it seems not great enough to explain the change shown in Table 4.4. However, the frequency of the bias field at the order of 250 Hz was chosen and used in the later measurements.

#### 4.2.3.2 Sensitivity to applied d.c. fields

As can be seen from Figure 4.39, output of the sensor is linear in all cases up to a maximum value of  $91 \times 160$  nT (about 14 560 nT). It can also be seen that the switched-bias field required is quite small around 0.485 Oe or 38.5 A/m. This is surprising since, even when the sensor is not operating on the linear part of curve the differential system is sufficiently effective in maintaining linearity. The results show that the sensor is linear over quite a wide range if used to measure very small fields in the tens or hundreds nano-Tesla region.

#### 4.2.4 Optimum sensitivity to a low field in the nano-Tesla range

Figure 4.40 shows the output response of a 7.5 nm sensor to an applied field ( $\delta H$ ) of about 160 nano-Tesla. The Channel 1 curve in Figure 4.40 (a) is the original signal output of sensor from Lock-in amplifier at zero field. After switching on an about 160 nano-Tesla field, the record of channel 1 is as shown as in Figure 4.40 (b). The change of output is about 4.4 mV for 160 nano-Tesla. Channel 2 is used for the signal output of the sensor before the lock-in amplifier.



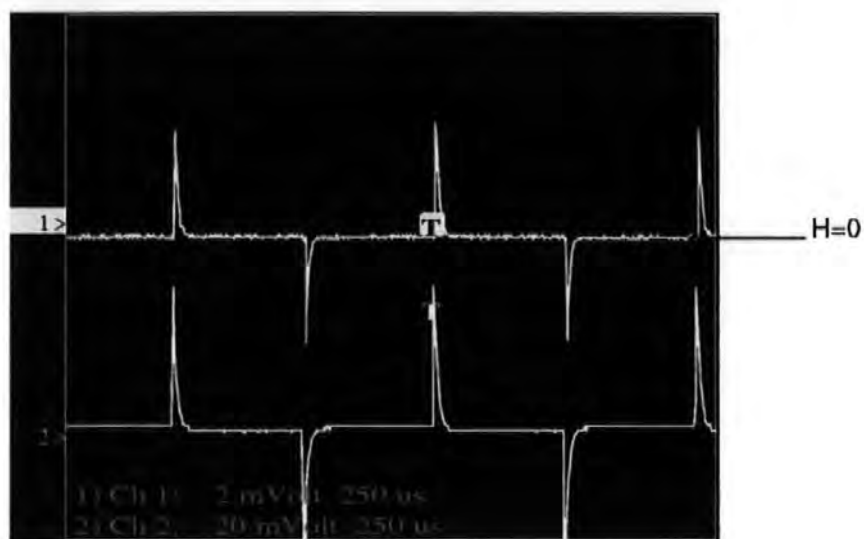
#### *Chapter 4: Results and Discussion*

The curves of Figure 4.41 and 4.42 are the output response of 10 and 7.5 nm sensors for an applied field ( $\delta H$ ) of 160 nano-Tesla respectively. A convenient switched-bias frequency is chosen to match the low-pass filter in the lock-in amplifier system (250 Hz). The frequency of the linearising field (about 0.2 Oe or 16 A/m) is set at 15 kHz.

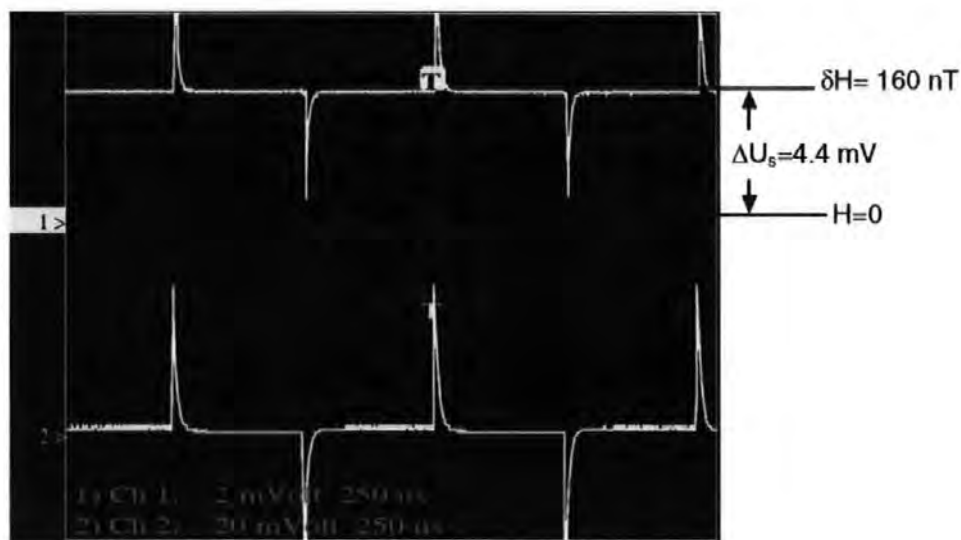
In the case of Figure 4.41, a 10 nm sensor was examined. In this case, the amplitude of the switched-bias current is varied and the output reaches a maximum at a current of 90 mA corresponding to a peak switched-bias field of 0.455 Oe (about 32 A/m). At this condition an output change of 24 mV is obtained for a  $\delta H$  field of about 160 nano-Tesla, and the noise level on this output is less than 1 mV.

Figure 4.42 shows the output response of a 7.5 nm sensor. A maximum output of 29 mV is obtained at a bias current of 60 mA corresponding to a peak switched-bias field of 0.27 Oe or 21.5 A/m for a  $\delta H$  field of about 160 nano-Tesla. This is to be expected as the thinner sensor has higher sensitivity and lower switched-bias field due to lower coercivity.

In the cases of Figure 4.41 and 4.42 the applied (constant) field ( $\delta H$ ) has been fixed at about 160 nT which is some 300 times smaller than the earth's field. In this case the expected peak with switched-bias current is found corresponding to the point of inflection on the MR characteristic. Because of the low noise level in this condition it appears that the sensor is capable of detecting changes much smaller than 160 nano-Tesla (e.g. 16 nano-Tesla) under ideal conditions.



(a) at zero field before switching on



(b) at 80 nano-Tesla field after switching on

Figure 4.40 The output response of 7.5 nm sensor (80 μm wide)

for a  $\delta H$  field of 160 nano-Tesla

(a) at zero field before switching on

(b) at 160 nano-Tesla field after switching on

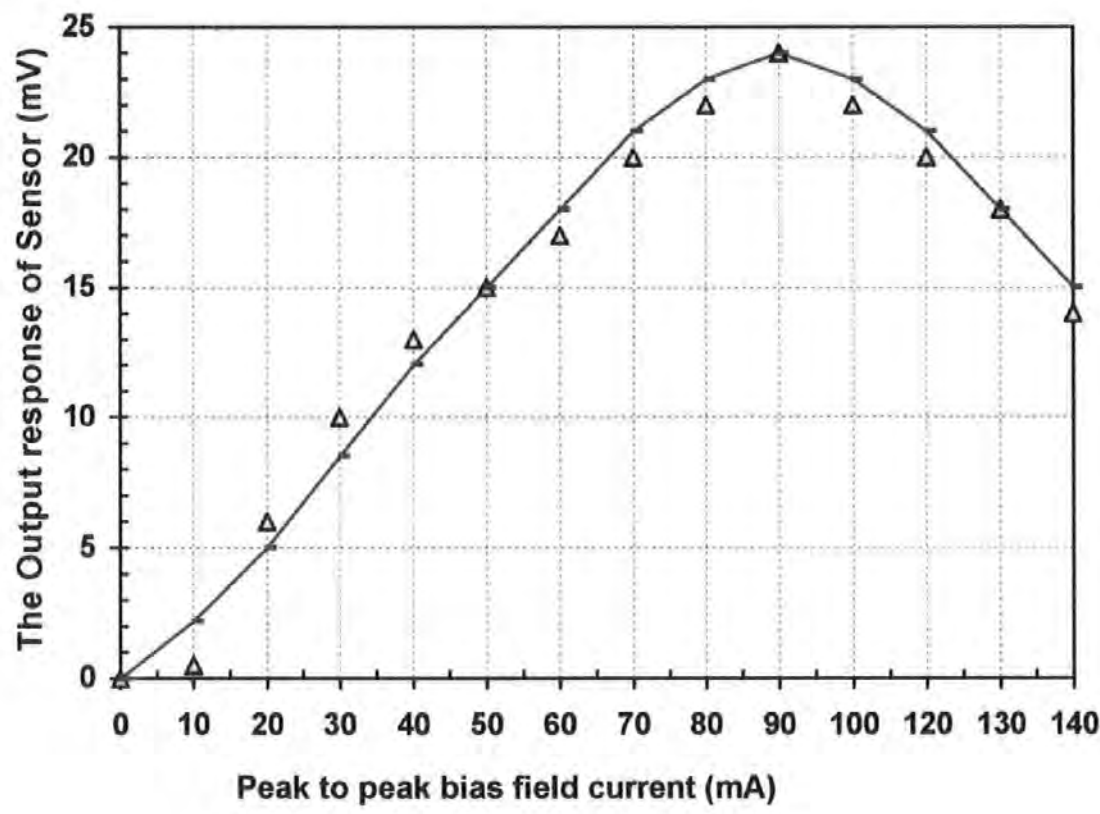


Figure 4.41 The output response of a 80  $\mu\text{m}$  wide, 10 nm thick sensor versus 250 Hz bias field (0.00906 Oe or 0.72 A/m per mA) for an applied field ( $\delta H$ ) of about 160 nano-Tesla

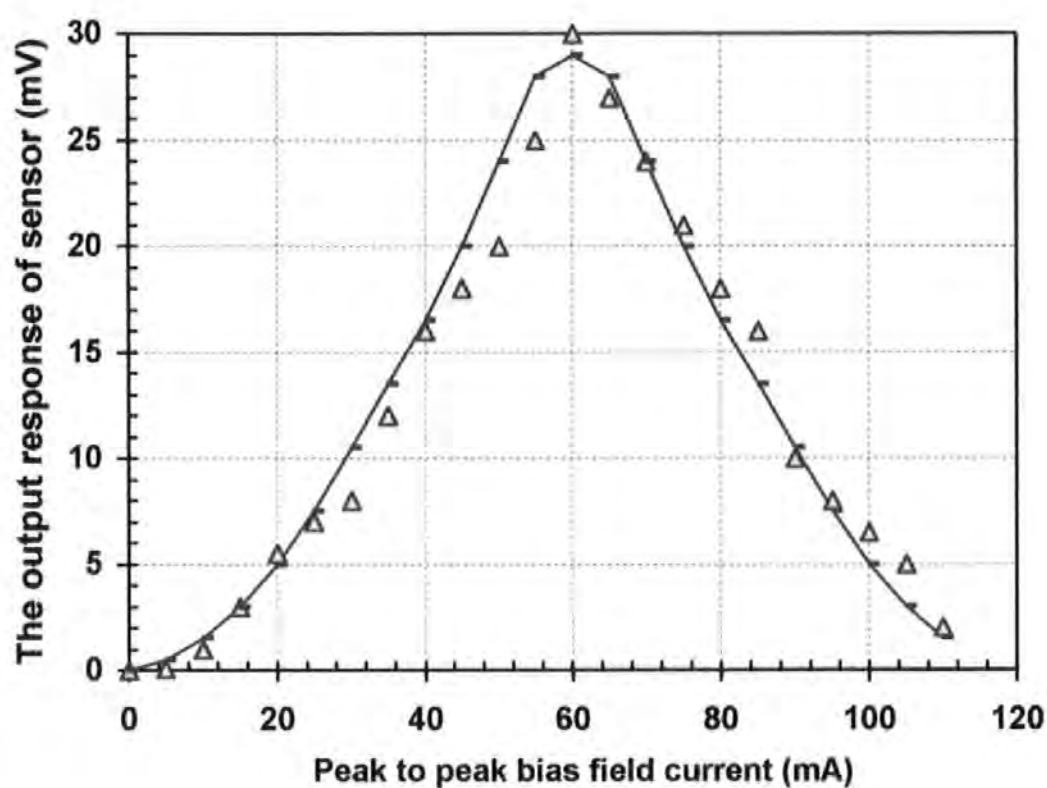


Figure 4.42 The output response of a 80  $\mu\text{m}$  wide, 7.5 nm thick sensor versus 250 Hz bias field (0.00906 Oe or 0.72 A/m per mA) for an applied field ( $\delta H$ ) of about 160 nano-Tesla.

### **4.3. Discussion**

As can be seen from section 4.1.1 to 4.1.3, magnetic properties such as coercivity and domain structure in thin  $\text{Ni}_{81}\text{Fe}_{19}$  films such as those below 30 nm thick exhibit marked differences with those in thicker films. Films with thicknesses in this range show a minimum in coercivity at a thickness of 7.5 nm where the grain size is about 5 nm. There are also distinct differences in the magnetic domain structure and magnetisation between the very thin  $\text{Ni}_{81}\text{Fe}_{19}$  films with and without a 5 nm Ta underlayer.

The correlation of the magnetic properties with the  $\text{Ni}_{81}\text{Fe}_{19}$  Permalloy films microstructure will be discussed in this section in conjunction with the classical models and theoretical development. Special attention is paid to the possible mechanisms of coercivity.

#### **4.3.1. Coercivity variation**

##### **I. Film thickness**

From Figure 4.1(a), it seems that the coercivity of these magnetic thin films is dependant on their thickness and there is a similar minimum in coercivity for about 7.5 nm film thickness in each case. The coercivity variation in two sets of films in a wider thickness range from 2.5 nm to 100 nm are also given in Figure 4.1.(b). In the range from 2.5 nm to 100 nm, the coercivity variation as a function of film thickness can be roughly divided into four ranges and described as follows:

- 2.5 to 7.5 nm: the coercivity increases with reducing film thickness. There is a minimum coercivity at a thickness of 7.5 nm.

#### *Chapter 4: Results and Discussion*

- 7.5 to 27.5 nm: the coercivity increases with increasing film thickness. There is a maximum in coercivity at a thickness about 27.5 nm.
- 27.5 to 50 nm: the coercivity decreases and then increases slightly with increasing film thickness. There is a minimum in coercivity at a thickness of about 40 nm and another maximum in coercivity at a thickness around 50 nm.
- 50 to 100 nm: the coercivity variation of films seems to be near constant with slightly increases or decreases until 100 nm.

It is surprising that these results do not seem to agree with the well known '4/3' law [Akhter et al., 1997]. Many experimental results (e.g. ref. [Mapps et al., 1991]) have been previously reported and show that the coercivity of magnetic thin films increases with decreasing film thickness and the variation of coercivity with film thickness agrees with  $t^{-4/3}$ .

Further studies of the variation of coercivity with film thickness have been carried out both in the literature and by experiment. Repeatable results have been obtained in this study and some films were also examined by CTEM, HRTEM and Lorentz TEM as shown in section 4.1.2.

It is well known that the coercivity of these films, in fact not only relate to the film thickness, but also depends on other factors such as composition and deposition conditions so the  $H_c$  mechanism proposed by Néel can not be only one. As stated in section 2.3.3, this '4/3' law is based on the assumption (a) the coercive force due to thickness variations dominates other effects and (b) that  $dt/dx$  (surface roughness) is independent of the thickness itself. Both assumptions are risky and the fact that deviations are found in experiments is 'not surprising' [Middelhoek, 1961].

#### *Chapter 4: Results and Discussion*

This '4/3' law has been queried by some researchers both in the experiments such as [Methfessel, et al., 1960], [Middelhoek, 1961], [Noreika & Francombe, 1962], [Prupton, 1964<sup>a</sup>], [Lo & Hanson, 1969], [Lo et al., 1987] and in the theories, for example, [Middelhoek, 1961]. The discrepancy was considered due to the differences in sample preparation [Lo & Hanson, 1969], chemical in-homogeneity [Noreika & Francombe, 1962] and measurement technique and not debated for many years [Ciureanu, 1992].

It was found that the comparison between the '4/3' law and experiment may start from the beginning of 1960's, when it was reported that for evaporated permalloy films, a maximum in coercivity was found at a thickness of around 75 nm [Methfessel, et al., 1960]. This maximum coercivity has been correlated with the possible transition from Néel to Bloch type domain walls.

Similar results were also found and reported by Middelhoek [Middelhoek, 1961]. Figure 4.43 shows the coercivity  $H_c$  variation in the easy direction as a function of the thickness. This is based on Figure 4.1b and together with a dotted line  $c$ , which is reprinted from reference [Middelhoek, 1961]. It can be seen from the curve  $c$  in Figure 4.43, that the 4/3 law of Néel seems only correct for Bloch walls in thick films such as  $t > 85$  nm. For thinner films, where Néel and Cross-tie walls occur, the 4/3 law loses its validity. There is a minimum in coercivity at about 45 nm and a maximum in coercivity at about 75 nm in line  $c$ . They concluded that this relative maximum is related to the transition from Bloch to Cross-tie wall and it was believed that the transition was associated with the decrease of coercivity [Middelhoek, 1961].

Figure 4.44 is a diagram showing the type of domain wall to be theoretically expected and experimentally observed as a function of the film thickness and the angle through



which the magnetisation turns in the wall. This is taken from reference [Middelhoek, 1963]. They assume that a magnetic field is applied in the hard axis. Under the influence of this field the magnetisation in domains on both sides of the wall will make an angle  $\phi_0$  or  $-\phi_0$  with the hard axis. In our experiments no hard-axis field was applied during observation so the angle  $2\phi_0$  of less than  $180^\circ$  happened naturally in zero applied field (e.g. see Figure 4.16). More details about the theoretical calculations and experiments also can be found in this reference. For example, the thickness at which the transition from Cross-tie to Bloch wall occurs is 85 to 90 nm. Furthermore, Néel walls dominate when roughly  $2\phi_0 < 150^\circ$ . Bloch walls occur for the thick films ( $> 90$  nm) and Cross-tie walls for the relative thin films ( $< 90$  nm but  $> 20$  nm).

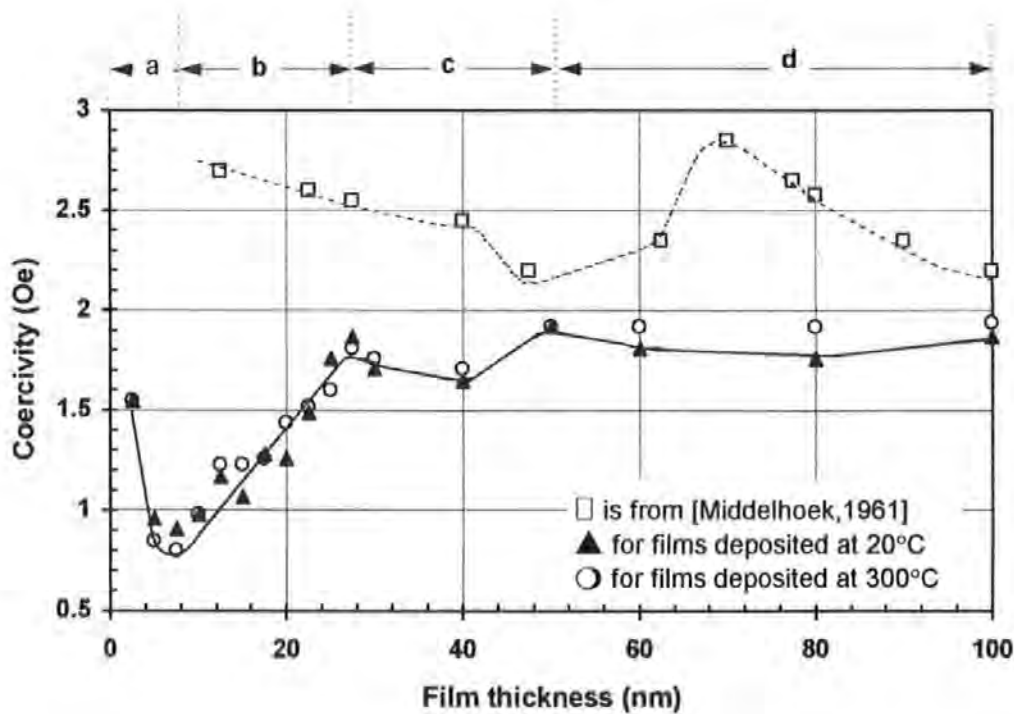


Figure 4.43 Showing the coercivity ( $H_c$ ) variation in the easy direction as a function of film thickness. The solid line is based on Figure 4.1b and the dotted line is after [Middelhoek, 1961]

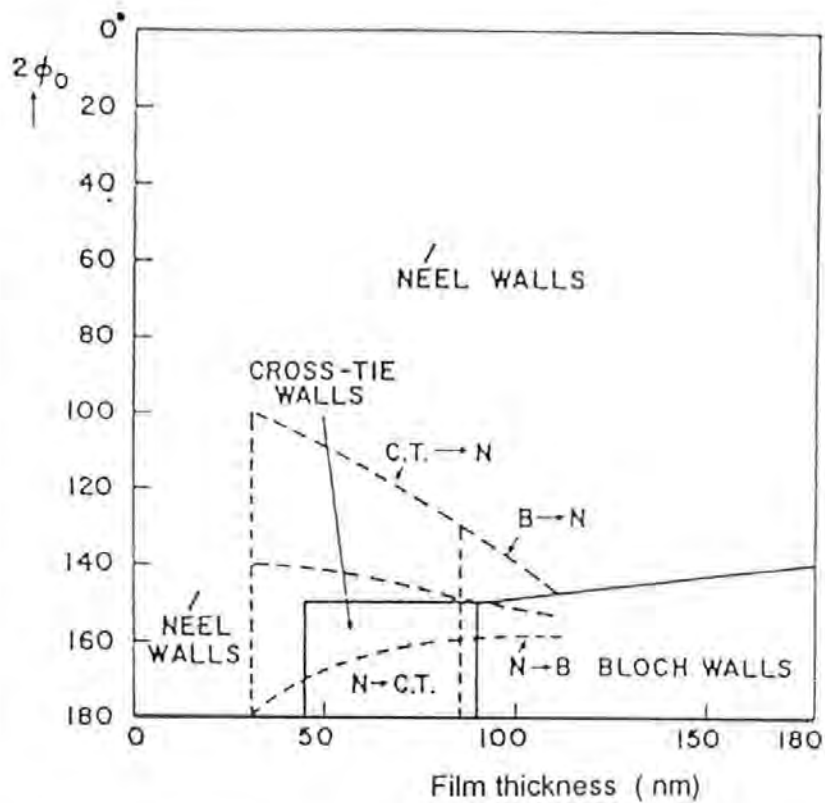


Figure 4.44 Diagram showing the type of wall to be theoretically expected (solid lines) and experimentally observed (dashed lines) as a function of the angle  $\phi_0$  (between magnetisation outside the wall and the direction normal to the wall) and the film thickness. (after [Middelhoek, 1963])

## II. The type of domain wall and the transition between walls

It has been reported by many researchers that the coercivity variation of magnetic thin films is related to the change of domain wall structure such as [Middelhoek, 1963], [Pruyton, 1964<sup>bl</sup>], [Lo & Hanson, 1969], [Grundy, 1997]. It can be clearly seen from Figure 4.44, there are three types of wall in the thickness range  $< 100$  nm and two possible transitions, one is from the Néel wall to the Cross-tie wall and another is from the Cross-tie wall to the Bloch wall.

#### *Chapter 4: Results and Discussion*

From our experiments shown in Figure 4.1.(b), and together with the observation by Lorentz TEM, a possible explanation about the coercivity variation related to the change of the type of wall can be given by:

- (a) 2.5 to 7.5 nm: Néel wall only but less continuous film. The coercivity increases with reducing film thickness due to inclusions etc.
- (b) 7.5 to 27.5 nm: Néel wall is the norm (continuous film), and the coercivity increases regularly with increasing film thickness.
- (c) 27.5 to 50 nm: Néel wall reducing, Cross-tie wall occurs and becomes the norm. The coercivity relating to Néel walls increases with increasing film thickness. Two peaks may relate to the possible transition between walls, such as from the Néel wall to the Cross-tie wall (at about 27.5 nm) and the Cross-tie wall to the Bloch wall (at around 50 nm). The relative minimum in coercivity at thickness around 40 nm may relate to the coercivity variation of Cross-tie wall with thickness due to the change in Cross-tie density (walls/mm) and Cross wall length [Middelhoek, 1963].
- (d) 50 nm to 100 nm: Néel wall (tend to zero) + Cross-tie wall (increasing then decreasing) + Bloch walls (becoming the norm). The coercivity variation of films in this thickness range is very complex and may depend on the variation of the total wall energy, which relates to the possible transition between the walls and relative energy contribution from these three walls. The energy of Bloch walls decreases with increasing film thickness in this range.

The Lorentz TEM results shown in section 4.1.1 and 4.1.2 are in agreement with the above explanation for the film thicknesses in range (a) and (b), partially correct for (c)

but there are no TEM results for (d). Further studies are needed both in theory and experiment.

The Bitter technique observations [Middelhoek, 1963] show that the Bloch-Néel wall transitions when increasing the field do not occur at the same field as the Néel-Bloch wall transitions on decreasing the field. Generally a hysteresis occurs in the wall transitions. The coercivity of these hysteresis loops depends on the film characteristics. If we consider that the average of the fields at which the transitions occur is the transition field. Then under the influence of the film characteristics, the disagreement between experimental results and agreement between experiment and theory seems to be reasonable and rather satisfactory.

As was reported by [Yeh et al., 1987], the Néel wall model (see Equation 2.6), is based on the assumption that the magnetisation rotates parallel to the film plane only so that the total wall energy has almost entirely no magnetostatic contribution. Both the exchange and the anisotropy contribution have been neglected in the Néel wall energy model. Unfortunately, when the thickness of film is very much smaller, such as less than 20 nm, the relative contribution from exchange, anisotropy and magnetostatic energy may become very complex [Ground, 1997].

No comprehensive data on the variation of coercivity with the distribution of these energies in films (relating to the transition between types of wall) over this thickness range have yet been published so evaluation of their effects on the coercivity cannot be made.

### III. Width of domain wall

Experimental results for observation by Lorentz TEM in this study show that the wall width of  $\text{Ni}_{81}\text{Fe}_{19}$  films without Ta in the thickness from 10 to 30 nm is approximately 100 nm.

In the case of curve (d) in Figure 4.1 (a), for films with 5 nm Ta underlayer, the width of walls observed by Lorentz TEM is about 300 nm.

As can be seen from Table 4.1, most experimental results show that the grain sizes of films with and without Ta underlayer are similar for the same thickness. According to Equation 2.18,  $H_c \propto D/w$  and the coercivity is proportional to the film thickness (grain size) but inversely proportional to the width of the wall, which is in good agreement with the experimental results in the thickness range from 7.5 nm to about 30 nm. Furthermore, the lower coercivity and Barkhausen Noise can be improved by using a Ta underlayer due to the experimental fact that the domain wall width of films with Ta is much wider than those of films without Ta underlayer [Akhter et al., 1998].

#### IV. Grain size

It is well known that the grain size of these films is proportional to film thickness but may be affected by other factors such as type of underlayer and substrate temperature. As can be seen from Table 4.1 and Figure 4.6, the variation of coercivity of  $\text{Ni}_{81}\text{Fe}_{19}$  films may depend on the grain size of the films. The experimental results show that the average crystallite size of these films is of the order of a few or a few tens of nm (typically 3 to 40 nm) within the thickness range from 2.5 to 30 nm. The TEM observation results also show that the very thin  $\text{Ni}_{81}\text{Fe}_{19}$  films are polycrystalline with a small grain size and random texture.

#### *Chapter 4: Results and Discussion*

It is well known that the good soft magnetic properties of magnetic materials require very large grains, which reflects the classical rule (e.g. Néel wall model). Recently, some researchers have been reported that good soft magnetic properties can also be found in the nanocrystalline materials and amorphous materials [Herzer, 1990,1991 and 1993], [Yoshizawa et al., 1988], [Grundy, 1997].

Amorphous films have lower coercivity because of the apparent absence of any discontinuities, at least on a scale approaching the domain wall width, so amorphous films can be extremely soft [Grundy,1997].

Very small coercivities can be realised and these are related to a uniform, nanocrystalline ( $< 10$  nm) microstructure [Lin et al., 1994] with the fairly high anisotropy of each grain moderated due to the large number of nano-crystallites in the characteristic coupling volume ( $1\text{ }\mu\text{m}$ ) [Takahashi and Shimatsu, 1990], [Grundy, 1997].

As described in section 2.3.3, Equation 2.17 and 2.18 show that the coercivity is proportional to  $w/D$  when grain size is greater than the width of wall ( $D \gg w$ ), but will become opposite when  $D \ll w$ . It is plausible that the coercivity will have a maximum when  $w$  and  $D$  are of the same order of magnitude, which has been in good agreement with experimental results as described in section 4.1.1.1.

Compared to the experimental data as shown in Figure 4.1a, 4.1.b, 4.6 and Table 4.1, the equation 2.18 may be also of some help for understanding why lower coercivities can be found in thin Permalloy films of thickness below 30 nm, which corresponds to a grain size smaller than 25 nm. The assumption ( $D \ll w$ ) is relevant here, so the coercivity decreases with decreasing film thickness in a range from 30 to 7.5 nm. It also indicates that films with relatively smaller grain size such as the films deposited on Ta underlayer,



may have lower coercivity than the films with relative greater grain size such as deposited on a Cr underlayer. Comparing the change in coercivity and grain size against thickness for such thin films, it is clear that as the grain size changes so does the coercivity. There is a minimum coercivity at a film thickness of 7.5 nm and a corresponding grain size of about 4 nm.

As can be seen from Figure 4.1a, 4.1b, 4.6 and Table 4.1, some experimental data show that, in fact, greater average grain size does not mean higher coercivity even if the films have the same thickness. Such a phenomenon seems in contrast to this model. Moreover, experimental data shows that the coercivity in these films depends on the grain size but no quantitative relationship has yet been seen.

For films (see Figure 4.1a) thinner than 5 nm, the TEM images show that the films become discontinuous leading to a large increase in non-magnetic 'holes' and inclusions that may result in a corresponding increase in coercivity and Barkhausen noise. If the film deposition processes could be improved to realise continuous films at thicknesses below 7.5 nm, then a lower coercivity and lower coercivity and lower Barkhausen noise performance can possibly be obtained.

Although there is some agreement between these models and experimental results, arguments are still to be expected when considering the other possible origins of coercivity such as stress, underlayer effects and surface roughness etc. In particular, such factors may play a more important role when film thicknesses reduce to a few or a few tens of nanometers. However, these models have provided some qualitative insight into the understanding of the variation of coercivity in very thin  $\text{Ni}_{81}\text{Fe}_{19}$  films and produced limited correlation with the experimental data presented here.



There is insufficient experimental data and theory describing the variation of the magnitude of coercivity with structural parameters for the  $\text{Ni}_{81}\text{Fe}_{19}$  films of thickness below 30 nm so the correlation between the micro-structure and coercivity in such films cannot be clearly evaluated. However, the coercivity of ferromagnetic films is not a well understood parameter and the theory of coercivity may be developed further [Pruett 1964<sup>b</sup>], [Kim and Oliveria, 1992], [Grundy, 1997].

### **4.3.2 Ta Underlayer effect**

In 1993 & 1994, Galitier et al., reported progress in the study of  $\text{Ni}_{80}\text{Fe}_{20}$  films, which have very similar properties to  $\text{Ni}_{81}\text{Fe}_{19}$  films. They found that for  $\text{Ni}_{80}\text{Fe}_{20}$  thin films with thickness below 100 nm, the nature of the underlayer deeply affects the structural characteristics such as grain size and texture, and is responsible for the observed magnetic properties. The coercivity of  $\text{Ni}_{80}\text{Fe}_{20}$  films (in hard axis) can be reduced from 1 Oe (8 A/m) to 0.1 Oe (0.8 A/m) by using a 5 nm Ta underlayer instead of Cr. Observation by transmission electron microscopy, shows that the permalloy ( $\text{Ni}_{80}\text{Fe}_{20}$ ) thin films deposited on Ta underlayers were strongly (111) textured and obtained smaller grain size. In the case of a Cr underlayer, permalloy thin films were mostly randomly textured and had a relatively large grain size. This suggests that the preferential orientation observed in permalloy films sputtered on Ta appears to be the dominant parameter responsible for low coercivity [Jerome et al., 1994] and this also reported by other researchers such as [Rijks et al., 1995].

Similar results have been obtained in this study and extensive experimental evidence has shown that with a 5 nm Ta underlayer, the magnetic properties such as coercivity,

## *Chapter 4: Results and Discussion*

hysteresis and Barkhausen noise in very thin  $\text{Ni}_{81}\text{Fe}_{19}$  films have been improved [Akhter et al., 1997 & 1998], [Mapps et al., 1998].

- Domain walls and domain structures

Some of the most interesting phenomena observed in this work are the domain magnetisation and domain wall configurations in these films. There are distinct differences between films with and without Ta underlayers. As can be seen from section 4.1.2, with no Ta underlayer the domain walls are very thin irregular, closely spaced and have cross-tie walls. Domain wall widths in this case are about 100 nm. Also the domain magnetisation varies in angle from 90 to 180° in adjacent domains with a strong rippling. In the case of a 5 nm Ta underlayer, the domain walls are wider, straighter and have less cross-ties, the domain magnetisation changes in angle by 90° across the wall with no rippling and the width of domain walls is about 300 nm. The domain size in the permalloy films is much bigger than the ones without Ta and is independent of the film thickness in the range from 5 nm to 30 nm.

Unfortunately, no other similar observations have been yet reported so that comparisons can not be made.

- Ta underlayer

It is well known that when a film is deposited on a crystalline underlayer or substrate, the orientation of the initial nucleation layers ( a few atomic layers) will be affected by the crystallographic orientation of the underlayer or substrate. When the film thickness

#### *Chapter 4: Results and Discussion*

reduces to the molecular level, the effect of an underlayer or substrate may play a more important role in the orientation of the film [Ohring, 1992].

There are two kinds of crystal structure of Ta. The bulk crystal structure of Ta is bcc texture with a lattice parameter of  $a$  (in OXY plane) about 0.234 or 0.331 nm [Galtier et al., 1994] and [Gill and Yamashita, 1984]. When sputtered in a thin film form, in general, it has an hcp crystal structure ( $\beta$ -Ta) with lattice parameters  $a$  about 0.235 or 0.283 and  $c$  (along OZ axis and perpendicular to the OXY plane) about 0.534 (varying with deposition conditions). It was reported by [Gill and Yamashita, 1984] that the hcp-Ta grains were more well-developed than the bcc-Ta, which may favour and influence the epitaxial growth and preferred orientation of some films.

The crystalline anisotropy in the (111) plane of permalloy is smaller than the other planes, so the increase of the effective anisotropy by grain growth is expected to be smaller than those of other oriented films resulting in smaller coercivity and good thermal stability [Pfeifer and Radeloff, 1980], [Li et al., 1994]. Sputtered  $\text{Ni}_{81}\text{Fe}_{19}$  films have an fcc crystal structure and may exhibit a predominantly (111) texture with  $\Delta\theta_{50}$  ranging between  $9^\circ$  to  $10^\circ$  [Yeh et al., 1987]. It was reported that the (111) d-spacing for sputtered  $\text{Ni}_{81}\text{Fe}_{19}$  films is about 0.2043 nm which corresponds to a lattice parameter of about 0.3539 nm [Yeh et al., 1987].

Frank and van der Merwe introduced a theoretical explanation in 1949, and predicted that any epitaxial layer having a lattice parameter mismatch with another layer (or substrate) of less than  $\sim 9\%$  would grow pseudo-morphically, i.e., for very thin films the deposit would be elastically strained to have the same inter-atomic spacing as the substrate [Ohring, 1992].

It may be difficult to say whether the fcc  $\text{Ni}_{81}\text{Fe}_{19}$  film lattice and Ta (bcc or hcp) lattice match well due the lack of sufficient experimental data., but this could result in a minimum interface stress. Further study such as with cross-section TEM observation may provide more information.

On the other hand, Ta is one of the transition elements, which can exhibit texture or randomly oriented microstructure or an amorphous atomic arrangement [Grundy, 1997]. When Ta is like an amorphous material, the effect from the underlayer should be less than those from a crystalline underlayer. It may be a possible explanation why the grain size of permalloy films deposited on Ta is smaller than films deposited on Cr. In view of the amorphous-like nature of Ta, the magnetic properties of permalloy films with Ta should to be similar to that of films deposited directly onto a glass substrate, but the Lorentz TEM images obtained in this study show this assumption was not correct.

Like coercivity, the effect of a Ta underlayer on the orientation of a  $\text{Ni}_{81}\text{Fe}_{19}$  film is a complex phenomenon and many probable reasons are yet not well known due the lack of sufficient experimental data.

#### 4.3.3 Thermal effects

The origin of [111] permalloy films on heated glass surfaces ( $260 \sim 500^\circ\text{C}$ ) has been reported but the reasons for the orientation are not certain [Bauer, 1963], [Pruett, 1964<sup>b</sup>]. A similar effect was also found by using a suitable annealing treatment (less than  $300^\circ\text{C}$  for  $\text{Ni}_{81}\text{Fe}_{19}$  films) [Narayan et al, 1992], [Li et al., 1994].

Figure 4.45 is an example which is calculated by using Equation 2.19 and 2.20 based on the ripple model , and is taken from reference [Hoffmann, 1979]

As can be seen from Figure 4.45, the calculated results of Hoffmann show that a substrate temperature of about 290°C gives minimum values for Structure Constant  $S$  ( $S = \frac{K_s D \sigma_1}{\sqrt{n}}$ ). The permalloy films with minimum  $S$  are the best possible approximations to ideal films (for which  $S=0$ ). At higher substrate temperature the crystallite size increases while at lower temperatures the intrinsic strains in the evaporated films increases, and both processes increase  $S$ . This theory has produced in good agreement with our experimental results shown in section 4.1.1.1.

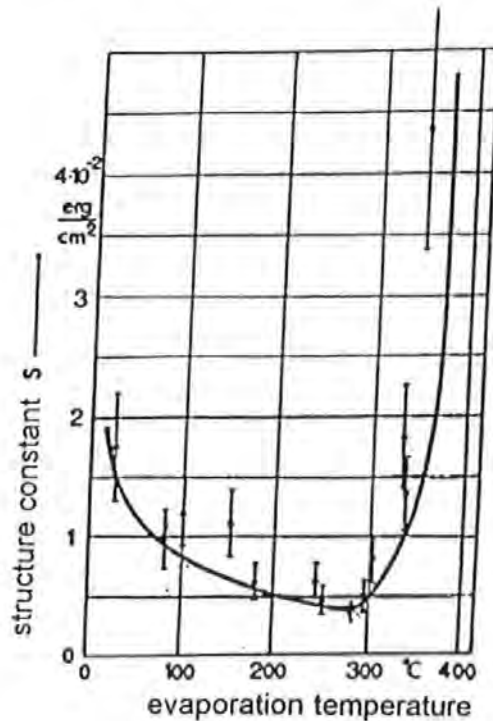


Figure 4.45 The dependence of the structure constant on evaporation (substrate) temperature for  $\text{Ni}_{81}\text{Fe}_{19}$  films (after [Hoffmann, 1979])

As Hoffmann said, practically all the magnetic properties of thin ferromagnetic films depend on the film structure but it is not possible to give an exhaustive description of all the relationships between magnetic properties and film structure. The film structure is

characterised by the crystal lattice, the range of ordering, the grain size, the film geometry (mainly the film thickness) and intrinsic stresses as well as film production conditions. However, it would be quite inappropriate to investigate the dependence of some magnetic properties on only one or two parameters without knowing the influence of these parameters on the film structure. In particular, some fundamental magnetic properties of permalloy films are now being changed due to the development of new techniques and applications. Therefore, further study of the correlation between the magnetic properties such as coercivity and  $\text{Ni}_{81}\text{Fe}_{19}$  film microstructure is needed and should be performed both in the theory and experiment.

## **CHAPTER 5**

### **CONCLUSIONS AND FUTURE WORK**

#### **5.1 Conclusions**

##### **5.1.1 Coercivity**

The effect of thickness and grain size on the coercivity of  $\text{Ni}_{81}\text{Fe}_{19}$  permalloy thin films deposited by r.f. sputtering with negative substrate bias is systematically investigated as a function of under-layer materials, film thickness, and substrate temperature. The results show that there is a minimum coercivity at a thickness of about 7.5 nm with a grain size of 4 nm. The experimental data indicates that the coercivity of very thin  $\text{Ni}_{81}\text{Fe}_{19}$  permalloy films in the range from 2.5 to 30 nm is dependant on the film thickness. It is affected by the nature of underlayer and substrate material as well as the deposition temperature. The reduction of coercivity in very thin  $\text{Ni}_{81}\text{Fe}_{19}$  permalloy films has been achieved by using a 5 nm Tantalum underlayer or depositing the films at a suitable elevated substrate temperature of about 280°C. This may be attributed to the grain size and domain wall width variation. A tantalum underlayer favours a (111) (low anisotropy) surface plane in  $\text{Ni}_{81}\text{Fe}_{19}$  permalloy films. Elevated deposition temperature may reduce defects in the films and may enhance the (111) orientation.

##### **5.1.2 Domain walls and Barkhausen noise**

A comparison of the magnetic domain wall structure and the state of magnetisation in the very thin (5 ~ 30 nm)  $\text{Ni}_{81}\text{Fe}_{19}$  permalloy thin films with and without a Ta under-layer



was observed by Lorentz TEM. The observation results suggest that the domain wall configuration and magnetisation may play a dominant role in the magnetic properties of these permalloy thin films for applications such as recording heads and sensors. The domain configuration, domain walls and magnetisation in very thin permalloy films deposited on Ta underlayer exhibit distinct differences with the ones without Ta. With no Ta underlayer, the domain walls are very thin irregular, closely spaced and have cross-tie walls. Domain wall width in this case is about 100 nm. Also the domain magnetisation varies in angle from 90 to 180° in adjacent domains with a strong rippling. In the case with a 5 nm Ta underlayer, the domain walls are wider, straighter and have fewer cross-ties. The domain magnetisation changes in angle by 90° across the wall with no rippling. The width of the domain walls is about 300 nm. The domain size in the permalloy films is much bigger than the ones without Ta and is independent of the film thickness in the range from 5 nm to 30 nm. The results suggest that by using tantalum as an underlayer, a reduction in the Barkhausen noise of sensors can be achieved.

Barkhausen noise studies of films were carried out by sweeping an ac field of 77 Hz onto the permalloy films and recording the induced search-coil output voltage due to the flux change as a function of time on a digital storage oscilloscope. Experimental results show that the films deposited on normal glass substrates have more Barkhausen noise than the ones deposited on Ta underlayer or at an elevated temperature (e.g. 280°C).

### 5.1.3 Switched-bias Sensor

A highly sensitive magnetoresistive sensor has been designed and fabricated by photolithography in a temperature and humidity controlled clean room. Sensor

## *Chapter 5: Conclusions and Future Work*

thicknesses are typically in the range from 5 nm to 40 nm and other dimensions typically (10  $\mu\text{m}$  ~ 80  $\mu\text{m}$  wide) and 6.4 mm long. Two sets of sensors with and without a 5 nm tantalum underlayer have been completed and about 120 types of sensors are available within 30 substrates.

Barkhausen noise and corresponding magnetic hysteresis of the sensor were studied by analysis of the M-R response of various sensors together with their magnetoresistive hysteresis. The properties of sensors with and without Ta were compared with and without a suitable external high frequency field (5 kHz to 20 kHz), by which the hysteresis of sensors can be reduced. The best linearising frequency appears to be about 10 kHz when the forward and reverse MR curves coincide although linearising fields at frequencies close to 10 kHz are found to be almost as effective. The linearising field required is quite small, typically around a 0.2 Oe or 16 A/m.

Variation in the sensitivity of the sensor to the magnitude of a switched-biasing field was measured by applying a very small alternating field and varying a transverse dc field component ( $H_x$ ). The effect of biasing field frequency and external linearising field on the sensitivities of the MR sensors was studied using an in-house built measurement system. Experimental data shows that the switching field of such sensors required is quite small and may be around a few tens of A/m (e.g. about 21.7 A/m or 0.27 Oe in the case of Figure 4.42).

The results show that the sensor is linear in the range from zero to 16,000 nT. The sensors produce an almost noise-free output of 20 ~ 30 millivolts for a field change of about 160 nano-Tesla. Because of its switched-bias nature, the sensor can be used with a

lock-in amplifier to produce an output which excludes any extraneous noise at frequencies other than the bias switching frequency of the sensor.

## **5.2 Future work**

The very thin  $\text{Ni}_{81}\text{Fe}_{19}$  permalloy film sensor developed in this study exhibits excellent M-R response and produces an almost noise-free output of 20 ~30 millivolts for a field change of about 160 nano-Tesla. The output of such a sensor is linear over quite a wide range if used to measure very small fields in the tens or hundreds nano-Tesla region. Further development of such sensors offers users the possibility of detecting much smaller fields such as a few tens nano Tesla or even lower and are of considerable interest for future M-R sensor applications.

It is also necessary to undertake further microstructure observation and performance examination of such sensors by high resolution TEM and Lorentz microscopy and to combine such examinations with Barkhausen noise analysis and MR response measurement. Such fundamental studies will greatly favour the thorough understanding of the correlation between the microstructure of  $\text{Ni}_{81}\text{Fe}_{19}$  permalloy films and the performance of such sensors, so that more knowledge about the limitations of sensors will be clear. The effect of a Ta underlayer on the microstructure of very thin  $\text{Ni}_{81}\text{Fe}_{19}$  permalloy films may be of some interest to future generation of sensors such as GMR, TMR and CMR. Therefore, further studies of this effect are also needed.

Limited experimental results of sensor performance have shown that the sensor is capable of detecting changes much smaller than 160 nano-Tesla (e.g. a few tens or a few nano-Tesla) under ideal conditions. The fabrication of many sensors has been carried out

## *Chapter 5: Conclusions and Future Work*

but the performance of all of the sensors has not yet been examined due to the limitations of time and the test system. This should be completed in the future. Further study of the optimisation of the insulating layer, new sensor structural design (e.g. add thin film flux concentrator [Smith et al., 1991]) and proper controlling of sensor performance during fabrication is needed so that new opportunities in the detecting of much weaker magnetic fields may be found and achieved [Mapps et al., 1998].

## *Appendix*

### **APPENDIX**

(Publications)

# Optimisation of Material and Structure for a Switched-bias Magnetoresistive Sensor

D J Mapps,<sup>\*</sup> Y Q Ma<sup>\*\*</sup> and M A Akhter<sup>\*\*\*</sup>

Centre for Research in Information Storage Technology, SECEE, University of Plymouth, Plymouth PL4 8AA, U. K.

## Abstract

This paper describes research on a magnetoresistive sensor consisting of two differentially connected Permalloy stripes with an overlay bias conductor (see ref. 1). A magnetic field derived from current flowing in the bias conductor switches the magnetisation in the sensor stripes alternately in opposite directions for each half-cycle of the bias field current. The material of the sensor is optimised for lowest Barkhausen noise (see ref. 2) and lowest demagnetising field. A number of sensors have been prepared with film thicknesses of 5 to 40 nm, stripe widths varying between 10 to 80  $\mu\text{m}$  and a standard length of 6 mm. Barkhausen noise and corresponding hysteresis is studied by analysis of MR response of the group of sensors, together with their magnetoresistive hysteresis, which may be reduced or improved by using a suitable external high frequency field (5 to 20 kHz). Variation in the sensitivity of the sensor to the magnitude of a switched-biasing field was measured by applying a very small alternating field (variable from a few tens to hundreds nano-Tesla) and a varying transverse dc field component ( $\delta H_x$ ). Advantages and limitations of the sensors will be discussed in the paper.

**Keywords:** Magnetoresistance, Sensor, Switched-bias, Permalloy, Thin-Film

## 1. Introduction

There is increasing interest in the use of very thin magnetoresistive films to make sensors of small physical size with low coercivity, low Barkhausen noise and high signal-to-noise ratio [ref. 3, 4 and 8]. There are very few publications concerning the fundamental magnetic properties of very thin film devices similar to those studied here [ref. 5]. Little has been reported on the switched-bias type MR sensor which consist of a pair of sensors alternately switched with transverse fields in opposite directions via an overlay bias conductor. The ultimate resolution of such sensors for detecting very small fields in the nano-Tesla region has not been fully explored therefore application limits are not yet recorded [ref. 6].

In our previous papers, dependence of coercivity on thickness and grain size in permalloy films, suitable for these sensors, in the range from 2.5 to 30 nm [ref. 2], was presented. Barkhausen noise origin and characteristics of these films were investigated by differentiating the B-H characteristic along with study of magnetic domain wall structures using Lorentz TEM observation [ref. 7].

In this paper, we report new progress in this study including the behaviour of the MR response and hysteresis, the effect on the amplitude and frequency of

bias field, and the influence of a high-frequency external (linearising) field on the output characteristics.

## 2. The switched-bias Sensor

The switched-bias sensor as described in ref. 1 consists of a pair of identical MR thin-film stripes in a bridge circuit subjected to transverse fields applied via currents in two overlaid thin-film bias conductors shown in figure 1.

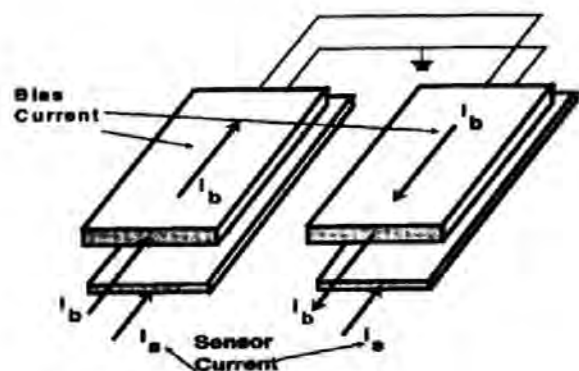


Figure 1 Diagram showing a typical Switched-bias Magnetoresistive sensor

\* Tel.: 0044-1752-232570; Fax: 0044-1752-232583; Email: dmapps@plymouth.ac.uk; \*\* E-mail: yma@plymouth.ac.uk \*\*\* E-mail: makhter@ecc.ac.ae



The transverse fields from these bias conductors are in opposite directions but are provided from the same current  $I_b$ , so that when  $I_b$  is reversed ( $I_b$  is a square-wave alternating current) the transverse bias field also reverses so that the bias point for each sensor switches to the other side of the MR characteristic and vice-versa. If the sensor is placed in a steady applied field the bridge is unbalanced and the output signal is a square wave whose amplitude is proportional to this steady field. One advantage of this system is that lock-in amplifier techniques can be used to extract the output signal almost totally free of noise, so making the sensor very effective for detecting small steady fields in noisy environments.

### 3. Materials and Geometry

Preparation procedure and structural characterisation of film used in this study has been described previously [ref. 2]. A number of sensors have been prepared for this investigation, the main structural dimensions are: (a) thickness ( $t_1$ ) of the permalloy layer used: 5, 7.5, 10, 15, 25 and 40 nm (b) widths ( $w_1$ ) of the etched permalloy stripes were 10, 20, 40, 60 and 80  $\mu\text{m}$  (c) length ( $l_1$ ) of the stripe = 6600  $\mu\text{m}$  (d) thickness ( $t_3$ ) of Cu bias layer = 0.55  $\mu\text{m}$  (e) width ( $w_3$ ) and length ( $l_3$ ) of bias stripe = 100  $\mu\text{m} \times 6000 \mu\text{m}$  (f) thickness ( $t_2$ ) of insulating layer = 1  $\mu\text{m}$  (g) the resistance of insulating layer  $\geq 40 \text{ M}\Omega$  (h) the thickness ( $t_4$ ) of Ta underlayer and capping layer is 5 nm. Figure 2 shows the geometric dimensions of sensor(s) and bias conductors.

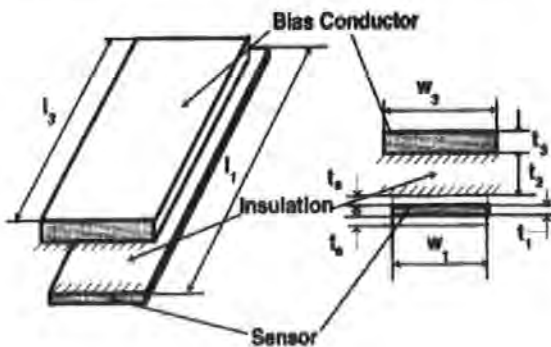


Figure 2 Showing the geometry of a Switched-bias MR sensor

In order to compare and check the effect of a Ta underlayer on the output of the sensors, two sets of sensor films with and without this Ta underlayer were prepared for sensor fabrication.

### 4. Experimental Details

#### 4.1. Fabrication

The total fabrication procedure consists of about 55 steps for each substrate and one set of eight photo-masks has been designed and used for the fabrication. 24 substrates (432 pairs of sensors) have been completed in this study.

#### 4.2. MR effect & Hysteresis Measurement

After preparation, the MR response and hysteresis loop for each sensor was obtained from a MR test instrument, purpose built at the CRIST Facility. The transverse field for the MR loop is set at  $\pm 20 \text{ Oe}$  and a typical current flowing in each sensor is 1 mA.

In order to reduce hysteresis in the sensors, a high-frequency external 'linearising' field method is used. This high-frequency field oscillates the magnetisation in the sensor so that the sensor magnetisation finds the lowest magnetic energy condition for all magnetisation conditions. In our experiments this high-frequency field at various amplitudes is applied both along the sensor long axis and transverse to it.

#### 4.3 Electronic drive and test system

A schematic diagram of the sensor electronics is shown in figure 3. The two sensors are connected as part of a Wheatstone bridge network with the output taken to a differential amplifier. The sensors are always biased in opposite directions so that any d.c. field ( $\delta H$ ) such as that produced from a pair of 10-turn Helmholtz coils used in this experiment, can unbalance the bridge. The output from the differential amplifier is a square wave containing some noise if the sensor is used to detect small fields. This output is fed into a lock-in amplifier and compared with a reference signal from the bias current used to 'drive' the bias stripes. This square-wave reference ensures that only signals of the same shape and repetition frequency will be registered in the output of the lock-in amplifier. This output is a d.c. level proportional to the applied field  $\delta H$ .

In addition to the applied field and sensor switching field (which can be from zero to 1 kHz) an additional high-frequency bias field can be supplied from another set of Helmholtz coils. This field reduces hysteresis and Barkhausen effects. The output from the lock-in amplifier is fed to an oscilloscope with an averaging capability to reduce any fluctuations in the output.

In the test system the substrate (which contains many prototype sensors) is mounted in a non-magnetic microprobe test system so that each dual sensor can be accessed and tested individually. Bias and sense currents can be supplied to the sensor and operational tests applied. The whole array is electrically screened by connecting all parts (including spare filaments in the microprobe card) to the system earth.



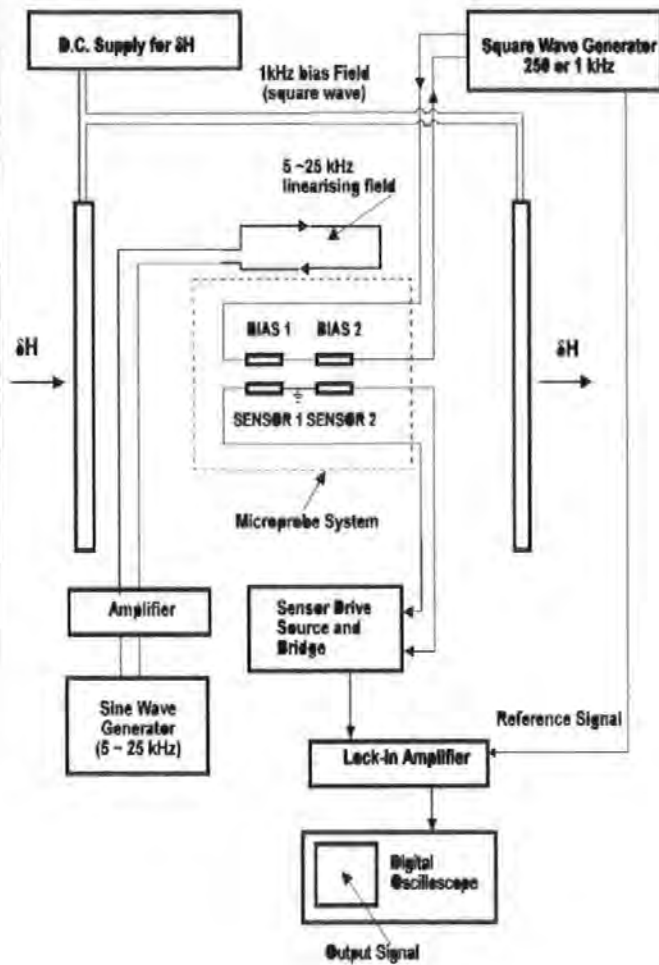


Figure 3 Electrical Schematic Diagram for Switched-bias MR Sensor

## 5. Experimental Results

### 5.1 Magnetoresistance/Field Characteristics

The MR/field characteristic is useful for checking the response of an MR sensor in respect of hysteresis and Barkhausen noise. An indicator of hysteresis is the separation of the forward and reverse curve around the vertical axis as shown by the apparent 'coercivity' in figure 4. In figure 4 the curves are from a 10 nm-thick sensor deposited on a tantalum film on a the glass substrate. In this case, with no high-frequency 'linearising' field applied, the separation of forward and reverse curves reaches a value of 0.7 Oersteds (55 A/m). Application of the high-frequency field along the sensor long axis reduces this for frequencies above 5 kHz. The best linearising frequency appears to be about 10 kHz when the forward and reverse MR curves coincide although linearising fields at frequencies close to 10kHz are found to be almost as effective.

### 5.2 Sensitivity to applied d.c. field ( $\delta H$ )

These results are shown in figure 5 for the sensor with 5 nm tantalum underlayer. The response is linear in all cases up to a maximum value of 16000 nT. It can be seen that the output is highly dependent on the magnitude of the switch-bias field, this is to be expected from the (bell) shape of the MR/ $\delta H$  characteristic seen in figure 4.

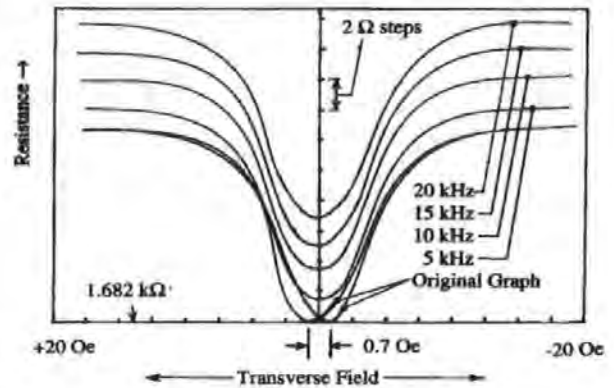


Figure 4 Graph showing the MR response and hysteresis variation of a 10 nm NiFe sensor (80  $\mu$ m wide) with 5 nm Ta underlayer vs. the frequency of linearising field (0.2 Oe)

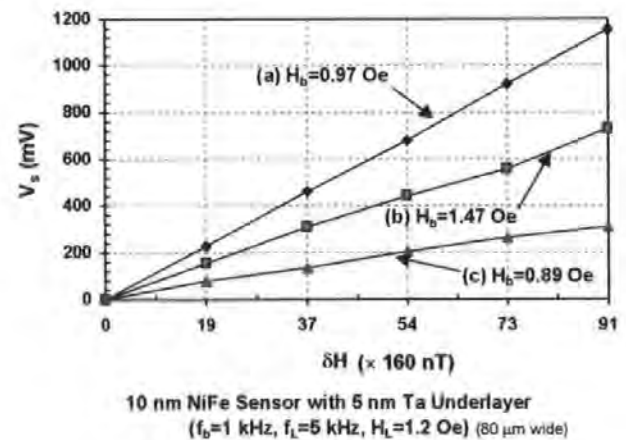


Figure 5 Showing the output of sensor vs. d.c. field for three bias fields

### 5.3 Optimum sensitivity to low fields

The curve of figure 6 is for an applied field ( $\delta H$ ) of 160 nano-Tesla. A convenient switched-bias frequency is chosen to match the low-pass filter in the lock-in amplifier system (250 Hz). The amplitude of the switch-bias current is varied and the output reaches a maximum at a current of 90 mA corresponding to a peak switch-bias field of 0.81 Oe (64 A/m). At this condition an output of 24 mV is obtained for a  $\delta H$  field of 160 nano-Tesla. The noise level on this output is less than 1 mV.

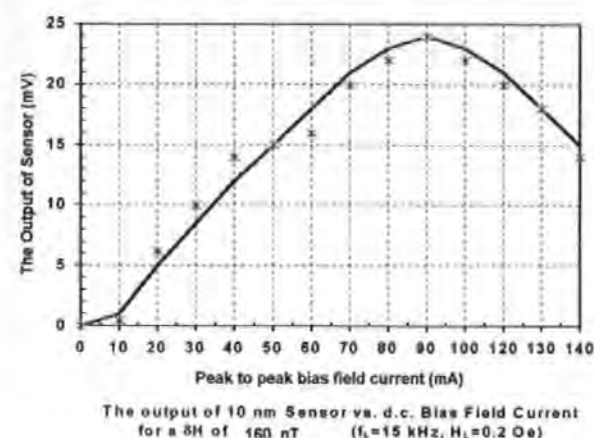


Figure 6 The output of 10 nm sensor vs. 250 Hz bias field (0.00906 Oe/mA) for an applied field ( $\delta H$ ) of 160 nano-Tesla

## 6. Discussion

The results show that the sensor is linear over quite a wide range if used to measure very small fields in the nano-Tesla region. This is surprising since, even when the sensor is not operating on the linear part of curve the differential system is sufficiently effective in maintaining linearity (see figure 5)

The result of figure 4 can be explained if it is realised that the effect of the tantalum underlayer is to promote microstructural growth in the NiFe film with its (111) crystallographic plane (Miller indices) parallel to the film surface. This leads to a more isotropic magnetic behaviour (see ref. 2 and 7).

In figure 6 the applied (constant) field ( $\delta H$ ) has been fixed at 160 nT which is some 300 times smaller than the earth's field. In this case the expected peak with switched-bias current is found, corresponding to the point of inflection on the MR characteristic. Because of the low noise level in this condition it appears that the sensor is capable of detecting changes much smaller than 160 nano-Tesla (e.g. a few nT) under ideal conditions.

## 7. Conclusions

A highly sensitive magnetoresistive sensor has been designed and fabricated. The sensor is linear in the range from zero to 16000 nT. It produces an almost noise-free output of several millivolts for a field change in the nano-Tesla range. Because of its switched-bias nature the sensor can be used with a lock-in amplifier to produce an output which excludes any extraneous noise at frequencies other than the bias switching frequency of the sensor.

## Acknowledgements

Thanks is extended to the University of Plymouth and all staff at the School of Electronic Communication and Electrical Engineering. In particular Mr S Warner and Mr P Brown at CRIST for their technical support.

## References

- [1] D J Mapps et al., A double bifilar magnetoresistor for earth's field detection, *IEEE Trans. Mag.*, Vol.23, No.5, (1987) 2413-2415.
- [2] M A Akhter, D J Mapps, Y Q Ma, A Petford-Long and R Doole, Thickness and grain size dependence of the coercivity of permalloy thin film, *J. of Appl. Phys.*, 81 (8), (1997), 4122-4124.
- [3] R Jerome et al, *IEEE Trans. Mag.*, Vol. 30, No.6 (1994) 4878-4880.
- [4] D J Mapps, Magnetoresistive Sensors, *J. of sensors and Actuators A* 59, (1997) 9-19.
- [5] D I Flynn, A New technique of noise reduction for large aspect magnetoresistor, *IEEE Trans. on Mag.*, Vol. 30, No.3, (1994) 1263-1266.
- [6] D J Mapps, British Patent No 2262635, 8<sup>th</sup> November 1991
- [7] M A Akhter, D J Mapps, Y Q Ma, A Petford-Long and R Doole, Domain walls and magnetic properties of very thin permalloy films for magnetoresistive sensors, in press *IEEE Trans. Magn.*, Vol. 34, (1998)
- [8] C Tsang et al., 5 Gb/in<sup>2</sup> Recording Demonstration with Conventional AMR Dual Element Heads & Thin Film Disks, *IEEE Trans. Magn.* Vol. 33, No5 (1997) 2866-2871.

## Biographies

\* *D J Mapps* is a Professor of Information Storage Engineering at the University of Plymouth, U. K.. He has authored or co-authored near 200 publications as well as a book chapter on Magnetoresistance. He is currently head of the Centre for Research in Information Storage Technology at Plymouth. He is a Fellow of the U. K. Institution of Electrical Engineers and the U. K. Institute of Physics.

\*\* *Y Q Ma* is a PhD candidate at the University of Plymouth, U.K. and currently involved in research on material and fabrication of M-R sensor. She received her B.Eng. degree in material science and engineering from the University of Zhejiang, China, in 1982, and experienced in the research and design of thin film, component, glass, ceramics, insulating materials and thermal engineering, and worked as a journalist as well.

\*\*\* *M A Akhter* is a Senior Lecturer in Electronics at the University of Plymouth. He is presently on sabbatical leave as Associate Professor at Etisalat College of Engineering, Sharjah, UAE. He has authored or co-authored near 27 papers on magnetic materials and M-R sensors. He is a member of Institute of Electrical Engineers, U.K. and IEEE, USA.

# Domain Walls and Magnetic Properties of Very Thin Permalloy Films for Magnetoresistive Sensors

M. A. Akhter, D. J. Mapps and Y. Q. Ma  
C.R.I.S.T., SECEE, University of Plymouth, Plymouth, PL4 8AA, U.K.  
and

A. K. Petford-Long and R. Doole  
Department of Materials, University of Oxford, Oxford, OX1 3PH, U.K.

**Abstract**—The magnetic properties (coercivity and magnetoresistance) of very thin permalloy films were studied for their use in magnetoresistive (MR) sensors. Permalloy films were deposited under different conditions and a comparison was made in their properties. Domain walls in these films were studied using a specially modified TEM. Barkhausen noise was studied by differentiating the M-H characteristic and its origin is discussed in the context of the magnetic domain wall structures.

**Index Terms**—Barkhausen noise, Domain wall, Magnetoresistive sensors, Permalloy thin films.

## I. INTRODUCTION

Magnetoresistive materials have been intensively studied for their applications in recording heads and sensors [1]. Modern anisotropic magnetoresistive (MR) sensors require high sensitivity with low Barkhausen noise. To achieve this, MR sensors must be very thin, have high permeability and low coercivity. These magnetic properties are strongly dependent on the crystalline grain size, crystalline structure and the underlayer used [2]. In our last paper we presented the dependence of coercivity on the thickness and grain size in permalloy films in the range from 2.5 nm ~ 30 nm [3].  $\text{Ni}_{81}\text{Fe}_{19}$  films prepared under different deposition conditions of thickness in the range of 2.5 nm ~ 10 nm show a minimum in coercivity at a thickness of 7.5 nm at which the grain size is about 4 nm. This minimum in coercivity may be attributed to the grain size via its relationship with domain wall width. In this paper we report Lorentz TEM studies of magnetic domain wall images in very thin (5 ~ 30 nm) permalloy films with and without tantalum (Ta) underlayers. Crystallography of the films using electron diffraction microscopy was studied. Coercivity and anisotropic magnetoresistance coefficient results for these permalloy films with and without Ta underlayer are presented. The behaviour of these films under an ac applied field was studied and analysed to help understand the origin of Barkhausen noise.

## II. EXPERIMENTAL PROCEDURE

Preparation procedure and structural characterisation used in this work has been described previously [3]. Two sets of permalloy ( $\text{Ni}_{81}\text{Fe}_{19}$ ) thin films of 5 nm ~ 100 nm thickness with and without 5 nm Ta underlayers were prepared for this study. For Lorentz TEM image observation the specimens were deposited onto copper grids covered with very thin Formvar coatings on glass slips. Normally in permalloy films the anisotropy is self-selecting but in this case a 40 Oe field was used to select anisotropy direction during deposition and the direction of anisotropy was marked on each grid.

The domain wall images shown in this work were taken using a EOL-4000 microscope fitted with a JEOL AMG-40 low-field pole-

piece operating at 400 kV. With a modified pole-piece the specimen sits above the objective lens in a field free region. The microscope was operated in the long camera length mode of Fresnel imaging. This mode is particularly useful for revealing magnetic domain boundaries. For this work the objective lens setting was at 2.0 and camera length at 4.0 n.m. Magnification of the images is  $\times 260$  on the negative. The magnetic domain images presented here are approximately 28  $\mu\text{m}$  in diameter. The Electron diffraction pattern for each sample was taken which showed that the film structure was not affected by the sample preparation method for Lorentz TEM observations.

Barkhausen noise studies were carried out by sweeping an ac field of 77 Hz onto the permalloy films and recording the induced output voltage due to the flux change on a digital storage oscilloscope. Every time a number of plots were taken and when consistent, the plots for the rate of change of flux as a function of time were recorded from the oscilloscope.

Measurements of coercivity and anisotropic magnetoresistance coefficient were made by using in-house built equipment. Data for each measurement was averaged over five readings.

## III. RESULTS AND DISCUSSION

### (a) Coercivity Measurements

Easy axis coercivity for the films deposited with and without Ta underlayer are shown in Fig. (1). The coercivity for the permalloy films grown on Ta underlayer is slightly higher compared with the ones without Ta underlayer.

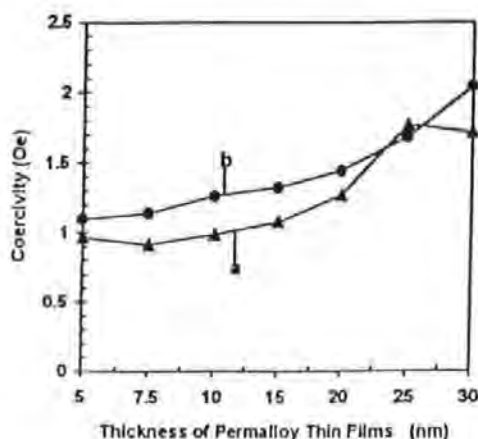


FIG. 1. Graph of Coercivity vs. Film Thickness for Permalloy ( $\text{Ni}_{81}\text{Fe}_{19}$ ) Thin Films (a) on glass substrate at normal temperature; (b) on glass substrate with 5 nm Ta underlayer at normal temperature.

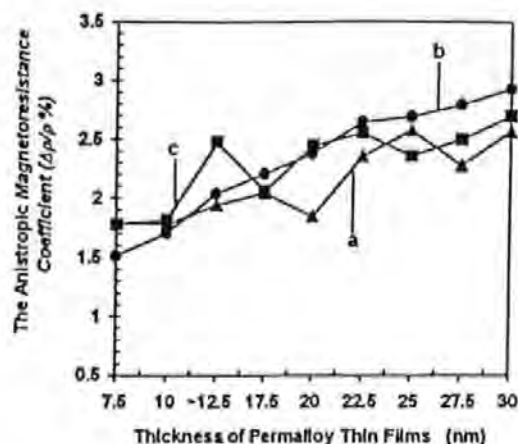


FIG. 2. Graph of The Anisotropic Magnetoresistance Coefficient ( $\Delta\rho/\rho\%$ ) vs. Film Thickness for Permalloy ( $\text{Ni}_{81}\text{Fe}_{19}$ ) Thin Films (a) on glass substrate at normal temperature; (b) on glass substrate with 5 nm Ta underlayer at normal temperature; (c) on glass substrate at 300°C.

#### (b) M-R Measurements

The results of anisotropic magnetoresistance coefficient for permalloy films deposited under different conditions are plotted in Fig. (2). This change is almost the same in thinner films but in permalloy thickness above 10 nm the change is slightly higher in the films grown on Ta underlayer. Also in this case the change is more stable.

#### (c) Barkhausen Noise Analysis

To analyse the Barkhausen noise the permalloy films were studied by applying an ac field ( $\pm 480$  A/m) of 77 Hz. The plots are shown in Fig. (3a to 3c). These plots are single test results but are representative of ~50 similar plots from a number of thin film samples for each case a, b, and c considered. The main peak is due to the magnetisation reversal of the films. The remaining part of the curve differs for each film and gives a qualitative insight into the Barkhausen noise. The large peak at 0.2 ms in Fig. (3a) is typical of a random Barkhausen peak in films deposited directly on glass at low temperature.

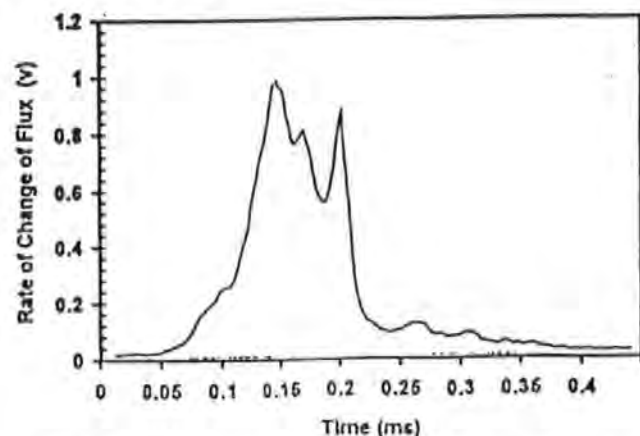


FIG. 3a. Rate of Change of Flux as Function of Time ( $\text{dB}/\text{dt}$ ) under an Applied ac Field of 77 Hz for a 20 nm  $\text{Ni}_{81}\text{Fe}_{19}$  Thin Film on Glass Substrate Deposited at normal temperature.

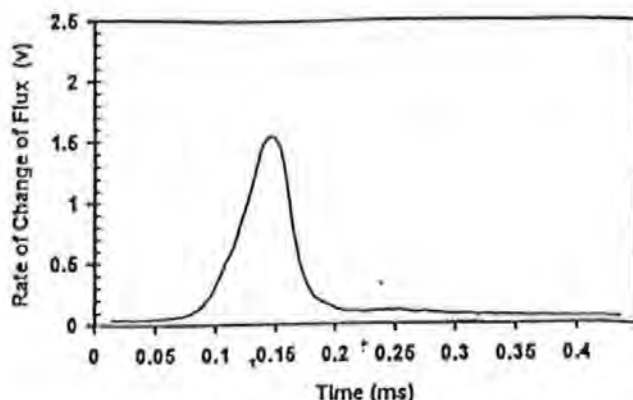


FIG. 3b. Rate of Change of Flux as Function of Time ( $\text{dB}/\text{dt}$ ) under an Applied ac Field of 77 Hz for a 20 nm  $\text{Ni}_{81}\text{Fe}_{19}$  Thin Film with 5 nm Ta Underlayer on Glass Substrate Deposited at normal temperature.

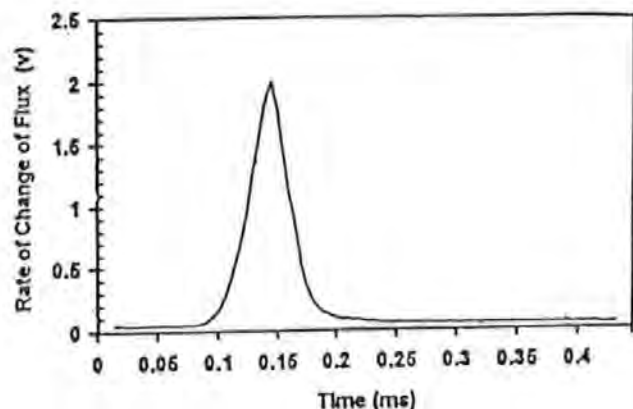


FIG. 3c. Rate of Change of Flux as Function of Time ( $\text{dB}/\text{dt}$ ) under an Applied ac Field of 77 Hz for a 20 nm  $\text{Ni}_{81}\text{Fe}_{19}$  Thin Film on Glass Substrate Deposited at 300 °C.

Comparison between the plots shows that the films deposited on glass substrates have more Barkhausen noise than the ones deposited on Ta or deposited at higher deposition temperature. We conclude that the films deposited with a Ta underlayer and at elevated temperatures have less Barkhausen noise. Our results also show that the Ta underlayer has very little effect on the reduction of Barkhausen noise below the permalloy film thickness of 20 nm.

#### (d) TEM Studies

In order to observe the domain wall patterns we studied the permalloy films with the Lorentz TEM. The domain wall images for 7.5 nm and 30 nm with and without Ta underlayer are shown in Fig. (4a to 4d). We observe that the domain walls of the films deposited without underlayer are very thin, irregular, closely spaced and have cross-ties. The domain wall width in this case is about 100 nm. Also the domain wall magnetization in adjacent domains vary in angle from  $90^\circ$  to  $180^\circ$  with strong rippling effect. On the other hand the domain walls in permalloy films deposited with a Ta underlayer are very well defined with less cross-ties. The domain wall width in this case is approximately 300 nm. Magnetization shows no rippling and the domain magnetisation rotates through  $90^\circ$  across the wall. Electron diffraction patterns for the films were studied. The films grown with Ta underlayer showed in-plane texture in permalloy induced due the presence of



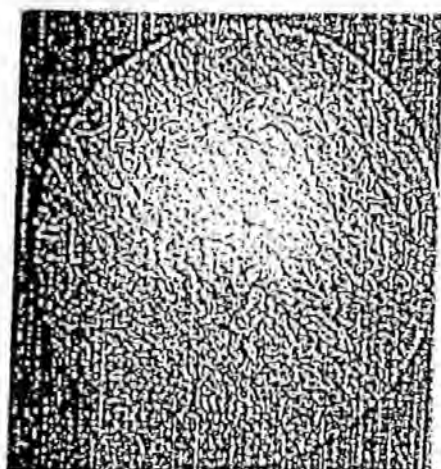


FIG. 4a. Lorentz TEM image of 7.5 nm  $\text{Ni}_{81}\text{Fe}_{19}$  Thin Film deposited at normal temperature. The size of magnetic domain image presented here is approximately 28  $\mu\text{m}$  in diameter.

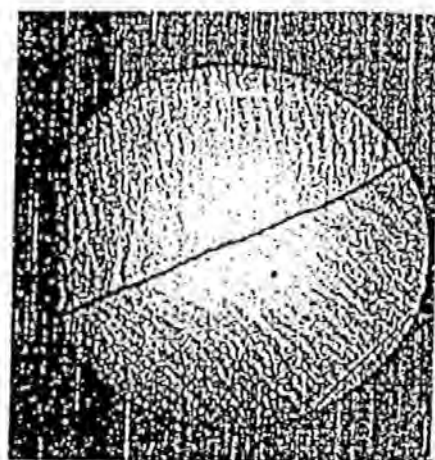


FIG. 4c. Lorentz TEM image of 7.5 nm  $\text{Ni}_{81}\text{Fe}_{19}$  Thin Film with 5 nm Ta underlayer deposited at normal temperature. The size of magnetic domain image presented here is approximately 28  $\mu\text{m}$  in diameter.

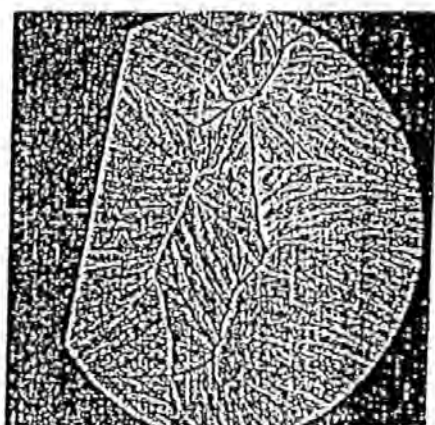


FIG. 4b. Lorentz TEM image of 30 nm  $\text{Ni}_{81}\text{Fe}_{19}$  Thin Film deposited at normal temperature. The size of magnetic domain image presented here is approximately 28  $\mu\text{m}$  in diameter.

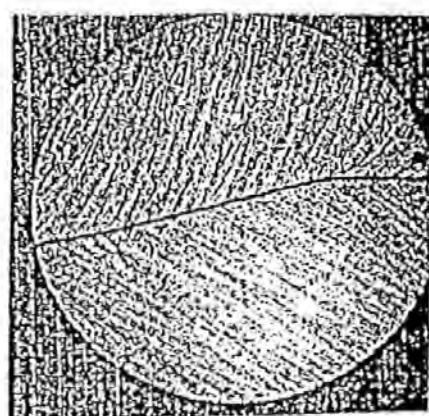


FIG. 4d. Lorentz TEM image of 30 nm  $\text{Ni}_{81}\text{Fe}_{19}$  Thin Film with 5 nm Ta underlayer deposited at normal temperature. The size of magnetic domain image presented here is approximately 28  $\mu\text{m}$  in diameter.

Ta, while the films grown without Ta underlayer had all rings showing fcc structure and there was a random texture.

The Barkhausen noise in permalloy films deposited on a Ta underlayer and the ones deposited directly on glass but at higher temperature is less compared with the films deposited directly on glass at normal temperature. This may be attributed to wider, straight and regular domain walls and is due to less rippling in magnetisation adjacent to the walls. This reduction in Barkhausen noise may also be due to less defects, smaller grain size and the microstructure of the films grown on Ta underlayer.

#### IV. CONCLUSIONS

Our study shows that the domain wall configuration and magnetisation play a dominant role in the properties of permalloy films for their use in recording heads and sensors. The domain walls structure and the state of magnetization in the very thin (5–30 nm) permalloy films with and without tantalum underlayers are different. With no Ta underlayer the domain walls are very thin, irregular, closely spaced and have cross-ties. Domain wall width in this case is about 100 nm. Also the domain magnetization varies in angle from  $90^\circ$  to  $180^\circ$  in adjacent walls with a strong rippling. But with 5 nm Ta underlayer, the domain walls are wider,

straight and have less cross-ties. The domain magnetization changes in angle by  $90^\circ$  across the wall with no rippling. The width of domain walls in this case is about 300 nm. The domain size in permalloy films with Ta underlayer is much bigger than the ones without Ta, which will reduce the Barkhausen noise. The wider, straight and regular domain walls with less rippling in magnetization in the adjacent walls reduces the Barkhausen noise. The reduced Barkhausen noise may also be due to less defects, smaller grain size and microstructure of the films grown on Ta underlayer [3]. The reduction in Barkhausen noise can be achieved by depositing the films at elevated temperatures.

#### REFERENCES

- [1] C. Tsang, T. Lin, S. MacDonald, et al., "5 Gbit/in<sup>2</sup> recording demonstration with conventional AMR dual element heads & thin film disks", *IEEE Trans. Magn.* Vol. 33 No. 5, pp2866-2871, Sept., 1997.
- [2] P. Galtier, R. Jerome and T. Valet, "Texture and grain size of permalloy thin films sputtered on silicon with Cr, Ta, and SiO<sub>2</sub> buffer layers", *Mater. Res. Soc. Symp. Proc.* 313, pp 417-422, 1993.
- [3] M. A. Akhter, D.J. Mapps, Y. Q. Ma Tan, A. Petford-Jones and R. Doolie "Thickness and grain size dependence of the coercivity in permalloy thin films." *J. Appl. Phys.* Vol. 81, No.8, pp4122-4124, 15 April 1997.

# Thickness and grain-size dependence of the coercivity in permalloy thin films

M. A. Akhter, D. J. Mapps, and Y. Q. Ma

Centre for Research in Information Storage Technology, S.E.C.E.E., University of Plymouth, Plymouth, PL4 8AA, England

Amanda Pettford-Long and R. Doole

Department of Materials, University of Oxford, Oxford, OX1 3PH, England

This paper reports the effect of thickness and grain size on the coercivity of  $\text{Ni}_{81}\text{Fe}_{19}$  permalloy thin films (2.5–30 nm) sputtered on glass substrates for their application in magnetoresistive sensors. Coercivity was systematically investigated as a function of underlayer materials, thickness, and substrate temperature. Lateral grain size of the sputtered films was investigated. The grain size reduced very quickly in the thinner films. It was also found that the coercivity of the films with very small lateral grain size is much lower than those with a normal grain size. The lowest coercivity ( $H_c = 0.8$  Oe) was observed in 7.5 nm thick film and having a grain size of 4 nm. When an underlayer is used, its crystallinity affects the lateral grain size in the permalloy and correlates with the observed coercivity variation [P. Galtier, R. Jerome, and T. Valet, *Mater. Res. Soc. Symp. Proc.* **313**, 417 (1993).] It was also observed that the coercivity of the permalloy is dependent on the nature of the underlayer. It was established that the coercivity of  $\text{Ni}_{81}\text{Fe}_{19}$  films increases when the thickness increased from a critical film thickness and grain size. The variation of the coercivity in thin  $\text{Ni}_{81}\text{Fe}_{19}$  films with lateral grain size and relationship with domain-wall width is discussed and compared with other theories for magnetization reversal. © 1997 American Institute of Physics. [S0021-8979(97)25008-5]

## INTRODUCTION

Intensive studies have been made on magnetoresistive materials for their application in sensors and recording heads.<sup>1</sup> For this purpose one has to look for materials with low coercivity, near zero magnetostriction, and low noise.  $\text{Ni}_{81}\text{Fe}_{19}$  as the magnetic material has been studied to a great depth for this purpose. It is well known that the magnetic properties of this permalloy are very sensitive to the preparation methods and also are effected by the underlayers used.<sup>2</sup> For this purpose, we have undertaken a study of structural (in particular grain size) and magnetic properties of  $\text{Ni}_{81}\text{Fe}_{19}$  thin films in the range from 2.5 to 30 nm. To a certain limitation, we have also studied the effect of substrate temperature on the magnetic properties of this material.

## EXPERIMENTAL PROCEDURE

$\text{Ni}_{81}\text{Fe}_{19}$  thin films were prepared using rf sputtering in a UHV high-vacuum deposition chamber. To reduce any oxygen in the film a low base pressure of  $2 \times 10^{-7}$  Torr was used although high base pressures (up to  $2 \times 10^{-6}$ ) are not a critical factor for oxygen contamination.<sup>3</sup> Also, by sputtering with negative substrate bias, film contamination is reduced. Experiments with 5 nm capping layers of Ta showed that surface absorption of oxygen was not a factor in changing coercivity after sample removal from the sputtering system. Samples were preheated to 300 °C prior to deposition.<sup>4</sup> In  $\text{NiFe}$  films, anisotropy is self-selecting but alignment can be determined and, in this case, a 40 Oe field was used. All targets used for deposition were of "999" research grade and were precleaned by plasma etching. Film thicknesses were measured by Talystep within an accuracy of  $\pm 1$  nm and averaged for five measurements. These were confirmed

by scanning electron microscopy. Coercivities of the films were measured using a laboratory built B-H testing instrument and were averaged for five measurements. Microstructures of the permalloy films were studied by transmission electron microscopy (TEM) images, electron diffraction patterns and x-ray diffraction. Experiments showed that the film structure was not affected by the sample preparation method for TEM measurements.

## III. RESULTS

### A. Magnetic properties

Four sets of multilayer structures were studied: (a)  $\text{Ni}_{81}\text{Fe}_{19}$  deposited on glass at a substrate temperature of 20 °C; (b)  $\text{Ni}_{81}\text{Fe}_{19}$  deposited on glass at a substrate temperature of 300 °C; (c)  $\text{Ni}_{81}\text{Fe}_{19}$  deposited on glass with 5 nm of  $\text{SiO}_2$  as underlayer at a substrate temperature of 20 °C, and (d)  $\text{Ni}_{81}\text{Fe}_{19}$  deposited on glass with a 5 nm of Ta underlayer at a substrate temperature of 20 °C. A set of samples was studied with permalloy thickness varying from 2.5 to 30 nm. The results of coercivity measured from B-H plots as a function of permalloy thickness are shown in Fig. 1. The plots in each case show a minimum in coercivity at 7.5 nm film thickness of  $\text{Ni}_{81}\text{Fe}_{19}$  permalloy. We found some change in coercivity as a function of substrate temperature.

### B. Structural properties

The TEM images are shown in Fig. 2 and 3. The microstructure of the films was studied for  $\text{Ni}_{81}\text{Fe}_{19}$  films deposited on a microscope grid. In each case, the darker regions correspond to the  $\text{Ni}_{81}\text{Fe}_{19}$  and the pale regions inbetween are the carbon underlayer as the grids were not cleaned prior to deposition. It can be seen that the films are not continuous

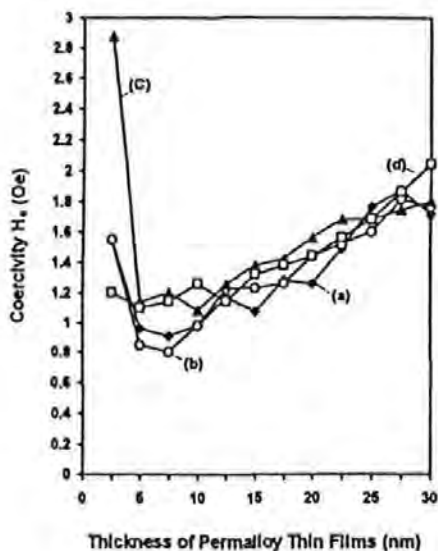


FIG. 1. Graphs of Coercivity vs. film thickness for  $\text{Ni}_{81}\text{Fe}_{19}$  films deposited on various surfaces. (a) on glass substrate at 20 °C; (b) on glass substrate at 300 °C; (c) on glass substrate with 5 nm  $\text{SiO}_2$  underlayer at 20 °C.

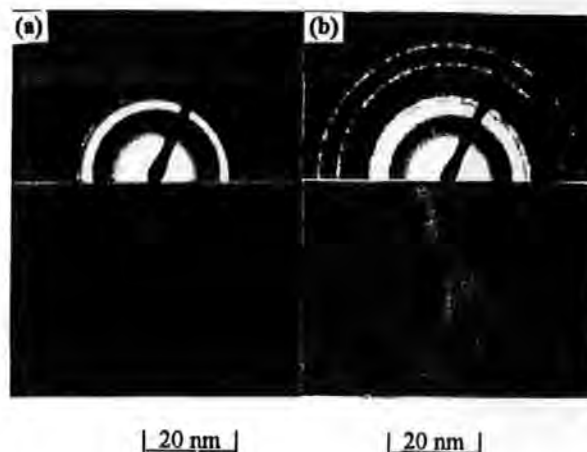


FIG. 3. (a) The TEM image and Electron Diffraction pattern of 7.5 nm thin film of  $\text{Ni}_{81}\text{Fe}_{19}$ . (b) The TEM image and Electron Diffraction pattern of 10 nm thin film of  $\text{Ni}_{81}\text{Fe}_{19}$ .

centered-cubic (fcc) became more clear. The ring diameter ratios are exact for a fcc structure and there is a random texture.

#### IV. DISCUSSION

Comparing the change in coercivity against thickness and the change in grain size against thickness for such thin  $\text{Ni}_{81}\text{Fe}_{19}$  films, it is clear that as the grain size changes so does the coercivity. We can see a minimum in coercivity at a grain size of about 4 nm, Figs. 1 and 4. It is also a well-known fact that for the grain size lower than 30 nm, the Barkhausen noise decreases.<sup>5</sup> A large number of publications have been produced showing that the wall energy is a function of the volume of the material it occupies,<sup>6</sup> so when part of the wall moves to a point where it occupies less volume (e.g., when it becomes shorter because of an edge defect in the film or when it intersects a nonmagnetic inclusion) this represents a low energy state. The depth of the local energy minima depends on the size of the defect or inclusion and the

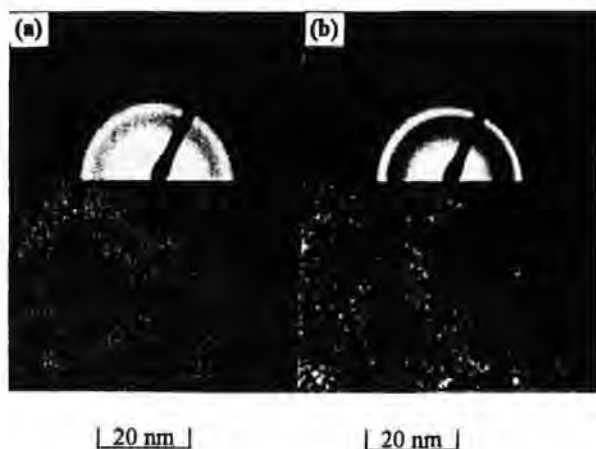


FIG. 2. (a) The Transmission Electron Microscopy (TEM) image and Electron Diffraction pattern of 2.5 nm thin film of  $\text{Ni}_{81}\text{Fe}_{19}$ . (b) The TEM image and Electron Diffraction pattern of 5 nm thin film of  $\text{Ni}_{81}\text{Fe}_{19}$ .

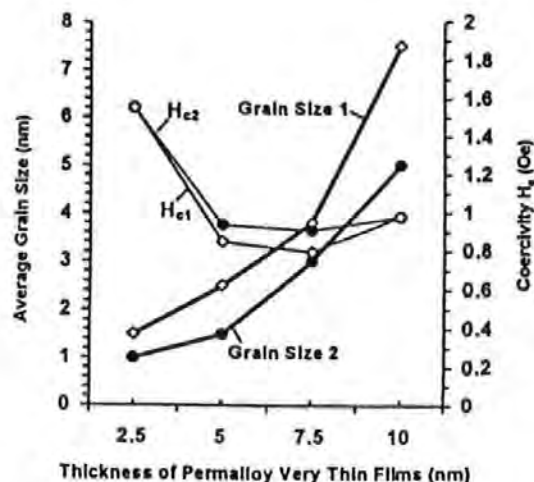


FIG. 4. Coercivity vs Grain size of  $\text{Ni}_{81}\text{Fe}_{19}$  thin films. Set 1 for  $\text{Ni}_{81}\text{Fe}_{19}$  thin film deposited at 300 °C. Set 2 for  $\text{Ni}_{81}\text{Fe}_{19}$  thin film deposited at 20 °C.



## **Bibliography**

[Akhter et al., 1997] M. A. Akhter, D. J. Mapps, Y. Q. Ma, A. Petford-Long and R. Doole, Thickness and grain-size dependence of the coercivity in permalloy thin films, *J. Appl. Phys.*, Vol. 81 (8), p4122~4124 1997.

[Akhter et al., 1998] M. A. Akhter, D. J. Mapps, Y. Q. Ma, A. Petford-Long and R. Doole, Domain Walls and Magnetic Properties of Very Thin Permalloy Films for Magnetoresistive Sensors, *IEEE Trans., Magn.*, Vol.34, No. 4, p1147~1149, 1998.

[Barkhausen, 1919] H. Barkhausen, *Physik Z.*, Vol. 20, p401, 1919.

[Bauer, 1963] E. Bauer, Growth of Oriented films on amorphous surface, p44-67, 1963.

[Brailsford 1966] F. Brailsford, *Physical Principles of Magnetism*, LCCC No 66-21547, D. Van Nostrand Co Ltd, London, 1966.

[Carey and Isaac, 1965] R. Carey and E.D. Isaac, *Magnetic domains and techniques for their observation*, LCCN 65-28612, Academic Press Inc. New York, 1965.

[Chapman, 1980] B. Chapman, *Glow discharge processes: sputtering and Plasma etching*, John Wiley & sons, Inc., ISBN 0471-07828-X, New York, 1984.

[Chapman, 1984] J.N. Chapman, The investigation of magnetic domain structures in thin foils by electron microscopy, *J. Phys. D: Appl. Phys.*, Vol. 17 p623-647, 1984.

[Chapman and Kirk, 1997a] J N Chapman and K J Kirk, Domains, domain walls and the magnetisation reversal process, in G. C. Hadjipanayis (ed) *Magnetic Hysteresis in Novel Magnetic Materials*, Kluwer Academic Publishers., , the Netherlands, p207-214, 1997.

## *Bibliography*

**[Chapman and Kirk, 1997b]** J N Chapman and K J Kirk, Domains, Imaging magnetic structures in the transmission electron microscope, in G.C. Hadjipanayis (ed) *Magnetic Hysteresis in Novel Magnetic Materials*, Kluwer Academic Publishers, the Netherlands, p195-205, 1997.

**[Chen, 1977]** C W Chen, *Magnetism and metallurgy of soft magnetic materials*, North-Holland Publishing Company, Amsterdam, ISBN 0 7204--0706-0, 1977.

**[Chikazumi, 1964]** S. Chikazumi, *Physics of magnetism*, John Wiley & Sons, New York, LCCCN: 64-14985, 1964.

**[Ciureanu, 1992]** P. Ciureanu et al., *Magnetoresistive Sensor*, in *Thin Film Resistive Sensors*, ch. 5, ISBN 0-7503-0173-2, IOP Publishing Ltd, 1992.

**[Daykin and Petford-Long, 1995]** A.C. Daykin and A.K. Petford-Long, Quantitative mapping of the magnetic induction distribution using Foucault images formed in a transmission electron microscopy, *Ultra-microscopy* Vol. 58, p365-380, 1995.

**[Decker and Tsang, 1980]** S.K. Decker, C. Tsang, Magnetoresistive response of small permalloy features, *IEEE. Trans. on Magn.*, Vol. Mag-16, No.5, p643-645, 1980.

**[Decker et al., 1981]** S.K. Decker, J. Dittmar and C. Tsang, Barkhausen noise characteristics of magnetoresistive sensors of different thickness, *IEEE, Trans. Magn.* Vol. Mag-17, No 6, p2662-2664, 1981.

**[Dibbern et al., 1983]** U. Dibbern et al., The Magnetoresistive Sensor-a Sensitive Device for Detecting Magnetic Field Variations, *Electronic Components and Applications*, Vol.5, No.3, p148~153, 1983.

**[Doole, 1996]** R Doole, The Lorentz TEM observation Lab. Notebook, 1996.

**[Engelman and Hardwick, 1963]** J.H. Engelman and A.J. Hardwick, *Trans. 9th National Vacuum Symposium*, New York : Macmillan, p100, 1963.

## *Bibliography*

[Farrel, 1994] G. P. Farrel, The Barkhausen Effect in Single layer and multilayers Thin Ni-Fe Films, *PhD Thesis* in Univ. Of Manchester, 1994.

[Flur, 1967] B. L. Flur, On the Magnetic Properties of Sputtered NiFe Films, *IBM J.* p563 ~569, Sept., 1967.

[Flynn, 1994] D.I. Flynn, A new Technique of Noise Reduction for large aspect magnetoresistor, *IEEE Trans. on Magn.*, Vol. 30 No. 3, p1263-1266, 1994.

[Flynn and Shi, 1994] D.I. Flynn and X. Shi, A mechanism for obtaining a single magnetisation state in permalloy films, *J. Appl. Phys.* 75(7), p3674-3677, 1994.

[Gallagher et al., 1997] W. J. Gallagher et al., Microstructured magnetic tunnel junctions, *J. Appl. Phys.* 81 (8), No. 8, p3741~3746, 1997.

[Galtier et al., 1993] P. Galtier, R. Jerome and T. Valet, Texture and Grain Size of Permalloy Thin Films Sputtered on Silicon with Cr, Ta and SiO<sub>2</sub> Buffer Layers, *Mat. Res. Soc. Symp. Proc.* Vol. 313. P417~423, 1993.

[Gill and Yamashita, 1984] H.S.Gill and T.Yamashita, The growth characteristics of ion-beam sputtered CoCr films on Ta isolation layers, *IEEE. Trans. on Magn.*, Vol. Mag-20, No. 5, p776-778, 1984.

[Grundy, 1997] P. J. Grundy, Microstructure and coercivity in thin films and multilayers, in G.C. Hadjipanayis(ed.), *Hysteresis in Novel Magnetic Materials*, p453-465, Kluwer Academic Publishers, the Netherlands, 1997.

[Heremans, 1993] J. Heremans, Solid State Magnetic Filed Sensors and Applications, *Phys. D: Appl. Phys.* Vol. 26, p1149~1168, 1993.

[Herzer, 1990] G., Herzer, Grain Size Dependence of Coercivity and Permeability in Nanocrystalline Ferromagnetism, *IEEE Trans., Magn.*, Vol. 26, p1397~1402, 1990.

[Herzer, 1995] G. Herzer, Soft Magnetic Nanocrystalline materials, *Scripta Metallurgica et Materialia*, Vol.33, Nos. 10/11, p1741-1756, 1995.

## *Bibliography*

[Hill et al., 1991] E. W. Hill, J.P. Li and J.K. Birtwistle, Magnetic and Structural Properties of Permalloy-tantalum Multi-layer Thin Films, *J. Appl. Phys.* 69(8), p4526-4628, 1991.

[Hoffmann, 1964] H. Hoffmann, Quantitative calculation of the magnetic ripple of uniaxial thin permalloy films, *J. of Applied physics*, Vol.35, No.6, p1790~1798, 1964.

[Hoffmann, 1979] H. Hoffmann, Magnetic Properties of Thin Ferromagnetic Films in Relation to Their Structure, *Thin Solid Films*, Vol. 58, p223~233, 1979.

[Hosono and Shimada, 1990] A. Hosono and Y. Shimada, Crystal structure and magnetic softness of Fe-Si polycrystalline films, *J. Appl. Phys.* Vol. 67, No. 11, p6981-6990, 1990.

[Hou, et al., 1997] C. Hou, H. Fujiwara, T. J. Klemmer, R. M. Metzger and W. D. Doyle, Thermal effect on the coercivity of ultrathin NiFe films, *IEEE Trans. Magn.*, Vol. 33, No. 5, Spet., 1997 pp3625 ~ 3627.

[Hunt, 1971] R. P. Hunt, A Magnetoresistive Readout Transducer, *IEEE Trans. Magn.* Vol. 7, No1 1971.

[Huo et al., 1998] S. Huo, G. Pan, D. J. Mapps, W. W. Clegg, G. Heydon and W. M. Rainforth, Dependence of domain wall structures on the thickness of  $\text{Co}_{91}\text{Nb}_6\text{Zr}_3$ , *Paper accepted for J. Magn. Magn. Mater.* 1998.

[Jahnes et al., 1992] C.V. Jahnes, M.A. Russak, B. Petek and E. Klokholm, Ion beam sputter deposited permalloy thin film, *IEEE Trans. on Magn.* Vol. 28, No. 4, p1904-1910, 1992.

[Jenkins, 1995] T E Jenkins, Semiconductor science growth and characterisation techniques, *Prentice Hall International UK Ltd., ISBN 0-13-805771-0*, New York, 1995.

## *Bibliography*

**[J  rome et al., 1994]** R. J  rome et al., Correlation Between Magnetic and Structural Properties of Ni<sub>80</sub> Fe<sub>20</sub> Sputtered Thin Films Deposited on Cr and Ta Buffer Layers, *IEEE Trans. Magn.* Vol. 30, No.6, p4878~4880, Nov. 1994.

**[Jiles, 1991]** D. Jiles, *Introduction to Magnetism and Magnetic Materials*, ISBN 0-412-38640-2, Chapman & Hall, London, 1991.

**[Jhingan et al., 1984]** A.K. Jhingan, R.R. Dubin and L.F. Herte, Film growth characterisation of an underlayer for perpendicular magnetic recording, *IEEE Trans. on Magn.*, Vol. Mag-20, No. 5, 1984.

**[Kempter and Hoffmann, 1969]** Investigation of the structure of ferromagnetic films by means of the differential susceptibility., *Phys. Stat sol.*34., p237~248, 1969.

**[Kempter and Hoffmann, 1970]** The dependence of the structure constant of uniaxial permalloy films on the evaporation temperature and the alloy composition., *Journal De Physique*, Vol. 32., C1-397, p396~398, 1970.

**[Kim and Oliveria, 1993]** Y.K. Kim and M. Oliveria, Magnetic properties of sputtered Fe thin films: processing and thickness dependence, *J. Appl. Phys.* Vol. 74, No. 2, p1233 - 1241, 1993.

**[Kim and Slive., 1996]** Y.K. Kim and T.J. Silva, Magnetorestriction characteristics of ultrathin permalloy films, *J. Appl. Phys. Lett.*, Vol. 68, (20), 1996.

**[Krongelb, 1973]** S. Krongelb, The preparation and properties of magnetoresistive Permalloy films, *J. of Electronic materials*, Vol.2, No.2, p227-238, 1973.

**[Kronmuller, 1992]** H. Kronmuller, Coercivity Mechanism in Modern Magnetic Material, *Proc. Magneto-Optic Recording Int. Symp. J. Magn. Soc. Jpn.* 17, S1 p260, 1992.

## *Bibliography*

[Lee, et al., 1994] W.Y. Lee, G. Gorman, and R. Savoy, Giant magnetoresistance in as-sputter-deposited Au/NiFe multi-layer thin films, *Mat. Res. Spc. Symp. Proc.* Vol. 343, p405-410, 1994.

[Lenz, 1990] J.E. Lenz, A Review of Magnetic Sensors, *Proc. IEEE* Vol. 78, No.6, p973~989, 1990.

[Li et al., 1994] S Li, M Yan, C Yu and W Lai, Effect of interface on the properties of Ti/NiFe thin films, *J. Appl. Phys.*, Vol. 75, No.10, p6504~6506, 1994.

[Lin et al., 1994] Lin J. C., Chen L.J., and Chen C. J., Effects of nitrogen content on the microstructure and magnetic properties of FeTaN films, *IEEE Trans. Magn.*, No:30, p3912-3914, 1994.

[Lo and Hanson, 1969] D. S. Lo and M. M. Hanson, Magnetic Properties and creep observations of Ni-Fe Films 30 to 300 Å, *IEEE Trans. on Magn.* Vol. MAG-5, No.2, p115 ~ 117, 1969.

[Lo et al., 1987] J. Lo, C. Hwang, T. C. Huang and D Allee, Magnetic and structural properties of high rate dual ion-beam sputtered NiFe films, *J. Appl. Phys.*, 61(8), p3520 ~ 3525, April 1987.

[Lorentz et al., 1996] H Lorentz, et al., EPON SU-8: A low cost negative resist for MEMS, *SUSS report*, Vol 10, Q3/Q4, p1~3, 1996.

[Ma,1996] Y. Q. Ma, *Mphil/PhD transfer report*, at the University of Plymouth, 1996.

[Ma,1997] Y. Q. Ma, *Report for new mask design and fabrication of MR sensors*, at the University of Plymouth, 1997.

[Maissel and Glang, 1970] L.I. Maissel and R. Glang (ed.), *Handbook of thin film technology*, McGraw-Hill Book Company, New York, 1970.



## *Bibliography*

**[Mapps et al., 1985]** D. J. Mapps et al., Asymmetric biasing fields from mismatched current-carrying overlay conductors on magnetoresistive replay sensors, *J. Appl. Phys.*, Vol. 57 (1), p3982 ~ 3984, 1985

**[Mapps and Watson, 1985]** D.J. Mapps and M. L. Watson, Thin f-lm magnetoresistive sensors for Earth's field detection, Internal report at Plymouth Polytechnic, 1985.

**[Mapps, 1987]** D. J. Mapps, Innovative methods for teaching the fundamentals of Magnetism, Paper at *UNESCO-SEFI International Symposium on Innovative Methods in Technological Education*, 1987.

**[Mapps et al., 1987]** D. J. Mapps, M. L. Watson and N. Fry, A double bifilar magnetoresistor for Earth's field detection, *IEEE, Trans. On Magn.* Vol. Mag-23, No.5, pp2413 ~ 2415, 1987.

**[Mapps,1991]**, D. J. Mapps, British Patent No 2262635, 8th November, 1991.

**[Mapps et al., 1991]** D. J. Mapps et al, Cobalt-Niobium-Iron Soft Magnetic Back Layer for Glass Computer Disks, *J. of Appl. Phys.*, Vol. 69, No. 8, p5178 ~ 5180, 1991.

**[Mapps, 1994]** D. J. Mapps, Magnetoresistance, an chapter in R. Gerber et al., (ed.) *Applied Magnetism*, Kluwer Academia Pub., p376 ~ 406, the Netherlands, 1994.

**[Mapps, 1997]** D. J. Mapps, Magnetoresistive Sensor, *J. Sensors and Actuators A* 59., p9 ~ 19, 1997.

**[Mapps et al., 1998]** D.J. Mapps, Y.Q. Ma and M. A. Akhter, Optimisation of material and structure for a switched-bias magnetoresistive sensor, in press at *J. Sensors and Actuators*, 1998.

**[Matzkanin et al., 1979]** G.A. Matzkanin, R. E. Beissner and C. M. Teller, The Barkhausen effect and its applications to non-destructive evaluation, *NTIAC-79-2* p1~49, 1979

## *Bibliography*

[McClure and Schroder, 1976] J.C. McClure, and J.K. Schroder, The Barkhausen effect, *CRC Critical reviews in Solid State Sciences*, p45-83, Jan., 1976.

[Methfessel et al., 1960] S. Methfessel, S. Middelhoek and H. Thomas, *IBM, J. Research Develop*, Vol: 4, p96, 1960.

[Middelhoek, 1961] S. Middelhoek, Ferromagnetic Domain in thin Ni-Fe films, *Thesis*, University of Amsterdam, Holland, 1961.

[Middelhoek, 1963] S. Middelhoek, Domain walls in thin Ni-Fe films, *J. of Appl. Phys.*, Vol.34, No.4 (part 2), p1054-1059, 1963.

[Miller et al., 1994] M.S. Miller et al., Influence of r.f. magnetron sputtering conditions on the magnetic, crystalline, and electrical properties of thin nickel films, *J. Appl. Phys.* Vol. 75, No.10, p5779-5781, 1994.

[Miltat, 1994] J Miltat, Domains and domain walls in soft magnetic materials, an chapter in R. Gerber et al., (ed.) *Applied Magnetism*, Kluwer Academia Pub., p221-308, the Netherlands, 1994.

[Narayan et al., 1992] P B Naarayan, R D Silkensen, S Bryant and S Dey, *IEEE, Trans. Magn.* Vol. 28, p2934, 1992.

[Néel, 1946] L. Néel, Principles of a New General Theory of the Coercive Force, *Ann Univ. Gerenable*, 22 p299~341, 1946.

[Néel, 1955] L. Néel, Energie des parois de Bloch dans les couches minces, *Compt. Rend. Acad. Sci. Paris*, Vol. 241, p533-536, 1955.

[Nishioka et al., 1996] K. Nishioka et al., *J. Applied Physics*, Vol:79, p4970, 1996.

## *Bibliography*

**[Noreika & Francombe, 1962]** A. J. Noreika and M. H. Francombe, Factors Influencing Coercive Force Values in Sputtered Permalloy Films, *J. Applied. Physics.*, Vol.33, No 3, p1119 ~ 1120, 1962.

**[Ohring,1992]** M. Ohring, *The materials science of thin films*, Academic Press, ISBN 012-524990-X, San Diego, 1992

**[Pan, 1993]** G. Pan, Investigation into the microstructure, magnetic properties and read/write performance of thin-film media for perpendicular recording computer disks, *PhD thesis*, at University of Plymouth, 1993.

**[Petford-Long, 1996]** A. K. Petford-Long, *Private communication*, 1996

**[Pfeifer and Radeloff, 1980]**, F Pfeifer and Radeloff, Soft Magnetic NiFe and CoFe alloys—some physical and metallurgical aspects, *J. of Magn. Magn. Mat.*, Vol.19, p190~207, 1980.

**[Prutton, 1964a]** M. Prutton, The Structure and Properties of Ferromagnetic Films, *Brit. J. Applied. Physics.*, Vol. 15 p815~824, 1964.

**[Prutton, 1964b]** M. Prutton, *Thin ferromagnetic films*, Butterworths & Co. (Pub) Ltd., London, 1964

**[Rijks et al., 1995]** Th. G.S.M. Rijks, R.L.H. Sour, et al., Influence of grain size on the transport properties of Ni<sub>80</sub>Fe<sub>20</sub> and Cu thin films, *IEEE trans. on Magn.* Vol. 31, No. 6, p3865-3867, Nov. 1995.

**[Smith et al., 1991]**N. Smith et al., A High-sensitivity magnetoresistive magnetometer, *J. Appl. Phys.* 69(80) 15 p5082~5084, 1991.

**[Stewart, 1991,1992 and1993]** K. Stewart, Serpentine thin film magnetoresistive sensors for navigational applications, 1st, 2nd, 3rd, 4th, six-monthly reports, at Polytechnic Plymouth and university of Plymouth, 1991,1992,1993.

## *Bibliography*

**[Takahashi and Shimatsu, 1990]** Takahashi M. and Shimatsu T., Soft magnetism of crystalline Fe-based alloy sputtered films, *IEEE Trans. Magn.*, No:26, p1485~1490, 1990.

**[Tsang and Decker, 1981]** C. Tsang and S.K. Decker, The origin of Barkhausen in small permalloy magnetoresistive sensors, *J. Appl. Phys.* 53 (3), 2465~2467, 1981.

**[Tsang and Decker, 1982]** C. Tsang and S.K. Decker, Study of domain formation in small permalloy magnetoresistive elements, *J. Appl. Phys.* 53 (3), 2602~2604, 1982.

**[Tsang et al, 1991]** C. Tsang et al., Design and Performance Considerations in High Density Longitudinal Recording, *J. Appl. Phys.* 69(8), p5393~5398, 1991.

**[Tsang et al., 1993]** C. Tsang et al., Gigabit-Density Magnetic Recording, *Proc. of IEEE* Vol. 81, No8 p1344 ~ 1359, 1993.

**[Tsang et al, 1996]** C. Tsang et al., 3 Gb/in<sup>2</sup> Recording Demonstration with Dual Element Heads & Thin Film Disks, *IEEE Trans. Magn.* Vol. 32 No.1, p7 ~12, 1996.

**[Tsang et al, 1997]** C. Tsang, T Lin, S MacDonald, et al., 5 Gb/in<sup>2</sup> Recording Demonstration with Conventional AMR Dual Element heads & Thin Film Disks, *IEEE Trans. Magn.* Vol. 33 No. 5, pp2866-2871, Sept., 1997.

**[Watson, 1986]** M L Watson, A multiple-film magnetoresistive replay head for audio applications, *PhD thesis*, at the University of Plymouth, U.K 1986

**[Williams and Carter, 1996]** D.B. Williams and C.B. Carter, *Transmission Electron Microscopy*, Plenum Press, New York, 1996.

**[Wikswo, 1995]** J. P. Wikswo, SQUID magnetometers for bio-magnetism and non-destructive testing: important question and initial answer, *IEEE trans.on Appl. Superconductivity*, Vol. 5, No2, p1-7, 1995.

## *Bibliography*

**[Yeh et al., 1987]** T. Yeh, M Sivertsen and J H Judy, Thickness Dependence of the Magnetoresistance Effect in RF Sputtered Thin Permalloy Films, *IEEE Trans. Magn.* Vol.23, No.5 p2215~2217, 1987.

**[Yoshizawa et al., 1988]** Y. Yoshizawa et al., New Fe-Based Soft Magnetic Alloys Composed of Ultra-fine Grain Structure, *J. Appl. Phys.*, Vol. 64, p6044~6046, 1988.